Metallocluster Site-Differentiation and Subsite Specific Heterometal Substitution

Trever M. Bostelaar

B.S. Chemistry, University of Michigan (2017)
M.S. Chemistry, University of Michigan (2018)

Submitted to the Department of Chemistry in partial fulfillment
of the requirements for the degree of

Doctor of Philosophy in Chemistry

at the

Massachusetts Institute of Technology

September 2023

Signature of author:____
Department of Chemistry
August 18th, 2023

Certified by: ____
Daniel L.M. Suess
Associate Professor of Chemistry
Thesis Supervisor

Accepted by: ____
Adam Willard
Professor of Chemistry
Graduate Officer

This doctoral thesis has been examined by a committee of the
Department of Chemistry as follows:

Professor Yogesh Surendranath: ____

Thesis Committee Chair
Professor of Chemistry

Professor Daniel L.M. Suess: ____

Thesis Supervisor
Associate Professor of Chemistry

Professor Christopher C. Cummins: ____

Thesis Committee Member
Henry Dreyfus Professor of Chemistry

Metallocluster Site-Differentiation and Subsite Specific Heterometal Substitution

Trever M. Bostelaar

Submitted to the Department of Chemistry on August 18th, 2023 in partial fulfillment of the requirements for the degree of Doctor of Philosophy in Chemistry

Abstract

The deployment of metalloclusters in applications such as catalysis and materials synthesis requires robust methods for site-differentiation: the conversion of clusters with symmetric ligand spheres to those with unsymmetrical ligand spheres. However, imparting precise patterns of site-differentiation is challenging because, compared with mononuclear complexes, the ligands bound to clusters exert limited spatial and electronic influence on one another. In Chapter 2, we described a method that used sterically encumbering ligands to bind to only a subset of a cluster's coordination sites. Specifically, we showed that homoleptic, phosphine-ligated Fe–S clusters undergo ligand substitution with *N*-heterocyclic carbenes to give heteroleptic clusters in which the resultant clusters' site-differentiation patterns are encoded by the steric profile of the incoming *N*-heterocyclic carbene. This method afforded access to every site-differentiation pattern for cuboidal $[Fe_4S_4]$ clusters and was extended to other cluster types in Chapter 3, particularly in the stereoselective synthesis of site-differentiated Chevrel-type $[Fe_6S_8]$ clusters. In Chapter 4, we further utilized the 3:1 site-differentiation of cuboidal $[M_4S_4]$ (M = Fe or Co) clusters to perform subsite specific metal atom substitution at each cluster. Specifically, we showed that the unique metal sites of homometallic clusters of the form $[M_4S_4(IMes)_3Cl]^+$ can be selectively excised by addition of 2 equiv TlTp. Reconstitution with $M'Cl_2$ (M′ = Co, Fe, for M = Fe, Co, respectively) yielded the heterometallic clusters $[CoFe_3S_4(IMes)_3Cl]^+$ and $[FeCo_3S_4(IMes)_3Cl]^+$. The reduced clusters, $[M'M_3S_4(IMes)_3Cl]$, as well as the CO-bound clusters, $[M'M_3S_4(IMes)_3(CO)]$, were also prepared, and a comparative analysis of the properties of all three series of clusters was undertaken. Low-valent electronic configurations are accessed in all four clusters, $[Fe_4S_4(IMes)_3(CO)]$, $[CoFe_3S_4(IMes)_3(CO)]$, $[Co_4S_4(IMes)_3(CO)]$, and $[FeCo_3S_4(IMes)_3(CO)]$, and this studied further reveals how heterometal substitution modulates the degree of C–O bond weakening.

Thesis Supervisor: Daniel L.M. Suess

Title: Associate Professor of Chemistry

Acknowledgements

Coming to MIT has been an honor greater than I can put into words, and I am only here because of generosity and encouragement of many educators, mentors, friends, and family. First and foremost, I am deeply grateful to my advisor Prof. Daniel Suess, whose guidance, expertise, and unwavering support throughout this journey have been instrumental in shaping my research and academic growth. His mentorship and encouragement have been invaluable, and I am truly fortunate to have had him as my mentor. I extend my heartfelt thanks to the members of my thesis committee, Prof. Yogi Surendranath and Prof. Kit Cummins, for their insightful feedback, valuable suggestions, and constructive critiques that have significantly enhanced the quality of this work.

I owe a debt of gratitude to Dr. Walt Massefski, Dr. John Grimes, and Dr. Bruce Adams of the DCIF for their technical assistance and support, which have been essential to the smooth progress of my experiments. This work would not have been possible without the help of Dr. Peter Müller, who, on more than one occasion, transmuted the ugly black shards of bastard pyrite I brought him into precious and prismatic gemstones. I would also like to thank Prof. Stephen J. Lippard, and the families of Prof. Daniel S. Kemp and Prof. Alan Davison for their financial support via fellowships through the MIT Department of Chemistry. Their generous funding has been crucial in enabling me to conduct experiments and pursue my scientific inquiries.

I would like to thank my fellow lab members and colleagues for fostering a collaborative and stimulating research environment. First, I have to thank Dr. Gil Namkoong for his camaraderie; together, we were the lab's second crop of students and well out-numbered. I am thankful to all of my seniors in the lab, Drs. Edward Badding, Alex Brown, Arun Sridharan, Suppachai "Soop" Srisantitham, and Mengshan Ye for all their guidance, compassion, and friendship over these last five years. I am grateful for the lab's first post-docs, Prof. Alex McSkimming and Dr. Niklas Thompson, for their mentorship. Much of the synthetic work in this thesis is thanks to the skills I developed working closely with McSkimming. I am also indebted to our lab's newer students: Brighton Skeel, Jessica Kim, Brittany Linn, and Hyunsoo Kim. I have learned a great deal from each of you and your exciting ideas and creativity. I would also like to thank our lab's recent post-docs, Prof. Youngsuk Kim, and Drs. Madeleine Ehweiner and Dr. Mackenzie Field, for thoughtful discussions and wisdom. Finally, I would like to thank our lab's undergraduate students, past and present. Both Anna Bair and Josh Lian brightened the lab with enthusiasm and curiosity. I feel very fortunate to have worked alongside so many intelligent and hardworking people. I am grateful to my friends outside the Suess lab, An Chu, Daniel Harper, Roger Jin, Noah Lewis, and Bryan Tang for your friendship, support, and thoughtful conversations. It is hard to believe how quickly the time went.

The road here began long before MIT. I owe a great debt to the multitude of educators and mentors who encouraged me to do and be more. A great and longtime positive influence in my early life was my orchestra instructor from fifth grade all through to Senior year of high-school, Mr. Christopher Meyer, who taught me patience, discipline, and kindness. Mr. Michael Jaeger, who sparked my love for science and encouraged me to pursue a degree in Chemistry. I want to thank M-STEM academies, Tony DeRuiter, Shannon Zuniga, and all the staff of the program for giving me the skills to excel at the University of Michigan and for the many friends and opportunities they gave me.

I would not be where I am today if not for Prof. Ruma Banerjee and Dr. Victor Vitvitsky at the University of Michigan. Ruma, I will never forget your generosity in welcoming me to your lab. I am immensely honored by the faith you had in me. Victor, thank you for your endless patience, encouragement, and daily guidance. You both made me feel like I was in the right place and that I could do great things.

Of the many friends who supported me in this journey, I owe the greatest thanks to (in no particular order) Kevin Fanning, Daniel Nondorf, and Austin Rife. This summer marks the 9th year of our friendship. Your unwavering support, acceptance, and kindness have made this all possible. To my love, Ashley Cruz, thank you for patience, understanding, love, and respect.

This thesis is dedicated to my parents, Michael and Annie Bostelaar, without whom *I* would not be where I am today. All the sacrifices I have made in pursuit of these extra letters after my name pale in comparison to the sacrifices they made to put food in my mouth, clothes on my back, and a roof over my head. I want to thank my Aunt Brenda for her unceasing encouragement. I thank my grandparents, Larry and Sharon Bostelaar, for their wisdom and strength. This road has been long and taken me far from home. I will always remember where I came from.

Respective Contributions

This thesis contains work resulting from collaborations between the author and colleagues at MIT.

Chapter 2: This work was a collaboration between the author, Dr. Alexandra C. Brown, and Dr. Arun Sridharan. Alex provided initial characterization of $[Fe_4S_4(IMes)_3(PCy_3)]^+$ and $[Fe_4S_4(IPr)_2(PCy_3)_2]^+$. Arun assisted with ^{31}P NMR characterization. The author conducted all other experiments.

Chapter 4: This work was a collaboration between the author, Dr. Alexandra C. Brown, and Joseph Roddy. Alex developed the synthetic methodology for heterometal substitution of $[Fe_4S_4(IMes)_3Cl]^+$ and provided initial characterization of $[TlFe_3S_4(IMes)_3]^+$ and $[CoFe_3S_4(IMes)_3Cl]^+$. Joe performed preliminary experiments in the site-differentiation of $[Co_4S_4]$ clusters, including the initial characterization of $[Co_4S_4(IMes)_3Cl]$. The author conducted all other experiments.

Table of Contents

Table of Figures

Table of Supplemental Figures

Table of Schemes

Table of Charts

Table of Tables

Table of Supplemental Tables

Chapter 1

Site-differentiation of atomically precise metalloclusters[†]

Compared with single metal centers, metalloclusters offer additional compositional tunability, novel electronic structures and unique modes of reactivity with substrates (taking advantage of, for example, metal–metal cooperativity or multisite reactivity).[1–8] For these and other reasons, atomically precise metalloclusters are finding increasing use in various contexts including bioinorganic chemistry,[9–12] materials synthesis,[13–20] and catalysis.[21–23] Synthetic methodology is foundational to these efforts, underlying both cluster assembly and coordination chemistry. Regarding the latter, it is critical to be able to control a cluster's coordination sphere—the identity and stereochemical arrangement of its ligands—ideally with similar precision as has been achieved for mononuclear complexes.[24] A major obstacle is that, unlike for mononuclear complexes, the ligands in clusters are bound to different metal centers, which are typically separated by at least several angstroms. As a result, the spatial and electronic interactions between a ligand and the rest of the cluster (the metal centers as well as the other ligands) are weak. This fundamental difference between the coordination chemistry of clusters and that of mononuclear complexes has several consequences, and in this chapter I focus on how it affects one of the simplest elementary reactions: ligand substitution, particularly in the conversion of highly symmetric, undifferentiated clusters (in which the same ligands bind to chemically equivalent metal centers) to site-differentiated clusters (in which a particular ligand binds to only a subset of the metal centers, thereby imparting chemical inequivalence).

Site-differentiated clusters have broad utility, including as structural and functional models of biological metalloclusters[25–33] and as building blocks in materials synthesis.[20,34–36] However, imparting site-differentiation remains a substantial synthetic challenge, as illustrated in Figure 1.1 for a generic cluster in which the metal ions are arranged in a tetrahedron (*e.g.*, in a cuboidal [Fe_4S_4] cluster). Typically, ligand substitution reactions at such clusters generate mixtures of unsubstituted, monosubstituted, disubstituted, trisubstituted, and tetrasubstituted products (n = 0–4, respectively, for n substitution events), where the ratio of the products depends primarily on the stoichiometry of the incoming ligand (x; Figure 1.1). Such mixtures are generated because, to a first approximation, ligand substitution at one site will minimally impact the kinetics or thermodynamics of ligand substitution at another, resulting in mixtures of partially substituted clusters.[37]

The stochastic nature of ligand substitution has been a long-standing challenge in metallocluster coordination chemistry,[37–40] and as a result a number of approaches to selectively generate site-differentiated clusters have been described. Broadly, the strategies rely on the unique solubility properties of partially substituted clusters,[20,41–43] on chromatographic separation of clusters with different site-differentiation patterns,[39,44] or on the use of carefully designed, chelating

---

[†] Adapted in part with permission from: Bostelaar, T. M.; Brown, A. C.; Sridharan, A.; Suess, D. L. M. *Nature Synthesis* **2023**, 1–9. © Springer Nature. All rights reserved.

ligands.[25,26,28–30,33] In this chapter, I discuss examples of these strategies to highlight the still present need for general and robust tools for metallocluster site-differentiation.

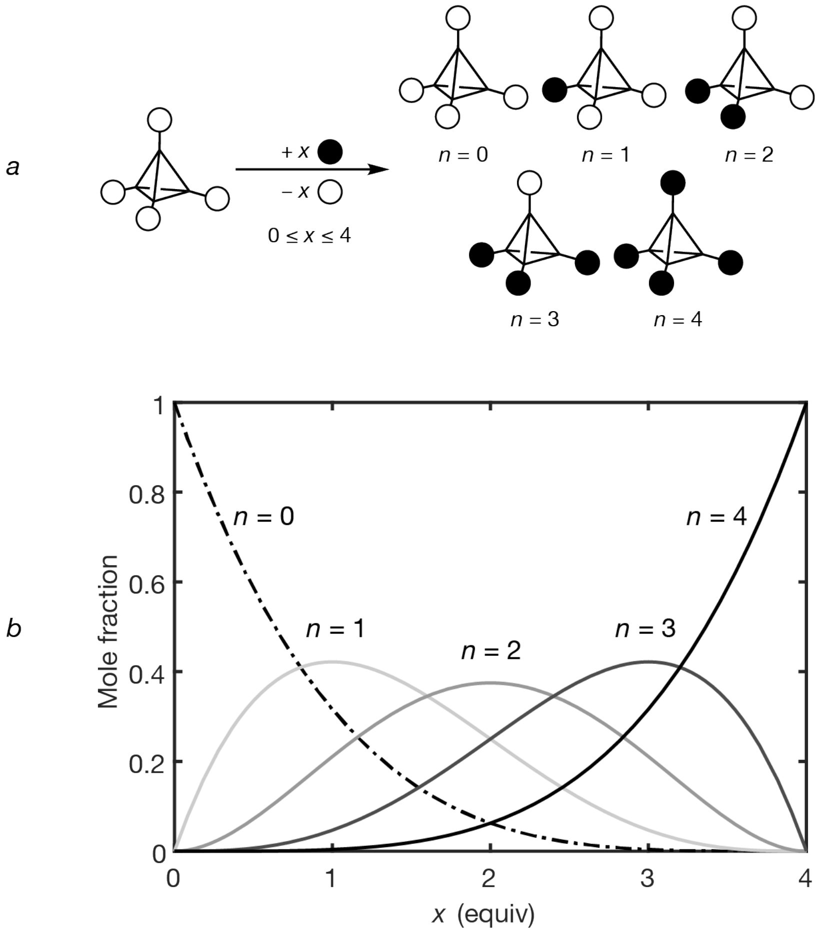

Figure 1.1. (*a*) Products resulting from unselective substitution of tetrahedral clusters under the assumption that the incoming ligand (black ball) is fully consumed in the reaction, producing an equimolar amount (x) of the departing ligand (white ball). (*b*) Binomial distribution model of stochastic ligand substitution at a tetrahedral cluster also under the assumption that each ligand substitution event is highly favorable. n = 0, 1, 2, 3 and 4 given by the dotted, light grey, grey, dark grey, and black traces, respectively (see experimental section of chapter 2 for details about the mathematical model).

Site-differentiation by cluster-chelating ligands

In 1987, Holm and Stack reported the synthesis and subsite-specific functionalization of a cuboidal $[Fe_4S_4]$ cluster using the trithiolate ligand illustrated in Chart 1.1.[25,45] The ligand design mimics the coordination environment of 3:1 site-differentiated $[Fe_4S_4]$ clusters in enzymes in which the cluster is typically ligated by three cysteinyl thiolates with the fourth Fe site available to bind substrates or non-cysteine amino acids. To study subsite-specific phenomena, a method for engendering and maintaining site-differentiation was necessary following observations that synthetic $[Fe_4S_4]$ clusters readily gave statistical distributions of isomers in attempts to prepare heteroleptic clusters through ligand substitution.[38,46,47] Holm's solution is perhaps the best-known example of this approach and has inspired the design of many cluster chelating ligands that followed from our lab and others (Chart 1.1).[25,26,29–31,33,45,48]

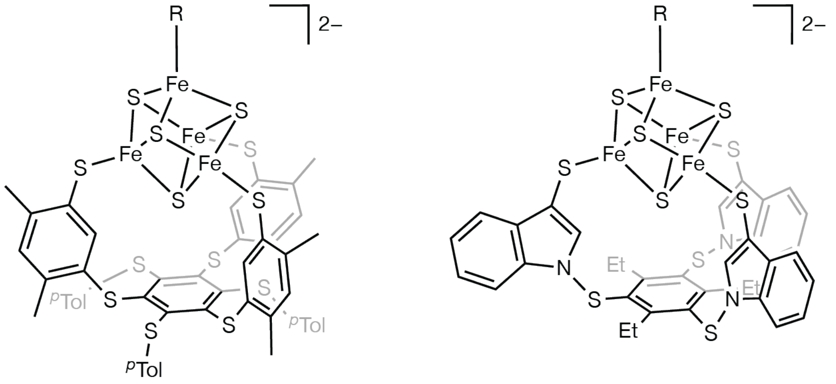

Holm (1987)
R = Cl, SEt

Saak and Pohl (1997)
R = Br, SPh

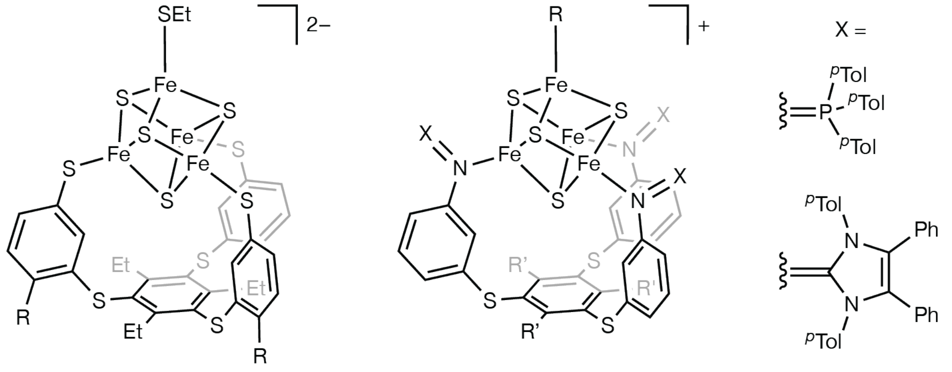

Tatsumi (2012)
R = F, OMe

Suess (2018–2020)
R = Cl, Et, Me
R’ = Et, H

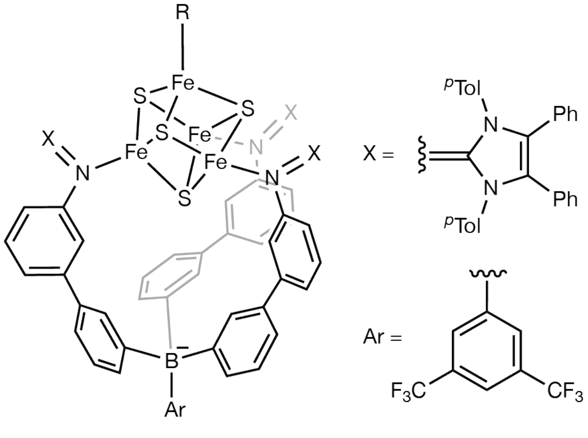

Suess (2020)
R = Cl, Me

Chart 1.1. Tridentate chelating ligands designed for 3:1 site-differentiation of [Fe_4S_4] clusters.

An advance in this approach includes our lab's report of a variation of the Holm ligand featuring neutral iminophosphorane donors (Chart 1.1).[31] The trianionic Holm ligand provided highly charged clusters incompatible with less polar solvents and was therefore precluded the synthesis of more reactive [Fe_4S_4] species. With the addition of an anionic, scorpionate-type ligand, tridentate ligands with neutral donors enabled the synthesis of the first structurally characterized [Fe_4S_4]$^{2+/3+}$-alkyl species (Chart 1.1).[33]

Despite the advances provided by these and other [Fe_4S_4] cluster chelating ligands, their application to other cluster-types is severely limited by the complexity of their design. These ligands highlighted above are largely based on the original design put forth by Holm and are specific to the structural metrics of [Fe_4S_4] cubanes. For example, our lab reported a modification of the Holm ligand employing imidazol-2-imine donors in place of thiolates (Chart 1.1).[30] When the *N*-imidazolyl substituent is a *p*-tolyl group, the desired, 3:1 site-differentiated cubane is obtained. However, when the *N*-imidazolyl substituents are methyl groups, ligand binding results in formation of a higher nuclearity [Fe_6S_6] cluster. These demonstrate the sensitivity of these cluster chelating ligands to small modifications in their steric and geometric properties. Beyond cuboidal clusters, to apply the cluster chelating strategy to octahedral, Chevrel-type clusters, for example, would require a totally new ligand platform, demanding considerable time and effort to engineer. For this reason, preparing and isolating site-differentiation clusters using monodentate ligands has been a major thrust of cluster research.

Chromatographic separation of heteroleptic clusters

Site-differentiated clusters are obtained as statistical mixtures from ligand substitution reactions. The ratios of these species are dictated largely by the binding energies of the different ligands and their stoichiometry. In some instances, the desired heteroleptic clusters may be separated. It is in this way that many site-differentiated Chevrel-type [M_6Q_8] clusters have been prepared.

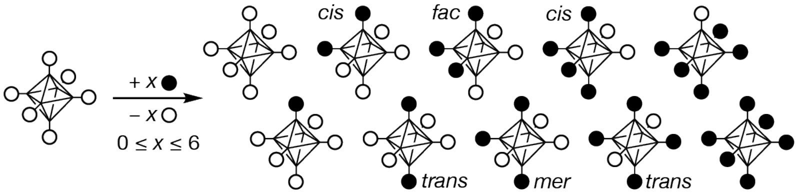

Figure 1.2. Products resulting from unselective substitution of octahedral clusters under the assumption that the incoming ligand (black ball) is fully consumed in the reaction, producing an equimolar amount (x) of the departing ligand (white ball).

Ligand substitution reactions with these clusters, composed of an octahedral arrangement of transition-metals with face-capping μ_3–chalcogenides, yield up to 10 products (Figure 1.2). Holm and coworkers showed that four heteroleptic [Re_6Se_8] clusters could be isolated from this mixture via column chromatography (Scheme 1.1).[42] The yields varied considerably, and the method required the two ligands be of differing charge (*e.g.*, a halide and a phosphine). The authors interest in these heteroleptic clusters arose from their potential as materials precursors. The structure and dimensionality of the resulting cluster-based materials might be programmable through rational design of the coordination environment of the clusters. Holm and coworkers demonstrated this application by preparing di- and trimeric clusters covalently linked with ditopic linker ligands.[35] Roy and Nuckolls extended this approach to prepare low-dimensional extended solids from site-differentiated $[Co_6Se_8(PEt_3)_{6-n}(CO)_n]$ precursors.[20,40,44]

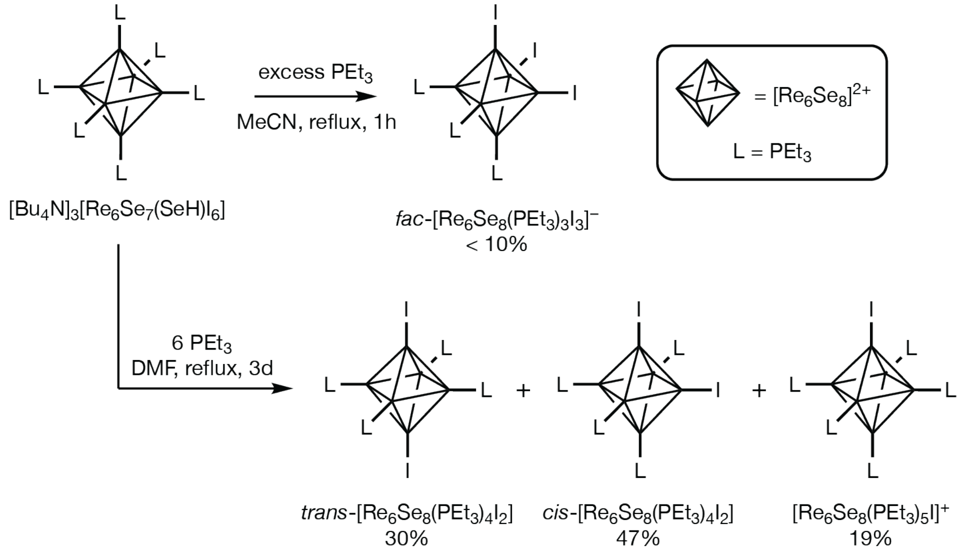

Scheme 1.1. Synthesis and chromatographic separation of heteroleptic $[Re_6Se_8]$ clusters by Holm.[42]

Although Roy and Nuckolls demonstrated that differences in cluster charge were not necessary for their separation, the success of this approach is still highly dependent on the identity of the two ligands. For example, DiSalvo reported a number of $[W_6S_8]$ Chevrel-type clusters with mixtures of pyridine, phosphine, and aryl/alkyl-isocyanide ligands that could not be separated.[37,49] Finally, the lack of selectivity means much of the cluster material is lost in the form of undesired substitution patterns. While this may be incrementally improved through optimization of the reaction conditions, a method for the selective synthesis of the desired cluster is desired.

Selectivity from cluster charge and solubility properties

A key assumption built into the model put forth in Figure 1.1b is that the thermodynamics of each successive ligand substitution at the cluster is equal—that the ligand substitutions at each site are independent of one another. This assumption is good when the incoming and incumbent ligands are similar in nature (*e.g.*, substitution of a halide by a thiolate). If the charges of the ligands are different this assumption may no longer be tenable, and reaction conditions may be optimized to exploit this.

Holm and coworkers refined the methodology set out by Coucouvanis[50] and reported numerous 3:1 site-differentiated $[Fe_4S_4]$ clusters (Scheme 1.2).[41,51] This procedure took advantage of the $[Fe_4S_4]^+$ charge state such that products with zero, two, three, or four Cl^- ligands, for example, would be disfavored in a low polarity solvent, such as CH_2Cl_2 or toluene. Although these clusters are easily prepared in high yield by this method, the site-differentiation is challenging to maintain. In addition to loss of site-differentiation from ligand redistribution, phosphine loss has been observed to result in the formation of $[Fe_8S_8]$ clusters and higher nuclearity aggregates.[41,51]

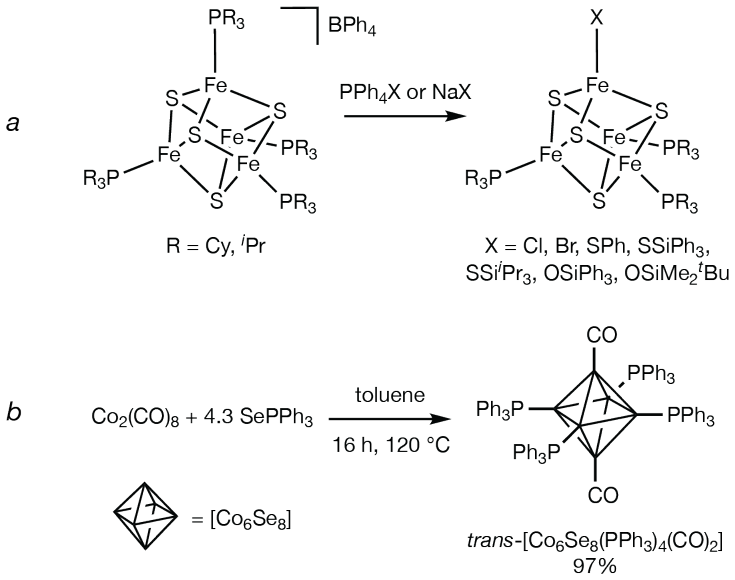

Scheme 1.2. (*a*) Synthesis of 3:1 site-differentiated [Fe_4S_4] clusters via salt-metathesis reported by Holm.[41,51] (*b*) Synthesis of *trans*-[$Co_6Se_8(PPh_3)_4(CO)_2$] reported by Roy.[20]

Similar results have been obtained with Chevrel-type clusters. Roy and coworkers observed that *trans*-[$Co_6Se_8(PPh_3)_4(CO)_2$] was obtained in 97% yield following crystallization from the self-assembly reaction mixture in toluene and water (Scheme 1.1b).[20] The authors hypothesized that the observed selectivity is driven by the extremely poor solubility of the product in toluene compared to clusters with fewer PPh_3 ligands; [$Co_6Se_8(CO)_6$] and PPh_3 are generated *in situ* from reaction of $Co_2(CO)_8$ with $SePPh_3$, and *trans*-[$Co_6Se_8(PPh_3)_4(CO)_2$] precipitates from solution before additional CO ligands can be substituted by PPh_3. Preparations using other phosphine ligands do not appear to reproduce the observed product selectivity. The authors attribute the *trans* regioselectivity to steric restraints imposed by the bulky PPh_3 ligands.

Conclusions and outlook

Despite decades of development in the fundamental coordination chemistry of metalloclusters, the selective preparation of site-differentiated clusters remains a significant challenge. Previous strategies have obtained reasonable success but are typically limited to a specific system. A general method for the site-differentiation of metalloclusters is essential to their applications in catalysis and materials.

Recently, our group reported a 3:1 site-differentiated [Fe_4S_4] cluster with bulky *N*-heterocyclic carbene (NHC) ligands (Scheme 1.3).[32] Addition of 3 equiv IMes (1,3-dimesitylimidazol-2-ylidene) or $I^{i}Pr^{Me}$ (1,3-bis(isopropyl)-4,5-dimethylimidazol-2-ylidene) to [$Fe_4S_4(PCy_3)_3Cl$] selectively substitutes the phosphine ligands. Upon halide abstraction from [$Fe_4S_4(I^{i}Pr^{Me})_3Cl$] in ether yields the homoleptic cluster [$Fe_4S_4(I^{i}Pr^{Me})_4$]$^+$ as the only soluble cluster product. However, when a bulky NHC like IMes is used, the ether adduct is obtained. That the homoleptic cluster [$Fe_4S_4IMes_4$]$^+$ is not obtained demonstrates that despite the physical separation of the Fe sites in the cluster, sufficiently and appropriately bulky NHC ligands may be able to control the substitution number and site-differentiation pattern of [Fe_4S_4] clusters.

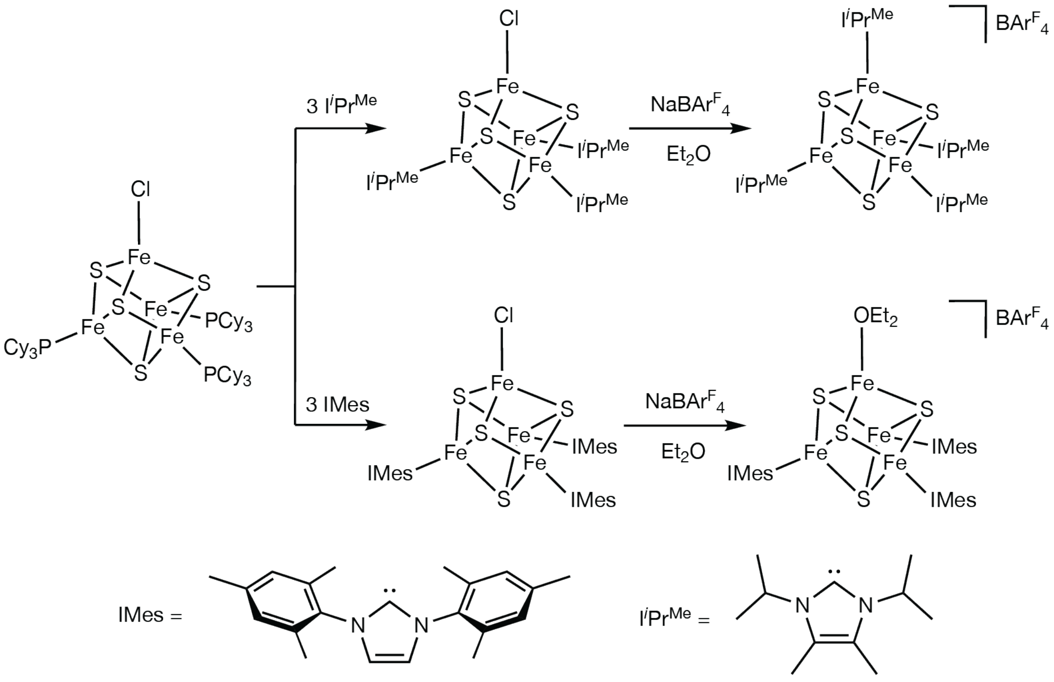

Scheme 1.3. Differential reactivity of site-differentiated [Fe_4S_4] clusters following halide abstraction due to NHC steric bulk.[32] ($BAr^F{}_4{}^-$, tetrakis(3,5-bis(trifluoromethyl)phenyl)borate).

Previous reports employing bulky ligands at [Fe_4S_4] clusters (e.g., phosphines and aryl thiolates) had not observed a significant impact on the selectivity of ligand substitution reactions due to steric effects.[52–54] However, support for this approach includes examples of metallocluster self-assembly reactions in which the product is dictated by the steric properties of the ligand[55–57] and reports of partial ligand substitution at polycarbonylated Fe clusters using bulky isocyanides or phosphines (giving rise to products with asymmetric substitution patterns).[58,59]

Chapter summaries

Chapters 2 pertains to the development of a method that uses the steric properties of NHC ligands to impart site-differentiation at [Fe_4S_4] clusters. Specifically, a series of site-differentiated [$Fe_4S_4(NHC)_m(PCy_3)_{4-m}$]$^+$ (m = 1–4) are prepared and structurally characterized. Insights from this series are discussed and used to assemble a library of structurally diverse NHC ligands. High-throughput titration experiments were conducted to ascertain the maximum substitution number of these NHCs and evaluated against quantitative steric parameters. This study was expanded to octahedral, Chevrel-type [Fe_6S_8] clusters in Chapter 3 to examine how this method may be applied to clusters of differing nuclearities and geometries. Three new NHC-bound [Fe_6S_8]$^+$ clusters were characterized and demonstrate the potential applications of this approach to an even greater range of cluster types.

In Chapter 4, we leveraged the subsite specificity engendered by our site-differentiation strategy to selectivity excise a specific metal site from the clusters. Reconstitution with M'Cl_2 produced [M'M_3S_4(IMes)$_3$Cl]$^+$ (M' = Co, Fe, for M = Fe, Co, respectively). The resulting heterobimetallic clusters maintained their site-differentiation upon reduction and terminal ligand substitution of the unique site for CO. A comparative analysis of the properties of the series of clusters at parity of core charge state and terminal ligation was undertaken. Regarding the carbonylated clusters, strong C–O bond weakening reflected low-valent electronic configurations for all four clusters.

References

(1) Muetterties, E. L. Metal Clusters in Catalysis III.—Clusters as Models for Chemisorption Processes and Heterogeneous Catalysis. *Bull. Sociétés Chim. Belg.* **1975**, *84* (10), 959–986.

(2) Lee, S. C.; Holm, R. H. Nonmolecular Metal Chalcogenide/Halide Solids and Their Molecular Cluster Analogues. *Angew. Chem. Int. Ed.* **1990**, *29* (8), 840–856.

(3) Beinert, H.; Holm, R. H.; Munck, E. Iron-Sulfur Clusters: Nature's Modular, Multipurpose Structures. *Science* **1997**, *277* (5326), 653–659.

(4) Sokolov, M. N.; Fedin, V. P.; Sykes, A. G. Chalcogenide-Containing Metal Clusters. In *Comprehensive Coordination Chemistry II*; McCleverty, J. A., Meyer, T. J., Wedd, A. G., Eds.; Elsevier Pergamon, 2003; Vol. 4, p 761.

(5) Degroot, M. W.; Corrigan, J. F. High Nuclearity Clusters: Metal–Chalcogenide Polynuclear Complexes. In *Comprehensive Coordination Chemistry II*; McCleverty, J. A., Meyer, T. J., Fujita, M., Powell, A. K., Creutz, C. A., Eds.; Elsevier Pergamon, 2003; Vol. 7, pp 57–123.

(6) Jena, P.; Sun, Q. Super Atomic Clusters: Design Rules and Potential for Building Blocks of Materials. *Chem. Rev.* **2018**, *118* (11), 5755–5870.

(7) Doud, E. A.; Voevodin, A.; Hochuli, T. J.; Champsaur, A. M.; Nuckolls, C.; Roy, X. Superatoms in Materials Science. *Nat. Rev. Mater.* **2020**, *5* (5), 371–387.

(8) Cesari, C.; Shon, J. H.; Zacchini, S.; Berben, L. A. Metal Carbonyl Clusters of Groups 8–10: Synthesis and Catalysis. *Chem. Soc. Rev.* **2021**, *50* (17), 9503–9539.

(9) Rao, P. V.; Holm, R. H. Synthetic Analogues of the Active Sites of Iron−Sulfur Proteins. **2004**.

(10) Lee, S. C.; Lo, W.; Holm, R. H. Developments in the Biomimetic Chemistry of Cubane-Type and Higher Nuclearity Iron–Sulfur Clusters. *Chem. Rev.* **2014**, *114* (7), 3579–3600.

(11) Rathnayaka, S. C.; Mankad, N. P. Coordination Chemistry of the CuZ Site in Nitrous Oxide Reductase and Its Synthetic Mimics. *Coord. Chem. Rev.* **2021**, *429*, 213718.

(12) Bigness, A.; Vaddypally, S.; Zdilla, M. J.; Mendoza-Cortes, J. L. Ubiquity of Cubanes in Bioinorganic Relevant Compounds. *Coord. Chem. Rev.* **2022**, *450*, 214168.

(13) Bag, S.; Trikalitis, P. N.; Chupas, P. J.; Armatas, G. S.; Kanatzidis, M. G. Porous Semiconducting Gels and Aerogels from Chalcogenide Clusters. *Science* **2007**, *317* (5837), 490–493.

(14) Claridge, S. A.; Castleman, A. W.; Khanna, S. N.; Murray, C. B.; Sen, A.; Weiss, P. S. Cluster-Assembled Materials. *ACS Nano* **2009**, *3* (2), 244–255.

(15) Roy, X.; Lee, C.-H.; Crowther, A. C.; Schenck, C. L.; Besara, T.; Lalancette, R. A.; Siegrist, T.; Stephens, P. W.; Brus, L. E.; Kim, P. Nanoscale Atoms in Solid-State Chemistry. *Science* **2013**, *341* (6142), 157–160.

(16) Tomalia, D. A.; Khanna, S. N. A Systematic Framework and Nanoperiodic Concept for Unifying Nanoscience: Hard/Soft Nanoelements, Superatoms, Meta-Atoms, New Emerging Properties, Periodic Property Patterns, and Predictive Mendeleev-like Nanoperiodic Tables. *Chem. Rev.* **2016**, *116* (4), 2705–2774.

(17) Horwitz, N. E.; Xie, J.; Filatov, A. S.; Papoular, R. J.; Shepard, W. E.; Zee, D. Z.; Grahn, M. P.; Gilder, C.; Anderson, J. S. Redox-Active 1D Coordination Polymers of Iron–Sulfur Clusters. *J. Am. Chem. Soc.* **2019**, *141* (9), 3940–3951.

(18) Zhang, J.; Bu, X.; Feng, P.; Wu, T. Metal Chalcogenide Supertetrahedral Clusters: Synthetic Control over Assembly, Dispersibility, and Their Functional Applications. *Acc. Chem. Res.* **2020**, *53* (10), 2261–2272.

(19) Gillen, J. H.; Moore, C. A.; Vuong, M.; Shajahan, J.; Anstey, M. R.; Alston, J. R.; Bejger, C. M. Synthesis and Disassembly of an Organometallic Polymer Comprising Redox-Active Co_4S_4 Clusters and Janus Biscarbene Linkers. *Chem. Commun.* **2022**, *58* (31), 4885–4888.

(20) Bartholomew, A. K.; Meirzadeh, E.; Stone, I. B.; Koay, C. S.; Nuckolls, C.; Steigerwald, M. L.; Crowther, A. C.; Roy, X. Superatom Regiochemistry Dictates the Assembly and Surface Reactivity of a Two-Dimensional Material. *J. Am. Chem. Soc.* **2022**, *144* (3), 1119–1124.

(21) Kephart, J. A.; Mitchell, B. S.; Kaminsky, W.; Velian, A. Multi-Active Site Dynamics on a Molecular Cr/Co/Se Cluster Catalyst. *J. Am. Chem. Soc.* **2022**, *144* (21), 9206–9211.

(22) McCool, N. S.; Robinson, D. M.; Sheats, J. E.; Dismukes, G. C. A Co4O4 Cubane Water Oxidation Catalyst Inspired by Photosynthesis. *J. Am. Chem. Soc.* **2011**, *133* (30), 11446–11449.

(23) Li, G.; Jin, R. Atomically Precise Gold Nanoclusters as New Model Catalysts. *Acc. Chem. Res.* **2013**, *46* (8), 1749–1758.

(24) Pombeiro, A. J. L.; Kukushkin, V. YU. Ligand Reactivity: General Introduction. In *Comprehensive Coordination Chemistry II*; McCleverty, J. A., Meyer, T. J., Lever, A. B. P., Eds.; Elsevier Pergamon, 2003; Vol. 1, pp 585–594.

(25) Stack, T. D. P.; Holm, R. H. Subsite-Specific Functionalization of the $[4Fe\text{-}4S]^{2+}$ Analogue of Iron-Sulfur Protein Clusters. *J. Am. Chem. Soc.* **1987**, *109* (8), 2546–2547.

(26) Walsdorff, C.; Saak, W.; Pohl, S. A New Preorganized Tridentate Ligand Bearing Three Indolethiolategroups. Preparation of 3∶1 Subsite-Differentiated Fe_4S_4 Clusters. *J. Chem. Soc. Dalton Trans.* **1997**, No. 11, 1857–1862.

(27) Ohki, Y.; Tanifuji, K.; Yamada, N.; Imada, M.; Tajima, T.; Tatsumi, K. Synthetic Analogues of [$Fe_4S_4(Cys)_3(His)$] in Hydrogenases and [$Fe_4S_4(Cys)_4$] in HiPIP Derived from All-Ferric [$Fe_4S_4\{N(SiMe_3)_2\}_4$]. *Proc. Natl. Acad. Sci.* **2011**, *108* (31), 12635–12640.

(28) Kanady, J. S.; Tsui, E. Y.; Day, M. W.; Agapie, T. A Synthetic Model of the Mn_3Ca Subsite of the Oxygen-Evolving Complex in Photosystem II. *Science* **2011**, *333* (6043), 733–736.

(29) Terada, T.; Wakimoto, T.; Nakamura, T.; Hirabayashi, K.; Tanaka, K.; Li, J.; Matsumoto, T.; Tatsumi, K. Tridentate Thiolate Ligands: Application to the Synthesis of the Site-Differentiated [4Fe-4S] Cluster Having a Hydrosulfide Ligand at the Unique Iron Center. *Chem. – Asian J.* **2012**, *7* (5), 920–929.

(30) McSkimming, A.; Suess, D. L. M. Selective Synthesis of Site-Differentiated Fe_4S_4 and Fe_6S_6 Clusters. *Inorg. Chem.* **2018**, *57* (23), 14904–14912.

(31) Ye, M.; Thompson, N. B.; Brown, A. C.; Suess, D. L. M. A Synthetic Model of Enzymatic [Fe_4S_4]–Alkyl Intermediates. *J. Am. Chem. Soc.* **2019**, *141* (34), 13330–13335.

(32) Brown, A. C.; Suess, D. L. M. Controlling Substrate Binding to Fe_4S_4 Clusters through Remote Steric Effects. *Inorg. Chem.* **2019**, *58*, 5273–5280.

(33) McSkimming, A.; Sridharan, A.; Thompson, N. B.; Müller, P.; Suess, D. L. M. An $[Fe_4S_4]^{3+}$-Alkyl Cluster Stabilized by an Expanded Scorpionate Ligand. *J. Am. Chem. Soc.* **2020**, *142* (33), 14314–14323.

(34) Long, J. R.; Williamson, A. S.; Holm, R. H. Dimensional Reduction of $Re_6Se_8Cl_2$: Sheets, Chains, and Discrete Clusters Composed of Chloride-Terminated $[Re_6Q_8]^{2+}$ (Q = S, Se) Cores. *Angew. Chem. Int. Ed.* **1995**, *34* (2), 226–229.

(35) Zheng, Z.; Gray, T. G.; Holm, R. H. Synthesis and Structures of Solvated Monoclusters and Bridged Di-and Triclusters Based on the Cubic Building Block $[Re_6(\mu_3\text{-}Se)_8]^{2+}$. *Inorg. Chem.* **1999**, *38* (21), 4888–4895.

(36) Champsaur, A. M.; Mézière, C.; Allain, M.; Paley, D. W.; Steigerwald, M. L.; Nuckolls, C.; Batail, P. Weaving Nanoscale Cloth through Electrostatic Templating. *J. Am. Chem. Soc.* **2017**, *139* (34), 11718–11721.

(37) Jin, S.; Adamchuk, J.; Xiang, B.; DiSalvo, F. J. The Dean−Evans Relation in ^{31}P NMR Spectroscopy and Its Application to the Chemistry of Octahedral Tungsten Sulfide Clusters. *J. Am. Chem. Soc.* **2002**, *124* (31), 9229–9240.

(38) Que, L.; Bobrik, M. A.; Ibers, J. A.; Holm, R. H. Synthetic Analogs of the Active Sites of Iron-Sulfur Proteins. VII. Ligand Substitution Reactions of the Tetranuclear Clusters $[Fe_4S_4(SR)_4]^{2-}$ and the Structure of $[(CH_3)_4N]_2[Fe_4S_4(SC_6H_5)_4]$. *J. Am. Chem. Soc.* **1974**, *96* (13), 4168–4178.

(39) Willer, M. W.; Long, J. R.; McLauchlan, C. C.; Holm, R. H. Ligand Substitution Reactions of $[Re_6S_8Br_6]^{4-}$: A Basis Set of Re_6S_8 Clusters for Building Multicluster Assemblies. *Inorg. Chem.* **1998**, *37* (2), 328–333.

(40) Reed, D. A.; Hochuli, T. J.; Gadjieva, N. A.; He, S.; Wiscons, R. A.; Bartholomew, A. K.; Champsaur, A. M.; Steigerwald, M. L.; Roy, X.; Nuckolls, C. Controlling Ligand Coordination Spheres and Cluster Fusion in Superatoms. *J. Am. Chem. Soc.* **2022**, *144* (1), 306–313.

(41) Zhou, H.-C.; Holm, R. H. Synthesis and Reactions of Cubane-Type Iron−Sulfur−Phosphine Clusters, Including Soluble Clusters of Nuclearities 8 and 16. *Inorg. Chem.* **2003**, *42* (1), 11–21.

(42) Zheng, Z.; Long, J. R.; Holm, R. H. A Basis Set of Re_6Se_8 Cluster Building Blocks and Demonstration of Their Linking Capability: Directed Synthesis of an $Re_{12}Se_{16}$ Dicluster. *J. Am. Chem. Soc.* **1997**, *119* (9), 2163–2171.

(43) Harmjanz, M.; Saak, W.; Haase, D.; Pohl, S. Aryl Isonitrile Binding to $[Fe_4S_4]$ Clusters: Formation of $[Fe_4S_4]^+$ and $[\{Fe_4S_4\}_2]^{2+}$ Cores. *Chem. Commun.* **1997**, *0* (10), 951–952.

(44) Champsaur, A. M.; Velian, A.; Paley, D. W.; Choi, B.; Roy, X.; Steigerwald, M. L.; Nuckolls, C. Building Diatomic and Triatomic Superatom Molecules. *Nano Lett.* **2016**, *16* (8), 5273–5277.

(45) Stack, T. D. P.; Holm, R. H. Subsite-Differentiated Analogues of Biological $[4Fe\text{-}4S]^{2+}$ Clusters: Synthesis, Solution and Solid-State Structures, and Subsite-Specific Reactions. *J. Am. Chem. Soc.* **1988**, *110* (8), 2484–2494.

(46) Johnson, R. W.; Holm, R. H. Reaction Chemistry of the Iron-Sulfur Protein Site Analogs $[Fe_4S_4(SR)_4]^{2-}$. Sequential Thiolate Ligand Substitution Reactions with Electrophiles. *J. Am. Chem. Soc.* **1978**, *100* (17), 5338–5344.

(47) Burt, R. J.; Ridge, B.; Rydon, H. N. Studies Relating to the Ferredoxins. Part 2. Exchange Reactions of Some Cysteine–Glycine Peptides with the Iron–Sulphur Cluster Compound Bis(Tetramethylammonium) Tetrakis(μ_3-Sulphido-t-Butylthioiron). *J. Chem. Soc. Dalton Trans.* **1980**, No. 7, 1228–1235.

(48) Walsdorff, C.; Saak, W. A Preorganised Doubly Tripodal Hexathiol: Syntheses and Crystal Structures of Complexes with Two 3:1 Subsite-Differentiated Fe_4S_4 Clusters. *Chem. Commun.* **1997**, No. 19, 1931–1932.

(49) Jin, S.; Zhou, R.; Scheuer, E. M.; Adamchuk, J.; Rayburn, L. L.; Disalvo, F. J. Synthesis, Characterization, and Ligand Exchange Studies of $W_6S_8L_6$ Cluster Compounds. *Inorg. Chem.* **2001**, *40* (12), 2666–2674.

(50) Tyson, M. A.; Demadis, K. D.; Coucouvanis, D. Uncharged Mixed-Ligand Clusters with the $[Fe_4S_4]^+$ and $[Fe_4S_4]^{2+}$ Cores. Synthesis, Structural Characterization, and Properties of

the $Fe_4S_4X(^tBu_3P)_3$ (X= Cl, Br, I) and $Fe_4S_4(SPh)_2(^tBu_3P)_2$ Cubanes. *Inorg. Chem.* **1995**, *34* (18), 4519–4520.

(51) Deng, L.; Majumdar, A.; Lo, W.; Holm, R. H. Stabilization of 3:1 Site-Differentiated Cubane-Type Clusters in the $[Fe_4S_4]^{1+}$ Core Oxidation State by Tertiary Phosphine Ligation: Synthesis, Core Structural Diversity, and S = 1/2 Ground States. *Inorg. Chem.* **2010**, *49* (23), 11118–11126.

(52) Tanifuji, K.; Yamada, N.; Tajima, T.; Sasamori, T.; Tokitoh, N.; Matsuo, T.; Tamao, K.; Ohki, Y.; Tatsumi, K. A Convenient Route to Synthetic Analogues of the Oxidized Form of High-Potential Iron–Sulfur Proteins. *Inorg. Chem.* **2014**, *53* (8), 4000–4009.

(53) Moula, G.; Matsumoto, T.; Miehlich, M. E.; Meyer, K.; Tatsumi, K. Synthesis of an All-Ferric Cuboidal Iron–Sulfur Cluster $[Fe^{III}_4S_4(SAr)_4]$. *Angew. Chem. Int. Ed.* **2018**, *57* (36), 11594–11597.

(54) Grunwald, L.; Clémancey, M.; Klose, D.; Dubois, L.; Gambarelli, S.; Jeschke, G.; Wörle, M.; Blondin, G.; Mougel, V. A Complete Biomimetic Iron-Sulfur Cubane Redox Series. *Proc. Natl. Acad. Sci.* **2022**, *119* (31), e2122677119.

(55) Steigerwald, M. L.; Siegrist, T.; Gyorgy, E. M.; Hessen, B.; Kwon, Y.-U.; Tanzler, S. M. Effect of Diverse Ligands on the Course of a Molecules-to-Solids Process and Properties of Its Intermediates. *Inorg. Chem.* **1994**, *33* (15), 3389–3395.

(56) Goh, C.; Segal, B. M.; Huang, J.; Long, J. R.; Holm, R. H. Polycubane Clusters: Synthesis of $[Fe_4S_4(PR_3)_4]^{1+,0}$ (R = Bu^t, Cy, Pr^i) and $[Fe_4S_4]^0$ Core Aggregation upon Loss of Phosphine. *J. Am. Chem. Soc.* **1996**, *118* (47), 11844–11853.

(57) Fuhr, O.; Dehnen, S.; Fenske, D. Chalcogenide Clusters of Copper and Silver from Silylated Chalcogenide Sources. *Chem. Soc. Rev.* **2013**, *42* (4), 1871–1906.

(58) Drance, M. J.; Mokhtarzadeh, C. C.; Melaimi, M.; Agnew, D. W.; Moore, C. E.; Rheingold, A. L.; Figueroa, J. S. Controlled Expansion of a Strong-Field Iron Nitride Cluster: Multi-Site Ligand Substitution as a Strategy for Activating Interstitial Nitride Nucleophilicity. *Angew. Chem. Int. Ed.* **2018**, *57* (40), 13057–13061.

(59) Loewen, N. D.; Pattanayak, S.; Herber, R.; Fettinger, J. C.; Berben, L. A. Quantification of the Electrostatic Effect on Redox Potential by Positive Charges in a Catalyst Microenvironment. *J. Phys. Chem. Lett.* **2021**, *12* (12), 3066–3073.

Chapter 2

Site-differentiation of cuboidal iron–sulfur clusters†

In this chapter, we report a method that uses the steric properties of monodentate ligands to impart site-differentiation. In this approach (Figure 2.1), the size of the incoming ligand dictates the maximum number of substitution events that can occur (*m*) whereby oversubstitution is prevented because additional ligands cannot fit around the cluster. Thus, a particular site-differentiation pattern can be obtained simply by adding an excess of a ligand ($x \geq m$) that has the appropriate steric properties. Support for this approach includes examples of metallocluster self-assembly reactions in which the product is dictated by the steric properties of the ligand[1–3] and reports of partial ligand substitution at polycarbonylated Fe clusters using bulky isocyanides or phosphines (giving rise to products with asymmetric substitution patterns).[4,5] Here we develop this method using cuboidal [Fe_4S_4] clusters, which serve as models for active sites of Fe–S proteins.[6–10] In Chapter 3, we show that it can be extended to Chevrel-type [Fe_6S_8] clusters, which have garnered interest as building blocks in extended solids.[11] Experiments with the Chevrel-type clusters demonstrate that, in addition to dictating the number of substitution events, the incoming ligand's steric profile can control the cluster's stereochemistry, enabling site-differentiation with high diastereoselectivity.

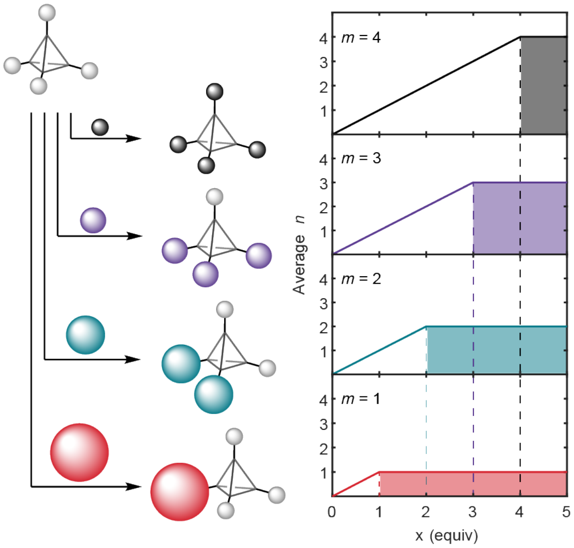

Figure 2.1. (*left*) Limiting the maximal substitution number, *m*, by tuning the steric properties of the incoming ligand. (*right*) Average substitution number of the product distribution as a function of amount added ligand, *x*. For ligands that dictate $m = 4$, 3, 2 and 1, (given by the black, purple, teal, and red traces, respectively) precise patterns of site-differentiation are obtained for $x \geq m$.

---

† Adapted in part with permission from: Bostelaar, T. M.; Brown, A. C.; Sridharan, A.; Suess, D. L. M. *Nature Synthesis* **2023**, 1–9. © Springer Nature. All rights reserved.

Synthesis and structural characterization of tetra-, tri-, di-, and monosubstituted iron-sulfur cubanes

We began this study by investigating substitution reactions of cuboidal [Fe_4S_4] clusters with *N*-heterocyclic carbenes (NHCs), which form relatively strong Fe–C bonds[12] and have highly tunable steric properties.[13] Moreover, previous work from our laboratory has established that installing bulky NHCs onto pre-site-differentiated clusters enhances the stability of the clusters with respect to disproportionation to undifferentiated clusters (a common side-reaction in metallocluster chemistry).[14] In this section, we utilize NHCs to transform *undifferentiated* clusters into clusters with precise patterns of site-differentiation.

We first examined the substitution of the PCy_3 ligands of the undifferentiated cluster [$Fe_4S_4(PCy_3)_4$][BPh_4] (**2.1**)[2] with a series of *N*-aryl NHCs in which the steric properties of the aryl groups are systematically tuned (Figure 2.2). Beginning with the smallest NHC in the series, ITol (1,3-di-*p*-tolylimidazol-2-ylidene), we observed that adding excess ITol (5 equiv) to **2.1** resulted in complete substitution of the PCy_3 ligands. This was evident from the crude ^{31}P NMR spectrum, which showed the disappearance of the resonance corresponding to **2.1** at 324 ppm, the generation of free PCy_3 at 10.7 ppm, and no additional resonances corresponding to species with cluster-bound PCy_3 ligands. The identity of the product as [Fe_4S_4(ITol)$_4$][BPh_4] (**2.2**) was confirmed by single-crystal X-ray diffraction (XRD) analysis (Figure 2.2c and Figure S2.46). Therefore, ITol, like the smaller *N*-alkyl NHC I^iPr^{Me} (I^iPr^{Me} = 1,3-diisopropyl-4,5-dimethylimidazol-2-ylidene) can bind [Fe_4S_4] clusters at all four Fe sites.[12,14]

The analogous reaction with IMes (1,3-dimesitylimidazol-2-ylidene; 5 equiv) yielded a different outcome. In addition to the peak corresponding to free PCy_3, a paramagnetically shifted peak was observed at 289 ppm in the ^{31}P NMR spectrum of the reaction mixture, indicating at least one PCy_3 ligand remained bound to the cluster. Purification and characterization of the product revealed its identity as the trisubstituted cluster [$Fe_4S_4(PCy_3)$(IMes)$_3$][BPh_4] (**2.3**). Here, despite the thermodynamic favorability of substituting a phosphine with an NHC,[12,15] complete substitution does not occur because a fourth IMes ligand is too sterically encumbering to bind. The partial substitution of [Fe_4S_4] clusters by bulky ligands has clear parallels in the chemistry of metalloclusters (*vide supra*) and mononuclear complexes, for example in substitution reactions of phosphines with NHCs in the synthesis of Ru metathesis catalysts.[15,16]

Further increasing the bulkiness of the ortho substituents from methyl to *iso*propyl (IPr; 1,3-bis(2,6-diisopropylphenyl)imidazol-2-ylidene) halts substitution after the second event. Specifically, the maximally substituted product of the reaction of excess IPr (5 equiv) with **2.1** is the disubstituted cluster [$Fe_4S_4(PCy_3)_2$(IPr)$_2$][BPh_4] (**2.4**) in which two PCy_3 ligands remain bound to the cluster ($\delta(^{31}P)$ = 390 ppm). Efficient conversion of **2.1** to **2.4** required refluxing the reaction mixture for 3 h. The relatively slow rate of ligand substitution, particularly for the second substitution event, is evident in reactions monitored by ^{31}P NMR spectroscopy at room temperature (Figure S2.4) and contrasts the behavior of the smaller NHCs (ITol and IMes) for which the maximally substituted clusters are obtained within minutes at room temperature. These observations highlight the importance of the size of the *ortho* substituent on the kinetics and the thermodynamics of ligand substitution.

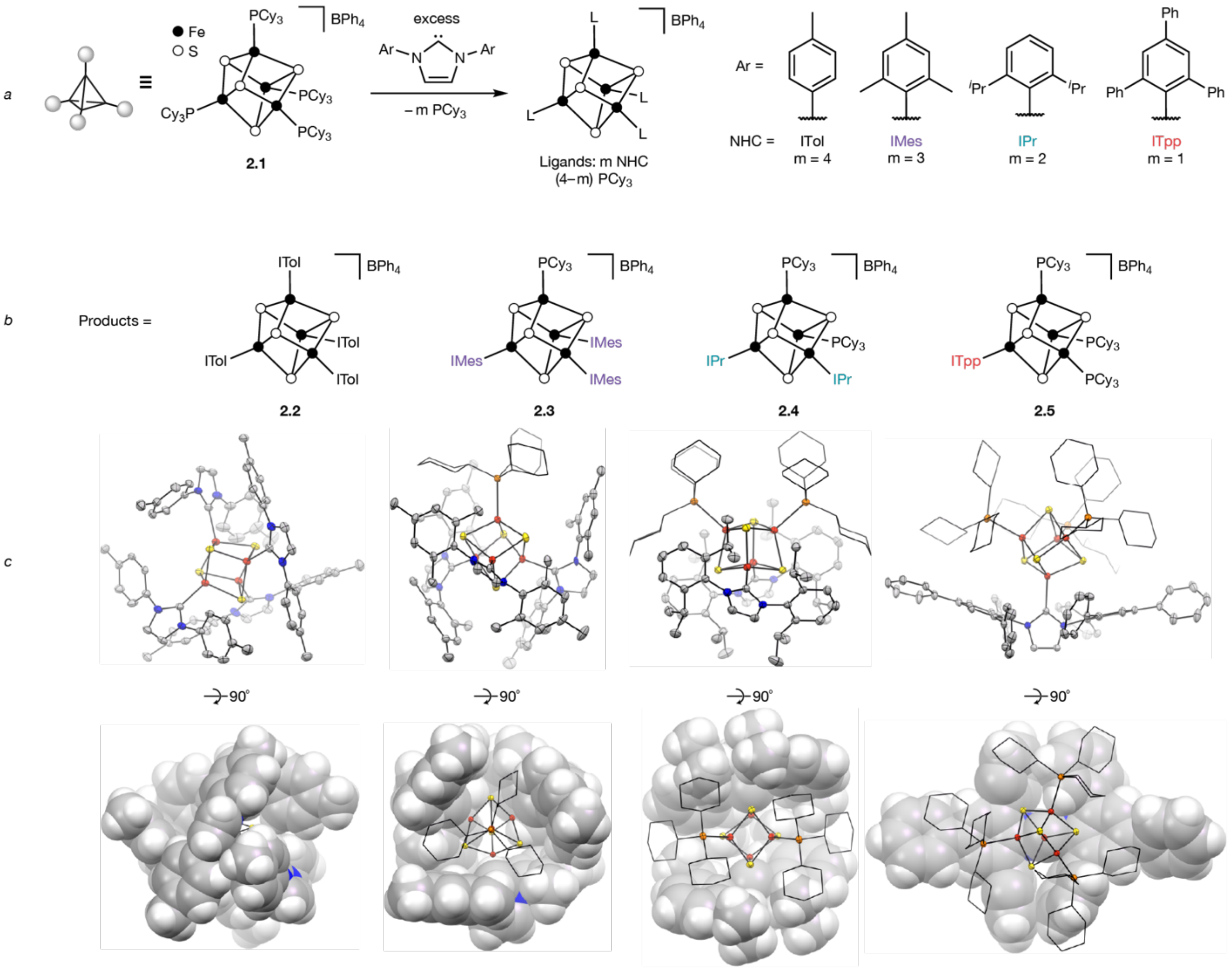

Figure 2.2. (*a*) Synthesis of site-differentiated clusters whereby the maximum number of ligand substitution events, *m*, is dictated by the identity of the NHC. (*b*) Thermal ellipsoid plots (50%; top) and corresponding space-filling illustrations (rotated 90o; bottom) of 2.2, 2.3, 2.4, and 2.5 (left to right). Hydrogen atoms, counter ions, solvent molecules, and thermal ellipsoids of PCy_3 ligands omitted for clarity. Color scheme: Fe(red), S (yellow), P (orange), N (blue), C (grey).

In an initial attempt to generate a monosubstituted cluster of the form $[\text{Fe}_4\text{S}_4(\text{PCy}_3)_3(\text{NHC})][\text{BPh}_4]$, we mixed **2.1** with the bulky NHC IPr* (1,3-bis(2,6-bis(diphenylmethyl)-4-methylphenyl)imidazol-2-ylidene). However, only slow decomposition was observed, with no evidence for ligand substitution; apparently, the *ortho*-diphenylmethyl substituents render IPr* too large to fit onto the cluster. Paring down the steric profile to ITpp (1,3-bis(2,4,6-triphenylphenyl)imidazol-2-ylidene) achieved the desired outcome: the monosubstituted cluster $[\text{Fe}_4\text{S}_4(\text{PCy}_3)_3(\text{ITpp})][\text{BPh}_4]$ (**2.5**; δ(31P) = 348 ppm). Here, the massive steric profile of ITpp—specifically, perpendicular to the imidazolyl ring—prevents a second substitution event, leaving the other three Fe sites bound to PCy_3 even in the presence of excess ITpp. Performing an analogous reaction with IDpp (1,3-bis(2,6-diphenylphenyl)imidazol-2-ylidene; identical to ITpp but lacking the para-phenyl substituents on the Ar group) also yields a monosubstituted cluster, $[\text{Fe}_4\text{S}_4(\text{PCy}_3)_3(\text{IDpp})][\text{BPh}_4]$ (**2.6**; δ(31P) = 339 ppm; *vide infra*). Thus, the *para*-phenyl substituents on the *N*-aryl groups of ITpp play no role in halting disubstitution, and the observed monosubstitution pattern for both can be attributed to the *ortho*-phenyl groups. Both ITpp and

IDpp react slowly with **2.1** and the reaction conditions that give high conversion (70 ˚C, THF) also yield some unidentified byproducts. As such, **2.5** and **2.6** were not isolated as pure materials, though NMR spectroscopic analysis of both species (Figure S2.5–Figure S2.7) and single-crystal XRD analysis of **2.5** (Figure 2.2c and Figure S2.49) confirmed their identities.

Notably, in the syntheses of **2.2**–**2.6**, under no conditions did we observe further substitution by additional NHC equivalents beyond the maximum shown in Figure 2.2. Although we attribute this to thermodynamic reasons (*i.e.*, that additional NHC ligands simply cannot fit around the cluster), we cannot rule out the possibility that additional substitution events are only kinetically disfavored. Regardless, the outcome is the same: precise site-differentiation patterns can be imparted to [Fe_4S_4] clusters by rationally tuning the *N*-aryl substitutions of NHCs.

The solid-state structures of **2.2**–**2.5** were established by single-crystal XRD analysis (Figure 2.2c, and Figure S2.46–Figure S2.50). The ligand sphere of **2.2** confers nearly S_4 symmetry to the cluster, whereas the three IMes ligands in **2.3** form a C_3-like pocket that harbors the cluster core and the PCy_3 ligand, similarly to other tris-IMes-ligated [Fe_4S_4] clusters.[14,17–22] Cluster **2.4** is positioned on a crystallographic two-fold rotational axis and its two IPr ligands form a clamshell-like pocket in which the cluster sits. The steric profile of the lone ITpp ligand in **2.5** is comparatively flat, and as suggested by the space-filling model, no more than one ITpp ligand can fit around the cluster. For **2.2**–**2.5**, the Fe–C bond lengths fall in a narrow range (the shortest distance is 2.060(2) Å in **2.5** and the longest is 2.082(1) Å in **2.2**) and are in line with those observed for other NHC-ligated [Fe_4S_4] clusters.[12,14,17–22] Similarly, the Fe–P bonds in the series fall between 2.3874(8) Å in **2.5** and 2.4159(8) Å in **2.4**, fully within the range of Fe–P distances reported for **2.1** (2.371(2)–2.428(3) Å).[2] Each NHC-ligated cluster displays a tetragonal compression along four Fe–S bonds as is commonly observed for $[Fe_4S_4]^+$ clusters,[23] and there is no statistically significant difference in the average Fe–S distances of NHC-ligated Fe sites compared to phosphine-ligated Fe sites. The absence of any meaningful differences in Fe–C, Fe–P, and cluster core bond metrics leads us to rule out the possibility that the observed site-differentiation patterns are a result of the bulky NHCs perturbing the cluster core's geometric or electronic structures (though, as expected from previous work,[12] substitution of phosphines by NHCs does make the clusters more electron-rich; see Figure S2.32 and Table S2.1 for the cyclic voltammograms of **2.1**–**2.4**)

Substitution behavior of structurally diverse N-heterocyclic carbenes

Although the trend observed for the series **2.2**–**2.5** is qualitatively sensible—the NHCs with larger aryl groups give rise to a decreased maximum number of ligand substitution events, *m*—we sought a parameter based on the NHC steric profile that would predict *m*. For this purpose, we needed to analyze the substitution chemistry of a larger number of NHCs with a broader range of structural features. This objective was accomplished by preparing a small library of NHCs (Chart 2.1), titrating each individually into solutions of **2.1**, and monitoring the reactions by ^{31}P NMR spectroscopy. To illustrate, we describe the results for IMes (Figure 2.3a). As stated above, the starting cluster **2.1** gives rise to a peak in the ^{31}P NMR spectrum at 324 ppm that decreases in intensity with added IMes. Intermediates *en route* to the fully substituted cluster **2.3** emerge first at 311 ppm, then at 233 ppm. These features disappear with ≥3 equiv IMes (at which point only **2.3** is present at 289 ppm) and can therefore be assigned to the mono- and disubstituted clusters, [$Fe_4S_4(PCy_3)_3$(IMes)][BPh_4] and [$Fe_4S_4(PCy_3)_2(IMes)_2$][BPh_4], respectively. Using this procedure, we determined the maximal substitution number for a total of eleven NHCs (Chart 2.1; see Figure S2.34–Figure S2.44 for spectra). Of the new clusters generated in these experiments, $[Fe_4S_4(IMesCy)_4][BPh_4]$ (**2.7**; IMesCy, 1-cyclohexyl-3-mesitylimidazol-2-ylidene) was isolated and structurally characterized (Figure S2.50). In short, we found that ITol, ICy (1,3-dicyclohexylimidazol-2-ylidene), and IMesCy fully substitute **2.1** (m = 4); IMes, IDep (1,3-bis(2,6-diethylphenyl)imidazol-2-ylidene), and IMesAd (1-adamantyl-3-mesitylimidazol-2-ylidene) result in trisubstitution (m = 3); IPr, SIAnt (1,3-di(anthracene-9-yl)-4,5-dihydroimidazol-2-ylidene), and ITppCy (1-cyclohexyl-3-(2,4,6-triphenylphenyl)imidazol-2-ylidene) substitute twice (m = 2); and ITpp and IDpp substitute once (m = 1; *vide supra*). The structural diversity of the NHCs that can effect well-defined site-differentiation—those having symmetric or asymmetric *N* substituents, alkyl and/or aryl substituents, and saturated or unsaturated backbone rings—highlights the generality of this approach.

With the m values for a wide range of NHCs in hand, we sought to identify a steric parameterization that could predict the experimentally observed substitution chemistry. We found that the solid angle[24] is suitable for this purpose; an alternative metric, the percent buried volume,[25] gives qualitatively similar but somewhat poorer results and is discussed in the experimental details and supplementary information section. The theoretical solid angles, G_T, were computed for each NHC in Chart 2.1 using atomic coordinates obtained from geometry optimizations of $FeCl_3(NHC)$ model complexes with a fixed Fe–C bond length of 2 Å (see the experimental details and supplemental information section for details), and the resulting values were plotted against m (Figure 2.3b). The calculated G_T values of each NHC correlate well with substitution number: NHCs with $G_T \leq 36\%$ are observed to substitute up to four times, those within the narrow range of $40\% \leq G_T \leq 41\%$ up to three times, and those with $42\% \leq G_T \leq 46\%$ up to twice. The observation that IPr substitutes twice while IDpp substitutes only once suggests that disubstitution stops at a G_T value between 46–50%.

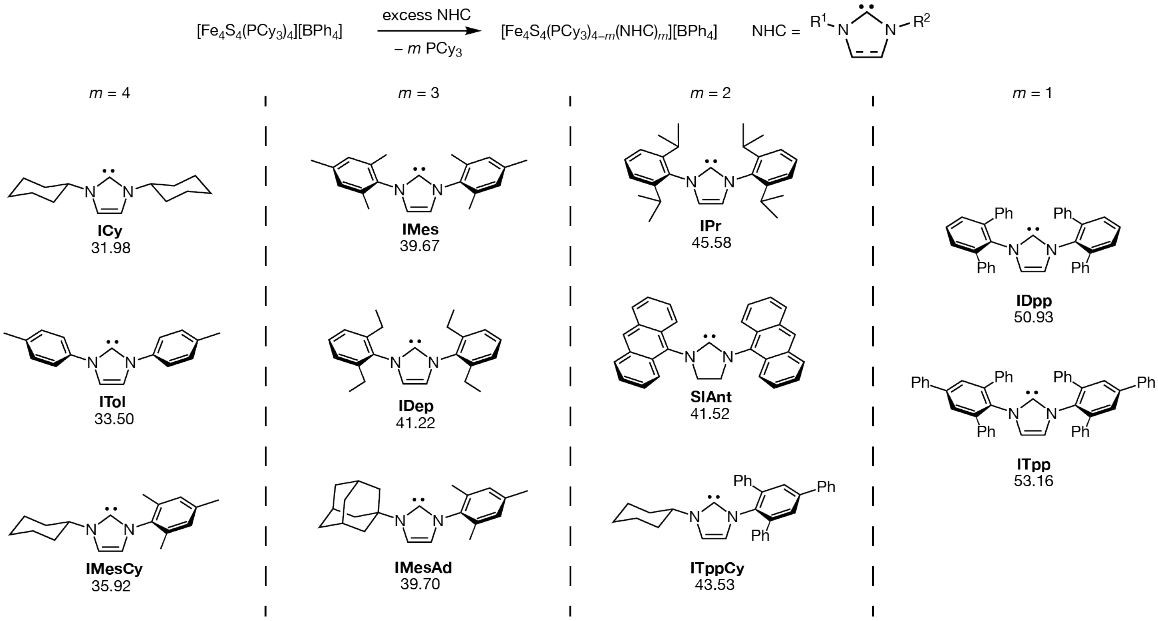

Chart 2.1. Chart of NHCs and their theoretical solid angles (G_T) organized according to their observed m values.

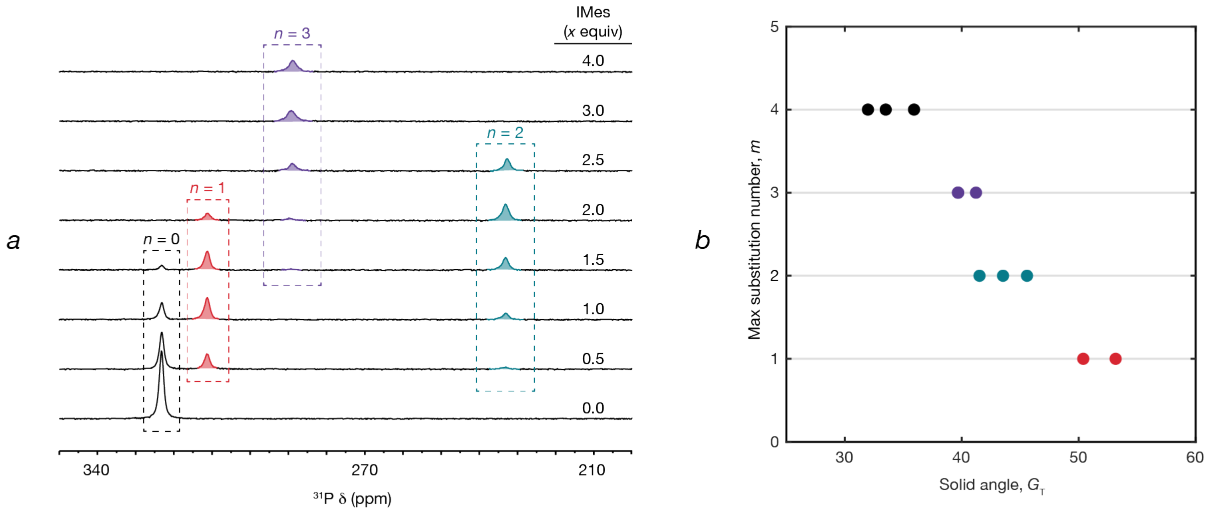

Figure 2.3. (*a*) ^{31}P NMR traces of the IMes titration reaction. The peaks are assigned as the number of bound IMes ligands, *n*. (*b*) Plot of maximal substitution number, *m*, against computed solid angle, G_T. Note that the points for IMes and IMesAd obscure one another.

Although the foregoing analysis demonstrates that G_T correlates strongly with *m*, there is likely no strict cutoff between *m* values because G_T (or any steric parameter) cannot fully capture the spatial considerations that influence these reactions. For example, IDep and SIAnt have nearly identical G_T values (41.2% and 41.5%, respectively), yet SIAnt substitutes twice and IDep substitutes thrice. Additionally, we note that G_T is not well-suited for predicting maximum substitution numbers for NHCs with steric bulk concentrated near the metal center. For example, I^{t}Bu (1,3-di-tert-butylimidazol-2-ylidene) has a relatively low G_T value of 36.2%, yet, under our reaction conditions, it does not bind **2.1**, presumably because of the significant steric bulk from the tertiary *N*-alkyl substituents oriented directly towards the metal center (*c.f.* ICy, with a G_T value of 32.0%, which has secondary *N*-alkyl substituents and fully substitutes the cluster). Nonetheless, outside of these exceptions (which are also not accurately predicted by the percent buried volume; see the experimental section), the solid angle is a useful metric for predicting the observed substitution behavior of NHCs on cuboidal [Fe_4S_4] clusters.

Conclusions

Simple ligand substitution reactions can convert homoleptic clusters to site-differentiated clusters, whereby the pattern of site-differentiation is dictated by the ligands' steric properties. For cuboidal [Fe_4S_4]$^+$ clusters, this enabled the selective preparation of site-differentiated clusters via the rational tuning of the aryl substituents of the incoming NHC ligands. We explored how a range of steric profiles influence the observed site-differentiation patterns with a gallery of structurally varied NHC ligands. We anticipate that this method can be generalized to metalloclusters of nearly any composition and geometry. In Chapter 3, we extend this site-differentiation strategy to another ubiquitous cluster structure, the octahedral, Chevrel-type clusters.

Experimental details and supplemental information

General Considerations

Unless otherwise noted, all manipulations were performed under an atmosphere of purified N_2 in an LC Technologies model LC-1 glovebox or using standard Schlenk techniques. Glassware was dried in an oven at 160 °C prior to use. Molecular sieves (3 Å) and Celite were activated/dried by heating to 250 °C under vacuum overnight and stored in the glovebox. Filtrations were performed using either fritted glass funnels or pipette filters plugged with oven-dried glass microfiber filter paper. Unless otherwise stated, all reagents and solvents were obtained from commercial suppliers and used as received. ICyHBF$_4$ and IMesAdHBF$_4$ were purchased from Strem. 2,4,6-triphenylaniline and 1,6-diphenylaniline were purchased from Ambeed. Benzene, toluene, pentane, diethyl ether, acetonitrile, and DCM were degassed by sparging with Ar and dried by passing through columns packed with alumina and Q5.[26] THF was dried/deoxygenated over Na benzophenone ketyl and distilled under N_2. *Ortho*-difluorobenzene and PhF were distilled from CaH_2. C_6D_6, DCM-d_2, and CD_3CN were degassed by three freeze-pump-thaw cycles. All solvents were stored over activated 3 Å molecular sieves in the glovebox for at least 12 h prior to use. $[Fe_4S_4(PCy_3)_4][BPh_4]$,[2] ITol,[27] IMesCy,[28] IMes,[29,30] IDep,[31] IPr,[29,30] and SIAnt[32] were prepared according to literature procedures. Abbreviations: *ortho*-difluorobenzene (DFB); sodium hexamethyldisilazide (NaHMDS); *N*-heterocyclic carbene (NHC); room temperature (RT).

Statement on compound purity

In accordance with the recommendation of the *Organometallics* editorial board,[33] we provide a statement on how we evaluated the purity of the novel compounds reported herein. The purity of clusters **2.2**–**2.4**, and **2.7**, as well as the novel organic compounds was established primarily by ^{1}H NMR spectroscopy. Additionally, all compounds as-prepared are freely soluble in organic solvents, precluding the presence of NMR-silent, insoluble species. Clusters **2.2**–**2.4**, and **2.7** were analyzed for their C, H, and N content by elemental analysis. Most values match the theoretical values within experimental error; deviations may be due to the presence of organic solvent in the lattice or incomplete combustion, as has been observed for other members of this class of molecules[18,34] and in other contexts.[35] As described in the text, **2.5** and **2.6** were not isolated as pure solids, and as such, elemental analysis was not obtained for these molecules; the identities of **2.5** and **2.6** were established by NMR spectroscopy, and **2.5** was further characterized by XRD analysis (see below).

Spectroscopy and other characterization techniques

^{1}H, ^{13}C, ^{31}P, and ^{19}F NMR spectra were collected on Bruker Avance 400 MHz or Neo 500 MHz spectrometers. Chemical shifts are reported relative to tetramethylsilane using residual solvent as an internal standard. Solvent suppression for NMR in protonated solvents was carried out using WET solvent suppression.[36] UV/visible spectra were recorded on a Cary 50 spectrophotometer. FT-IR spectra were recorded in the glovebox as powders or thin films prepared by evaporation of DCM solutions using a Bruker Alpha Platinum attenuated total reflection (ATR) spectrometer operating at 2 cm^{-1} resolution. Elemental analysis was performed by Midwest Microlab (Indianapolis, IN). HRMS data were collected on a high-resolution JEOL AccuTOF 4G LC-plus equipped with an ionSense DART (Direct Analysis in Real Time) source. The system operates with an accuracy of 5 ppm and a resolving power of greater than 10,000 (FWHM) in DART positive ion mode.

X-ray crystallography

X-ray structure determinations were performed at the MIT X-ray Diffraction Facility using a Bruker D8 Venture diffractometer equipped with a Photon2 CPAD detector, employing Mo K_{α} radiation (λ = 0.71073 Å) at 100(2) K and performing ϕ- and ω-scans. Diffraction data were collected, integrated, and corrected for absorption using Bruker APEX3 software and its associated modules (SAINT, SADABS, TWINABS). The structures were solved by direct methods using SHELXT-2015 and refined against F^2 on all data by full-matrix least-squares with SHELXL-2018. Non-hydrogen atoms were refined anisotropically. Hydrogen atoms were included in the model at geometrically calculated positions and refined using a riding model. The isotropic displacement parameters of all hydrogen atoms were fixed to 1.2 times the U value of the atoms they are linked to (1.5 times for methyl groups). Similarity and rigid bond restraints were placed on all atoms. Additional crystallographic data is provided in Table S2.3.

Cyclic voltammetry (CV)

Experiments were performed using a GAMRY Reference 600 potentiostat. The cell consisted of a glassy carbon working electrode, an Ag wire auxiliary electrode, and an Ag wire pseudo-reference electrode. CVs were internally referenced to the Fc/Fc$^+$ redox couple. The electrolyte [^{n}Bu$_4$N][PF$_6$] was recrystallized from methanol five times.

Ligand substitution product distribution

The product distributions of ligand substitution reactions were modeled by a binomial distribution function adapted from DiSalvo.[37] The following equation is the binomial distribution function where P is the probability of n number of metal sites in a cluster undergoing net ligand substitution of a total m number of metal sites in the cluster, each metal site having a probability of ligand substitution p.

$$P = \frac{m!}{(m-n)!\,n!} p^n (1-p)^{m-n}$$

p can be understood as the probability of finding a metal atom bound to the incoming ligand where f is the mole fraction of the incoming ligand and ΔG is the binding free energy difference between the ligands:

$$p = \frac{f e^{-\Delta G/RT}}{(1-f) + f e^{-\Delta G/RT}}$$

When $\Delta G = 0$, p can be simplified as the nominal mole fraction of the new ligand, where x is the amount of added new ligand:

$$p = x/(x + m)$$

When the binding of the incoming ligand is strongly thermodynamically favored ($\Delta G \to -\infty$), p becomes

$$p = x/m$$

The plots presented in Chapter 1, 2, and 3 assume a strong thermodynamic driving force for NHC binding in place of phosphine: $\Delta G = -10$ kcal/mol (at $T = 298$ K).

Synthetic procedures

*[Fe_4S_4(ITol)$_4$][BPh_4] (**2.2**)*

ITol (100.0 mg, 0.4027 mmol) suspended in THF (2 mL) was added to a stirring solution of **2.1** (154.0 mg, 0.8591 mmol) in THF (4 mL). After 0.5 h, the mixture was filtered through Celite. The filtrate was concentrated *in vacuo* and the product precipitated by addition of *n*-pentane (12 mL). The resulting black solids were washed thoroughly with *n*-pentane (4 × 2 mL) and diethyl ether (4 × 2 mL). The product was extracted into minimal THF (2 mL). The solution was filtered and layered with *n*-pentane (12 mL). Compound **2.2** was obtained as a black crystalline solid (117.2 mg, 82% yield). Crystals for structure determination were obtained from layering a saturated THF solution with cyclohexane (Figure S2.46). ^{1}H NMR (THF, 400 MHz, 298K): δ (ppm) 8.49 (s, 16H, *o-H*), 7.83 (s, 8H, backbone C*H*), 7.30 (t, 8H, BPh_4 *o-H*), 7.13 (s, 16H, *m-H*), 6.84 (t, 8H, BPh_4 *m-H*), 6.69 (t, 4H, BPh_4 *p-H*), 2.69 (s, 24H, *p*-CH_3). Anal. Found (Calc.): C, 66.79% (66.40%); H, 5.64% (5.09%); N, 6.81% (6.73%).

*[Fe_4S_4(IMes)$_3$(PCy_3)][BPh_4] (**2.3**)*

IMes (136.0 mg, 0.4467 mmol) in THF (2 mL) was added to a stirring solution of **2.1** (200.0 mg, 0.1115 mmol) in THF (5 mL). After 0.5 h, the mixture was filtered through Celite. The filtrate was concentrated *in vacuo* and the product precipitated by addition of *n*-pentane (15 mL). The resulting black solids were washed thoroughly with *n*-pentane (4 × 2 mL) and diethyl ether (4 × 2 mL). Compound **2.3** was obtained as a black crystalline solid following recrystallization from THF and *n*-pentane (173.7 mg, 83% yield). Crystals for structure determination were obtained from layering a saturated THF solution with diethyl ether (Figure S2.47). ^{1}H NMR (DCM, 500 MHz, 293 K): δ (ppm) 7.29 (m, 8H, BPh_4 *o-H*), 7.10 (s, 6H, backbone C*H*), 7.02 – 6.99 (s + t, 12H + 8H, J = 7.4 Hz, Mes *m-H* + BPh_4 *m-H*), 6.85 (t, 4H, J = 7.3 Hz, BPh_4 *p-H*), 4.00 (s, 3H, PC*H*), 2.39 (s, 18H, *o*-CH_3), 2.30 (d, 6H, J = 11.2 Hz, PCy_3 CH_2), 2.11 (br, 24H + 12H, Mes *o*-CH_3 + PCy_3 CH_2), 1.95 (br, 4H, PCy_3 CH_2), 1.47 (br, 8H, PCy_3 CH_2); ^{31}P NMR (DCM-d_2, 202 MHz, 293 K): δ (ppm) 324.56. Anal. Found (Calc.): C, 67.83% (67.64%); H, 7.54% (6.76%); N, 4.39% (4.51%).

*[Fe_4S_4(IPr)$_2$(PCy_3)$_2$][BPh_4] (**2.4**)*

IPr (325.0 mg, 0.8363 mmol) in THF (3 mL) was added to a stirring solution of **2.1** (600.0 mg, 0.3347 mmol) in THF (12 mL) in a thick-walled flask and the flask was sealed. The mixture was stirred at 70 °C for 3 h, then allowed to cool to RT. The mixture was filtered through Celite and concentrated *in vacuo*. The product was precipitated by addition of *n*-pentane (20 mL). The resulting black solids were washed thoroughly with *n*-pentane (3 × 5 mL) and diethyl ether (3 × 5 mL). Compound **2.4** was obtained as a black crystalline solid following recrystallization from THF and *n*-pentane (472.0 mg, 70% yield). Crystals for structure determination were obtained from layering a saturated PhF solution with diethyl ether (Figure S2.48). ^{1}H NMR (DCM-d_2, 400 MHz, 293 K): δ (ppm) 7.56 (s, 4H, backbone C*H*), 7.31 (m, 8H, BPh_4 *o-H*), 7.19 (d, 8H, *J* = 7.0 Hz, *m-H*), 7.03 (t + s, 8H + 4H, *J* = 7.4 Hz, BPh_4 *m-H* + Dipp *p-H*), 6.87 (t, 4H, *J* = 7.4 Hz, BPh_4 *p-H*), 4.16 (s, 6H, PCy_3 PC*H*), 3.02 (s, 8H, Dipp C*H*($CH_3)_2$), 2.29 (d, 12H, *J* = 11.1 Hz, PCy_3 CH_2), 2.15 (s, 20H, PCy_3 CH_2), 2.03 (br, 18H, PCy_3 CH_2), 1.68-1.58 (br d, 24H, *J* = 47.2 Hz, Dipp CH(C$H_3)_2$), 1.41 (br, 8H, PCy_3 CH_2), 1.17 (s, 24H, Dipp CH(C$H_3)_2$); ^{31}P NMR (DCM-d_2, 202 MHz, 293 K): δ (ppm) 390.98. Anal. Found (Calc.): C, 66.47% (68.16%); H, 8.08% (7.93%); N, 2.74% (2.79%).

[Fe_4S_4(ITpp)($PCy_3)_3$][BPh_4] (**2.5**)

ITpp (19.0 mg, 0.0281 mmol) in THF (0.5 mL) was added to a stirring solution of **2.1** (20.0 mg, 0.0112 mmol) in THF (0.5 mL). The mixture was stirred for 2 hours at 70 °C, filtered through Celite, concentrated *in vacuo*, and the product was precipitated with *n*-pentane (10 mL). The resulting black solids were washed with *n*-pentane (3 × 3 mL) and diethyl ether (3 × 3 mL) then recrystallized from THF and *n*-pentane (Figure S2.49). ^{1}H NMR spectra of **2.5** (Figure S2.5 and Figure S2.6) show that the major contaminant is ITppHBPh_4. ^{1}H NMR of **2.5** (THF, 400 MHz, 293 K): δ (ppm) 8.57 (s, 8H, ITpp), 7.58 (m, 20H, ITpp), 7.34 (t, 8H, ITpp), 7.31 – 7.24 (m, 46H, ITpp + BPh_4 *o-H*), 7.82 (t, 30H, BPh_4 *m-H*), 6.67 (t, 18H, BPh_4 *p-H*), 4.95 (s, 9H, PCy_3 C*H*), 2.29 (s, 50H, PCy_3 CH_2), 2.08 (s, 40H, PCy_3 CH_2); ^{31}P NMR (DFB, 162 MHz, 293 K): δ (ppm) 353.72.

[Fe_4S_4(IDpp)($PCy_3)_3$][BPh_4] (**2.6**)

Compound **2.6** was prepared utilizing identical reaction conditions to the synthesis of **2.5** with 14.6 mg of IDpp (0.0278mmol) in THF (0.5 mL) and 20.0 mg of **2.1** (0.0112 mmol) in THF (0.5 mL). As with **2.5**, pure samples of **2.6** could not be obtained with one contaminant being IDppHBPh_4 (Figure S2.7). ^{1}H NMR of **2.6** (DFB, 400 MHz, 293 K): δ (ppm) 8.18 (s, 8H, IDpp), 7.73 (t, 18H, BPh_4 *o-H*), 4.85 (s, 9H, PCy_3 C*H*), 2.21 (s, 34H, PCy_3 CH_2), 1.92 (s, 16H, PCy_3 CH_2), 1.85 (d, 14H, PCy_3 CH_2), 1.62 (s, 20H, PCy_3 CH_2), 1.24 (s, 10H, PCy_3 CH_2); ^{31}P NMR (DFB, 162 MHz, 293 K): δ (ppm) 344.73.

[Fe_4S_4(IMesCy)$_4$][BPh_4] (**2.7**)

IMesCy (39.4 mg, 0.147 mmol) in THF (1 mL) was added to a stirring solution of **2.1** (50.6 mg, 0.0282 mmol) in THF (2 mL). After 0.5 h, the mixture was filtered through Celite. The filtrate was concentrated *in vacuo* and the product precipitated by addition of *n*-pentane (12 mL). The resulting black solids were washed thoroughly with *n*-pentane (3 × 3 mL) and diethyl ether (3 × 3 mL). The product was obtained as a black crystalline solid following recrystallization with DFB and *n*-pentane (43.1 mg, 87% yield). Crystals for structure determination were obtained from layering a saturated PhF solution with *n*-pentane (Figure S2.50). ^{1}H NMR (DCM, 400 MHz, 293 K): δ (ppm) 7.65 (s, 4H, backbone C*H*), 7.32 (t, 8H, *J* = 5.6 Hz, BPh_4 *o-H*), 7.03 (t, 8H, *J* = 7.4 Hz, BPh_4 *m-H*), 6.88 (t, 4H, *J* = 7.2 Hz, BPh_4 *p-H*), 6.73 (s, 8H, Mes *m-H*), 6.49 (s, 4H, backbone C*H*), 2.91 (s, 16H, CH_2), 2.49 (s, 8H, CH_2), 2.25 (s, 24H, *o*-CH_3), 2.19 (s, 12H, *p*-CH_3), 2.00 (br, 18H, CH_2). Anal. Found (Calc.): C, 65.88% (66.10%); H, 7.17% (6.70%); N, 6.21% (6.42%).

1-(2,4,6-triphenylphenyl)-3-(cyclohexyl)imidazolium tetrafluoroborate (ITppCyHBF$_4$)

ITppCyHBF$_4$ was synthesized via a one-pot reaction under air adapted from Baslé, Mauduit, and coworkers.[28,38] 2,4,6-triphenylaniline (250 mg, 0.778 mmol) and cyclohexylamine (77 mg, 0.778 mmol) were combined in a 25 mL round-bottom flask with HOAc (1 mL). In a separate 5 mL round-bottom flask, 37% formaldehyde (63 mg, 0.778 mmol) and 40% glyoxal (116 mg, 0.778 mmol) were combined with HOAc (1 mL). Both vessels were warmed to 50 °C with stirring, then the glyoxal/paraformaldehyde mixture was added at once to the aniline/amine mixture at 50 °C. The mixture was stirred at 50 °C for 30 minutes, then allowed to cool to RT. The reaction mixture was diluted with DCM (20 mL) and washed thoroughly with water (5 x 20 mL) and brine (5 x 20 mL) to remove residual HOAc. The organic fractions were combined, dried with MgSO$_4$, and concentrated to dryness *in vacuo*. The product was isolated as an off-white powder (234 mg, 61%) by recrystallization from boiling EtOAc. ^{1}H NMR (DMSO-d_6, 500 MHz, 293 K): δ (ppm) 9.29 (s, 1H, Im-*H*), 7.92 (s, 2H, *m-H*), 7.92 (d, 2H, *J* = 7.06 Hz, *p,o-H*), 7.78 (t, 1H, *J* = 1.8 Hz, backbone C*H*), 7.70 (t, 1H, *J* = 1.8 Hz, backbone C*H*), 7.54 (t, 2H, *J* = 7.4 Hz, *o,p-H*), 7.48 (t, 1H, *J* = 7.3 Hz, *p,p-H*), 7.40 (d, 2H, *J* = 1.3 Hz, *p,m-H*), 7.39 (d, 4H, *J* = 2.1 Hz, *o,m-H*), 7.33 – 7.31 (m, 4H, *o,o-H*), 4.16 (t, 1H, *J* = 11.3 Hz, C*H*), 1.75 – 1.67 (m, 4H, C*H*$_2$), 1.60 (d, 1H, *J* = 12.8 Hz, C*H*$_2$), 1.42 (q, 2H, *J* = 12.0 Hz, C*H*$_2$), 1.30 (q, 2H, *J* = 12.4 Hz, C*H*$_2$), 1.10 (q, 1H, *J* = 12.8 Hz, C*H*$_2$); ^{13}C NMR (DMSO-d_6, 126 MHz, 293 K): δ (ppm) 143.34, 140.46, 138.69, 137.20, 136.95, 130.38, 129.66, 129.05, 128.87, 128.72, 127.88, 126.15, 121.20, 58.97, 32.78, 24.64, 24.47; HRMS for [ITppCyH]$^+$ calculated: *m*/*z* = 455.24818, found: 455.24717.

1-(2,4,6-triphenylphenyl)-3-(cyclohexyl)imidazole-2-ylidene (ITppCy)

ITppCyHBF$_4$ (165.4 mg, 0.3049 mmol) was suspended in benzene (4 mL). With stirring, NaHMDS (53.0 mg, 0.289 mmol) suspended in benzene (1 mL) was added. After 1 h, the solution was filtered through Celite and concentrated to dryness *in vacuo*. The filtrate was again extracted with benzene (4 mL) and the solution filtered through Celite. The filtrate was concentrated to dryness *in vacuo* and washed with diethyl ether (3 x 2 mL). The product was isolated as an off-white solid (130.2 mg, 98%) and stored under inert atmosphere at −30 °C. ^{1}H NMR (C$_6$D$_6$, 400 MHz, 293 K): δ (ppm) 7.66 (s, 2H, *m-H*), 7.46 (t, 6H, *J* = 7.1 Hz, Ar-*H*), 7.22 (t, 2H, *J* = 7.4 Hz, Ar-*H*), 7.14 (m, 4H, Ar-*H*), 7.07 (t, 2H, *J* = 7.6 Hz, Ar-*H*), 6.36 (s, 1H, backbone C*H*), 6.22 (s, 1H, backbone C*H*), 3.91 (t, 1H, *J* = 11.8 Hz, C*H*), 1.83 (d, 2H, *J* = 12.3 Hz, C*H*$_2$), 1.55 (d, 2H, *J* = 11.3 Hz, C*H*$_2$), 1.5 – 1.38 (m, 3H, C*H*$_2$), 1.06 – 0.87 (m, 3H, C*H*$_2$); ^{13}C NMR (C$_6$D$_6$, 101 MHz, 293 K): δ (ppm) 217.97, 141.38, 140.78, 140.41, 138.53, 129.77, 129.13, 129.09, 127.69, 127.08, 121.83, 116.38, 59.46, 34.98, 25.73.

N^1,N^2-bis(2,4,6-triphenylphenyl)ethane-1,2-diimine

Synthesized according to a procedure adapted from Morris, et al.[39] In air, 2,4,6-triphenylaniline (2.00 g, 6.22 mmol) was suspended in MeCN (20 mL). 40% glyoxal (0.336 mL, 2.96 mmol) was added dropwise, and the mixture was stirred at 50 °C for 3 d with a reflux condenser. The product precipitated as a yellow powder over the course of the reaction and was collected by filtration and washed with MeCN (2 × 15 mL) and diethyl ether (10 mL). The product was dried *in vacuo* at RT for several hours (1.287 g, 66%). ^{1}H NMR (C$_6$D$_6$, 400 MHz, 293 K): δ (ppm) 7.56 (s, 2H, C*H*), 7.54 (s, 4H, *m-H*), 7.26 – 7.19 (m, 16H, Ar-*H*), 7.17 – 7.15 (m); HRMS for [C$_{50}$H$_{36}$N$_2$–H]$^+$ calculated: *m*/*z* = 665.29513, found: 665.29983.

1,3-bis(2,4,6-triphenylphenyl)imidazolium tetrafluoroborate (ITppHBF$_4$)

Synthesized according to a procedure adapted from Morris, et al.[39] (Chloromethoxy)ethane (3.9 mL, 44 mmol) was added to solid *N^1*,*N^2*-bis(2,4,6-triphenylphenyl)ethane-1,2-diimine (1.25 g, 1.88 mmol) with stirring under air atmosphere. After a few minutes, MeCN (10 mL) was added. The mixture was allowed to stir for 3 h during which time the color changed from yellow to dark orange and the solids dissolved. The solution was filtered through Celite and the volatiles were removed *in vacuo*. This material was suspended in water (150 mL) and solid NaBF$_4$ (800 mg, 7.29 mmol) was added. Immediately, a dark orange solid precipitated. The mixture was diluted with DCM (200 mL) and washed with water (2 × 100 mL). The organic fractions were combined, dried with MgSO$_4$, and concentrated to dryness *in vacuo*. The product was isolated as a pale pink solid (1.129 g, 79%) by recrystallization from DCM with diethyl ether. ^{1}H NMR (CDCl$_3$, 500 MHz, 293 K): δ (ppm) 8.18 (t, 1H, *J* = 1.6 Hz, Im-*H*), 7.61 (d, 4H, *J* = 6.9 Hz, *p*,*o*-*H*), 7.60 (s, 4H, *m*-*H*), 7.46 (t, 6H, *J* = 7.2 Hz, *p*,*m*-*H*), 7.43 (t, 2H, *J* = 1.4 Hz, *p*,*p*-*H*), 7.41 – 7.40 (m, 12H, *o*,*p*-*H* + *o*,*m*-*H*), 7.09 – 7.06 (m, 8H, *o*,*o*-*H*), 6.82 (d, 2H, *J* = 1.6 Hz, backbone C*H*); ^{13}C NMR (CDCl$_3$, 126 MHz, 293 K): δ (ppm) 143.70, 139.23, 138.42, 137.31, 136.39, 130.26, 129.25, 129.07, 128.81, 128.74, 128.68, 128.20, 127.39, 124.60; HRMS for [ITppH]$^+$ calculated: *m*/*z* = 677.29513, found: 677.29124.

1,3-bis(2,4,6-triphenylphenyl)imidazole-2-ylidene (ITpp)

ITppHBF$_4$ (200.0 mg, 0.2616 mmol) was suspended in benzene (3 mL). With stirring, NaHMDS (45.6 mg, 0.248 mmol) suspended in benzene (2 mL) was added. After 1 h, the solution was filtered through Celite and concentrated to dryness *in vacuo*. The filtrate was again extracted with benzene (5 mL) and the solution filtered through Celite. The product was isolated as a pale pink solid (168.0 mg, 99%) by recrystallization from benzene and *n*-pentane. ITpp was stored under inert atmosphere at −30 °C. ^{1}H NMR (THF, 400 MHz, 293 K): δ (ppm) 7.73 (d, 4H, *J* = 8.5 Hz, *p*,*o*-*H*), 7.61 (s, 4H, *m*-*H*), 7.43 (t, 4H, *J* = 7.6 Hz, *p*,*m*-*H*), 7.35 (*t*, 2H, *J* = 7.3 Hz, *p*,*p*-*H*), 7.26 – 7.23 (m, 8H, *o*,*o*-*H*), 7.16 (m, 12H, *o*,*m*-*H* + *o*,*p*-*H*), 6.00 (s, 2H, backbone C*H*); ^{13}C NMR (THF, 101 MHz, 293 K): δ (ppm) 223.95, 141.10, 140.77, 140.64, 137.68, 130.72, 129.84, 129.40, 128.19, 127.71, 127.35, 122.10.

N^1,N^2-bis(2,6-diphenylphenyl)ethane-1,2-diimine

Synthesized according to a procedure adapted from Morris, et al.[39] In air, 2,6-diphenylaniline (987 mg, 4.02 mmol) was suspended in MeCN (10 mL). 40% glyoxal (0.217 mL, 1.91 mmol) was added dropwise and the mixture was stirred at 50 °C for 3 d with a reflux condenser. The product precipitated as a yellow powder over the course of the reaction and was collected by filtration and washed with MeCN (2 × 15 mL) and diethyl ether (10 mL). The product was dried *in vacuo* at RT for several hours (489.8 mg g, 50%). ^{1}H NMR (C$_6$D$_6$, 500 MHz, 293 K): δ (ppm) 7.44 (s, 2H, C*H*), 7.18 (s, 2H, Ar-*H*), 7.17 (d, 2H, *J* = 1.8 Hz, C*H*), 7.15 (m, 20H, Ar-*H*), 7.12 (t, 2H, *J* = 2.0 Hz, Ar-*H*), 7.11 (m, 4H, Ar-*H*), 7.09 – 7.07 (m, 6H, Ar-*H*), 6.97 (t, 2H, *J* = 7.8 Hz, Ar-*H*); ^{13}C NMR (C$_6$D$_6$, 126 MHz, 293 K): δ (ppm) 165.16, 147.78, 140.00, 133.43, 130.34, 130.23, 128.31, 126.96, 125.63.; HRMS for [C$_{38}$H$_{28}$N$_2$–H]$^+$ calculated: *m*/*z* = 513.23253, found: 513.23407.

1,3-bis(2,6-diphenylphenyl)imidazolium tetrafluoroborate (IDppHBF$_4$)

Synthesized according to a procedure adapted from Morris, et al.[39] (Chloromethoxy)ethane (1.53 mL, 17.2 mmol) was added to solid *N*^{1},*N*^{2}-bis(2,6-diphenylphenyl)ethane-1,2-diimine (400 mg, 0.780 mmol) with stirring under air atmosphere. After a few minutes, MeCN (5 mL) was added. The mixture was allowed to stir for 3 h during which time the color changed from yellow to dark orange and the solids dissolved. The solution was filtered through Celite, and the volatiles were removed *in vacuo*. This material was suspended in water (70 mL) and solid NaBF$_4$ (343 mg, 3.12 mmol) was added in excess. Immediately, a dark orange solid precipitated. The mixture was diluted with DCM (50 mL) and washed with water (2 × 50 mL). The organic fractions were combined, dried with MgSO$_4$, and concentrated to dryness *in vacuo*. The product was isolated as a pale orange solid (321.4 mg, 67%) by recrystallization from boiling EtOAc. ^{1}H NMR (CDCl$_3$, 400 MHz, 293 K): δ (ppm) 8.20 (s, 1H, Im-*H*), 7.62 (t, 2H, *J* = 7.7 Hz, *p-H*), 7.42 (d, 4H, *J* = 7.6 Hz, *m-H*), 7.40 – 7.37 (t, 12H, *J* = 3.6 Hz, *o,m-H* + *o,p-H*), 7.01 (q, 8H, *J* = 3.4 Hz, *o,o-H*), 6.72 (d, 2H, *J* = 1.7 Hz, backbone C*H*); ^{13}C NMR (CDCl$_3$, 101 MHz): δ (ppm) 138.96, 137.58, 136.48, 131.98, 130.91, 129.31, 128.93, 128.76, 124.49; HRMS for [IDppH]$^+$ calculated: *m*/*z* = 525.23253, found: 525.23132.

1,3-bis(2,6-diphenylphenyl)imidazole-2-ylidene (IDpp)

IDppHBF$_4$ (159.9 mg, 0.2611 mmol) was suspended in benzene (3 mL). With stirring, NaHMDS (45.6 mg, 0.248 mmol) suspended in benzene (2 mL) was added. After 1 h, the solution was filtered through Celite and concentrated to dryness *in vacuo*. The filtrate was again extracted with benzene (5 mL) and the solution was filtered through Celite. Solvent was removed *in vacuo*. The resulting solids were washed with *n*-pentane (2 × 2 mL) and diethyl ether (3 × 2 mL), then dried *in vacuo* to yield pale orange product (217.2 mg, 98%). Stored under inert atmosphere at −30 °C. ^{1}H NMR (THF, 400 MHz, 293 K): δ (ppm) 7.47 (t, 2H, *J* = 7.6 Hz, *p-H*), 7.37 (d, 4H, *J* = 6.9 Hz, *m-H*), 7.21 – 7.15 (m, 20H, *o,o-H* + *o,m-H* + *o,p-H*), 5.97 (s, 2H, backbone C*H*); ^{13}C NMR (THF, 101 MHz, 293 K): δ (ppm) 223.84, 140.71, 140.62, 138.47, 131.34, 130.64, 128.11, 127.67, 127.21, 122.04.

Spectroscopic and electrochemical data

NMR spectra

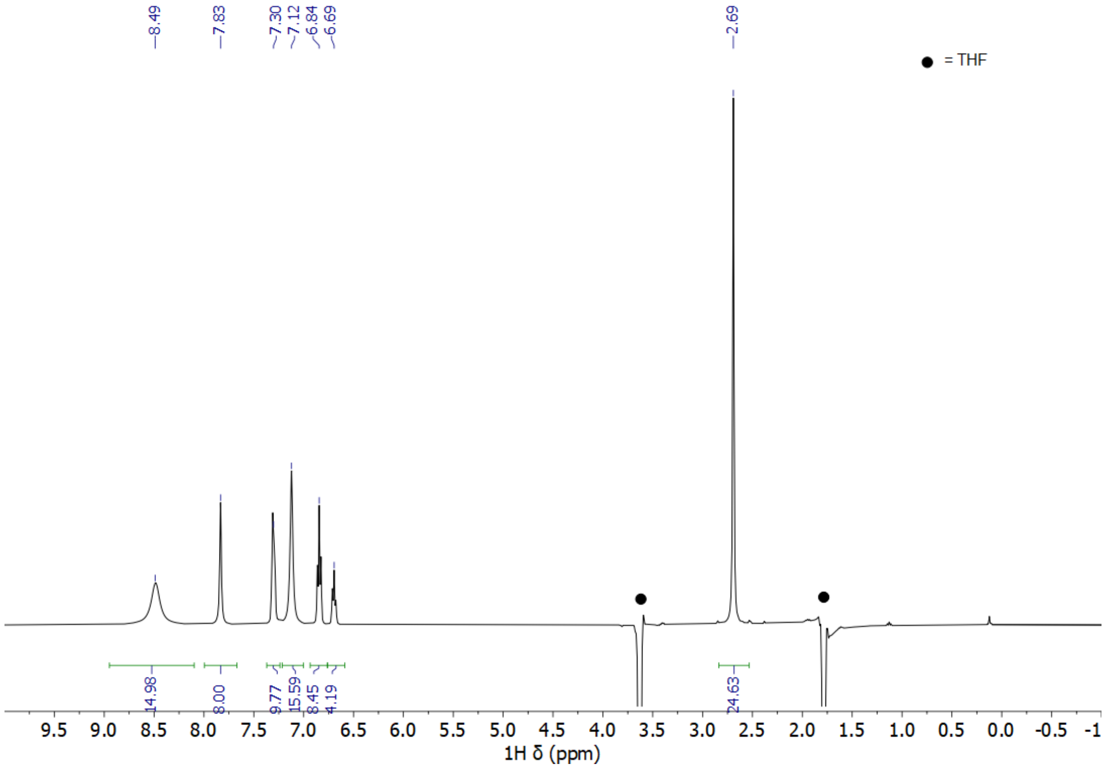

Figure S2.1. Solvent-suppressed ^{1}H NMR spectrum of **2.2** in THF (400 MHz, 293 K).

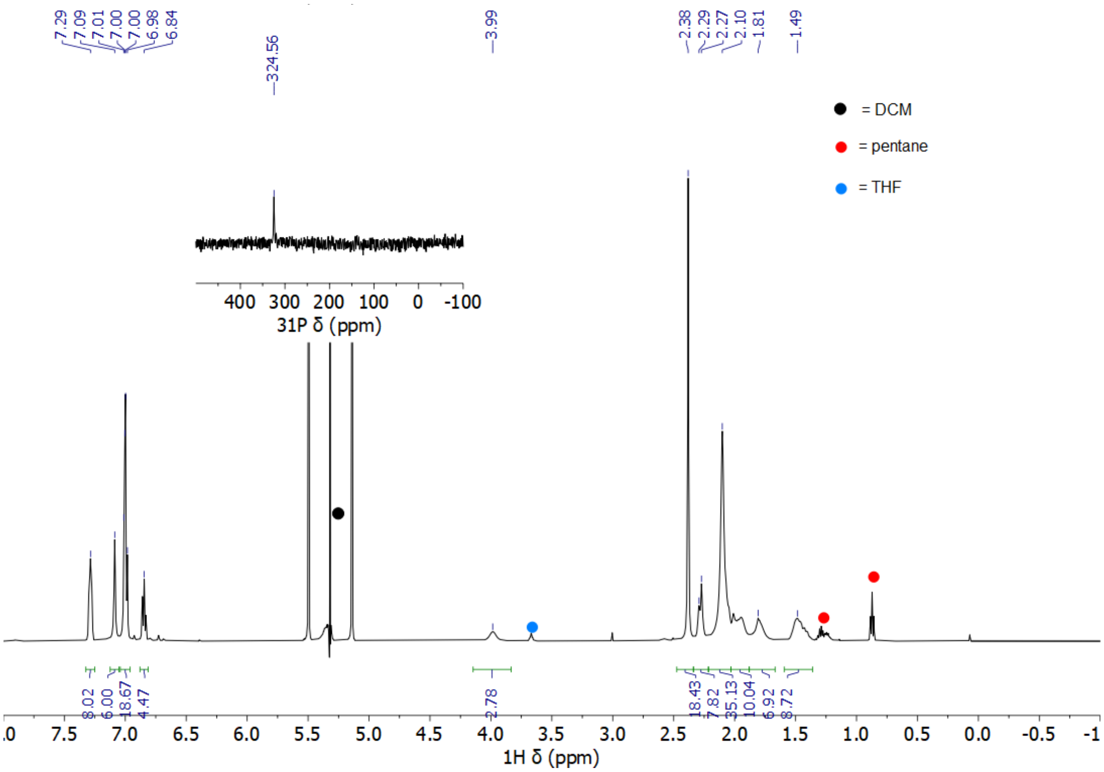

Figure S2.2. ^{1}H and ^{31}P (inset) NMR spectra of **2.3** in DCM (500 MHz, 202 MHz, respectively, 293 K).

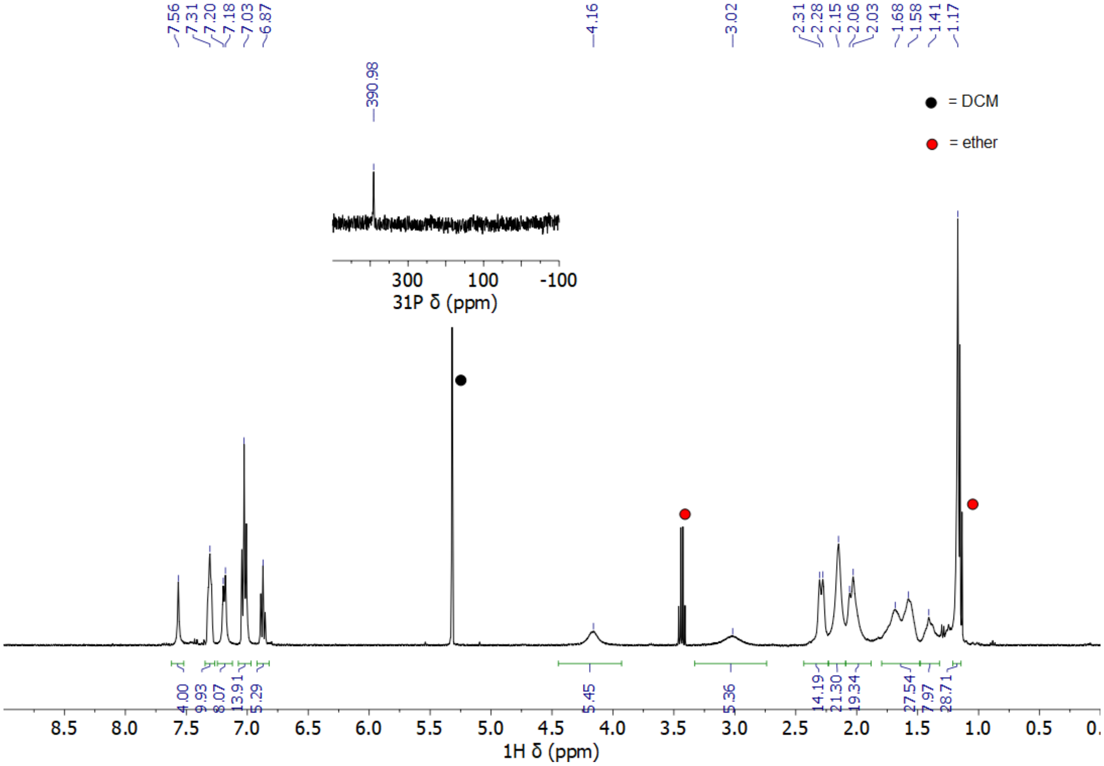

Figure S2.3. ^{1}H and ^{31}P (inset) NMR spectra of **2.4** in DCM-d_2 (400 MHz, 202 MHz, respectively, 293 K).

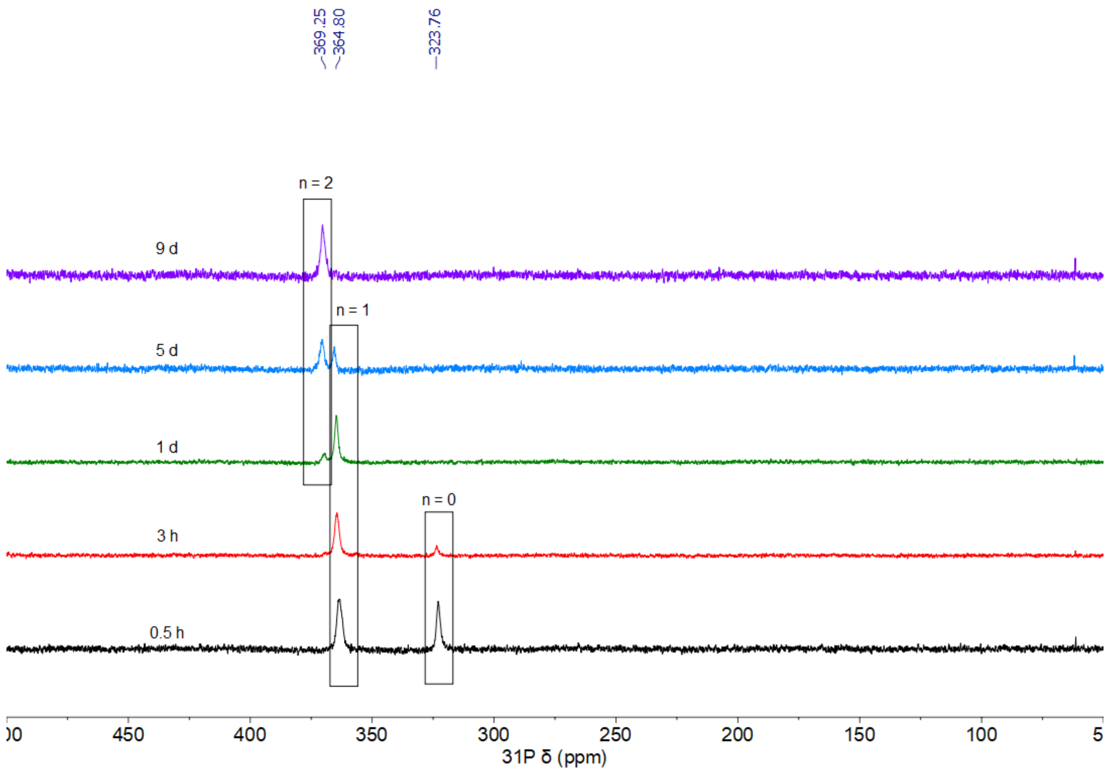

Figure S2.4. ^{31}P NMR spectra of reaction of 3 equiv IPr and **2.1** in THF (202 MHz, 293 K). Spectra recorded at 0.5 h, 3 h, 1 d, 5 d, and 9 d (black, red, green, blue, and violet traces, respectively).

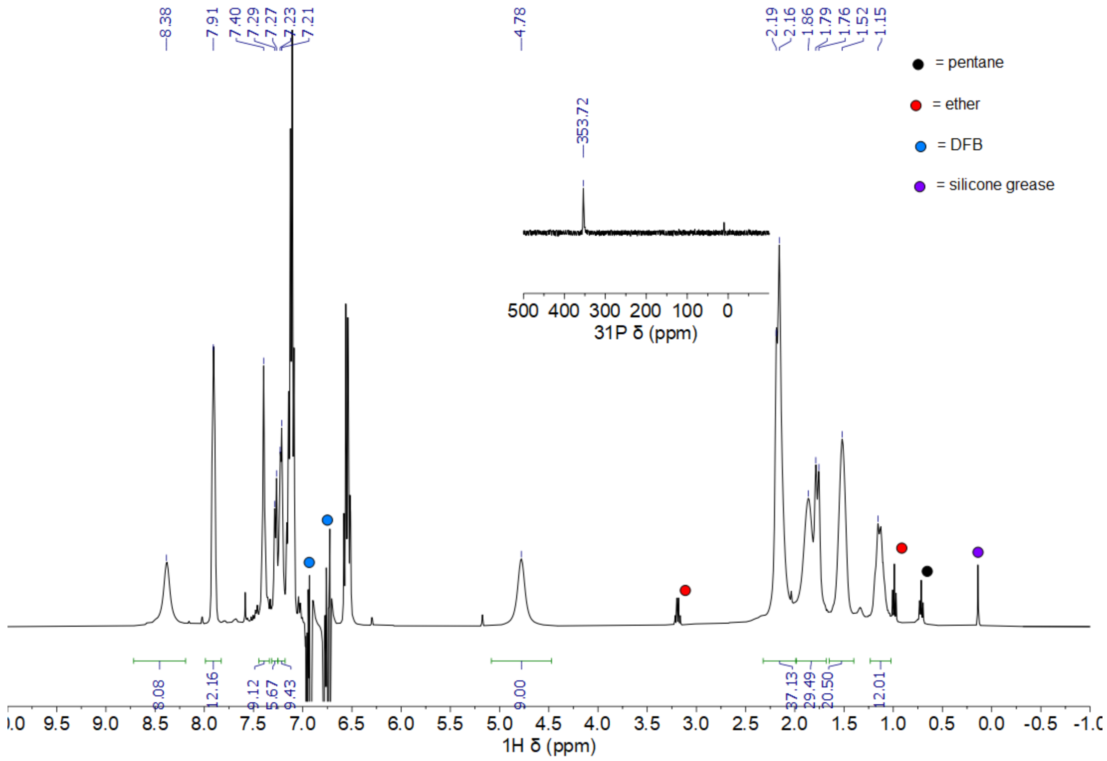

Figure S2.5. Solvent-suppressed ^{1}H and ^{31}P (inset) NMR spectra of **2.5** in DFB (400 MHz, 162 MHz, respectively, 293 K).

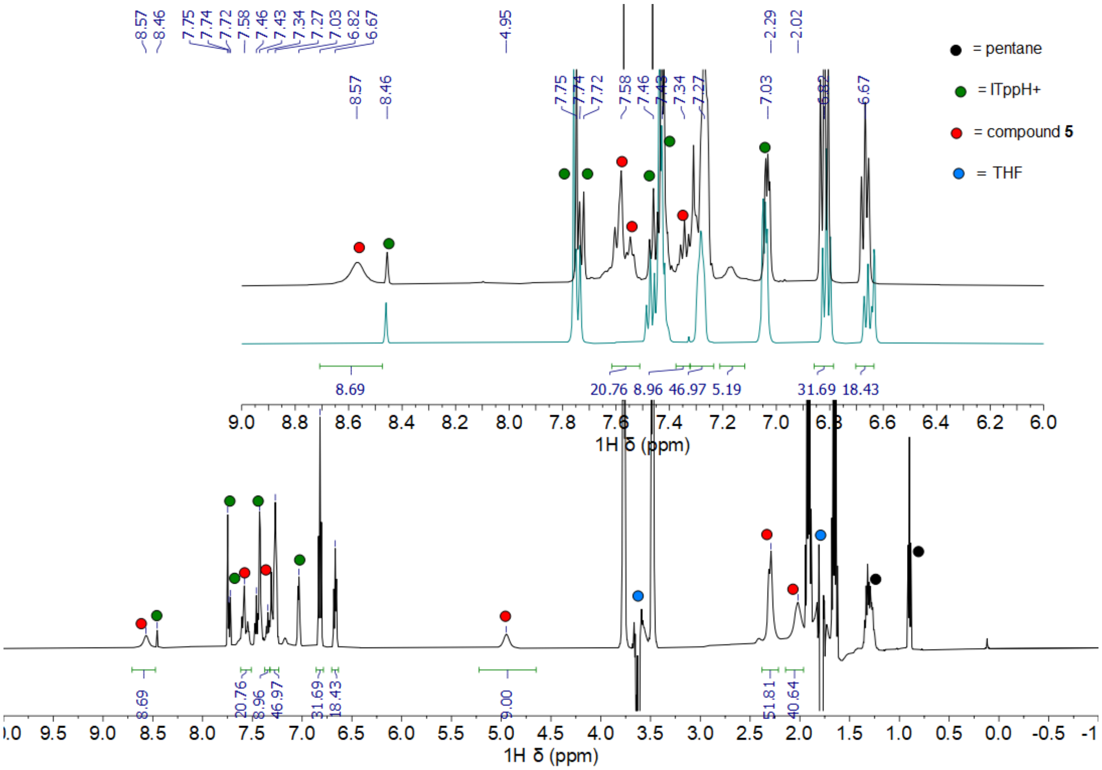

Figure S2.6. Solvent-suppressed ^{1}H NMR spectrum of **2.5** in THF (400 MHz, 293 K). Inset show comparison of ITppHBPh4 (teal trace) and 5 (black trace, integrated).

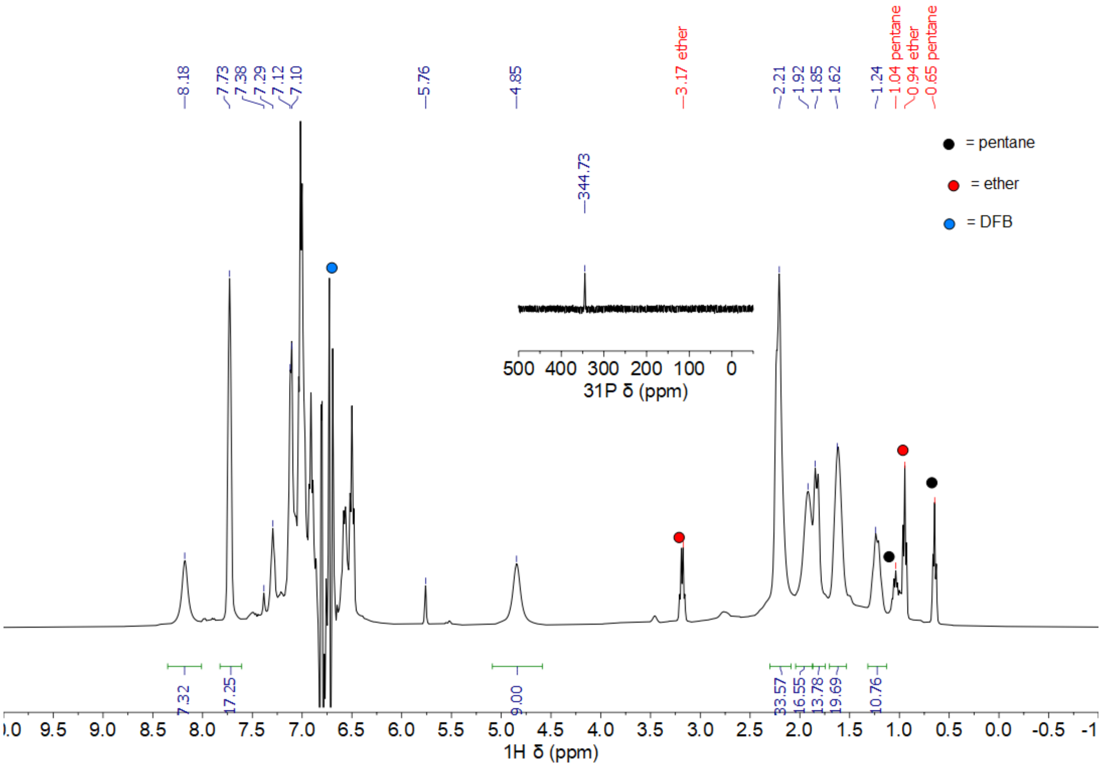

Figure S2.7. Solvent-suppressed ^{1}H and ^{31}P (inset) NMR spectra of **2.6** in DFB (400 MHz, 162 MHz, respectively, 293 K).

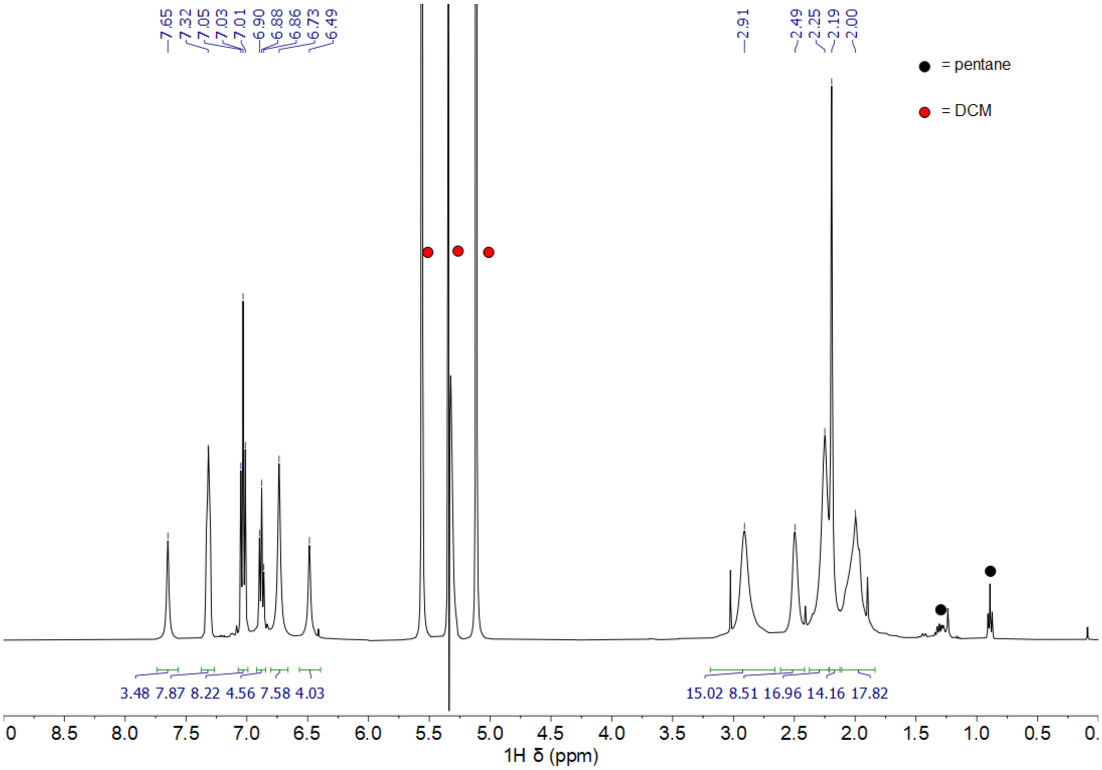

Figure S2.8. Solvent-suppressed ^{1}H NMR spectrum of **2.7** in DCM (400 MHz, 293 K).

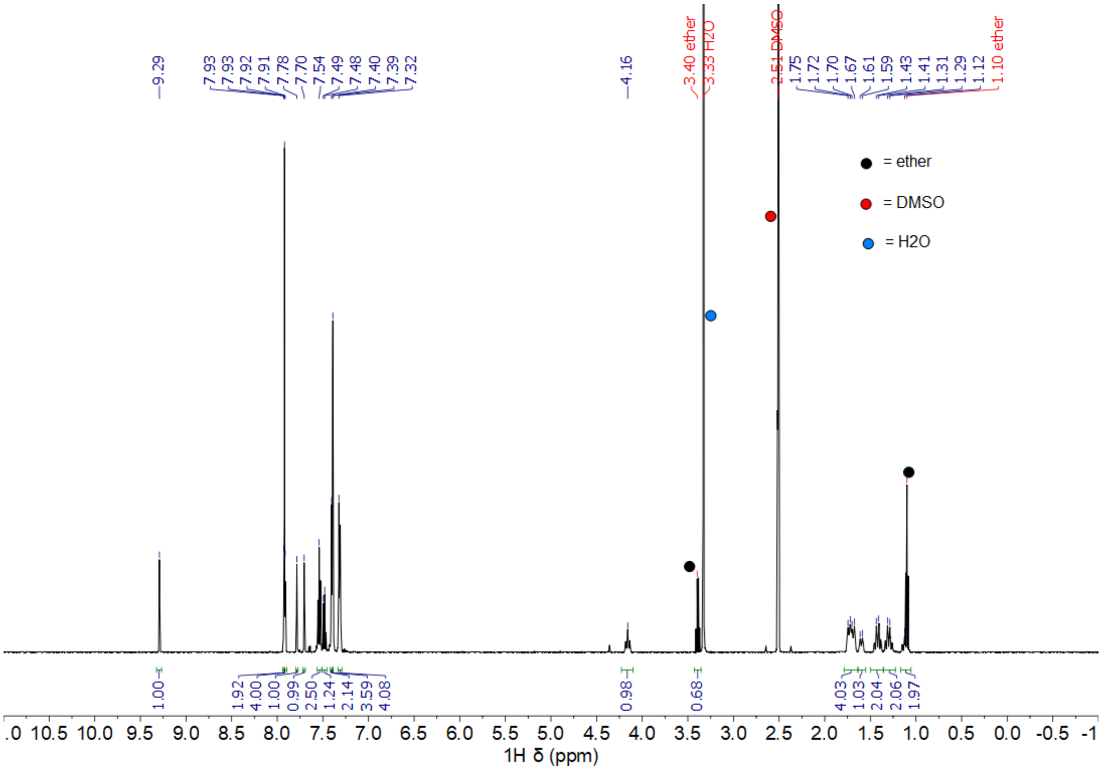

Figure S2.9. ^{1}H NMR spectrum of ITppCyHBF$_4$ in DMSO-d_6 (500 MHz, 293 K).

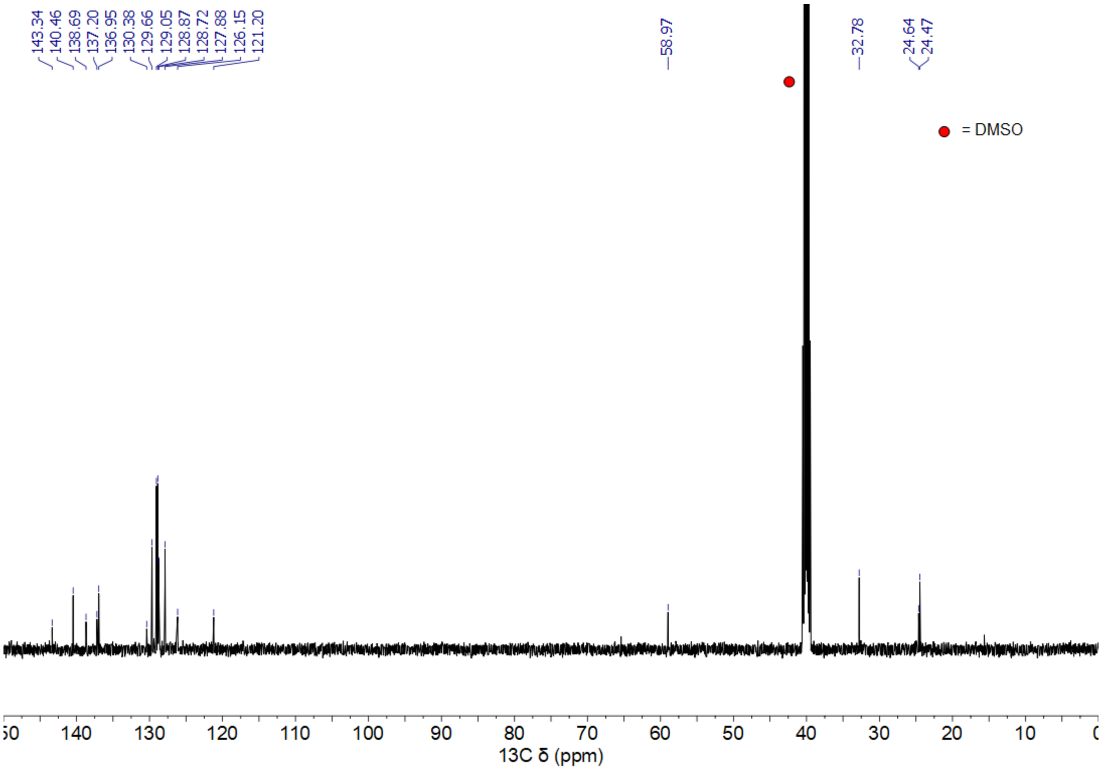

Figure S2.10. ^{13}C NMR spectrum of ITppCyHBF$_4$ in DMSO-d_6 (126 MHz, 293 K).

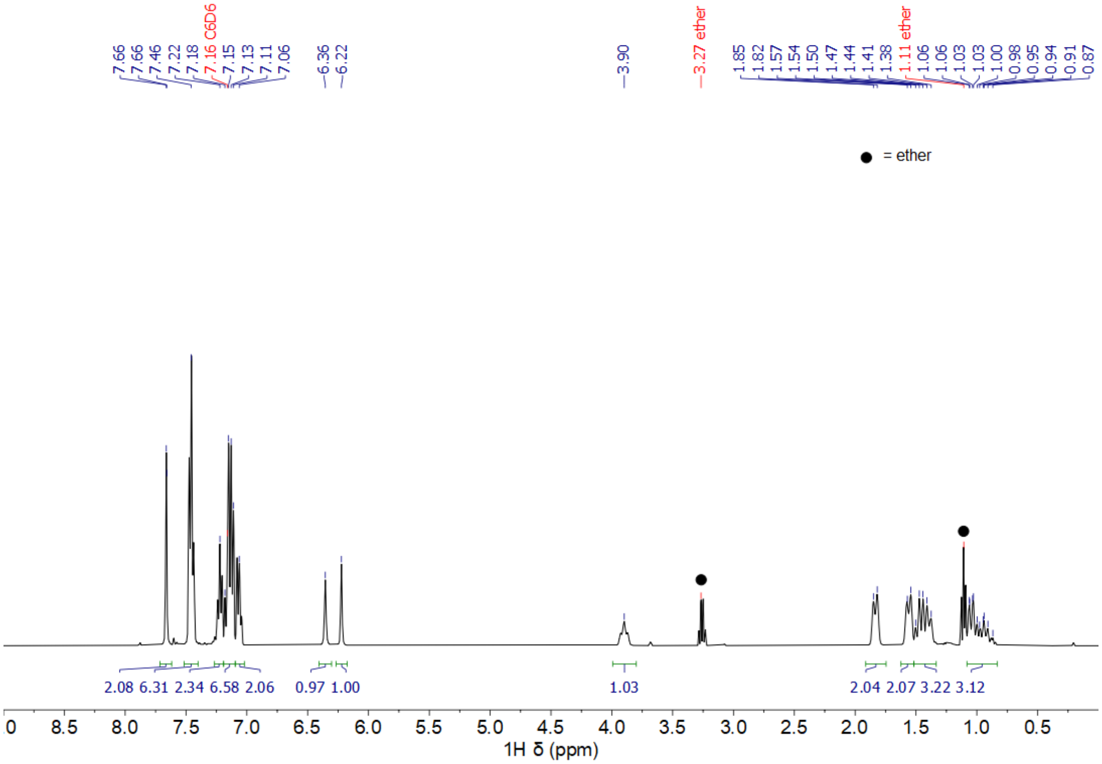

Figure S2.11. ^{1}H NMR spectrum of ITppCy in C$_6$D$_6$ (400 MHz, 293 K).

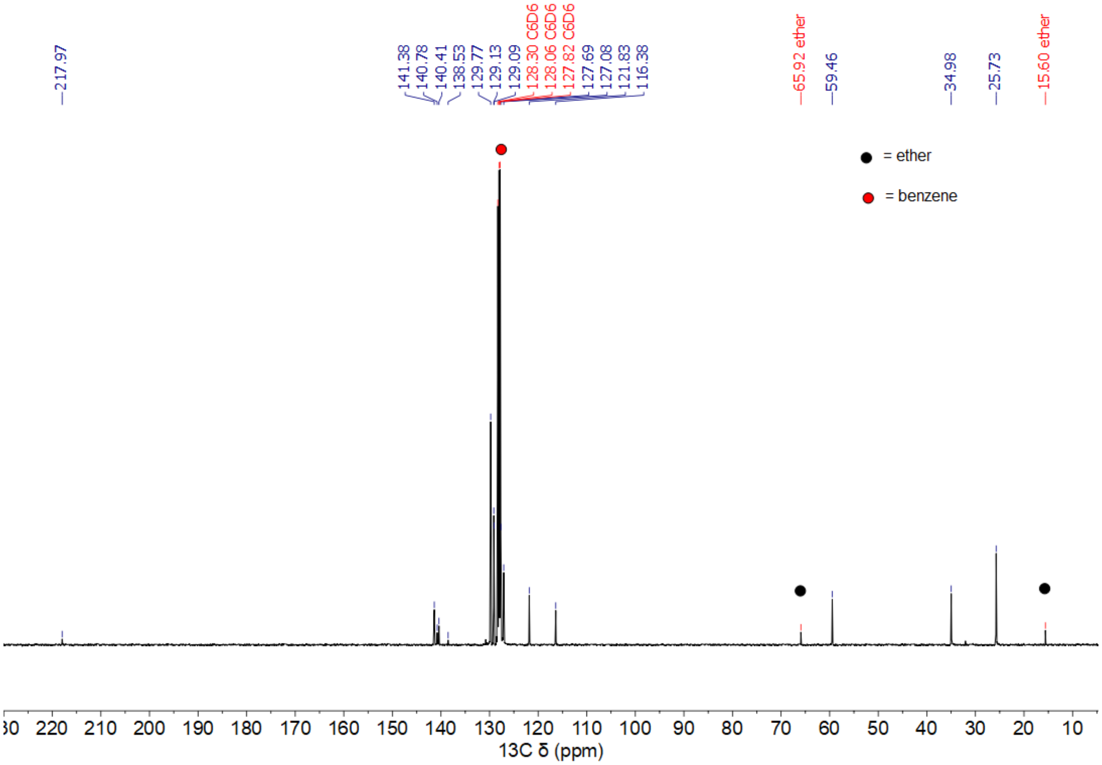

Figure S2.12. ^{13}C NMR spectrum of ITppCy in C_6D_6 (101 MHz, 293 K).

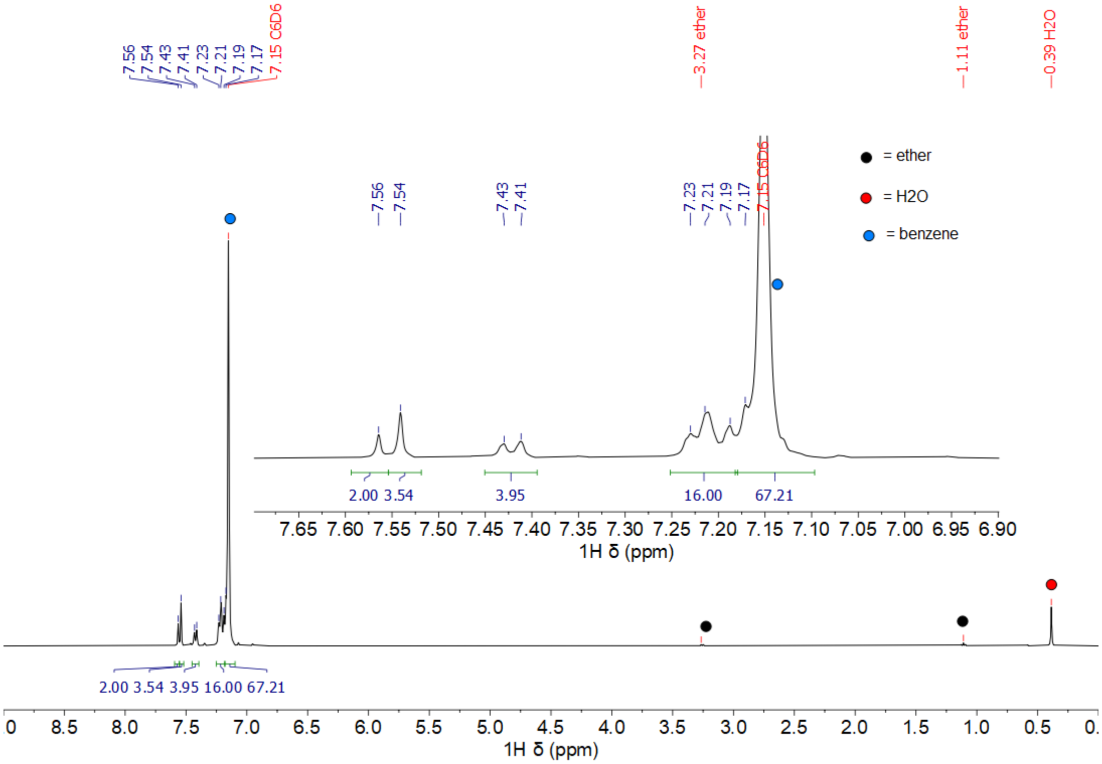

Figure S2.13. ^{1}H NMR spectrum of N^1,N^2-bis(2,4,6-triphenylphenyl)ethane-1,2-diimine in C_6D_6 (400 MHz, 293 K).

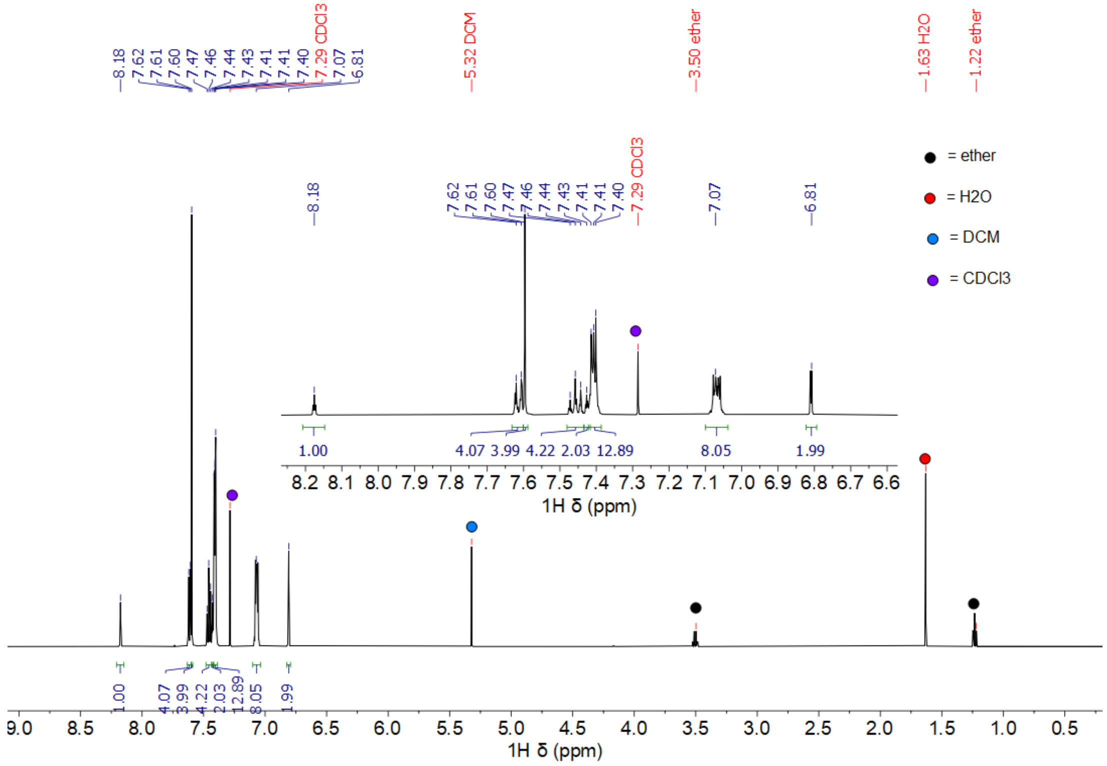

Figure S2.14. ^{1}H NMR spectrum of ITppHBF$_4$ in CDCl$_3$ (500 MHz, 293 K).

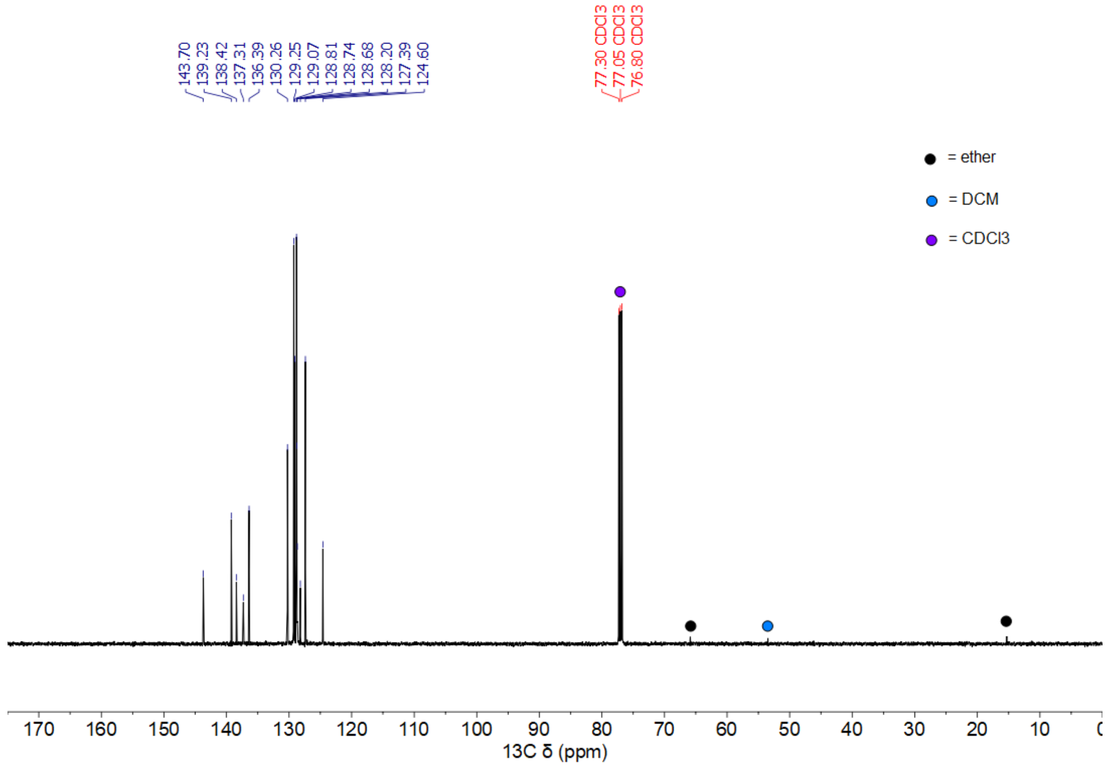

Figure S2.15. ^{13}C NMR spectrum of ITppHBF$_4$ in CDCl$_3$ (126 MHz, 293 K).

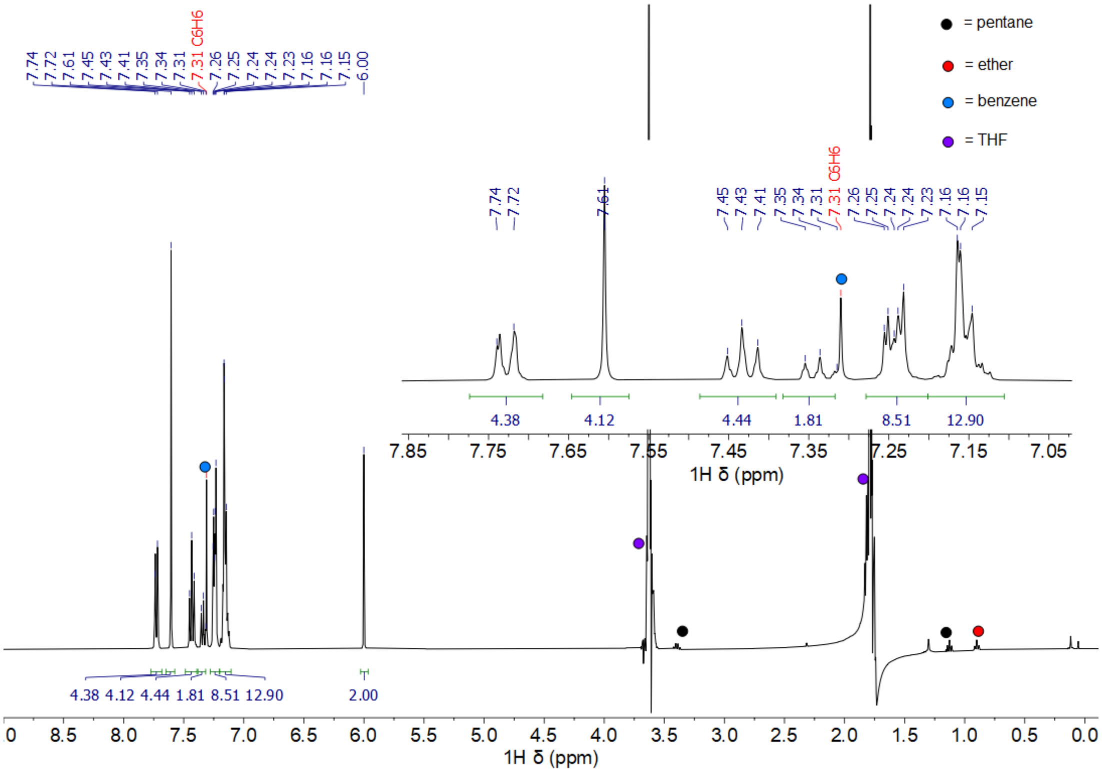

Figure S2.16. Solvent-suppressed ^{1}H NMR spectrum of ITpp in THF (400 MHz, 293 K).

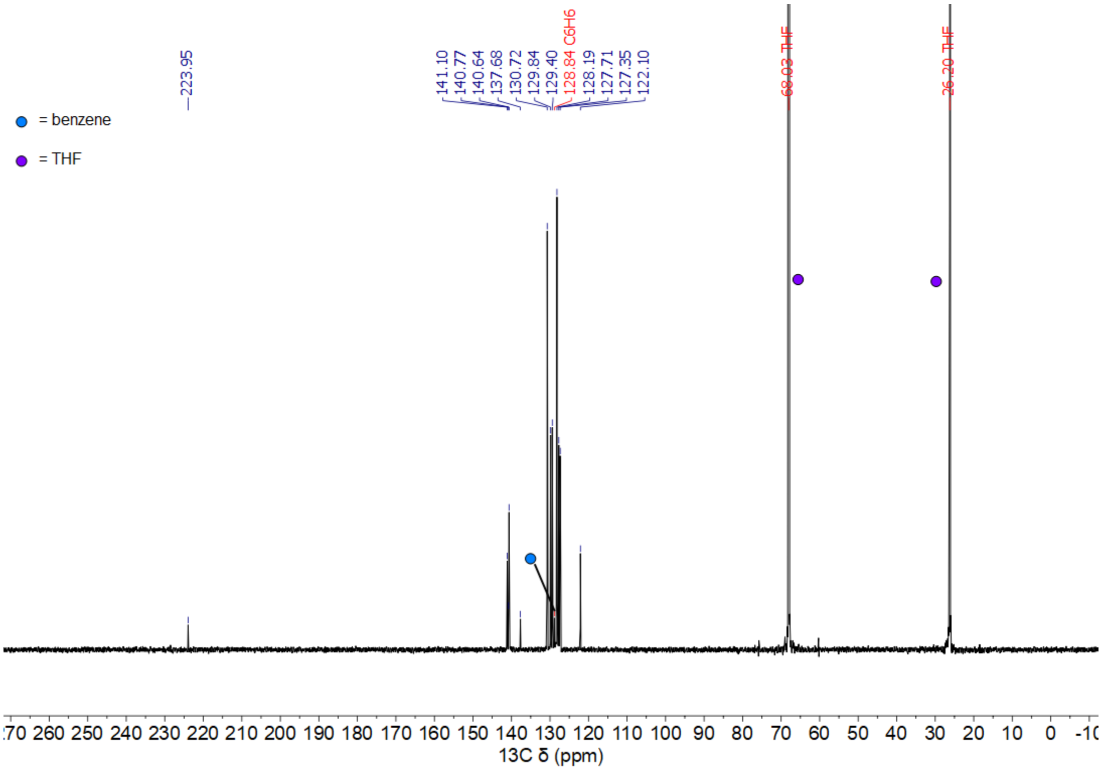

Figure S2.17. ^{13}C NMR spectrum of ITpp in THF (101 MHz, 293 K).

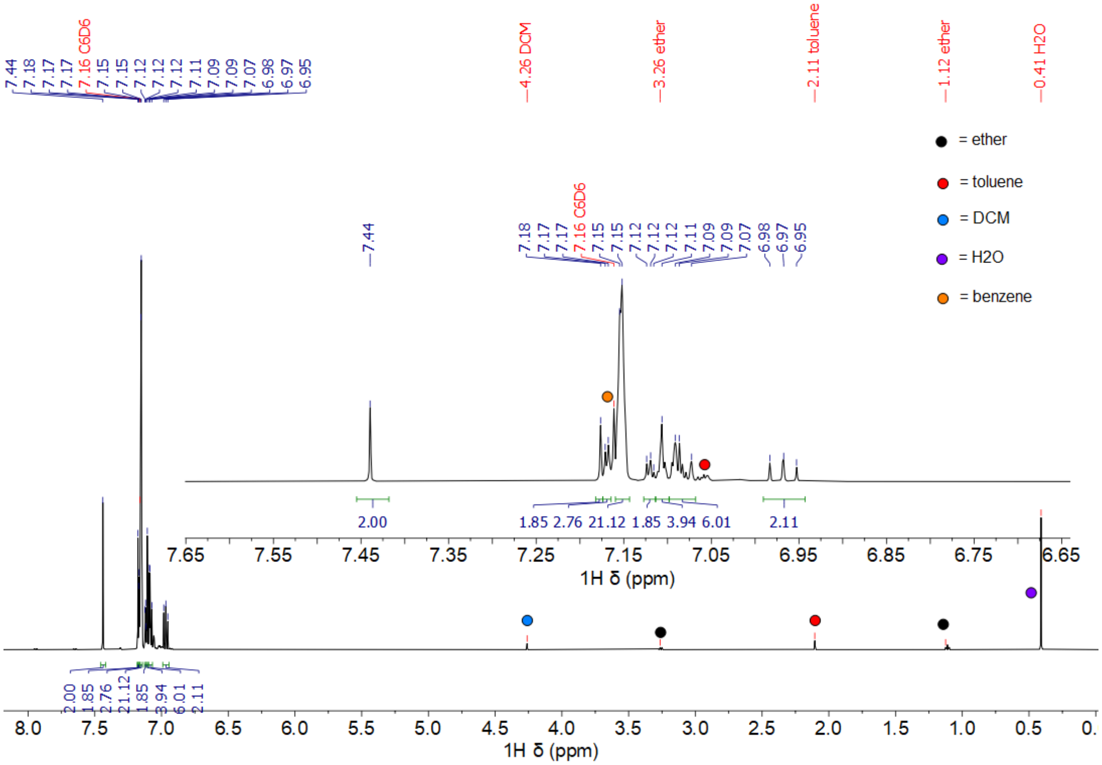

Figure S2.18. ^{1}H NMR spectrum of N^1,N^2-bis(2,6-diphenylphenyl)ethane-1,2-diimine in C_6D_6 (500 MHz, 293 K).

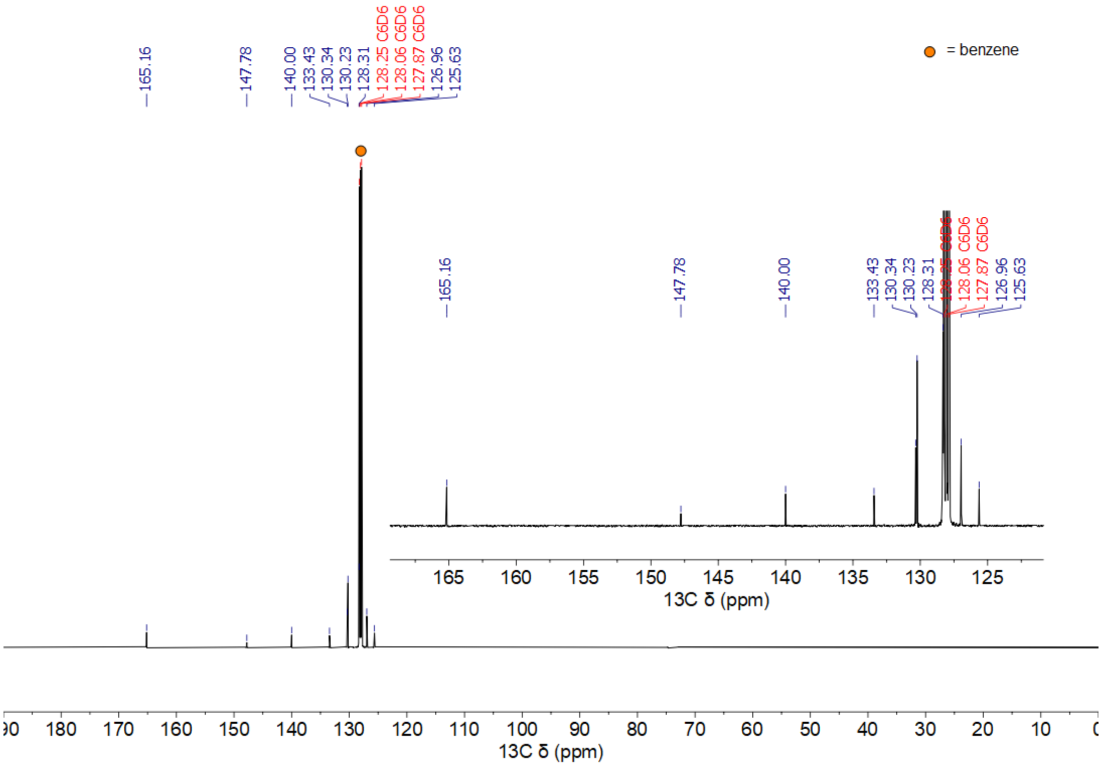

Figure S2.19. ^{13}C NMR spectrum of N^1,N^2-bis(2,6-diphenylphenyl)ethane-1,2-diimine in C_6D_6 (126 MHz, 293 K).

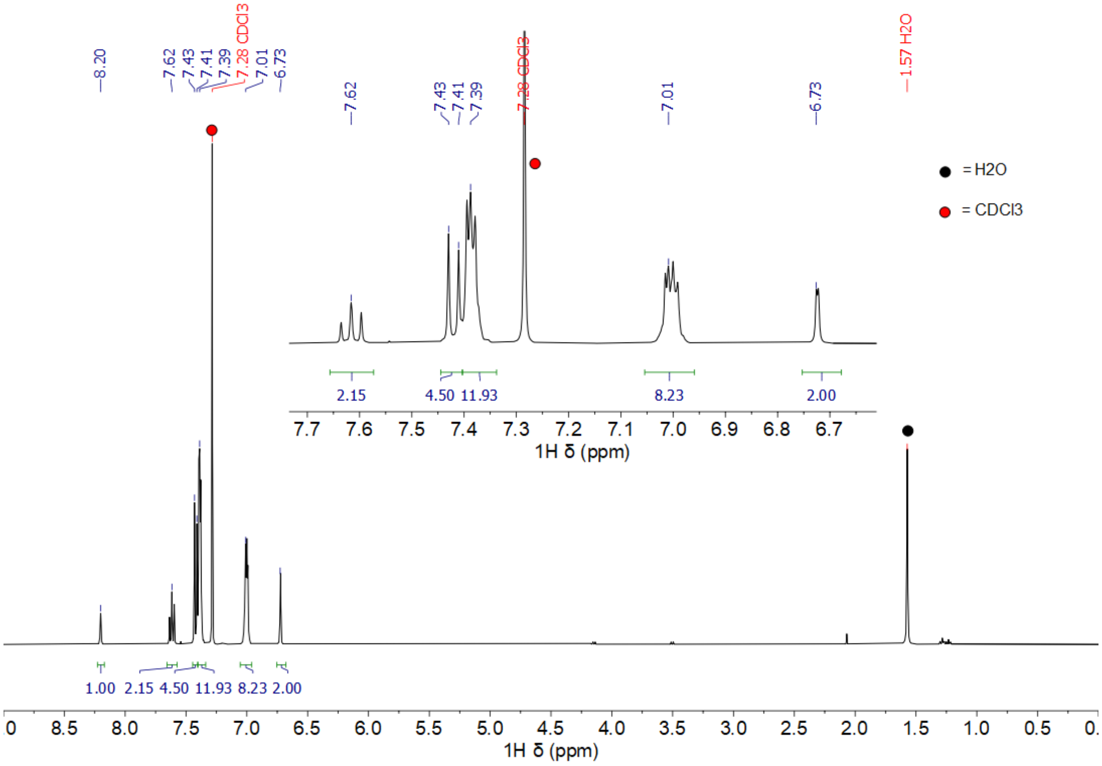

Figure S2.20. ^{1}H NMR spectrum of IDppHBF$_4$ in $CDCl_3$ (400 MHz, 293 K).

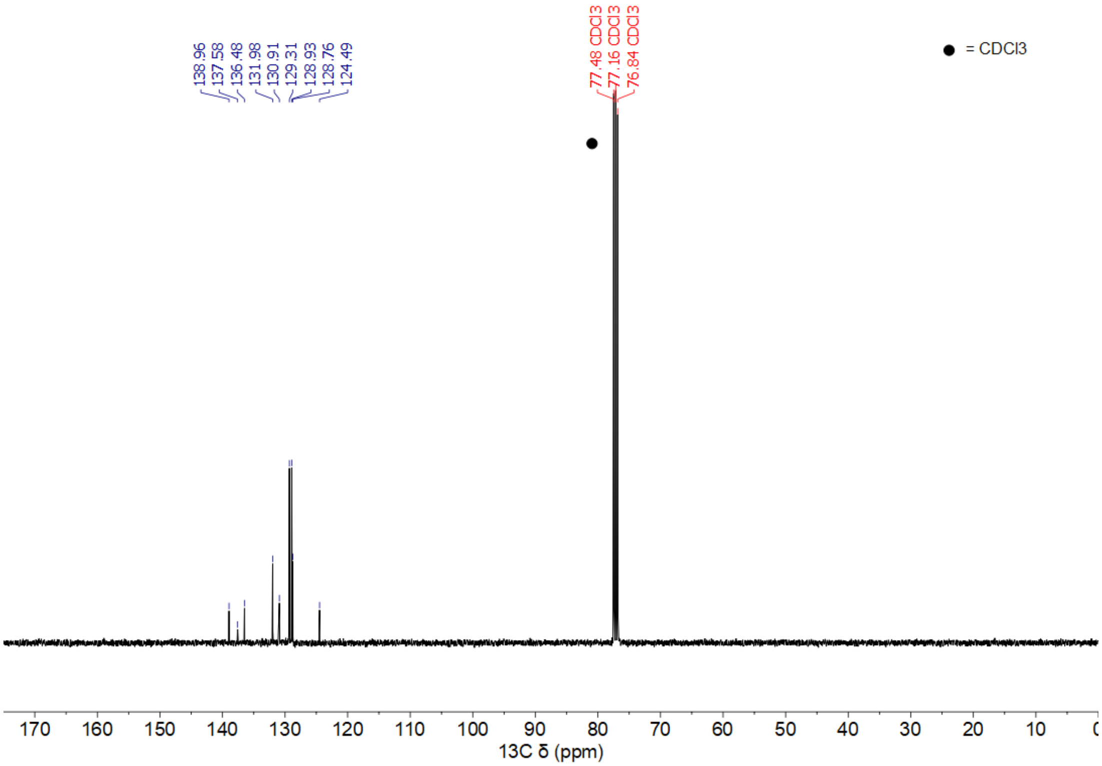

Figure S2.21. ^{13}C NMR spectrum of IDppHBF$_4$ in $CDCl_3$ (101 MHz, 293 K).

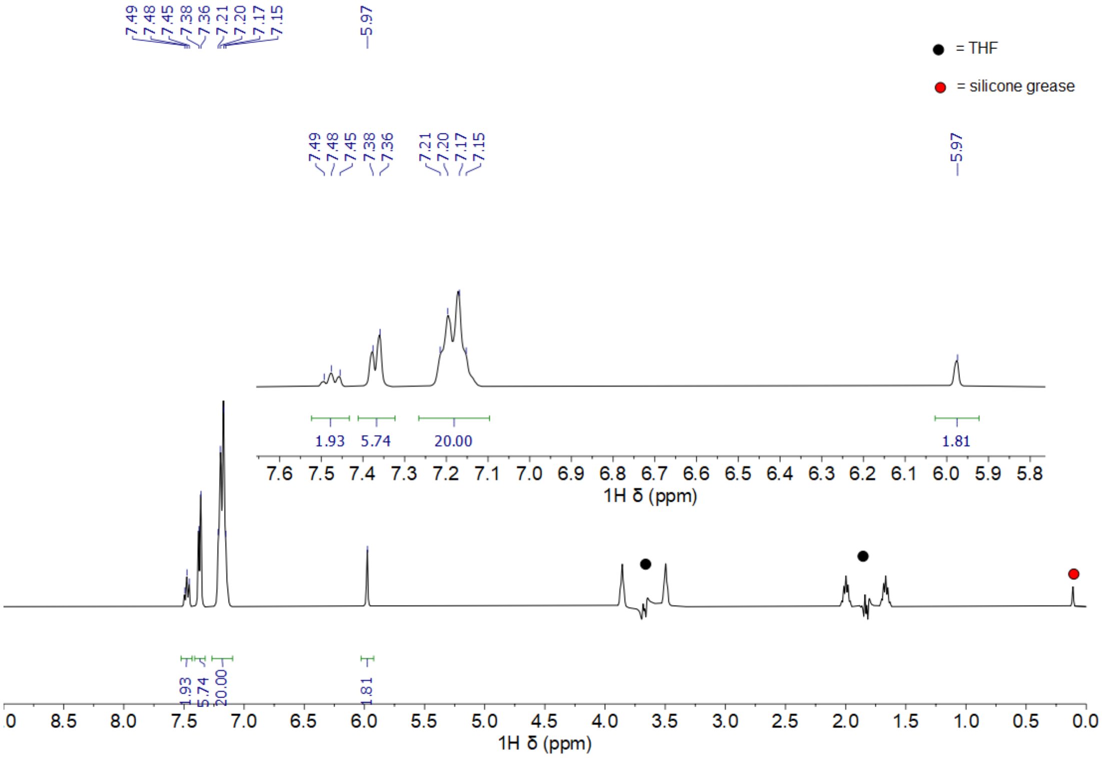

Figure S2.22. Solvent-suppressed ^{1}H NMR spectrum of IDpp in THF (400 MHz, 293 K).

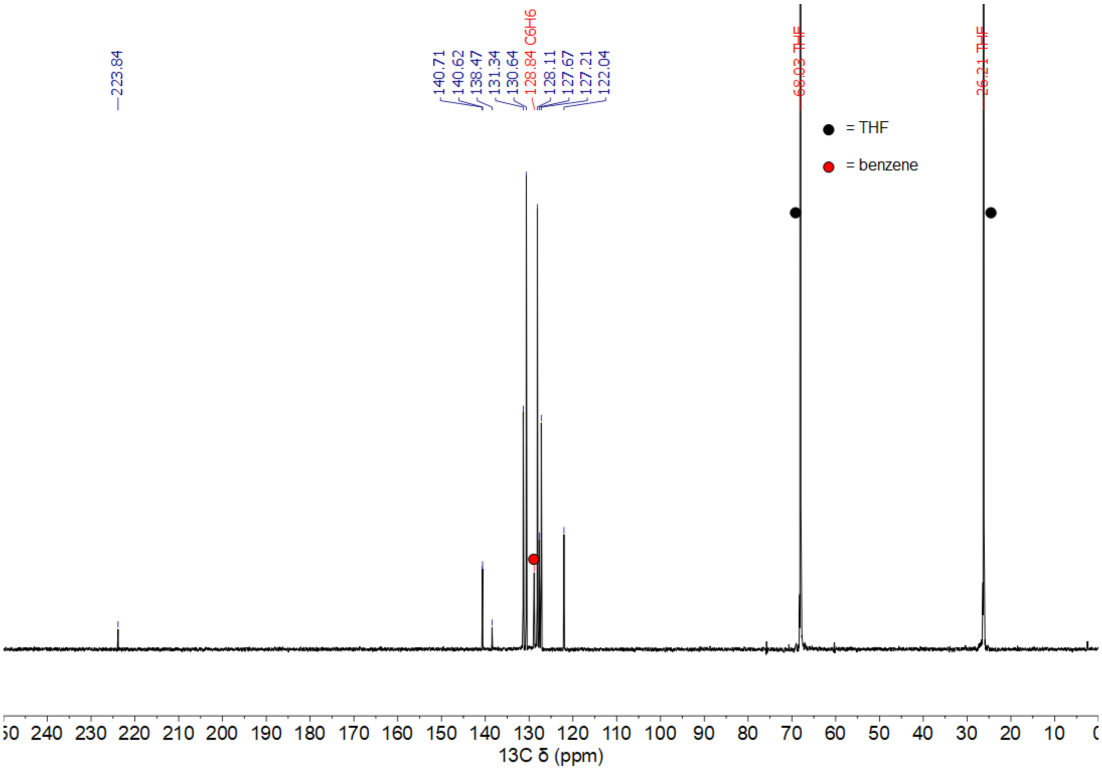

Figure S2.23. ^{13}C NMR spectrum of IDpp in THF (101 MHz, 293 K).

FT-IR spectra

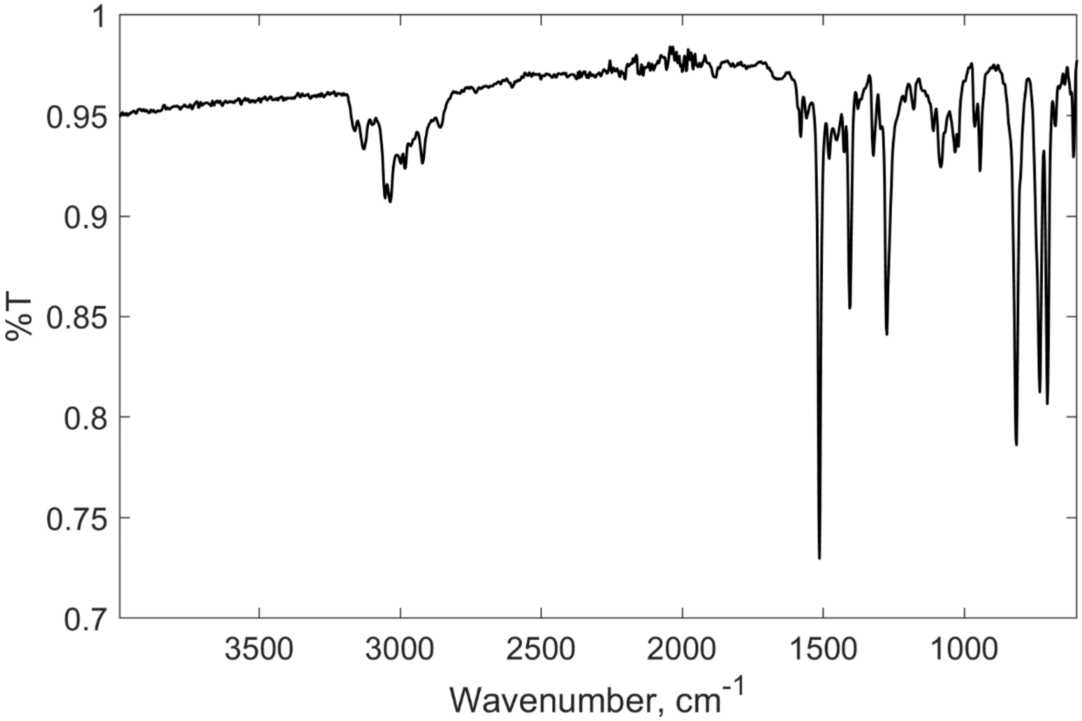

Figure S2.24. Thin film FT-IR spectrum of **2.2**.

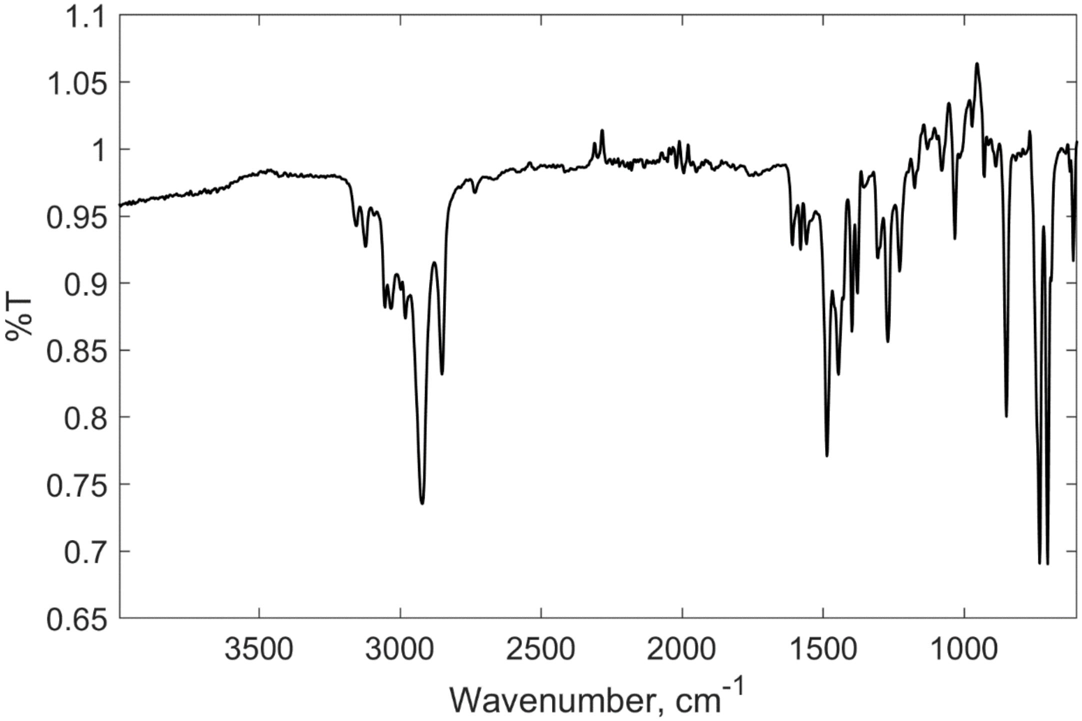

Figure S2.25. Thin film FT-IR spectrum of **2.3**.

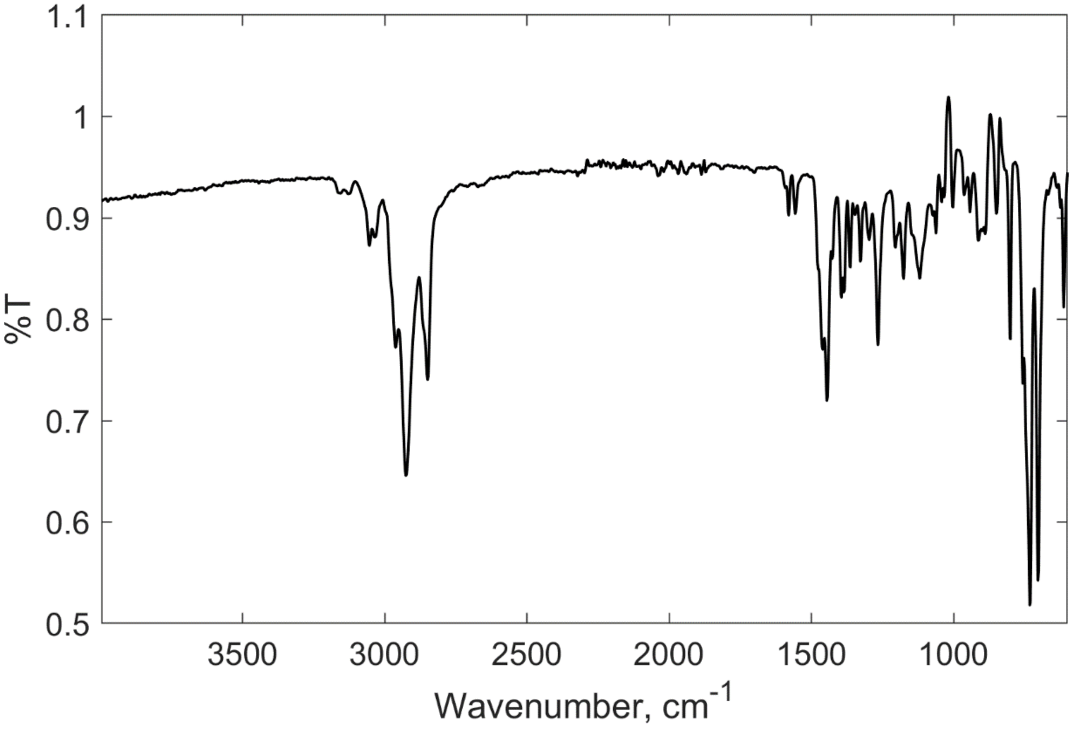

Figure S2.26. Thin film FT-IR spectrum of **2.4**.

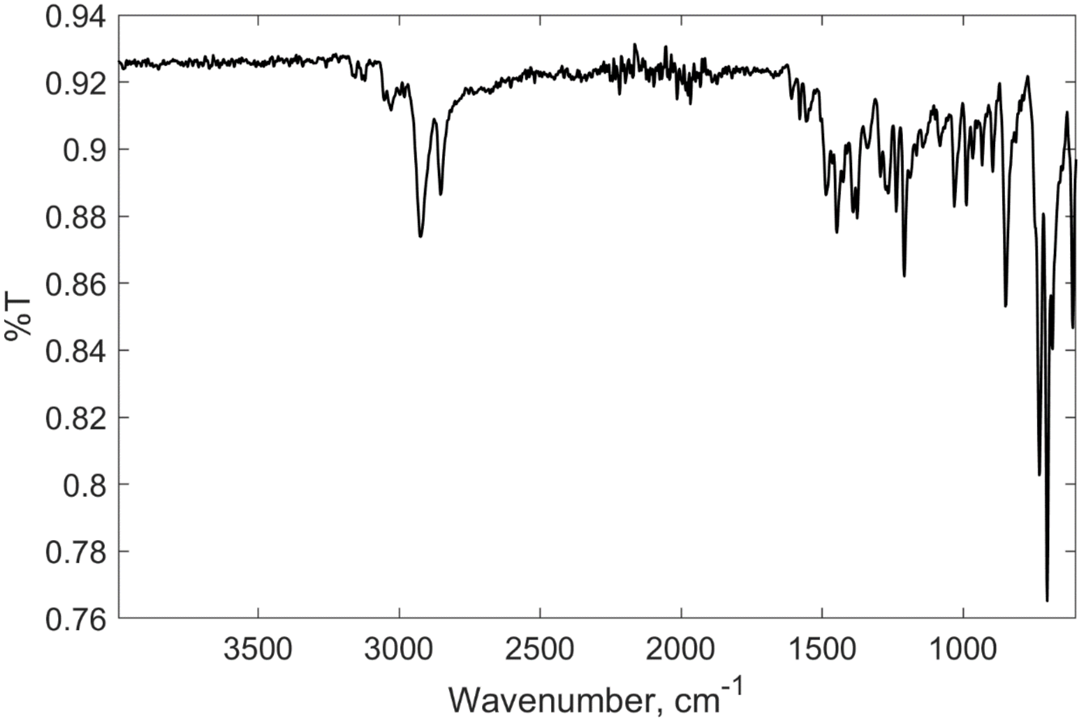

Figure S2.27. Powder FT-IR spectrum of **2.7**.

UV/vis spectra

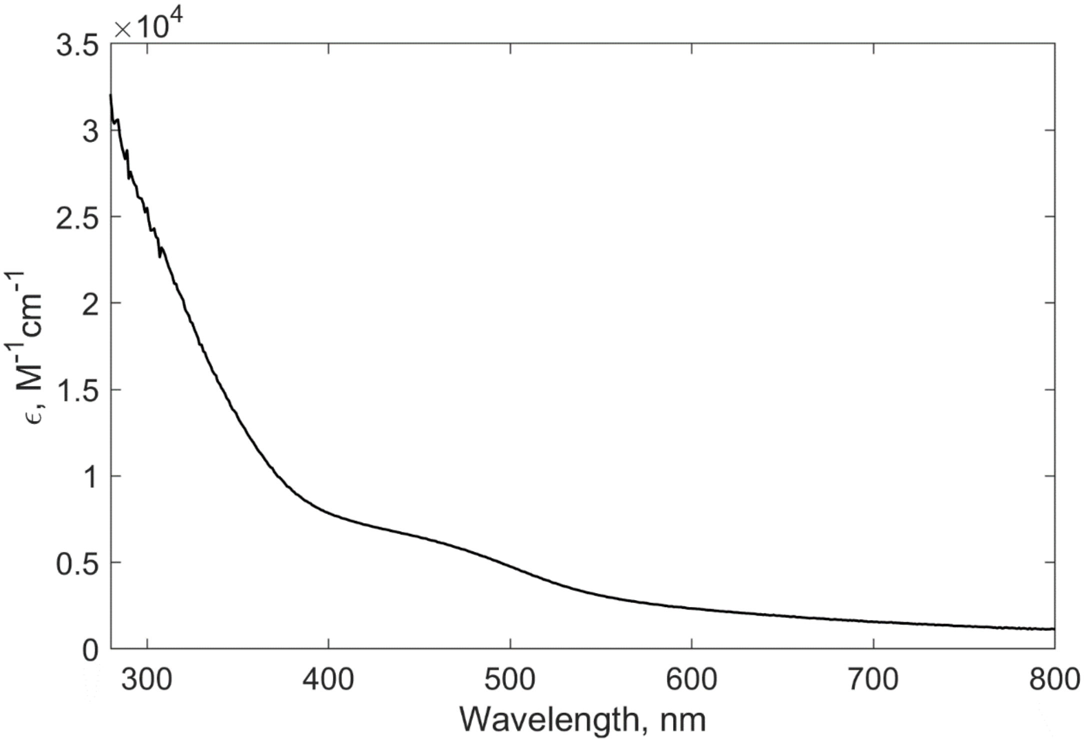

Figure S2.28. UV/vis spectrum of **2.2** (0.1 mM) in THF.

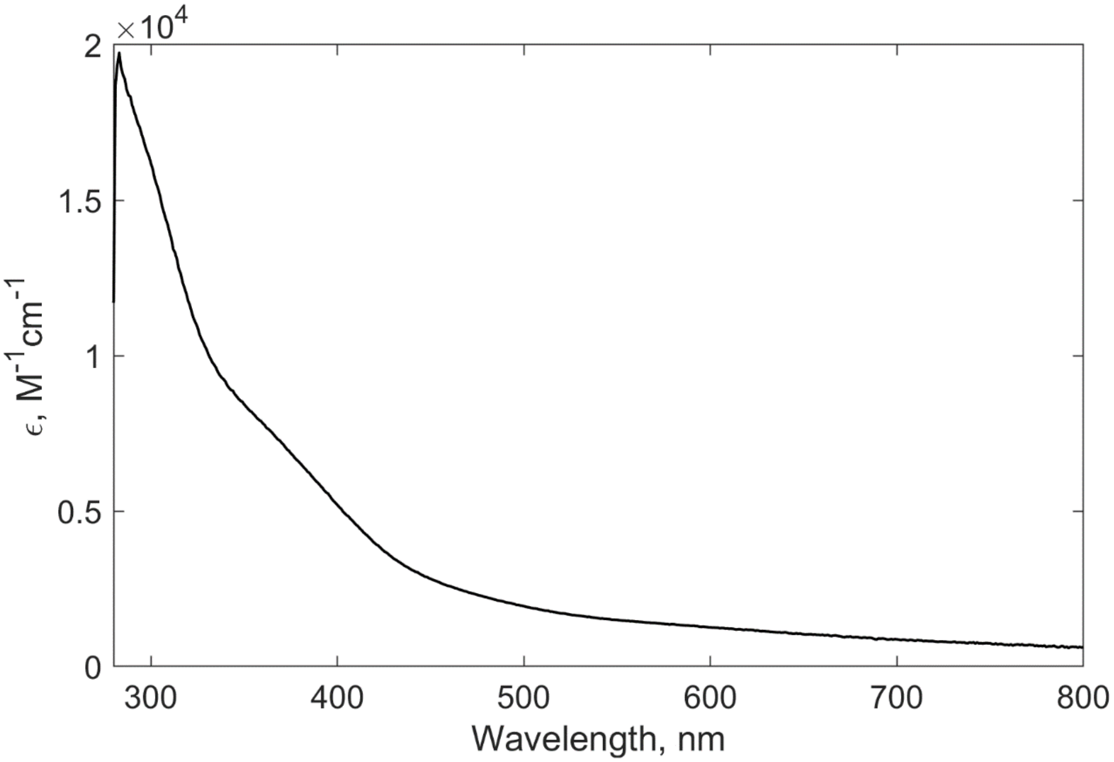

Figure S2.29. UV/vis spectrum of **2.3** (0.1 mM) in PhF.

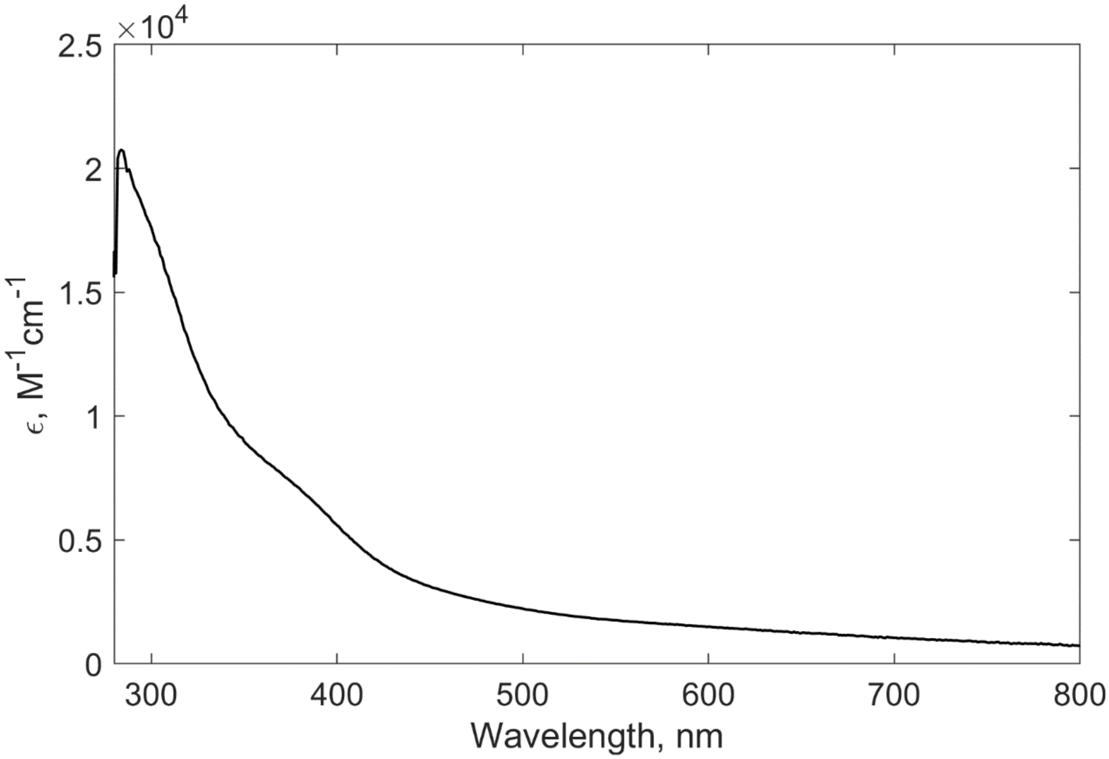

Figure S2.30. UV/vis spectrum of **2.4** (0.1 mM) in PhF.

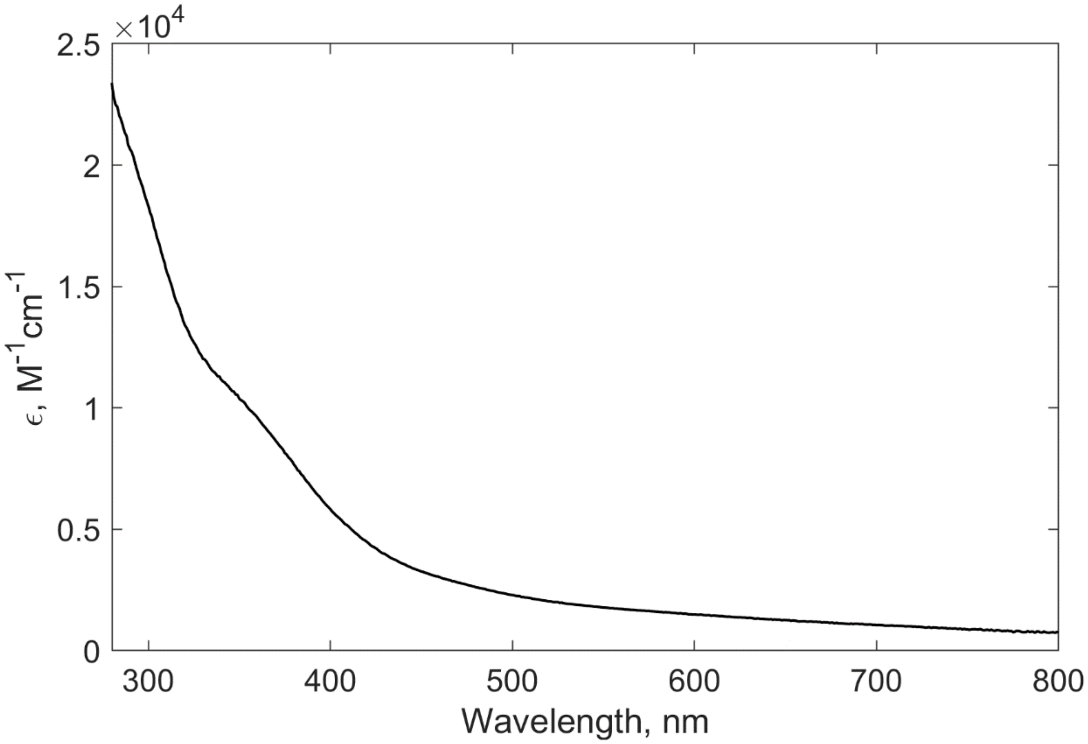

Figure S2.31. UV/vis spectrum of **2.7** (0.1 mM) in THF.

Cyclic Voltammograms

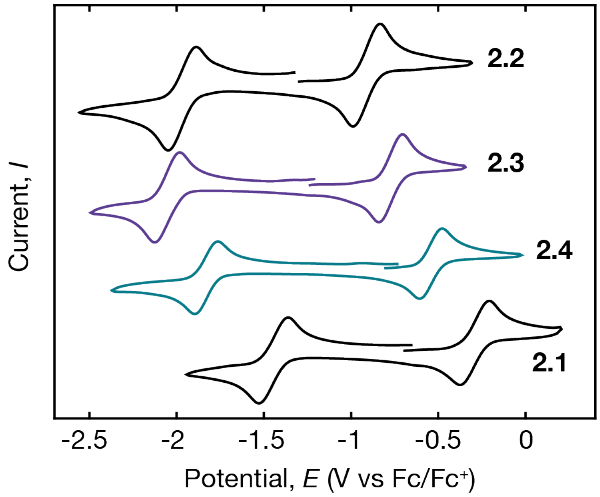

Figure S2.32. CV plot of **2.1**–**2.4** at 200 mV/s in DFB with [^{n}Bu$_4$N][PF$_6$] (0.5 M) as electrolyte.

Table S2.1. $E_{1/2}$ values (V vs Fc/Fc$^+$) for **2.1**–**2.4** (5 mM in DFB with 0.5 M [^{n}Bu$_4$N][PF$_6$]).

Compound	$E_{1/2}$(0/1+) (V vs Fc/Fc$^+$)	$E_{1/2}$(1+/2+) (V vs Fc/Fc$^+$)
2.2 (four NHCs)	−1.963	−0.909
2.3 (three NHCs)	−2.054	−0.772
2.4 (two NHCs)	−1.834	−0.541
2.1 (zero NHCs)	−1.449	−0.290

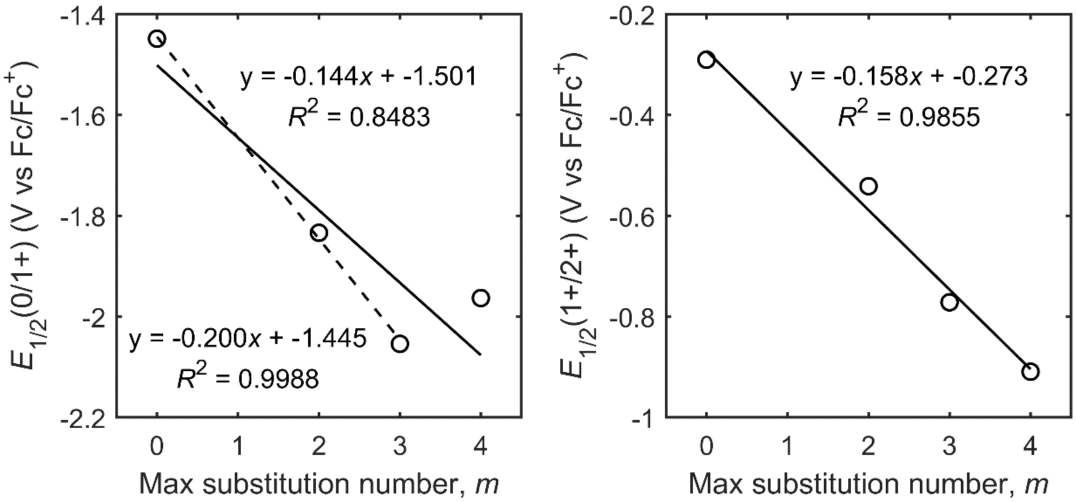

Figure S2.33. Impact of substitution number on $E_{1/2}$ (*left*, 0/1+; *right*, 1+/2+) of **2.1**–**2.4**. Substitution of PCy$_3$ for an NHC results in an anodic shift in $E_{1/2}$ for the 0/1+ and 1+/2+ couples. **2.2** (m = 4) deviates from this trend and has an $E_{1/2}$(0/1+) more positive than expected. Omission of this outlier yields an improved fit (dashed line)

Titration experiments

General remarks

we have employed ^{31}P NMR spectroscopy to monitor the number and qualitative amounts of $[Fe_4S_4]^+$ clusters containing phosphine ligands in ligand substitution reactions with NHCs. Due to the fast relaxation of the ^{31}P NMR signals, quantification of the species by ^{31}P NMR could not be performed. As expected from the model for uncoupled, sequential substitution reactions, adding NHC quantities lower than the maximal substitution number ($x < m$, where m varies for each NHC) results in mixtures of $[Fe_4S_4(PCy_3)_{4-n}(NHC)_n]^+$ clusters. Only clusters containing phosphine ligands (i.e., $n < 4$) are observed by ^{31}P NMR. For NHCs with $m = 4$, the presence of the $[Fe_4S_4(NHC)_4]^+$ is inferred from a lack of any cluster-derived ^{31}P NMR signal. The number of observed cluster-derived ^{31}P NMR signals detected and their relative intensities as a function of the amount of added NHC establishes the number and identity of the intermediates. In the case of IDep (Figure S2.38), at least two species are observed in the presence of excess NHC (> 3 equiv), and we attribute this to an equilibrium between IDep and PCy_3 binding after two substitution events. Thus, IDep has $m = 3$ even though the third NHC binds with similar strength to PCy_3.

Experimental procedure

Titration experiments were conducted via two procedures depending on the solubility of the NHC. Each titration point (for example, 1 equiv, 2 equiv and so on) was prepared independently from stock solutions, as opposed to sequential addition of NHC to a single sample. That each sample was at equilibrium was established by monitoring the composition by ^{1}H and ^{31}P NMR spectra over a 3 h time period. All NMR spectra were recorded using identical acquisition parameters, and all titration points for each NHC were collected on the same instrument.

Procedure A: this method was used for NHCs with good solubility in THF (ICy, IMesCy, IMesAd, IMes, IDep and IPr). In an NMR tube containing a solution of **2.1** (15.2 mM) in THF, aliquots of an NHC stock solution in THF (164 mM) were added via syringe. For IPr, the reaction was heated to 70 °C for 3 h.

Procedure B: this method was used for NHCs with poor solubility in THF (ITol, SIAnt, ITppCy, IDpp and ITpp). Solid NHC was weighed into small crystallization vials. The solid NHC was suspended in 250 µl THF and, with vigorous stirring, a stock solution of **2.1** (15.2 mM) in THF was added rapidly via syringe. For IDpp and ITpp, the reactions were heated to 70 °C for 2 h.

^{31}P NMR spectra for the titration experiments

ICy (*m* = 4):

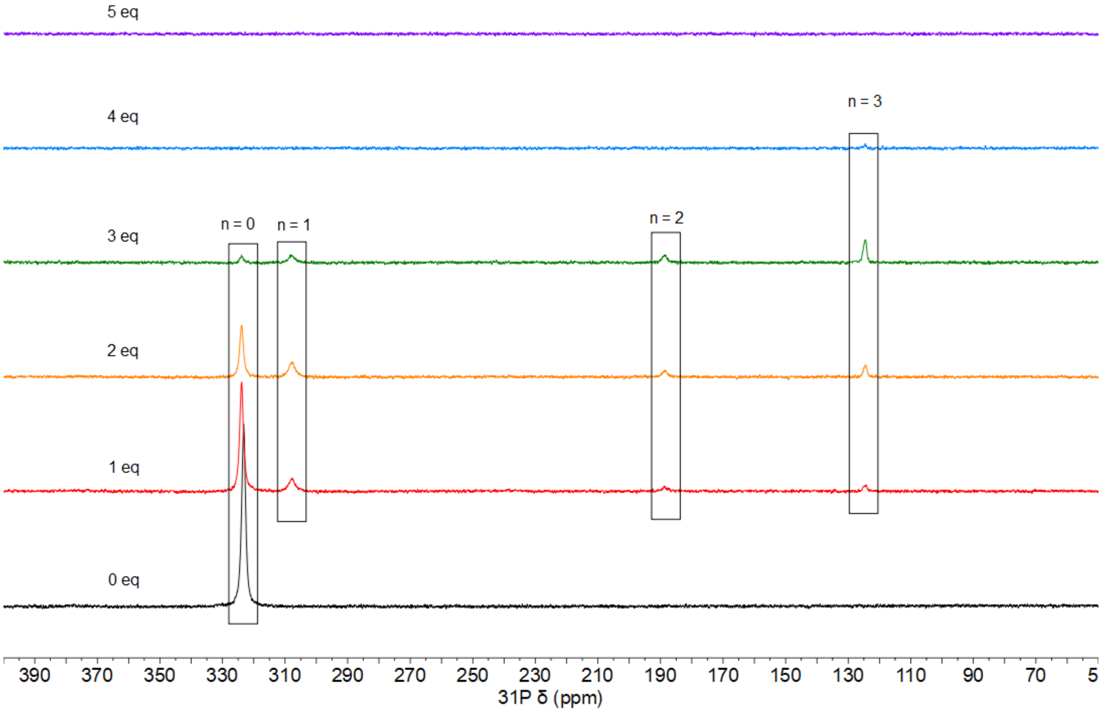

Figure S2.34. ^{31}P NMR spectra of ICy titration of **2.1** in THF.

ITol (*m* = 4):

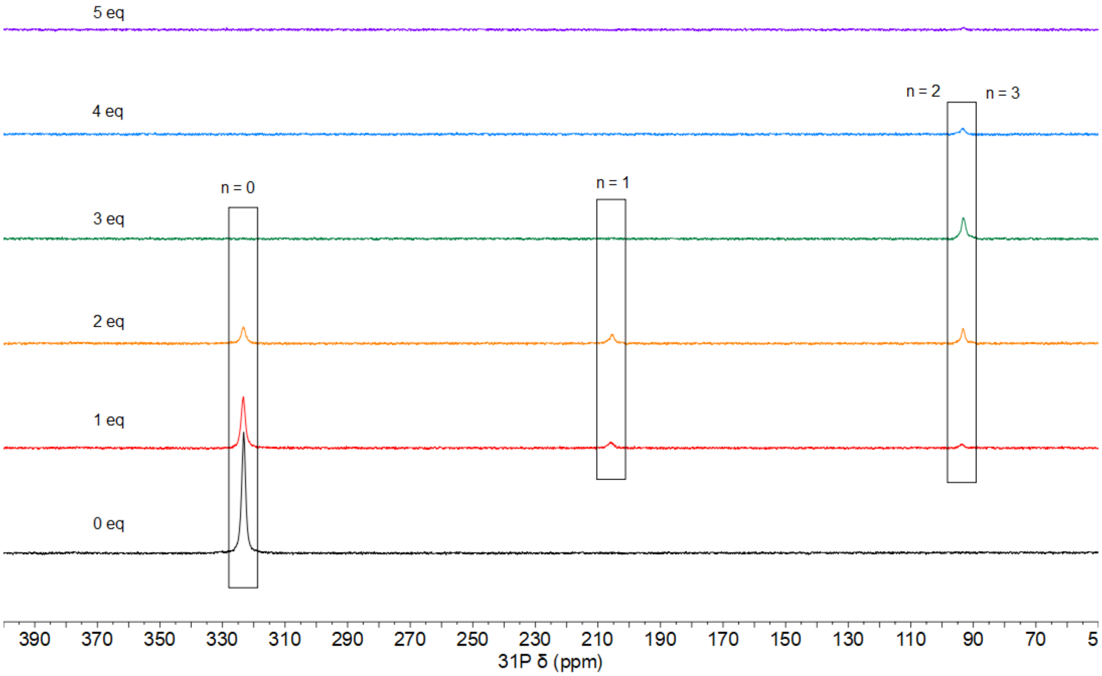

Figure S2.35. ^{31}P NMR spectra of ITol titration of **2.1** in THF.

IMesCy (*m* = 4):

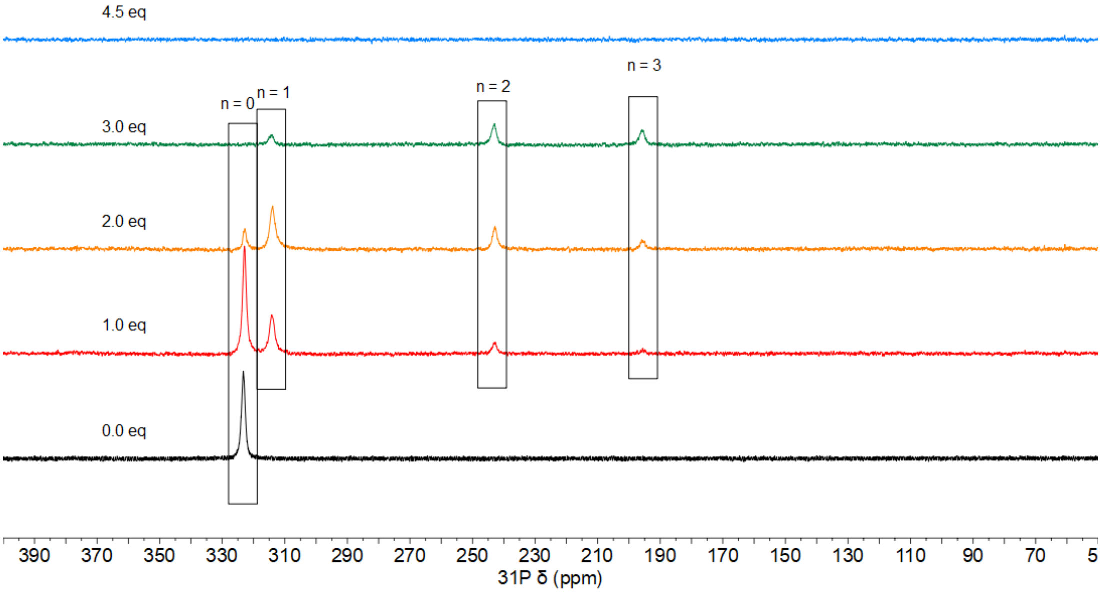

Figure S2.36. ^{31}P NMR spectra of IMesCy titration of **2.1** in THF.

IMes (*m* = 3):

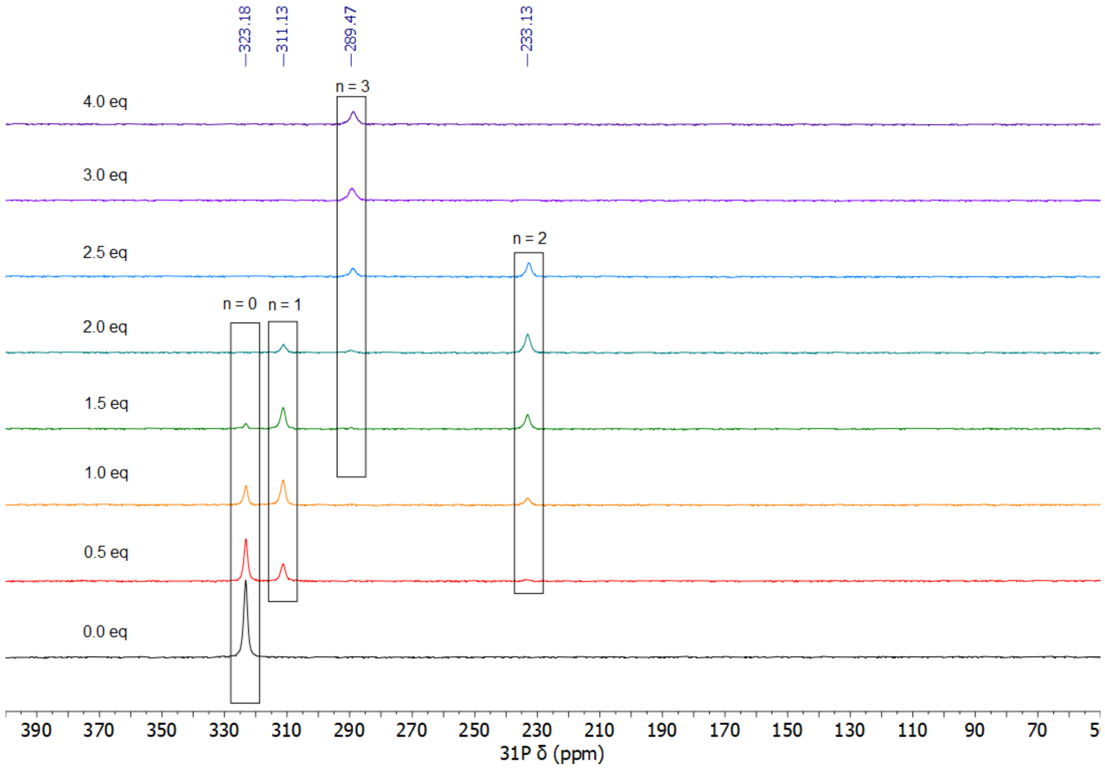

Figure S2.37. ^{31}P NMR spectra of IMes titration of **2.1** in THF.

IDep (*m* = 3):

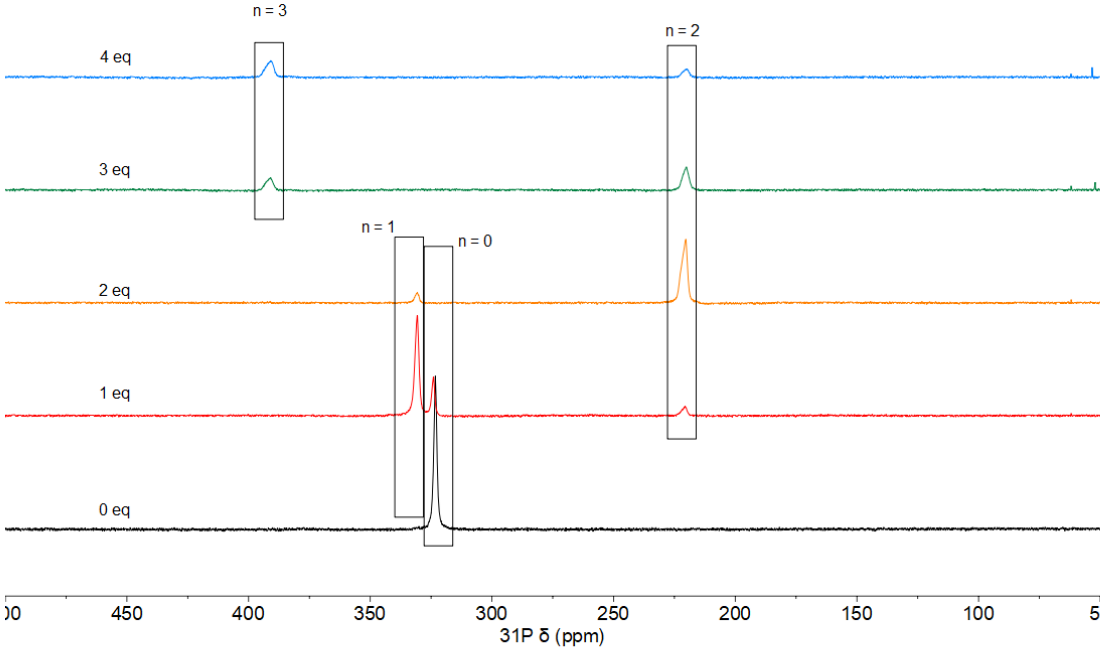

Figure S2.38. ^{31}P NMR spectra of IDep titration of **2.1** in THF.

IMesAd (m = 3):

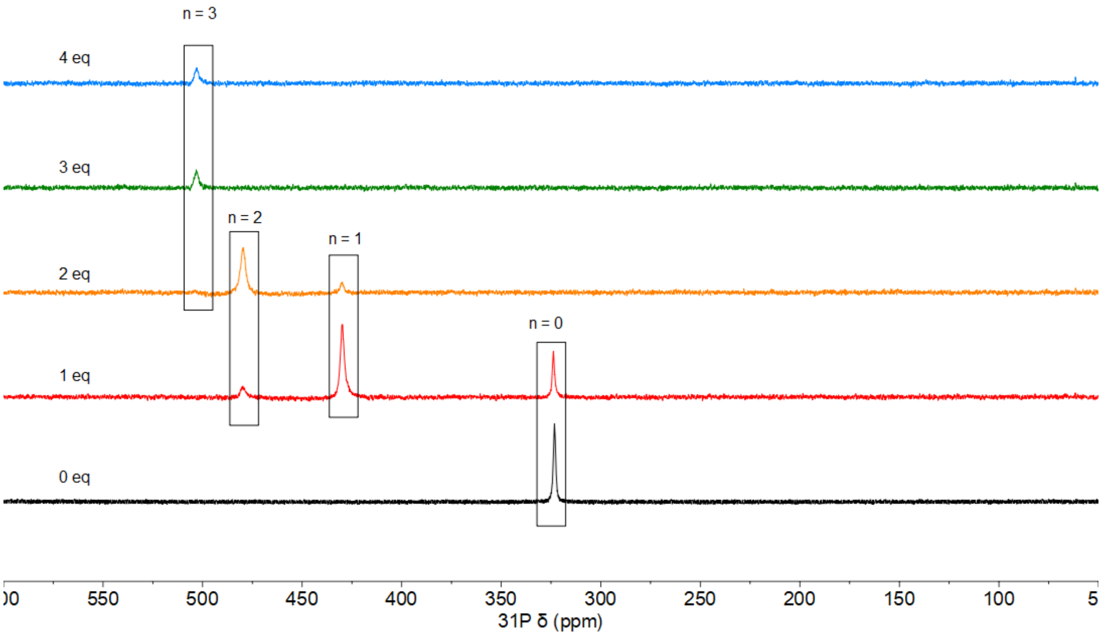

Figure S2.39. ^{31}P NMR spectra of IMesAd titration of **2.1** in THF.

IPr (m = 2):

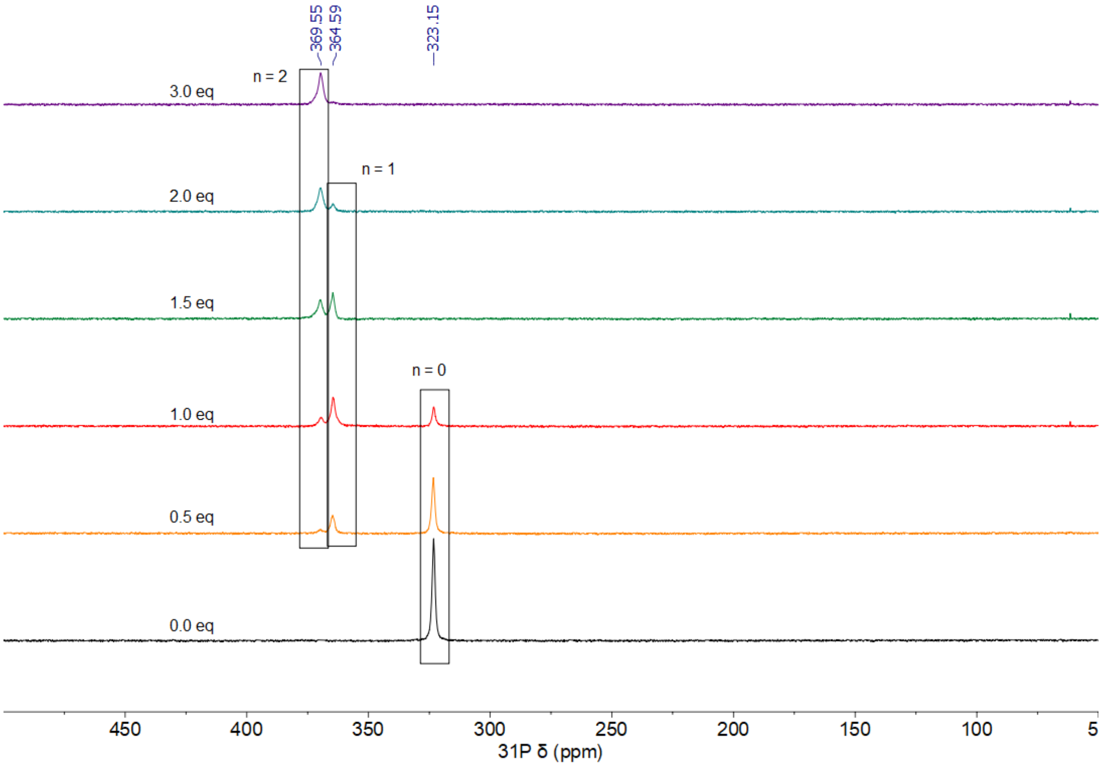

Figure S2.40. ^{31}P NMR spectra of IPr titration of **2.1** in THF.

SIAnt (*m* = 2):

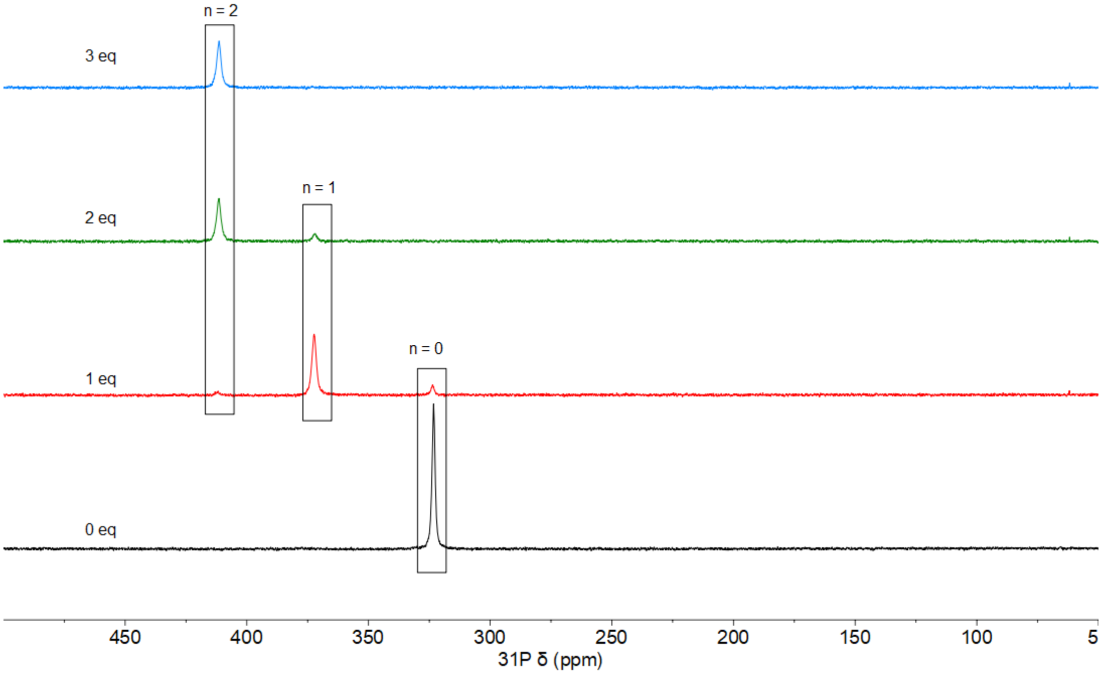

Figure S2.41. ^{31}P NMR spectra of SIAnt titration of **2.1** in THF.

ITppCy (*m* = 2):

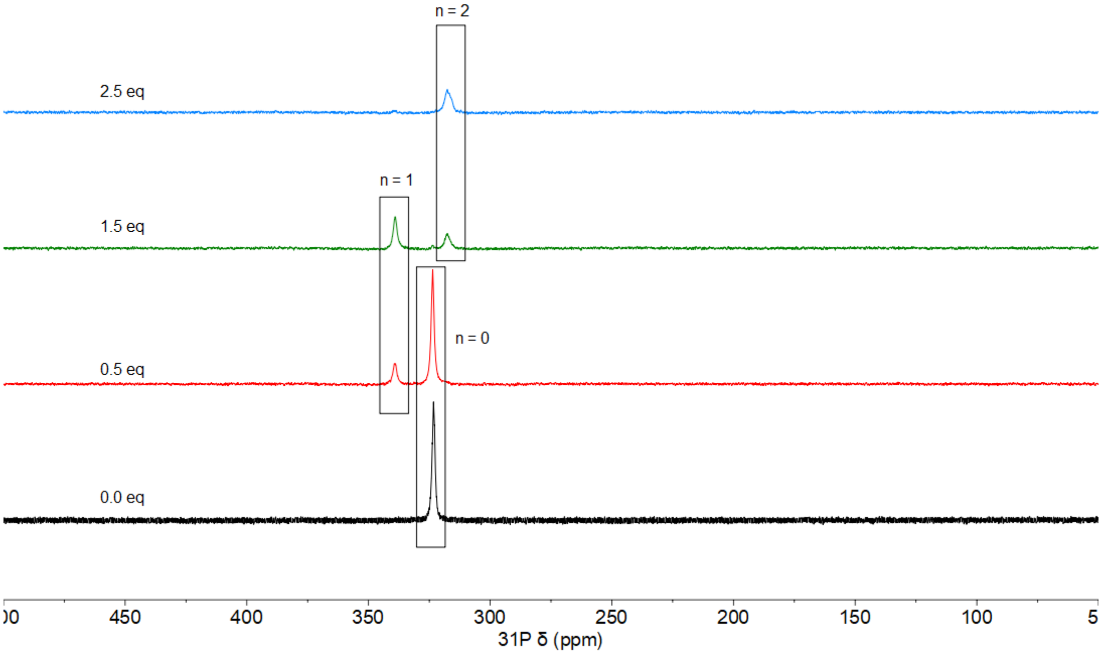

Figure S2.42. ^{31}P NMR spectra of ITppCy titration of **2.1** in THF.

ITpp (m = 1):

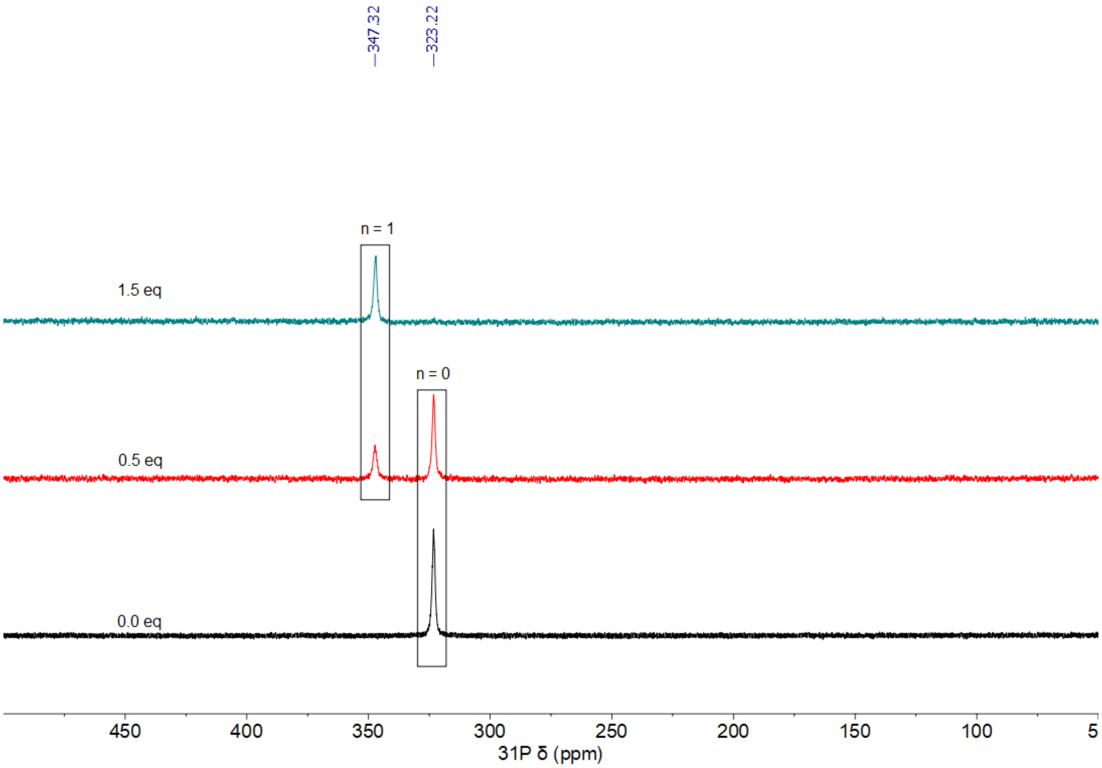

Figure S2.43. ^{31}P NMR spectra of ITpp titration of **2.1** in THF.

IDpp (m = 1):

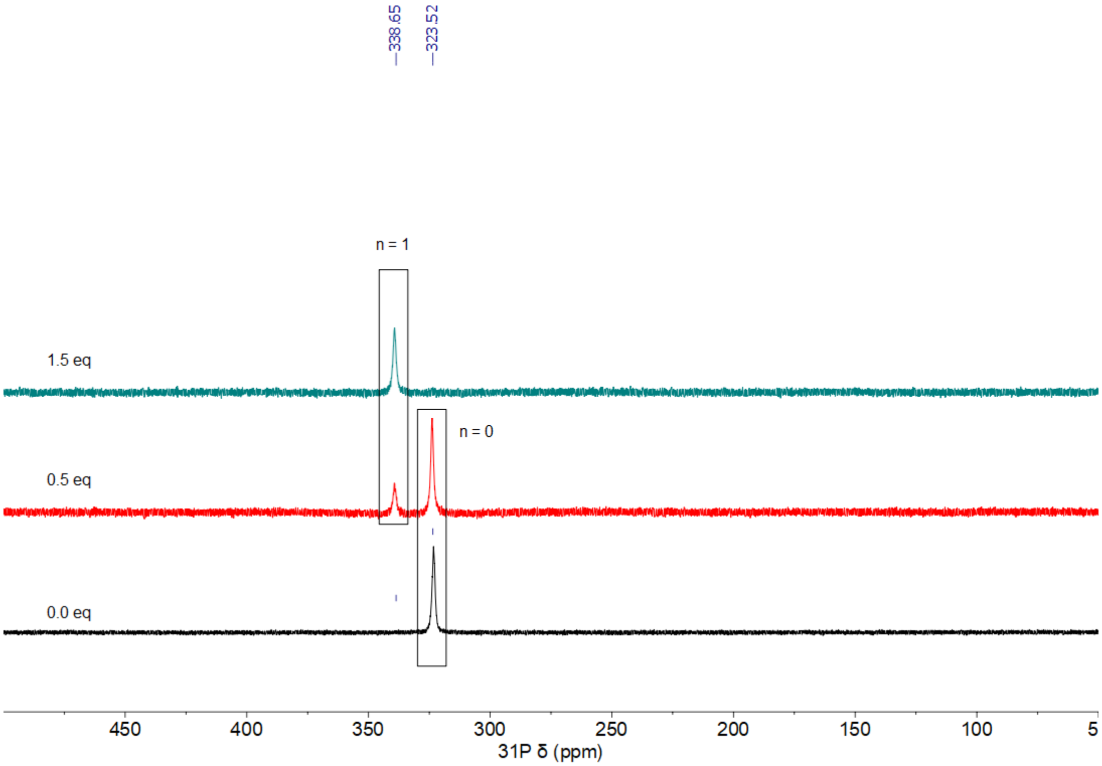

Figure S2.44. ^{31}P NMR spectra of IDpp titration of **2.1** in THF.

Computational details

General methods

All calculations were carried out using version 5.0.0 of the ORCA program package.[40] Coordinates for the mononuclear model complexes $FeCl_3$(NHC) were obtained from geometry optimizations on the S = ⁵⁄₂ surface via unrestricted Kohn-Sham DFT using the GGA exchange-correlation functional BP86 and employing the def2-TZVP basis set on Fe and the def2-SVP basis set on C, N, Cl, and H.[41] For all atoms, the auxiliary Coulomb fitting basis (def2/J)[42] was employed, along with Grimme's atom-pairwise correction with Becke–Johnson damping (D3BJ) to account for the effects of dispersion.[43,44] To directly compare the steric profiles of each NHC, the Fe–C bond length was constrained to 2.00 Å in all calculations.

Theoretical solid angle (G_T) and percent buried volume ($\%V_b$) calculations

Solid angles were computed using the program Solid-G on geometry-optimized $FeCl_3$(NHC) model complexes.[24] Normalization of the Fe–C(NHC) bond length to 2.28 Å was performed automatically by Solid-G without performing a second geometry optimization. Percent buried volume was calculated using the program SambVca 2.1 with hydrogen atoms included, using the default parameters: 1.17 Bondi radii and a coordination sphere of radius 3.5 Å.[25] Percent buried volume calculations were performed on the same atomic coordinates as used in the solid angle calculations.

Table S2.2 tabulates the computed percent buried volume and solid angles. The left panel of Figure S2.45 compares the calculated solid angles for Fe–C = 2.00 Å (closed circles) and normalized to 2.28 Å (open circles) against the observed maximal substitution numbers, *m*, as determined from the titration experiments (*vide supra*). The right panel of Figure S2.45 illustrates the poorer correlation of percent buried volume and *m*, specifically the overlap in the range of $\%V_b$ of NHCs with $m = 3$ and $m = 2$. Ligand substitution by I^tBu and IPr* were not observed. G_T and $\%V_b$ values of IPr* are the greatest among the NHCs presented here, establishing that beyond a certain threshold an NHC is unable to bind to the cluster even once. I^tBu has G_T values that predict tetrasubstitution ($m = 4$). Its $\%V_b$, while higher than that of other NHCs with similar G_T (ICy, ITol, IMesCy, etc.), is similar to the $\%\underline{V}_b$ of IPr and ITppCy ($m = 2$). Evidently, $\%V_b$ and G_T values alone failed to predict the substitution behavior of I^tBu.

Table S2.2. Calculated solid angle, G_{T}, and percent buried volume, $\%V_{\mathrm{b}}$, of NHC ligands using atomic coordinates from geometry optimized $FeCl_3$(NHC) model complexes.

NHC	G_{T} (2.00 Å)	G_{T} (2.00 Å)	$\%V_{\mathrm{b}}$ (2.00 Å)
ICy	32.0	27.9	30.6
ITol	33.5	29.7	33.3
IMesCy	35.9	32.2	33.4
I^{t}Bu	36.2	31.2	39.0
IMes	39.7	36.2	37.0
IMesAd	39.7	35.6	38.6
IDep	41.2	38.1	37.3
SIAnt	41.5	38.7	36.3
ITppCy	43.5	40.1	39.5
IPr	45.6	42.2	40.5
IDpp	50.9	47.2	42.9
ITpp	53.2	50.2	42.9
IPr*	54.5	51.8	45.8

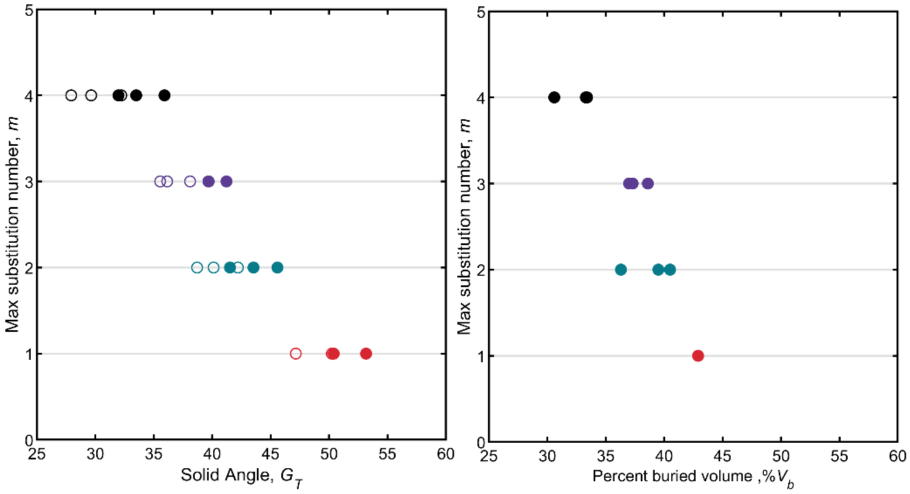

Figure S2.45. (*Left*) Observed maximal substitution number of NHCs depends on the theoretical solid angle, G_{T}, for Fe–C = 2.00 Å (closed circles) and normalized to 2.28 Å (open circles) computed from geometry optimized model complex [$FeCl_3$(NHC)]. (*Right*) Observed maximal substitution number of NHCs with respect to the calculated percent buried volume using the same atomic coordinates as with solid angle calculations.

X-ray refinement details

*$[Fe_4S_4(ITol)_4][BPh_4]$ (**2.2**):* Crystalizes in the monoclinic, centrosymmetric space group $P2_1/n$ with one cluster molecule and one BPh_4^- counterion in the asymmetric unit. Three well-ordered THF solvent molecules and one disordered over two positions were found and independently refined.

*$[Fe_4S_4(IMes)_3(PCy_3)][BPh_4]$ (**2.3**):* Crystallizes in the monoclinic, centrosymmetric space group $P2_1/c$ with one cluster molecule and one BPh_4^- counterion in the asymmetric unit. Disorder in one cyclohexyl moiety of the PCy_3 ligand was refined. One well-ordered ether and one ether disordered over a *c*-glide plane with a disordered THF molecule were found and refined. Five reflections are omitted from the final dataset for having estimated standard deviations >10.

*$[Fe_4S_4(IPr)_2(PCy_3)_2][BPh_4]$ (**2.4**):* Crystallizes in the monoclinic space group $P2/n$ with half of a cluster molecule and half a BPh_4^- counterion in the asymmetric unit. The cluster displays whole molecule disorder via a 90° rotation about its center of mass. The two components of the disorder were refined and converged to a ratio of 0.87:0.13. One disordered PhF solvent molecule was found at a special position. Seven reflections were omitted from the final dataset for having estimated standard deviations >10.

*$[Fe_4S_4(ITpp)(PCy_3)_3][BPh_4]$ (**2.5**):* Crystallizes in the triclinic, centrosymmetric space group $P{-}1$ with one cluster molecule and one BPh_4^- counterion in the asymmetric unit. Of the three disordered DFB solvent molecules found; one could be satisfactorily refined. The remaining two were omitted using *PLATON* SQUEEZE.[45] Five reflections were omitted from the final dataset for having estimated standard deviations >10.

*$[Fe_4S_4(IMesCy)_4][BPh_4]$ (**2.7**):* Crystallizes in the triclinic, centrosymmetric space group $P{-}1$ with one cluster molecule and one BPh_4^- counterion in the asymmetric unit. One well-ordered and one disordered PhF solvent molecule were found and independently refined.

Table S2.3. Crystallographic data for **2.2** and **2.3**.

	2.2	**2.3**
CCDC deposition number	2214363	2214362
Empirical formula	$C_{104}H_{108}BFe_4N_8O_3S_4$	$C_{113}H_{144.19}BFe_4N_6O_2PS_4$
Color, habit	Brown, block	Black, block
Formula weight	1880.43	2011.95
T [K]	100(2)	100(2)
λ [Å]	0.71073	0.71073
Crystal system	Monoclinic	Monoclinic
Space group	$P2_1/n$	$P2_1/c$
a [Å]	13.3051(8)	15.9781(2)
b [Å]	18.4610(10)	24.8067(7)
c [Å]	37.963(2)	27.0186(9)
α [°]	90	90
β [°]	92.422(2)	96.2160(10)
γ [°]	90	90
V [Å^3]	9316.3(9)	10646.2(5)
Z	4	4
d_{calc} [g cm^{-1}]	1.341	1.255
Radiation type	Mo K_α	Mo K_α
μ [mm^{-1}]	0.756	0.679
$F(000)$	3940	4273
Crystal size [mm^3]	0.670 × 0.470 × 0.250	0.360 × 0.220 × 0.190
θ range for data collection [°]	1.227–31.575	1.282–33.136
Miller index ranges	$-19 \le h \le 19$ $-26 \le k \le 27$ $-55 \le l \le 55$	$-24 \le h \le 24$ $-38 \le k \le 38$ $-41 \le l \le 41$
Reflections collected	734284	831175
Independent reflections	31163 (R_{int} = 0.0548)	40551 (R_{int} = 0.0496)
Completeness to θ = 25.242° [%]	100.0	100.0
Absorption correction	Semi-empirical from equivalents	Semi-empirical from equivalents
Refinement method	Full-matrix least-squares on F^2	Full-matrix least-squares on F^2
Data / restraints / parameters	31163 / 2087 / 1212	40551 / 2331 / 1303
Goodness-of-fit on F^2	1.047	1.074
Final R indices ($I > 2\sigma(I)$)	$R_1 = 0.0342$, $wR_2 = 0.0796$	$R_1 = 0.0394$, $wR_2 = 0.1110$
R indices (all data)	$R_1 = 0.0475$, $wR_2 = 0.0872$	$R_1 = 0.0526$, $wR_2 = 0.1168$
$\Delta\rho_{max}$, $\Delta\rho_{min}$ [e Å^{-3}]	0.521, −0.545	1.709, −0.929

Table S2.4. Crystallographic data for **2.4** and **2.5**.

	2.4	**2.5**
CCDC deposition number	2214361	2214359
Empirical formula	$C_{60.04}H_{81.08}B_{0.5}F_{0.5}Fe_2N_2PS_2$	$C_{67.5}H_{79.5}B_{0.50}FFe_2NP_{1.5}S_2$
Color, habit	Black, needle	Black, block
Formula weight	1052.55	1151.50
T [K]	100(2)	100(2)
λ [Å]	0.71073	0.71073
Crystal system	Monoclinic	Triclinic
Space group	$P2/\mathrm{n}$	$P{-}1$
a [Å]	19.054(2)	15.901(2)
b [Å]	14.5808(16)	19.316(3)
c [Å]	20.579(2)	24.370(3)
α [°]	90	78.295(5)
β [°]	93.555(2)	78.209(5)
γ [°]	90	66.525(5)
V [Å^3]	5706.2(11)	6658.9(15)
Z	4	4
d_{calc} [g cm^{-1}]	1.225	1.149
Radiation type	Mo K_α	Mo K_α
μ [mm^{-1}]	0.649	0.574
$F(000)$	2245	2438
Crystal size [mm^3]	0.80 × 0.60 × 0.157	0.200 × 0.190 × 0.180
θ range for data collection [°]	1.397–31.952	1.348–31.606
Miller index ranges	$-28 \leq h \leq 28$ $-21 \leq k \leq 21$ $-30 \leq l \leq 30$	$-23 \leq h \leq 23$ $-28 \leq k \leq 28$ $-35 \leq l \leq 35$
Reflections collected	368563	344427
Independent reflections	19713 ($R_{\mathrm{int}} = 0.1089$)	44634 ($R_{\mathrm{int}} = 0.0559$)
Completeness to $\theta = 25.242°$ [%]	99.9	100.0
Absorption correction	Semi-empirical from equivalents	Semi-empirical from equivalents
Refinement method	Full-matrix least-squares on F^2	Full-matrix least-squares on F^2
Data / restraints / parameters	19713 / 2050 / 1163	44634 / 2230 / 1370
Goodness-of-fit on F^2	1.063	1.035
Final R indices ($I > 2\sigma(I)$)	$R_1 = 0.0441$, $wR_2 = 0.0915$	$R_1 = 0.0418$, $wR_2 = 0.0935$
R indices (all data)	$R_1 = 0.0819$, $wR_2 = 0.1066$	$R_1 = 0.0601$, $wR_2 = 0.1022$
$\Delta\rho_{\mathrm{max}}$, $\Delta\rho_{\mathrm{min}}$ [e Å^{-3}]	0.407, −0.415	0.681, −0.647

Table S2.5. Crystallographic data for **2.7**.

	2.7
CCDC deposition number	2214360
Empirical formula	$C_{106.81}H_{125.01}BF_{1.8}Fe_4N_8S_4$
Color, habit	Black, plate
Formula weight	1917.50
T [K]	100(2)
λ [Å]	0.71073
Crystal system	Triclinic
Space group	$P-1$
a [Å]	15.2614(8)
b [Å]	17.1019(9)
c [Å]	20.0173(10)
α [°]	80.992(2)
β [°]	77.416(2)
γ [°]	77.207(2)
V [Å^3]	4940.1(4)
Z	2
d_{calc} [g cm^{-1}]	1.289
Radiation type	Mo K_α
μ [mm^{-1}]	0.715
F(000)	2022
Crystal size [mm^3]	0.160 × 0.140 × 0.020
θ range for data collection [°]	1.229–30.636
Miller index ranges	$-21 \leq h \leq 21$ $-24 \leq k \leq 24$ $-28 \leq l \leq 28$
Reflections collected	381199
Independent reflections	30376 (R_{int} = 0.0561)
Completeness to θ = 25.242° [%]	100.0
Absorption correction	Semi-empirical from equivalents
Refinement method	Full-matrix least-squares on F^2
Data / restraints / parameters	30376 / 411 / 1221
Goodness-of-fit on F^2	1.056
Final R indices ($I > 2\sigma(I)$)	R_1 = 0.0411, wR_2 = 0.0991
R indices (all data)	R_1 = 0.0570, wR_2 = 0.1085
$\Delta\rho_{\mathrm{max}}$, $\Delta\rho_{\mathrm{min}}$ [e Å^{-3}]	1.576, −0.824

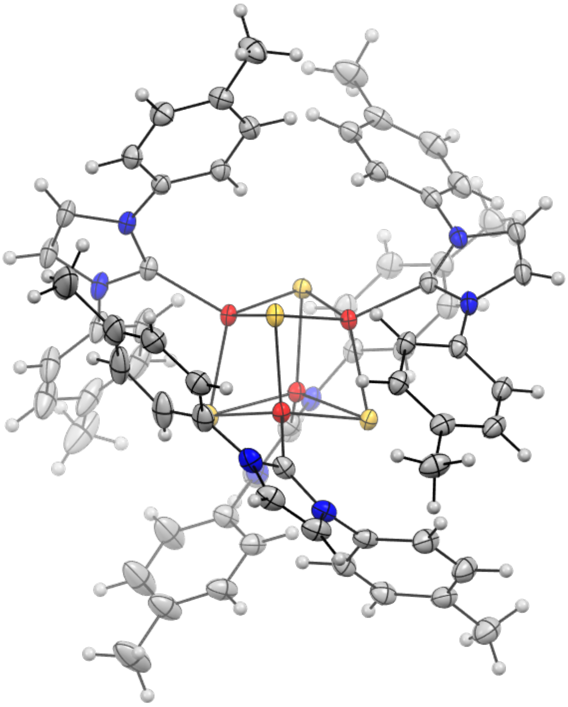

Figure S2.46. Thermal ellipsoid plot (50%) of **2.2**. Counter ion and solvent molecules omitted for clarity. Color scheme: Fe (red), S (yellow), N (blue), C (gray), H (white).

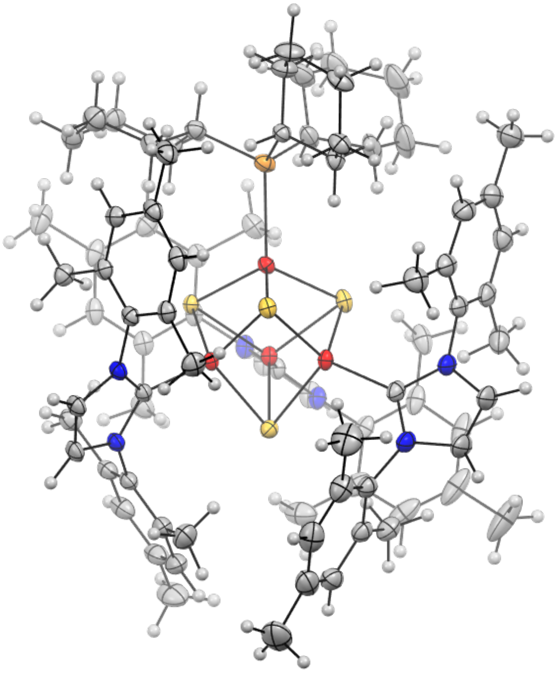

Figure S2.47. Thermal ellipsoid plot (50%) of **2.3**. Counter ion and solvent molecules omitted for clarity. Color scheme: Fe (red), S (yellow), N (blue), C (gray), H (white).

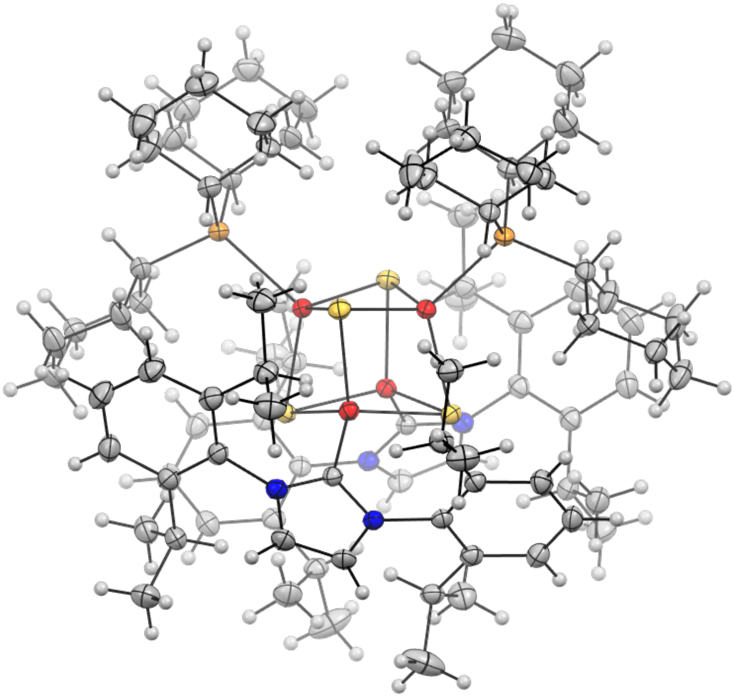

Figure S2.48. Thermal ellipsoid plot (50%) of **2.4**. Counter ion and solvent molecules omitted for clarity. Color scheme: Fe (red), S (yellow), N (blue), C (gray), H (white).

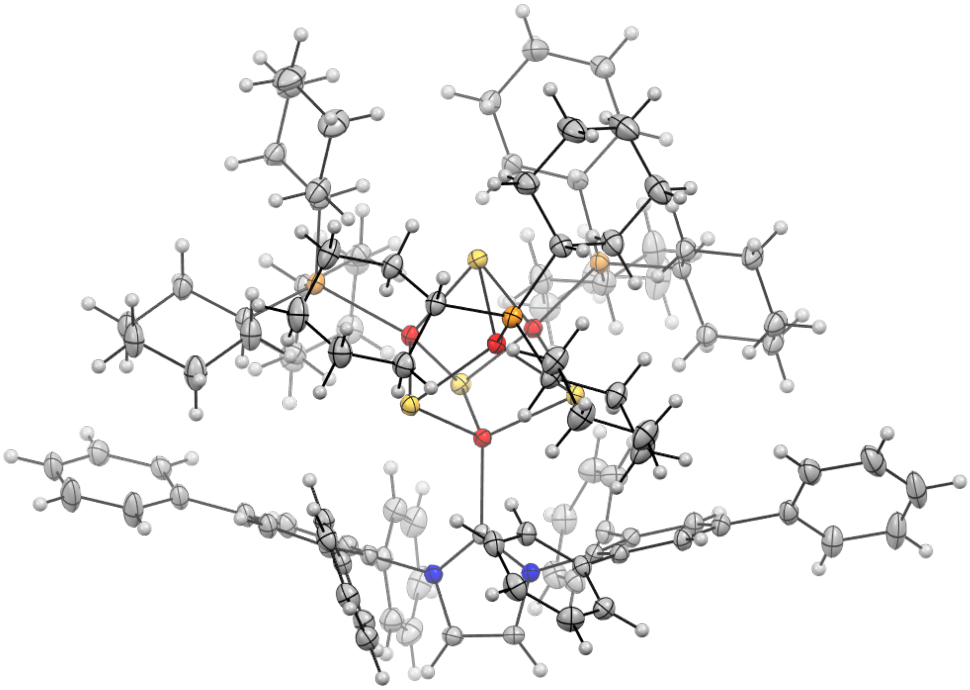

Figure S2.49. Thermal ellipsoid plot (50%) of **2.5**. Counter ion and solvent molecules omitted for clarity. Color scheme: Fe (red), S (yellow), N (blue), C (gray), H (white).

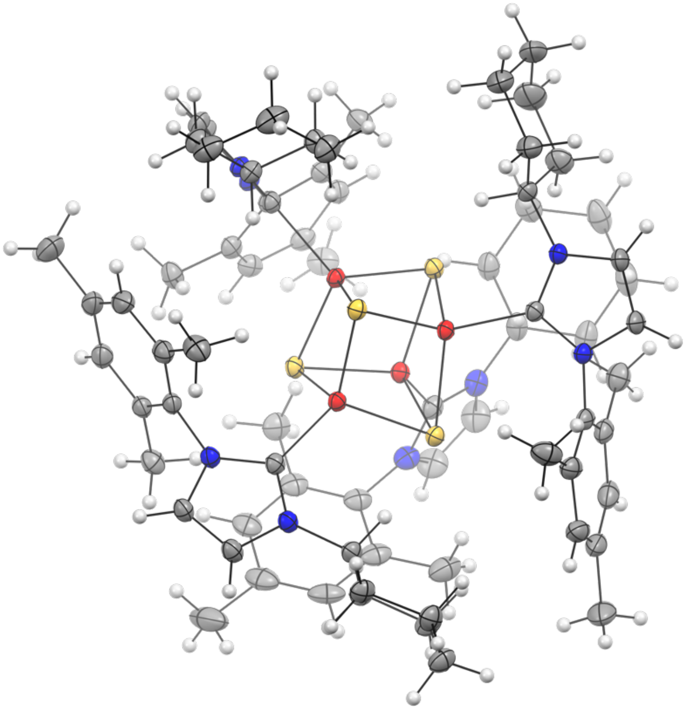

Figure S2.50. Thermal ellipsoid plot (50%) of **2.7**. Counter ion and solvent molecules omitted for clarity. Color scheme: Fe (red), S (yellow), N (blue), C (gray), H (white).

References

(1) Steigerwald, M. L.; Siegrist, T.; Gyorgy, E. M.; Hessen, B.; Kwon, Y.-U.; Tanzler, S. M. Effect of Diverse Ligands on the Course of a Molecules-to-Solids Process and Properties of Its Intermediates. *Inorg. Chem.* **1994**, *33* (15), 3389–3395.

(2) Goh, C.; Segal, B. M.; Huang, J.; Long, J. R.; Holm, R. H. Polycubane Clusters: Synthesis of $[Fe_4S_4(PR_3)_4]^{1+,0}$ (R = Bu^t, Cy, Pr^i) and $[Fe_4S_4]^0$ Core Aggregation upon Loss of Phosphine. *J. Am. Chem. Soc.* **1996**, *118* (47), 11844–11853.

(3) Fuhr, O.; Dehnen, S.; Fenske, D. Chalcogenide Clusters of Copper and Silver from Silylated Chalcogenide Sources. *Chem. Soc. Rev.* **2013**, *42* (4), 1871–1906.

(4) Drance, M. J.; Mokhtarzadeh, C. C.; Melaimi, M.; Agnew, D. W.; Moore, C. E.; Rheingold, A. L.; Figueroa, J. S. Controlled Expansion of a Strong-Field Iron Nitride Cluster: Multi-Site Ligand Substitution as a Strategy for Activating Interstitial Nitride Nucleophilicity. *Angew. Chem. Int. Ed.* **2018**, *57* (40), 13057–13061.

(5) Loewen, N. D.; Pattanayak, S.; Herber, R.; Fettinger, J. C.; Berben, L. A. Quantification of the Electrostatic Effect on Redox Potential by Positive Charges in a Catalyst Microenvironment. *J. Phys. Chem. Lett.* **2021**, *12* (12), 3066–3073.

(6) Beinert, H.; Holm, R. H.; Munck, E. Iron-Sulfur Clusters: Nature's Modular, Multipurpose Structures. *Science* **1997**, *277* (5326), 653–659.

(7) Bigness, A.; Vaddypally, S.; Zdilla, M. J.; Mendoza-Cortes, J. L. Ubiquity of Cubanes in Bioinorganic Relevant Compounds. *Coord. Chem. Rev.* **2022**, *450*, 214168.

(8) Cammack, R. Iron Sulfur Proteins. In *Advances in inorganic chemistry*; Elsevier, 1992; Vol. 38, pp 281–322.

(9) Rees, D. C.; Howard, J. B. The Interface between the Biological and Inorganic Worlds: Iron-Sulfur Metalloclusters. *Science* **2003**, *300* (5621), 929–931.

(10) Rouault, T. A. Iron-Sulfur Proteins Hiding in Plain Sight. *Nat. Chem. Biol.* **2015**, *11* (7), S442–445.

(11) Bista, D.; Aydt, A. P.; Anderton, K. J.; Paley, D. W.; Betley, T. A.; Reber, A. C.; Chauhan, V.; Bartholomew, A. K.; Roy, X.; Khanna, S. N. High-Spin Superatom Stabilized by Dual Subshell Filling. *J. Am. Chem. Soc.* **2022**, *144* (11), 5172–5179.

(12) Deng, L.; Holm, R. H. Stabilization of Fully Reduced Iron-Sulfur Clusters by Carbene Ligation: The $[Fe_nS_n]^0$ Oxidation Levels (n = 4, 8). *J. Am. Chem. Soc.* **2008**, *130* (30), 9878–9886..

(13) Díez-González, S.; Nolan, S. P. Stereoelectronic Parameters Associated with *N*-Heterocyclic Carbene (NHC) Ligands: A Quest for Understanding. *Coord. Chem. Rev.* **2007**, *251* (5–6), 874–883.

(14) Brown, A. C.; Suess, D. L. M. Controlling Substrate Binding to Fe_4S_4 Clusters through Remote Steric Effects. *Inorg. Chem.* **2019**, *58*, 5273–5280.

(15) Huang, J.; Stevens, E. D.; Nolan, S. P.; Petersen, J. L. Olefin Metathesis-Active Ruthenium Complexes Bearing a Nucleophilic Carbene Ligand. *J. Am. Chem. Soc.* **1999**, *121* (12), 2674–2678.

(16) Weskamp, T.; Schattenmann, W. C.; Spiegler, M.; Herrmann, W. A. A Novel Class of Ruthenium Catalysts for Olefin Metathesis. *Angew. Chem. Int. Ed.* **1998**, *37* (18), 2490–2493.

(17) Brown, A. C.; Suess, D. L. M. Reversible Formation of Alkyl Radicals at [Fe_4S_4] Clusters and Its Implications for Selectivity in Radical SAM Enzymes. *J. Am. Chem. Soc.* **2020**, *142* (33), 14240–14248.

(18) Sridharan, A.; Brown, A. C.; Suess, D. L. M. A Terminal Imido Complex of an Iron–Sulfur Cluster. *Angew. Chem. Int. Ed.* **2021**, *60* (23), 12802–12806.

(19) Brown, A. C.; Thompson, N. B.; Suess, D. L. M. Evidence for Low-Valent Electronic Configurations in Iron-Sulfur Clusters. *J. Am. Chem. Soc.* **2022**, *144* (20), 9066–9073.

(20) Ye, M.; Brown, A. C.; Suess, D. L. M. Reversible Alkyl-Group Migration between Iron and Sulfur in [Fe_4S_4] Clusters. *J. Am. Chem. Soc.* **2022**, *144* (29), 13184–13195.

(62) Brown, A. C.; Suess, D. L. M. Valence Localization in Alkyne and Alkene Adducts of Synthetic [Fe_4S_4]$^+$ Clusters. *Inorg. Chem.* **2022**.

(22) Kim, Y.; Sridharan, A.; Suess, D. L. M. The Elusive Mononitrosylated [Fe_4S_4] Cluster in Three Redox States. *Angew. Chem. Int. Ed.* **2022**, *61* (47), e202213032.

(23) Tan, L. L.; Holm, R. H.; Lee, S. C. Structural Analysis of Cubane-Type Iron Clusters. *Polyhedron* **2013**, *58*, 206–217.

(24) Guzei, I. A.; Wendt, M. An Improved Method for the Computation of Ligand Steric Effects Based on Solid Angles. *Dalton Trans.* **2006**, No. 33, 3991.

(25) Falivene, L.; Cao, Z.; Petta, A.; Serra, L.; Poater, A.; Oliva, R.; Scarano, V.; Cavallo, L. Towards the Online Computer-Aided Design of Catalytic Pockets. *Nat. Chem.* **2019**, *11* (10), 872–879.

(26) Pangborn, A. B.; Giardello, M. A.; Grubbs, R. H.; Rosen, R. K.; Timmers, F. J. Safe and Convenient Procedure for Solvent Purification. *Organometallics* **1996**, *15* (5), 1518–1520.

(27) Arduengo, A. J.; Dias, H. V. R.; Harlow, R. L.; Kline, M. Electronic Stabilization of Nucleophilic Carbenes. *J. Am. Chem. Soc.* **1992**, *114* (14), 5530–5534.

(28) Queval, P.; Jahier, C.; Rouen, M.; Artur, I.; Legeay, J.-C.; Falivene, L.; Toupet, L.; Crévisy, C.; Cavallo, L.; Baslé, O.; Mauduit, M. Multicomponent Synthesis of

Unsymmetrical Unsaturated *N*-Heterocyclic Carbene Precursors and Their Related Transition-Metal Complexes. *Angew. Chem.* **2013**, *125* (52), 14353–14357.

(29) Hintermann, L. Expedient Syntheses of the *N*-Heterocyclic Carbene Precursor Imidazolium Salts IPrHCl, IMesHCl and IXyHCl. *Beilstein J. Org. Chem.* **2007**, *3*, 22.

(30) Bantreil, X.; Nolan, S. P. Synthesis of *N*-Heterocyclic Carbene Ligands and Derived Ruthenium Olefin Metathesis Catalysts. *Nat. Protoc.* **2011**, *6* (1), 69–77.

(31) Kyan, R.; Sato, K.; Mase, N.; Watanabe, N.; Narumi, T. Tuning the Catalyst Reactivity of Imidazolylidene Catalysts through Substituent Effects on the *N*-Aryl Groups. *Org. Lett.* **2017**, *19* (10), 2750–2753.

(32) Luan, X.; Mariz, R.; Gatti, M.; Costabile, C.; Poater, A.; Cavallo, L.; Linden, A.; Dorta, R. Identification and Characterization of a New Family of Catalytically Highly Active Imidazolin-2-Ylidenes. *J. Am. Chem. Soc.* **2008**, *130* (21), 6848–6858.

(33) Gabbaï, F. P.; Chirik, P. J.; Fogg, D. E.; Meyer, K.; Mindiola, D. J.; Schafer, L. L.; You, S.-L. An Editorial About Elemental Analysis. *Organometallics* **2016**, *35* (19), 3255–3256.

(34) McSkimming, A.; Suess, D. L. M. Dinitrogen Binding and Activation at a Molybdenum–Iron–Sulfur Cluster. *Nat. Chem. 2021 137* **2021**, *13* (7), 666–670.

(35) Kuveke, R. E. H.; Barwise, L.; van Ingen, Y.; Vashisth, K.; Roberts, N.; Chitnis, S. S.; Dutton, J. L.; Martin, C. D.; Melen, R. L. An International Study Evaluating Elemental Analysis. *ACS Cent. Sci.* **2022**, *8* (7), 855–863.

(36) Smallcombe, S. H.; Patt, S. L.; Keifer, P. A. WET Solvent Suppression and Its Applications to LC NMR and High-Resolution NMR Spectroscopy. *J. Magn. Reson. A* **1995**, *117* (2), 295–303.

(37) Jin, S.; Adamchuk, J.; Xiang, B.; DiSalvo, F. J. The Dean−Evans Relation in ^{31}P NMR Spectroscopy and Its Application to the Chemistry of Octahedral Tungsten Sulfide Clusters. *J. Am. Chem. Soc.* **2002**, *124* (31), 9229–9240.

(38) Wang, J.; Cheng, X.; Liu, Y.; Zhang, J. Multicomponent Synthesis of Unsymmetrical 4,5-Disubstituted Imidazolium Salts as *N*-Heterocyclic Carbene Precursors: Applications in Palladium-Catalyzed Cross-Coupling Reactions. *J. Org. Chem.* **2021**, *86* (9), 6278–6288.

(39) Alexander, S. G.; Cole, M. L.; Morris, J. C. Preparation of a Super Bulky Silver N-Heterocyclic Carbene Complex. *New J. Chem.* **2009**, *33* (4), 720.

(40) Neese, F.; Wennmohs, F.; Becker, U.; Riplinger, C. The ORCA Quantum Chemistry Program Package. *J. Chem. Phys.* **2020**, *152* (22), 224108.

(41) Weigend, F.; Ahlrichs, R. Balanced Basis Sets of Split Valence, Triple Zeta Valence and Quadruple Zeta Valence Quality for H to Rn: Design and Assessment of Accuracy. *Phys. Chem. Chem. Phys.* **2005**, *7* (18), 3297.

(42) Weigend, F. Accurate Coulomb-Fitting Basis Sets for H to Rn. *Phys. Chem. Chem. Phys.* **2006**, *8* (9), 1057.

(43) Grimme, S.; Antony, J.; Ehrlich, S.; Krieg, H. A Consistent and Accurate *Ab Initio* Parametrization of Density Functional Dispersion Correction (DFT-D) for the 94 Elements H-Pu. *J. Chem. Phys.* **2010**, *132* (15), 154104.

(44) Grimme, S.; Ehrlich, S.; Goerigk, L. Effect of the Damping Function in Dispersion Corrected Density Functional Theory. *J. Comput. Chem.* **2011**, *32* (7), 1456–1465.

(45) Spek, A. L. PLATON SQUEEZE: A Tool for the Calculation of the Disordered Solvent Contribution to the Calculated Structure Factors. *Acta Crystallogr. Sect. C Struct. Chem.* **2015**, *71* (1), 9–18.

Chapter 3

Site-differentiation of octahedral iron–sulfur clusters[†]

As noted in Chapter 2, the difficulty in imparting site-differentiation–in particular, the stochastic nature of ligand substitution–is not unique to cuboidal clusters featuring tetrahedral metal cores, and instead applies to virtually any highly symmetric, polyhedral cluster. Of these, octahedral $[M_6E_8L_6]$ Chevrel-type clusters present substantial challenges because ligand substitution reactions can yield reaction mixtures with up to ten possible species, several of which are stereoisomers (Figure 3.1). We hypothesized that, as for the cuboidal $[Fe_4S_4]$ clusters, the distal bulk of NHCs could be leveraged to exert steric control over both the substitution number and the stereochemistry of the site-differentiated Chevrel-type clusters.

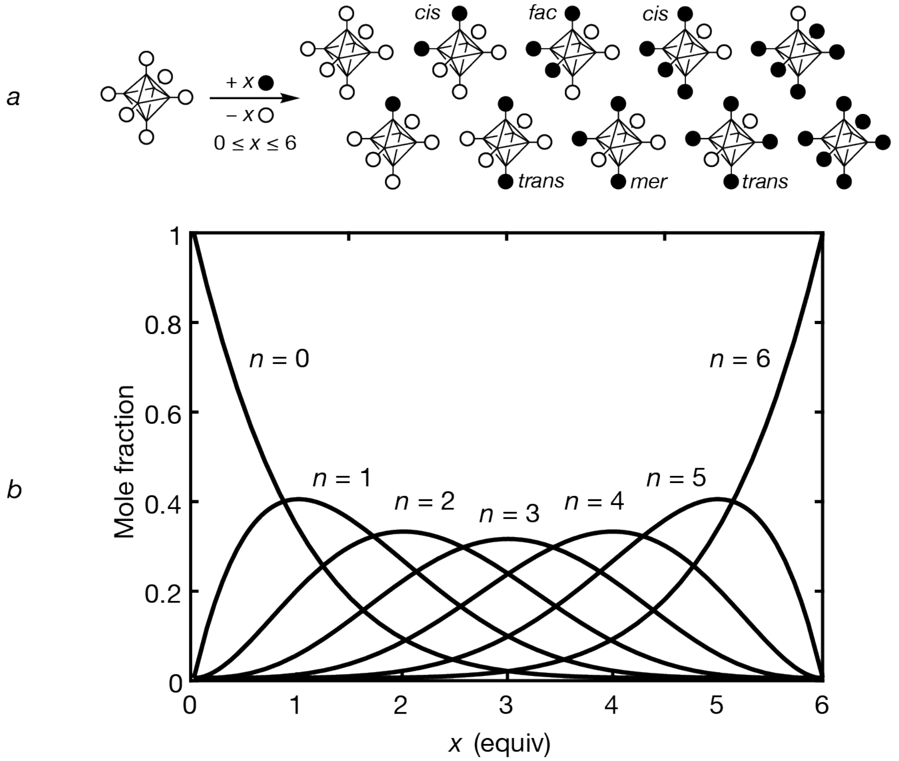

Figure 3.1. (*a*) Products resulting from unselective substitution of octahedral clusters under the assumption that the incoming ligand (black ball) is fully consumed in the reaction, producing an equimolar amount (*x*) of the departing ligand (white ball). (*b*) Binomial distribution model of stochastic ligand substitution at an octahedral cluster also under the assumption that each ligand substitution event is highly favorable. (see experimental details and supplemental information section of Chapter 2 for details about the mathematical model).

[†] Adapted in part with permission from: Bostelaar, T. M.; Brown, A. C.; Sridharan, A.; Suess, D. L. M. *Nature Synthesis* **2023**, 1–9. © Springer Nature. All rights reserved.

Stereoselective site-differentiation of Chevrel-type Fe-S clusters

To test this hypothesis, we conducted analogous experiments to those described in Chapter 2, except using $[Fe_6S_8(PEt_3)_6][BF_4]$ (**3.1**)[1] instead of **2.1**. I first mixed **3.1** with an excess (8 equiv) of the relatively small NHC, ICy, which resulted in the precipitation of a black solid identified as $[Fe_6S_8(ICy)_6][BF_4]$ (**3.2**) in which all six PEt_3 ligands from **3.1** had been substituted by ICy (Scheme 3.1). Interestingly, a relatively modest increase in the NHC steric profile from ICy to IMes resulted in a dramatically different reaction outcome (Scheme 3.2). Specifically, mixing **3.1** with IMes (4 equiv) yielded two products depending on the reaction conditions. When IMes was added in a non-coordinating solvent such as *ortho*-difluorobenzene (DFB), the monosubstituted cluster $[Fe_6S_8(IMes)(PEt_3)_5][BF_4]$ (**3.3**) was the sole product. However, in the presence of coordinating solvents like THF or MeCN, the disubstituted cluster *trans*-$[Fe_6S_8(PEt_3)_4(IMes)_2][BF_4]$ (**3.4**) was the final product (Scheme 3.2).

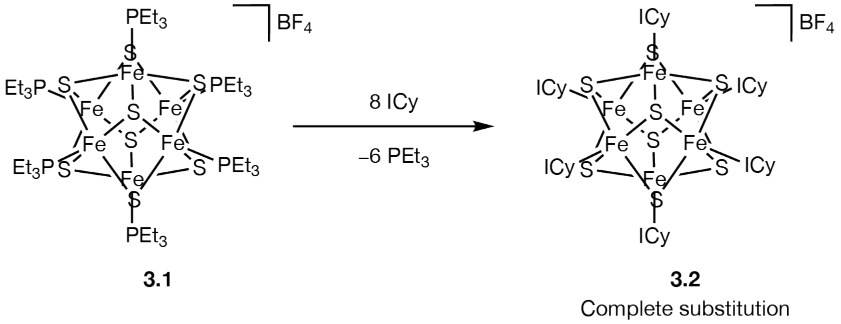

Scheme 3.1. Synthesis of **3.2** via hexasubstitution of **3.1**.

That the second equivalent of IMes was unable to substitute in the absence of a coordinating solvent suggests a difference in the mechanism for the first and second ligand substitutions. Although ^1H NMR of **3.1**–**3.4** could be recorded, the high ground spin state of the clusters precluded quantification of kinetics experiments by ^1H NMR (Figure S3.1 and Figure S3.3). UV/vis spectroscopy was a promising alternative, but the similarity in the UV/vis spectra of **3.1**–**3.4** prevented accurate quantification of the reaction kinetics (Figure S3.9). Despite these challenges, we proposed an associative mechanism for the first substitution event in the conversion of **3.1** to **3.3** in which one PEt_3 ligand was substituted directly by an incoming IMes ligand (Figure 3.2a). The long-range steric bulk of the IMes ligand then resulted in some increase in the steric crowding around the *trans* Fe site, preventing direct associative substitution by an additional IMes ligand. This second IMes ligand likely substituted via associative substitution of a THF or MeCN bound Fe that, as a result of the smaller size of the solvent ligands compared to PEt_3, allowed the bulky IMes ligand to approach (Figure 3.2b). The requirement for a coordinating solvent in the conversion of **3.3** to **3.4** was in support of such a mechanism for the substitution of the second IMes ligand.

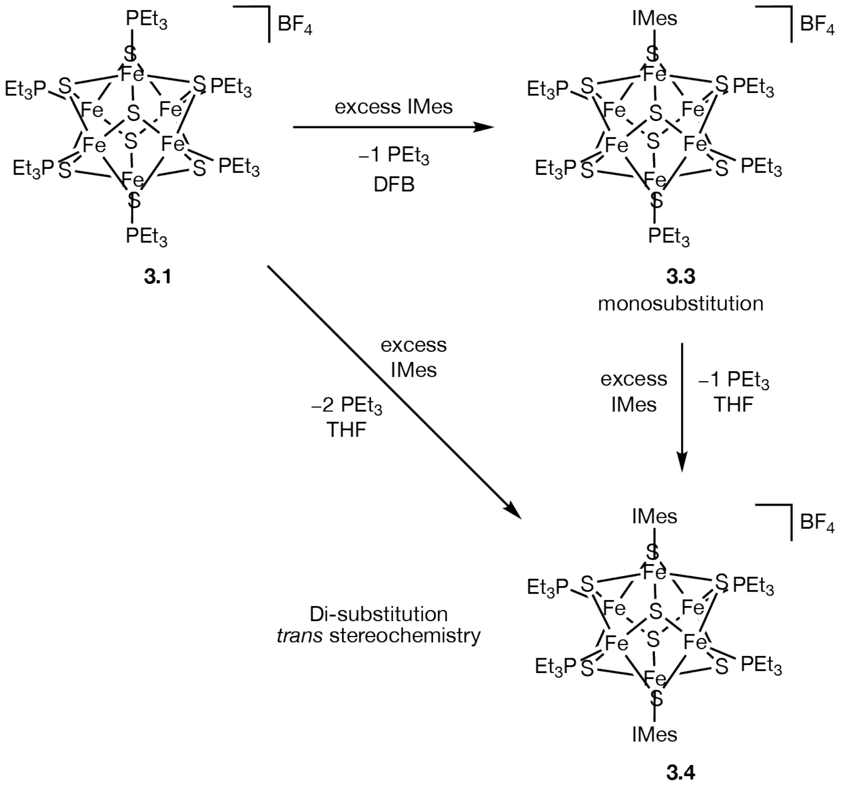

Scheme 3.2. Synthesis of site-differentiated clusters **3.3** and **3.4**.

Although we prefer the associative mechanism described above, we cannot rule out the possibility of alternative mechanism, such as a dissociative mechanism, without kinetics analysis. In a dissociative mechanism, the IMes substitutes onto a four-coordinate Fe intermediate following PEt_3 dissociation. As a result of its' six π-acidic PEt_3 ligands, **3.1** is less electron rich and therefore engaging in poorer π-backbonding to PEt_3. Upon binding of one IMes ligand, the cluster, **3.3**, is more electron rich than **3.1** and engages in greater π-backbonding to PEt_3. Therefore, **3.1** is expected to undergo dissociative ligand substitution at a greater rate than **3.3**. While this situation is consistent with the relative rates of the first and second substitution reactions in coordinating solvents, it does not predict the observed solvent dependence of the second substitution. However, it is possible that the two substitution steps proceed by completely different mechanisms. For example, the first substitution may occur through a dissociative mechanism, but the second substitution step may have an associative mechanism. Without further experiments to determine the rate law of the reactions, the exact mechanism of substitution could not be confidently concluded. Kinetic analysis was not attempted because the substitution reactions are not clean: small amounts of $IMesH^+$ and intractable black solids were observed.

Under no conditions have we observed either further substitution of **3.4** by IMes or formation of the *cis* isomer of **3.4**. Thus, **3.4** was produced without complications from oversubstitution and with perfect stereoselectivity. Moreover, the fact that hexasubstitution occurs in the preparation of **3.2** indicated that IMes (which, like ICy, was a stronger donor than PEt_3)[2,3] would likewise undergo six substitution events if not for its more imposing steric profile; we therefore conclude that the basis for stereoselective disubstitution in **3.4** is steric rather than electronic in origin. The imposing steric profile of IMes with respect to the $[Fe_6S_8]^+$ cluster was evident by the observation that IMes and PEt_3 bind competitively (necessitating the removal of PEt_3 in the synthesis of **3.4**; see experimental details and supplemental information section). Notably, a few $[M_6E_8]$ clusters bearing NHC ligands have been reported, and each shows a similar trans disposition of the NHC ligands;[4] however, as each was prepared from heteroleptic clusters, the site-differentiation pattern and stereochemistry of the product were likely derived from the starting cluster rather than from the steric profile of the NHC.

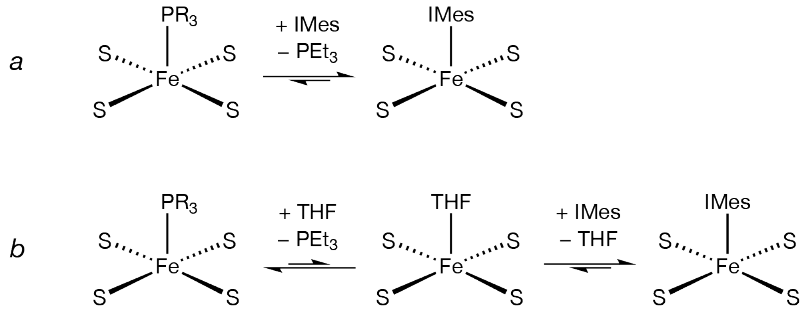

Figure 3.2. (*a*) Proposed mechanism of associative ligand substitution for binding of the first equiv IMes to **3.1**. (*b*) Proposed mechanism of ligand substitution for binding of the second equiv of IMes to **3.3** in the presence of THF.

Both **3.2** and **3.4** crystallized in $P{-}1$ with two half clusters in the asymmetric unit to give two crystallographically unique clusters that each lie on an inversion center; **3.2** was crystallographically characterized with a $[BPh_4]^-$ anion, installed via salt metathesis (see experimental section). In **3.2**, each of the 12 cyclohexyl methine protons bisect the S–Fe–S angle (Figure 3.3). This arrangement yields a configuration in which the cyclohexyl groups reside over a neighboring imidazolyl ring, giving a cluster with approximate T_h symmetry. For IMes, the *ortho*-methyl groups project over the imidazolyl ring (Figure 3.4), and thus would block such an arrangement and prevent binding of *cis*-IMes ligands. Furthermore, the orientation of the IMes ligands in **3.4** is rotated *ca.* 45° with respect to the ICy ligands in **3.2**, and this configuration may allow the *ortho*-methyl protons to avoid clashing with the bridging sulfides and/or the equatorial PEt_3 ligands (Figure 3.4). This dihedral preference for IMes is conserved in **3.3**, which crystallized in $P{-}1$ as well with two half clusters in the asymmetric unit (Figure 3.5).

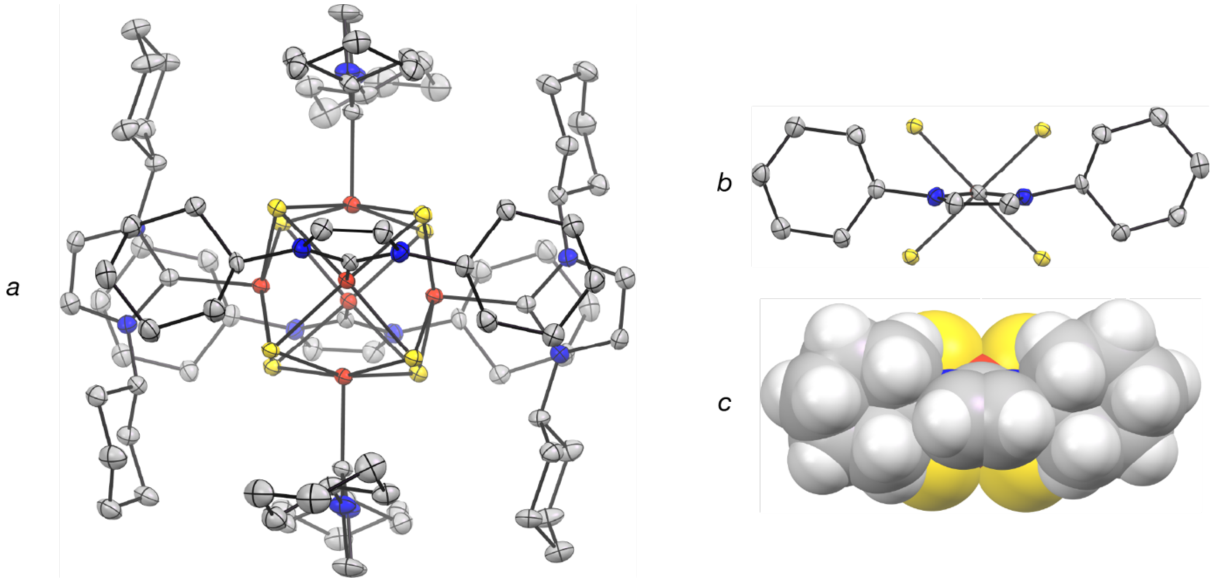

Figure 3.3. (*a*) Thermal ellipsoid plot (50%) of **3.2**. Solvent molecules, hydrogen atoms, and counterions were removed for clarity. (*b-c*) Thermal ellipsoid plot (50%) and space-filling diagram of one Fe–NHC site of **3.2** depicting the ∠SFeCN dihedral angle of approx. 45°. Color scheme: Fe (red), S (yellow), N (blue), C (gray), H (white).

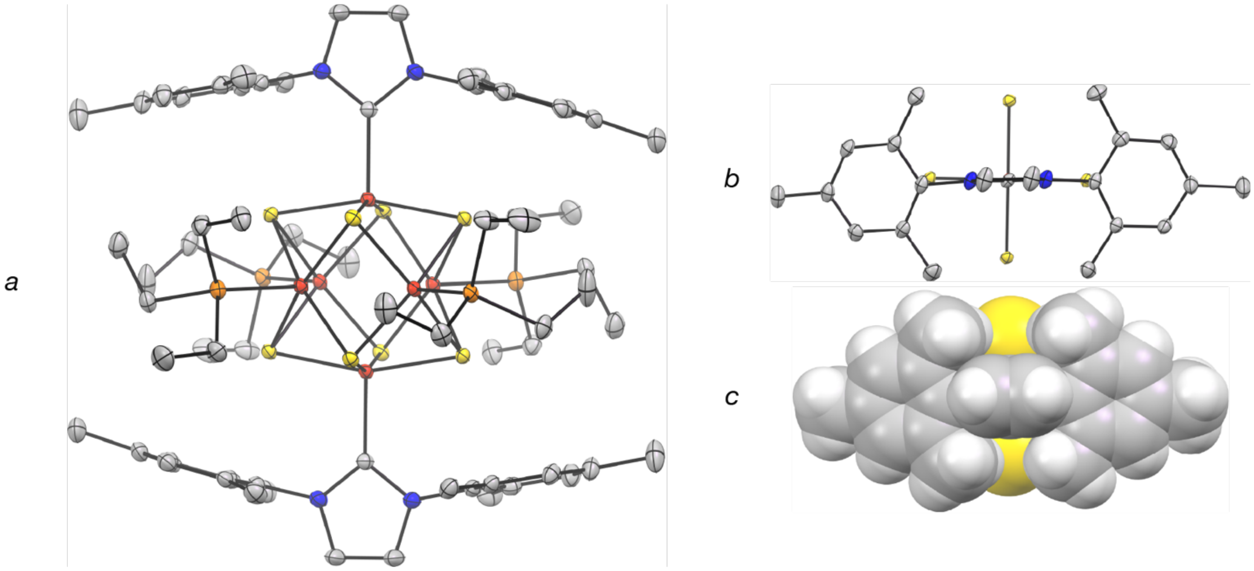

Figure 3.4. (a) Thermal ellipsoid plot (50%) of **3.4**. Solvent molecules, hydrogen atoms, and counterions were removed for clarity. (*b-c*) Thermal ellipsoid plot (50%) and space-filling diagram of one Fe–NHC site of **3.4** depicting the ∠SFeCN dihedral angle of approx. 90°. Color scheme: Fe (red), S (yellow), P (orange), N (blue), C (gray), H (white).

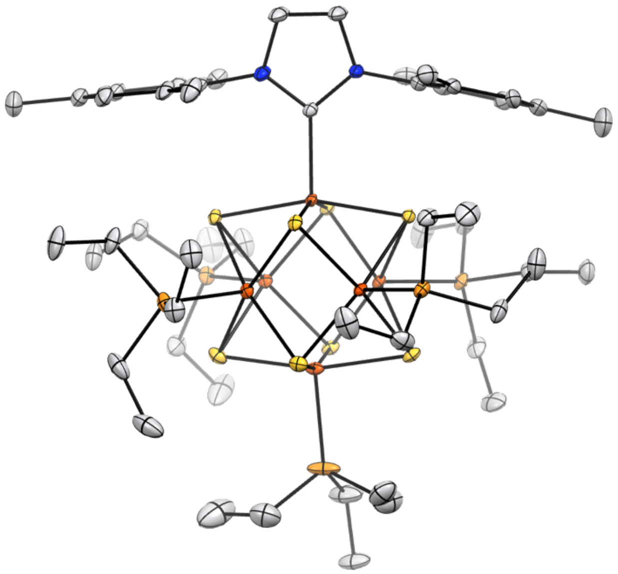

Figure 3.5. Thermal ellipsoid plot (50%) of **3.3**. Solvent molecules, hydrogen atoms, and counterions were omitted for clarity. Color scheme: Fe (red), S (yellow), P (orange), N (blue), C (gray), H (white).

The solid-state structures of **3.2**–**3.4** (*vide supra*) suggested that the dihedral preference of the NHC may play an underappreciated role in the stereochemistry and substitution number. Based on the dihedral angle arguments discussed above, we expected that other substitution patterns might require a dihedral preference like that of ICy or none whatsoever in addition to careful tuning of remote steric bulk. With this in mind, we synthesized two *N,N'*-dialkyl NHCs with greater remote steric bulk than ICy, but with an anticipated dihedral preference. Interestingly both NHCs, 1,3-bis(1,2,3,4-tetrahydronaphthalenyl)imidazol-2-ylidene ($\text{ITet}^{R,R}$) and 1,3-bis(cyclododecyl)imidazol-2-ylidene (IDD), were observed to yield the homoleptic, hexasubstituted clusters $[Fe_6S_8(\text{ITet}^{R,R})_6][BF_4]$ and $[Fe_6S_8(\text{IDD})_6][BF_4]$ when added in excess (8 equiv) to **3.1** in THF or MeCN. These clusters were not structurally characterized, but hexasubstitution is evident from their ^{1}H NMR (Figure S3.4 and Figure S3.5). The ^{1}H NMR of phosphine-bound $[Fe_6S_8]^+$ clusters (**3.1**, **3.3**, and **3.4**) had characteristic peaks upfield of –20 ppm corresponding to the ethyl protons of bound PEt_3. Like **3.2**, the ^{1}H NMR spectra of the products of the reactions with $\text{ITet}^{R,R}$ and IDD had no detectable peaks in this region, and so have been proposed to be $[Fe_6S_8(\text{ITet}^{R,R})_6][BF_4]$ and $[Fe_6S_8(\text{IDD})_6][BF_4]$, respectively. Further characterization of $[Fe_6S_8(\text{ITet}^{R,R})_6][BF_4]$ and $[Fe_6S_8(\text{IDD})_6][BF_4]$ was not performed.

We anticipated that ITol would not display a dihedral preference due to the lack of *ortho*-methyl groups and the lack of an *N*-methine. However, we observed no reaction between ITol and **3.1** in THF, MeCN, nor DFB, with or without heating. It is possible that the lack of *ortho*-substituents in ITol allows for the *p*-tolyl rings to adopt a nearly planar arrangement with respect to the imidazolyl ring.[5] This orientation of the *N*-aryl substituents may have prevented substitution due to crowding of the carbenic carbon. That this was not apparently problematic for $[Fe_4S_4]$ clusters (see Chapter 2) was likely the result of the less congested local coordination geometries of the Fe sites in $[Fe_4S_4]$ compared to $[Fe_6S_8]$.

Conclusion

We demonstrated in Chapter 2 that the site-differentiation pattern of cuboidal [Fe_4S_4] clusters could be controlled through simple ligand substitution reactions utilizing bulky NHC ligands. In an extension to octahedral, Chevrel-type clusters in this chapter, we demonstrated that site-differentiated clusters can be obtained in a similar manner and with high stereoselectivity. We showed that IMes was selective for disubstitution with the *trans* isomer as the sole cluster product. That this selectivity was steric in origin (rather than electronic) was supported by the synthesis of homoleptic clusters when smaller NHCs, such as ICy, were employed. We anticipate that this method can be generalized to metalloclusters of nearly any composition and geometry, and that these findings will accelerate the application of metalloclusters in catalysis and materials science.

Experimental details and supplemental information

General Considerations

Unless otherwise noted, all manipulations were performed under an atmosphere of purified N_2 in an LC Technologies model LC-1 glovebox or using standard Schlenk techniques. Glassware was dried in an oven at 160 °C prior to use. Molecular sieves (3 Å) and Celite were activated/dried by heating to 250 °C under vacuum overnight and stored in the glovebox. Filtrations were performed using either fritted glass funnels or pipette filters plugged with oven-dried glass microfiber filter paper. Unless otherwise stated, all reagents and solvents were obtained from commercial suppliers and used as received. $ICyHBF_4$ was purchased from Strem. Benzene, toluene, pentane, Et_2O, acetonitrile, and DCM were degassed by sparging with Ar and dried by passing through columns packed with alumina and Q5.[6] THF was dried/deoxygenated over Na benzophenone ketyl and distilled under N_2. *Ortho*-difluorobenzene was distilled from CaH_2. C_6D_6, DCM-d_2, and CD_3CN were degassed by three freeze-pump-thaw cycles. All solvents were stored over activated 3 Å molecular sieves in the glovebox for at least 12 h prior to use. ITol,[5] IMes,[7,8] $\text{ITet}^{R,R}$,[9] and IDD[10] were prepared according to literature procedures. Abbreviations: *ortho*-difluorobenzene (DFB); sodium hexamethyldisilazide (NaHMDS); *N*-heterocyclic carbene (NHC); room temperature (RT).

Spectroscopy and other characterization techniques

^{1}H, ^{13}C, ^{31}P, and ^{19}F NMR spectra were collected on Bruker Avance 400 MHz or Neo 500 MHz spectrometers. Chemical shifts are reported relative to tetramethylsilane using residual solvent as an internal standard. Solvent suppression for NMR in protonated solvents was carried out using WET solvent suppression.[11] UV/visible spectra were recorded on a Cary 50 spectrophotometer. FT-IR spectra were recorded in the glovebox as powders or thin films prepared by evaporation of DCM solutions using a Bruker Alpha Platinum attenuated total reflection (ATR) spectrometer operating at 2 cm^{-1} resolution. Elemental analysis was performed by Midwest Microlab (Indianapolis, IN).

X-ray crystallography

X-ray structure determinations were performed at the MIT X-ray Diffraction Facility using a Bruker D8 Venture diffractometer equipped with a Photon2 CPAD detector, employing Mo K_α radiation (λ = 0.71073 Å) at 100(2) K and performing ϕ- and ω-scans. Diffraction data were collected, integrated, and corrected for absorption using Bruker APEX3 software and its associated modules (SAINT, SADABS, TWINABS). The structures were solved by direct methods using SHELXT-2015 and refined against F^2 on all data by full-matrix least-squares with SHELXL-2018. Non-hydrogen atoms were refined anisotropically. Hydrogen atoms were included in the model at geometrically calculated positions and refined using a riding model. The isotropic displacement parameters of all hydrogen atoms were fixed to 1.2 times the U value of the atoms they are linked to (1.5 times for methyl groups). Similarity and rigid bond restraints were placed on all atoms. Additional crystallographic data is provided in Table S2.3.

Synthetic procedures

*[$Fe_6S_8(PEt_3)_6$][BF_4] (**3.1**)*

[$Fe_6S_8(PEt_3)_6$][BF_4] was prepared via modification of the procedure reported by Holm and coworkers.[1] PEt_3 (3.10 mL, 21.0 mmol) was added to a stirring slurry of [$Fe(MeCN)_6$][BF_4]$_2$ (2.50 g, 5.25 mmol) in THF (100 mL), resulting in a blood-orange suspension. After 45 min, solid Na_2S_2 (96.6 mg, 0.877 mmol) was added, immediately followed by solid Li_2S (200.4 mg, 4.362 mmol), rapidly resulting in a black mixture. The mixture was stirred at RT overnight. The solution was filtered through Celite, and the solids were washed with THF until the flow-through was colorless. The filtrate was concentrated to dryness *in vacuo*. Following removal of all volatiles, the solids were suspended in THF (30 mL). With stirring, solid S (84.2 mg, 2.63 mmol) was added. The suspension was stirred overnight and then filtered. The solids were washed with additional THF (3 × 2 mL) followed by Et_2O (3 × 3 mL). The product was extracted from the solids with DCM (5 mL), the solution was filtered, and the product was precipitated with excess pentane (15 mL). The solids were washed with dioxane (3 × 4 mL) and dried *in vacuo*. The product was obtained as a black microcrystalline powder (572.0 mg, 46% yield). The ^1H NMR spectrum of the product is in agreement with literature values.[1]

*[$Fe_6S_8(ICy)_6$][BF_4] (**3.2**)*

ICy (67.0 mg, 0.288 mmol) in MeCN (1 mL) was added to a stirring solution of **3.1** (50.0 mg, 0.0360 mmol) in MeCN (2 mL). The product precipitated as a black crystalline solid overnight and was collected via filtration. The solids were washed with MeCN (3 × 3 mL) and Et_2O (3 × 4 mL), then extracted with DCM (5 mL) and the solution was filtered. The product was precipitated from the filtrate with excess pentane (15 mL). Compound **3.2** was isolated as a brown-black crystalline solid following recrystallization from DCM and pentane (66.2 mg, 88% yield). ^1H NMR (DCM, 500 MHz, 293 K): δ (ppm) 2.19 (br), 0.70 (br), −4.63 (br), −11.87 (br). Crystals for structure determination were obtained from diffusion of pentane onto a saturated THF solution of [$Fe_6S_8(ICy)_6$][BPh_4], which was prepared from salt metathesis of **3.2** with $NaBPh_4$ in THF. Anal. Found (Calc.): C, 51.64% (52.16%); H, 7.55% (7.00%); N, 7.66% (8.11%).

$[Fe_6S_8(IMes)(PEt_3)_5][BF_4]$ (**3.3**)

IMes (7.9 mg, 0.026 mmol) in DFB (0.5 mL) was added to a stirring slurry of **3.1** (30.0 mg, 0.0216 mmol) in DFB (1 mL). After 4 h, the solution was filtered through Celite. The product was precipitated with the addition of pentane (10 mL). The resulting black solids were washed with Et_2O (3 × 3 mL), then extracted with DCM (2 mL). The DCM solution was filtered, concentrated to 1 mL, then layered with pentane (5 mL). **3.3** was obtained as a black crystalline solid (24.3 mg, 64%). Crystals for structure determination were obtained from layering a saturated DCM solution with pentane at RT. ^1H NMR (CD_3CN, 500 MHz, 293 K): δ (ppm) 6.50 (br), 0.96 (br), −0.5 (br), −8.75, −9.90, −11.31 (br), −66.86 (br).

$[Fe_6S_8(IMes)_2(PEt_3)_4][BF_4]$ (**3.4**)

IMes (44.0 mg, 0.144 mmol) in THF (0.5 mL) was added to a stirring slurry of **3.1** (50.0 mg, 0.036 mmol) in THF (1 mL). After 15 min, pentane (10 mL) was added, resulting in precipitation of black solids. The solids were washed with pentane (3 x 2 mL), then suspended in THF (1 mL). Additional IMes (44.0 mg, 0.144 mmol) in THF (0.5 mL) was added with stirring. This treatment was repeated a total of three times—until the reaction was complete by ^1H NMR spectroscopy—then the product was washed with Et_2O (3 x 3 mL) and dried *in vacuo*. Compound **3.4** was isolated as a black crystalline solid following recrystallization from THF and pentane (44.5 mg, 78% yield). Crystals for structure determination were obtained from diffusion of Et_2O onto a saturated solution of **3.4** in THF. ^1H NMR (CD_3CN, 500 MHz, 293 K): δ (ppm) 6.23 (s, *m-H*), 0.89 (s, *p*-C*H*$_3$), 0.09 (s, *o*-C*H*$_3$), −7.41 (s, backbone C*H*), −11.34 (s, PEt_3 C*H*$_2$), −62.40 (s, PEt_3 C*H*$_3$). Anal. Found (Calc.): C, 44.98% (45.04%); H, 6.56% (6.19%); N, 3.15% (3.18%).

Spectroscopic data

NMR spectra

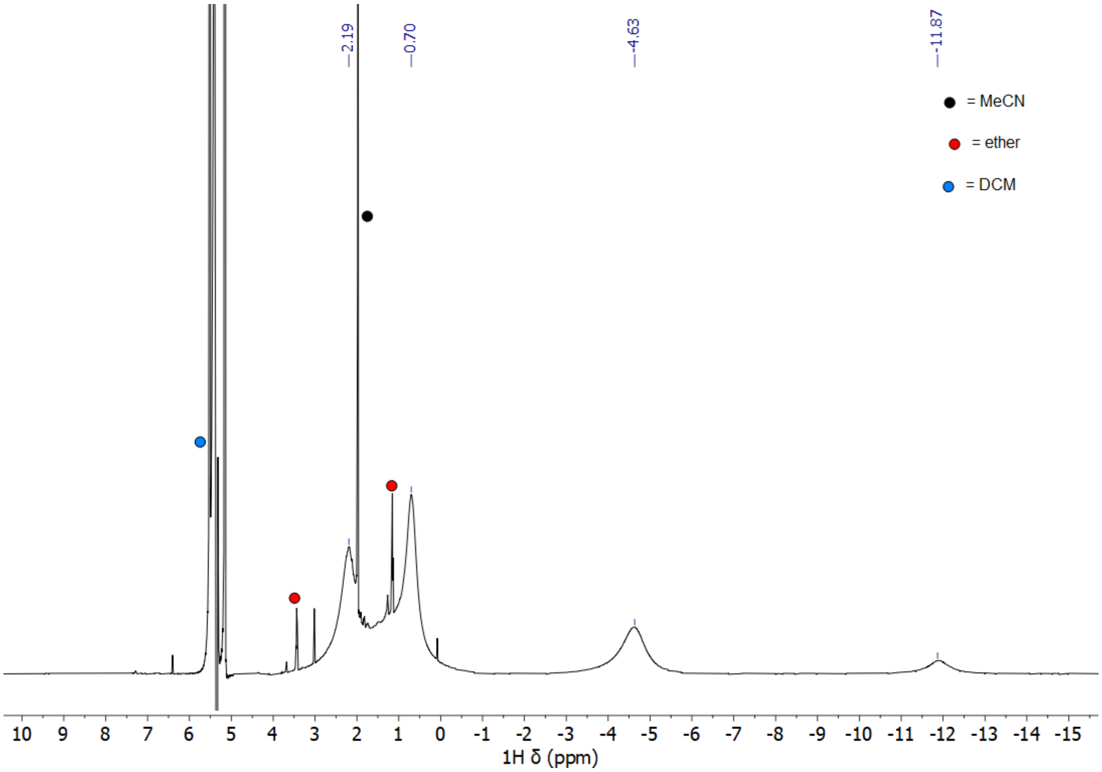

Figure S3.1. Solvent-suppressed ^{1}H NMR spectrum of **3.2** in DCM (500 MHz, 293 K).

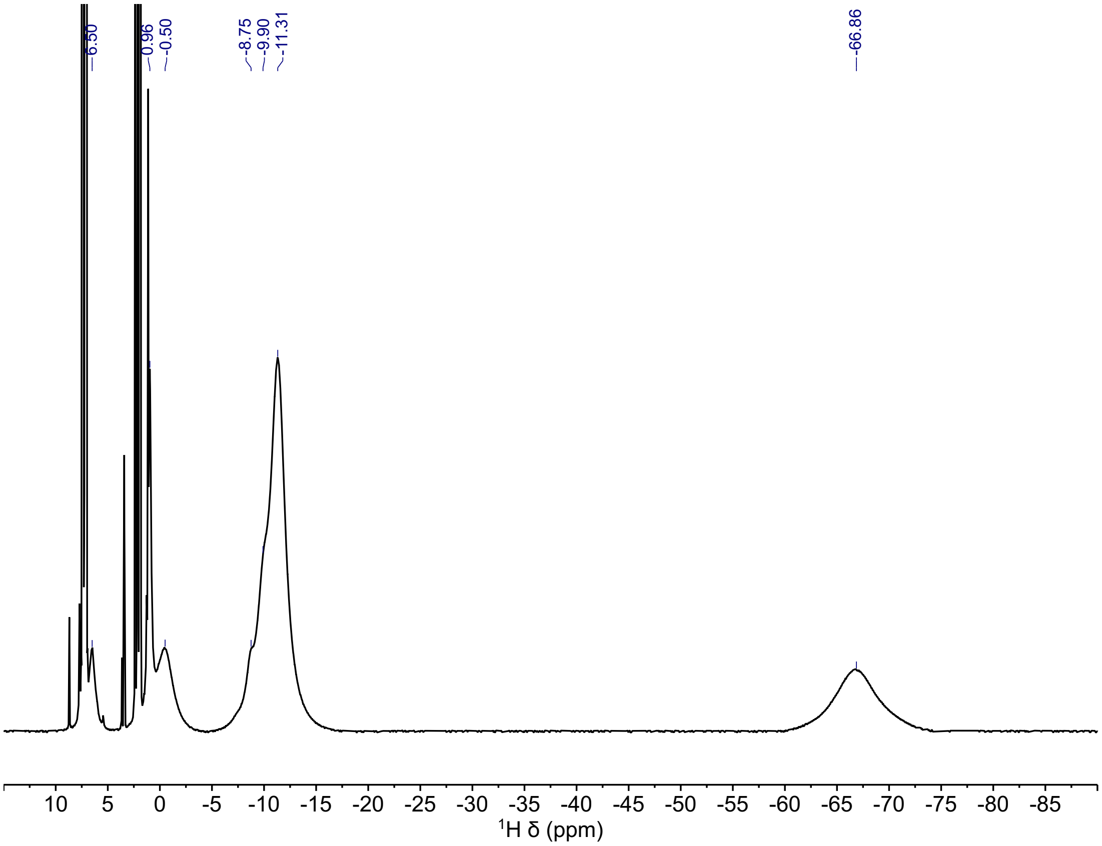

Figure S3.2. ^{1}H NMR spectrum of **3.3** in CD_3CN (500 MHz, 293 K).

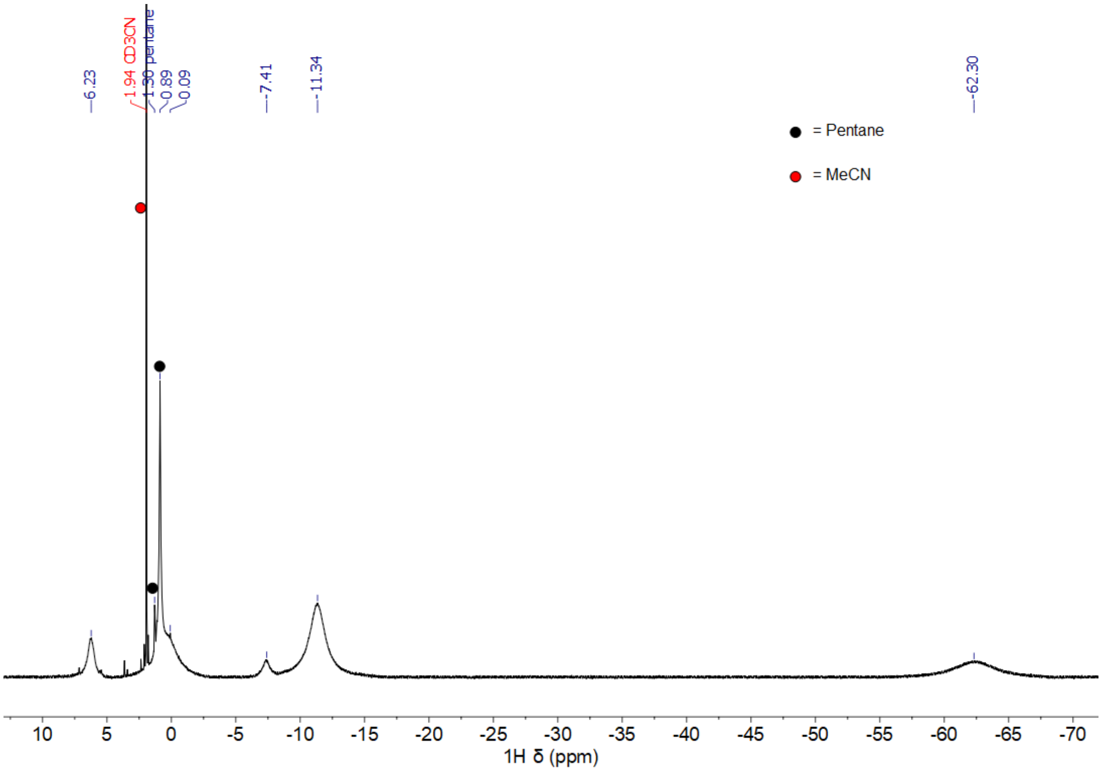

Figure S3.3. ^{1}H NMR spectrum of **3.4** in CD_3CN (500 MHz, 293 K).

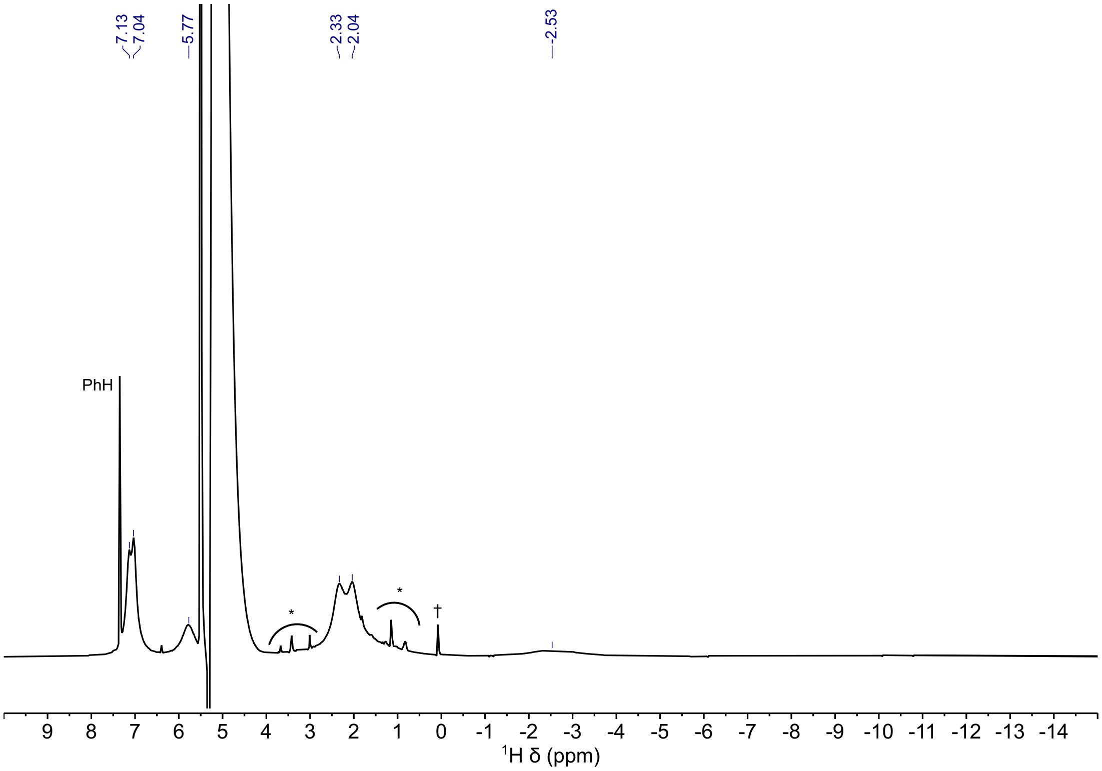

Figure S3.4. Solvent-suppressed ^{1}H NMR spectrum of $[Fe_6S_8(ITet^{R,R})_6][BF_4]$ in DCM indicative of hexasubstitution by the lack of upfield peaks beyond −20 ppm (400 MHz, 293 K; * = residual $ITet^{R,R}$, † = Si grease).

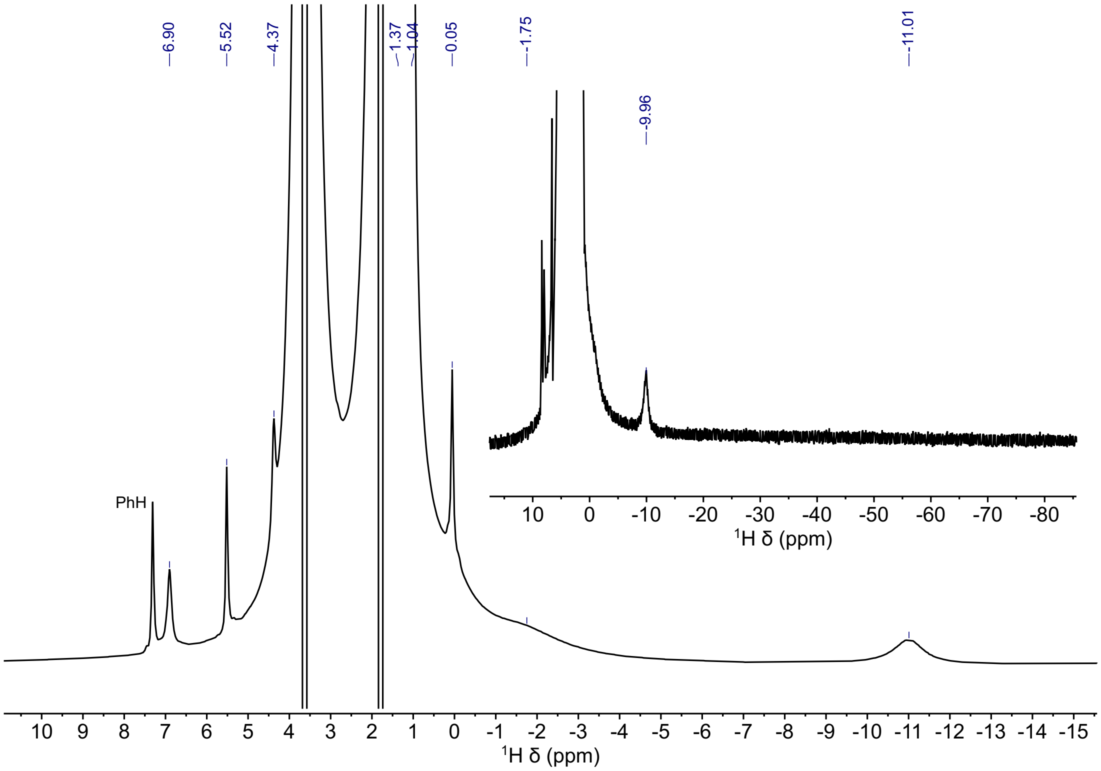

Figure S3.5. Solvent-suppressed ^{1}H NMR of crude reaction mixture of 8 equiv IDD and **3.1** in THF (500 MHz, 293 K). Lack of upfield peaks beyond −20 ppm is indicative of hexasubstitution ($[Fe_6S_8(IDD)_6][BF_4]$).

FT-IR spectra

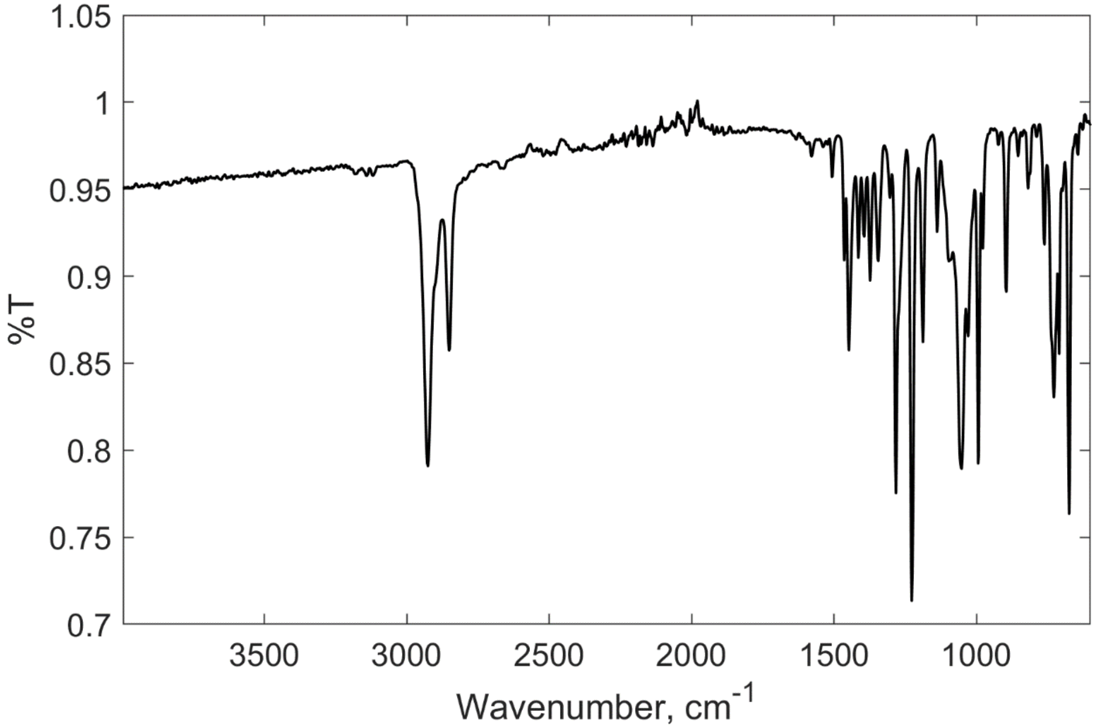

Figure S3.6. Powder FT-IR spectrum of **3.2**.

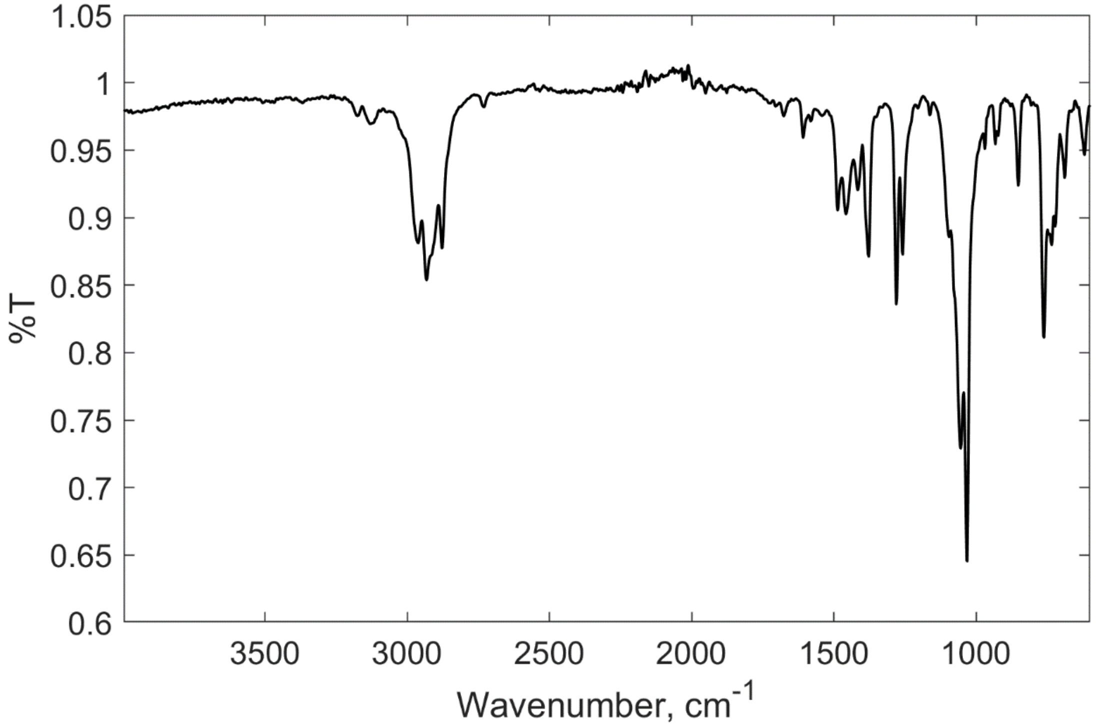

Figure S3.7. Thin film FT-IR spectrum of **3.4**.

UV/vis spectra

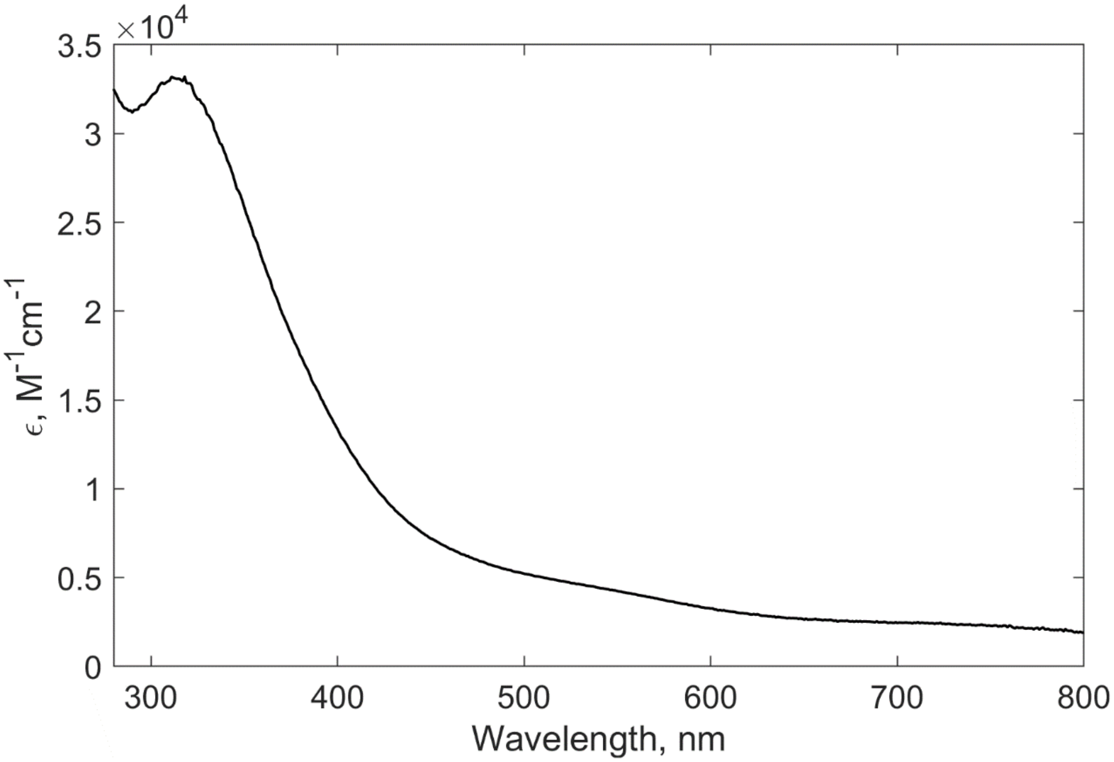

Figure S3.8. UV/vis spectrum of **3.2** (0.05 mM) in DCM.

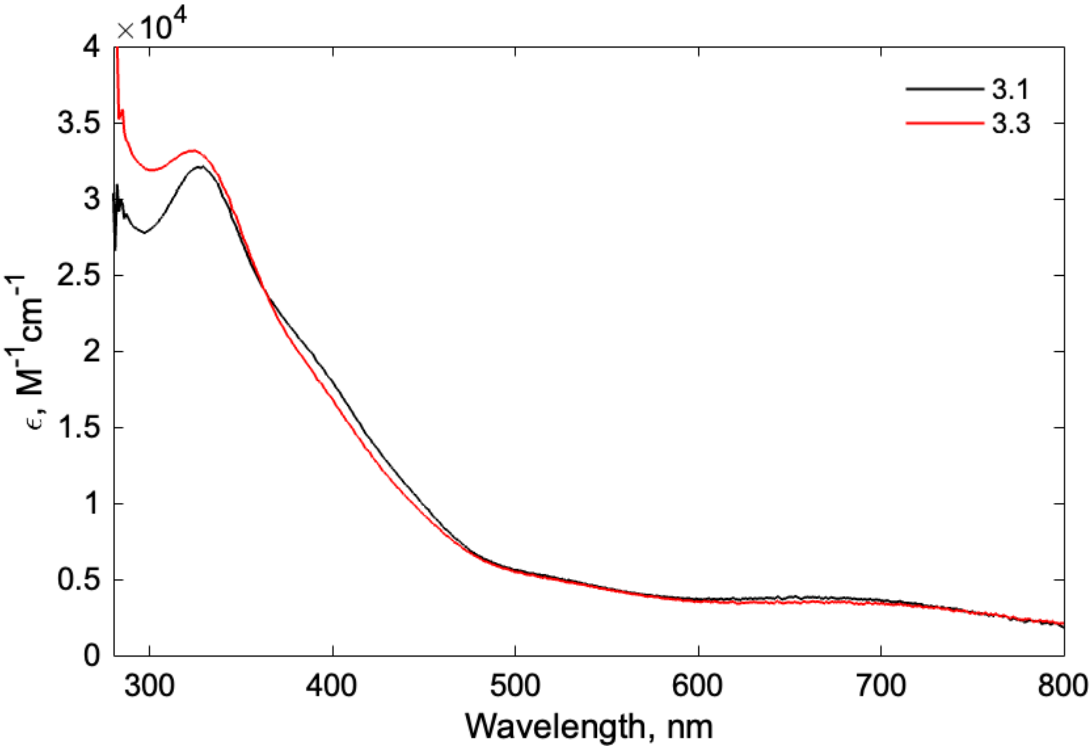

Figure S3.9. UV/vis spectra of **3.1** (black; 20 µM) and **3.3** (red; µM) in ODFB illustrating the small spectral differences between the two compounds.

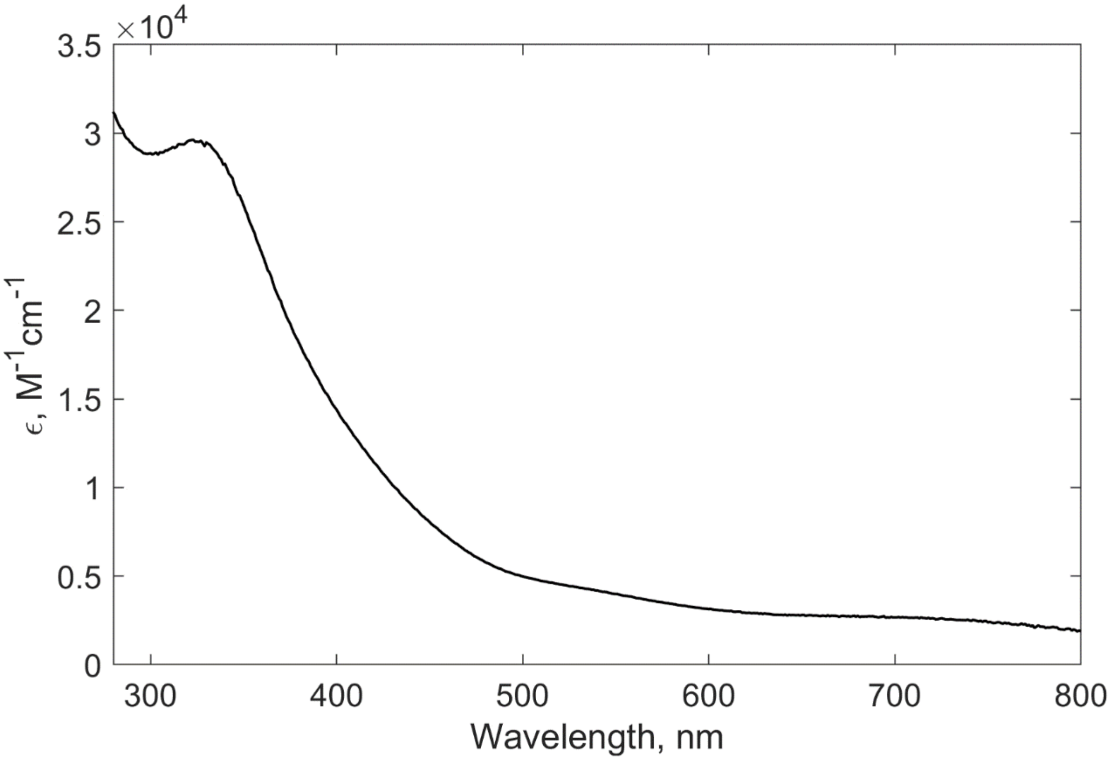

Figure S3.10. UV/vis spectrum of **3.4** (0.05 mM) in MeCN.

X-ray refinement details

*$[Fe_6S_8(ICy)_6][BPh_4]$ (**3.2**):* Crystallizes in the triclinic, centrosymmetric space group *P*−1 with two half-cluster molecules and one BPh_4^- counterion in the asymmetric unit. One of the half cluster molecules shows minor whole molecule disorder in which only the core Fe and S atoms could be found. Refinement of the partial cluster converged to a ratio of 0.98:0.02. Five well-ordered THF solvent molecules were found and independently refined. A sixth THF molecule is disordered over a center of inversion. Reflections with errors >10 esd (perhaps reflecting unresolved twinning or minor whole molecule disorder) were omitted from the final dataset.

*$[Fe_6S_8(IMes)(PEt_3)_5][BF_4]$ (**3.3**):* Crystallizes in the triclinic, centrosymmetric space group *P*−1 with two cluster molecules and two BF_4^- counterions in the asymmetric unit. One PEt_3 ligand is disordered over two positions refined to a ratio of 75:25. Two reflections with errors > 10 esd were omitted from the final dataset.

*$[Fe_6S_8(IMes)_2(PEt_3)_4][BF_4]$ (**3.4**):* Crystallizes in the triclinic, centrosymmetric space group *P*−1 with two half-cluster molecules and a BF_4^- counterion disordered over two positions in the asymmetric unit. Refinement of the two partial BF_4^- counterions converged to a ratio of 0.89:0.11. One half cluster has a PEt_3 ligand disordered via a 180° about the Fe–P bond. One PEt_3 ligand of the other half cluster in the asymmetric unit has one methyl moiety disordered about a slight rotation of the C–P bond.

Table S3.1. Crystallographic data for **3.2** and **3.3**.

	3.2	**3.3**
CCDC deposition number	2214357	
Empirical formula	$C_{136}H_{208}BFe_{6.02}N_{12}O_{5.5}PS_{8.02}$	$C_{51}H_{96.41}BF_4Fe_6N_2P_5S_8$
Color, habit	Black, plate	Black, block
Formula weight	2702.96	1570.94
T [K]	100(2)	100(2)
λ [Å]	0.71073	0.71073
Crystal system	Triclinic	Triclinic
Space group	$P-1$	$P-1$
a [Å]	15.455(8)	12.374(2)
b [Å]	15.819(8)	23.271(5)
c [Å]	29.031(15)	23.748(5)
α [°]	99.017(7)	90
β [°]	101.322(7)	101.038(5)
γ [°]	98.073(7)	90
V [Å^3]	6761(6)	6691(2)
Z	2	4
d_{calc} [g cm^{-1}]	1.328	1.560
Radiation type	Mo K_α	Mo K_α
μ [mm^{-1}]	0.810	1.683
$F(000)$	2883	3266
Crystal size [mm^3]	0.305 × 0.260 × 0.060	0.400 × 0.350 × 0.100
θ range for data collection [°]	0.729–28.348	0.876–32.154
Miller index ranges	$-20 \leq h \leq 20$	$-18 \leq h \leq 18$
	$-21 \leq k \leq 21$	$-34 \leq k \leq 34$
	$-38 \leq l \leq 38$	$-35 \leq l \leq 35$
Reflections collected	227044	357131
Independent reflections	33551 (R_{int} = 0.0972)	45276 (R_{int} = 0.0884)
Completeness to θ = 25.242° [%]	99.6	95.0
Absorption correction	Semi-empirical from equivalents	Semi-empirical from equivalents
Refinement method	Full-matrix least-squares on F^2	Full-matrix least-squares on F^2
Data / restraints / parameters	33551 / 2577 / 1624	45276 / 2290 / 1458
Goodness-of-fit on F^2	1.098	1.027
Final R indices ($I > 2\sigma(I)$)	$R_1 = 0.0739$, $wR_2 = 0.2151$	$R_1 = 0.0523$, $wR_2 = 0.1307$
R indices (all data)	$R_1 = 0.1192$, $wR_2 = 0.2481$	$R_1 = 0.0745$, $wR_2 = 0.1385$
$\Delta\rho_{max}$, $\Delta\rho_{min}$ [e Å^{-3}]	1.433, −0.979	2.998, −1.750

Table S3.2. Crystallographic data for **3.4**.

	3.4
CCDC deposition number	2214358
Empirical formula	$C_{66}H_{108}BF_4Fe_6N_4P_4S_8$
Color, habit	Black, block
Formula weight	1759.83
T [K]	100(2)
λ [Å]	0.71073
Crystal system	Triclinic
Space group	$P-1$
a [Å]	13.0760(5)
b [Å]	14.7624(6)
c [Å]	23.0584(9)
α [°]	76.054(2)
β [°]	86.607(2)
γ [°]	64.7520(10)
V [Å^3]	3902.3(3)
Z	2
d_{calc} [g cm^{-1}]	1.498
Radiation type	Mo K_α
μ [mm^{-1}]	1.433
$F(000)$	1834
Crystal size [mm^3]	0.350 × 0.300 × 0.250
θ range for data collection [°]	1.571–31.591
Miller index ranges	$-19 \leq h \leq 19$ $-21 \leq k \leq 21$ $-33 \leq l \leq 33$
Reflections collected	254576
Independent reflections	26118 (R_{int} = 0.0383)
Completeness to θ = 25.242° [%]	100.0
Absorption correction	Semi-empirical from equivalents
Refinement method	Full-matrix least-squares on F^2
Data / restraints / parameters	26118 / 1407 / 957
Goodness-of-fit on F^2	1.001
Final R indices ($I > 2\sigma(I)$)	$R_1 = 0.0351$, $wR_2 = 0.0872$
R indices (all data)	$R_1 = 0.0496$, $wR_2 = 0.0972$
$\Delta\rho_{\text{max}}$, $\Delta\rho_{\text{min}}$ [e Å^{-3}]	1.439, −0.847

References

(1) Goddard, C. A.; Long, J. R.; Holm, R. H. Synthesis and Characterization of Four Consecutive Members of the Five-Member $[Fe_6S_8(PEt_3)_6]^{n+}$ (n = 0−4) Cluster Electron Transfer Series. *Inorg. Chem.* **1996**, *35* (15), 4347–4354.

(2) Huang, J.; Schanz, H. J.; Stevens, E. D.; Nolan, S. P. Stereoelectronic Effects Characterizing Nucleophilic Carbene Ligands Bound to the Cp*RuCl (Cp* = η^5-C_5Me_5) Moiety: A Structural and Thermochemical Investigation. *Organometallics* **1999**, *18* (12), 2370–2375.

(3) Nelson, D. J.; Nolan, S. P. Quantifying and Understanding the Electronic Properties of *N*-Heterocyclic Carbenes. *Chem Soc Rev* **2013**, *42*, 6723.

(4) Durham, J. L.; Wilson, W. B.; Huh, D. N.; Mcdonald, R.; Szczepura, L. F. Organometallic Rhenium(III) Chalcogenide Clusters: Coordination of *N*-Heterocyclic Carbenes. *Chem. Commun.* **2015**, *51* (52), 10536–10538.

(5) Arduengo, A. J.; Dias, H. V. R.; Harlow, R. L.; Kline, M. Electronic Stabilization of Nucleophilic Carbenes. *J. Am. Chem. Soc.* **1992**, *114* (14), 5530–5534.

(6) Pangborn, A. B.; Giardello, M. A.; Grubbs, R. H.; Rosen, R. K.; Timmers, F. J. Safe and Convenient Procedure for Solvent Purification. *Organometallics* **1996**, *15* (5), 1518–1520.

(7) Hintermann, L. Expedient Syntheses of the *N*-Heterocyclic Carbene Precursor Imidazolium Salts IPrHCl, IMesHCl and IXyHCl. *Beilstein J. Org. Chem.* **2007**, *3*, 22.

(8) Bantreil, X.; Nolan, S. P. Synthesis of *N*-Heterocyclic Carbene Ligands and Derived Ruthenium Olefin Metathesis Catalysts. *Nat. Protoc.* **2011**, *6* (1), 69–77.

(9) Wang, M.; Pu, X.; Zhao, Y.; Wang, P.; Li, Z.; Zhu, C.; Shi, Z. Enantioselective Copper-Catalyzed Defluoroalkylation Using Arylboronate-Activated Alkyl Grignard Reagents. *J. Am. Chem. Soc.* **2018**, *140* (29), 9061–9065.

(10) de Frémont, P.; Scott, N. M.; Stevens, E. D.; Ramnial, T.; Lightbody, O. C.; Macdonald, C. L. B.; Clyburne, J. A. C.; Abernethy, C. D.; Nolan, S. P. Synthesis of Well-Defined *N*-Heterocyclic Carbene Silver(I) Complexes. *Organometallics* **2005**, *24* (26), 6301–6309.

(11) Smallcombe, S. H.; Patt, S. L.; Keifer, P. A. WET Solvent Suppression and Its Applications to LC NMR and High-Resolution NMR Spectroscopy. *J. Magn. Reson. A* **1995**, *117* (2), 295–303.

Chapter 4

Metal-metal cooperativity in iron/cobalt–sulfur clusters

The biosynthesis of Fe–S clusters is carefully regulated and results in clusters that contain Fe as their only metal.[1,2] However, some clusters undergo further biosynthetic manipulation, including substitution of an Fe center with a different metal (Figure 4.1).[3–14] For example, the nitrogenase catalytic cofactors (FeMo-co, FeV-co, and FeFe-co, for the Mo, V, and Fe-only nitrogenases, respectively)[3–8] are derived from an all-Fe precursor, the L-cluster, which is itself derived from two [Fe_4S_4] clusters.[15,16] Dedicated maturases exist for removing one of the terminal Fe centers of the L-cluster and inserting Mo or V, ultimately producing FeMo-co or FeV-co, respectively. Likewise, the active site of the NiFe carbon monoxide dehydrogenase (CODH) is first assembled from an Fe-only Fe–S cluster, followed by Ni ion insertion.[17,18]

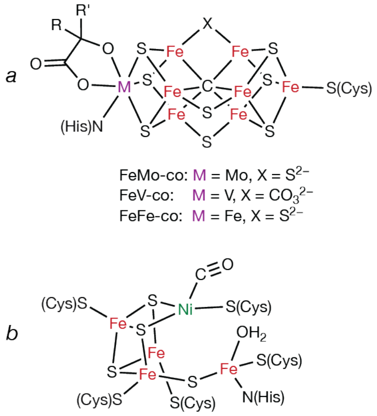

Figure 4.1. (*a*) FeM-co cofactors of the nitrogenase enzymes (R, $–CH_2CO_2^-$; R', $–(CH_2)_2CO_2^-$), and (*b*) CO-bound CO dehydrogenase C-cluster exemplifying heterometallic metalloclusters in biology.

Although the reason(s) for 'heterometal' ion incorporation are often poorly understood, it is clear that the heterometals have dramatic effects on catalysis. The activity and substrate selectivity vary dramatically among the three nitrogenase isozymes, and in the NiFe CODH mechanism, the Ni center plays a direct role in binding the C atom from CO_2 or CO in the redox interconversion of CO_2 and CO.[12,19–21] Similarly, metal atom substitution commonly results in improved performances or properties of heterometallic materials relevant to metallurgy or heterogeneous catalysis.[22–26] Mn-doped CoO_x and Fe-doped NiO_x oxygen evolution catalysts frequently outperform the undoped materials.[24,25,27] However, as for the biogenic heterometallic clusters, it is challenging to assess the role these heterometals play in the properties of these cofactors. For example, homometallic Fe–S clusters typically are not thought to have M–M bonds, but this may not be the case for Fe–S clusters containing early transition-metals.[28] Unlike Mo, V, and W, post-Fe transition-metals, such as Ni, possess more contracted orbitals. It is unclear whether the contracted M–S bonds shorten the intermetallic distances sufficiently to also invoke M–Fe bonding in these clusters.

Atomically precise, synthetic heterometallic clusters are well suited for systematic studies of the relationship between core metal atom composition and cluster properties.[29–41] Central to such studies are methods for the selective synthesis of heterometallic clusters. One challenge in this regard is that the high symmetry of polyhedral metalloclusters makes it difficult to control the number of heterometals and their relative positions within the cluster cores. In some cases, atomically precise heterometallic clusters may be obtained from self-assembly reactions, however, systematic variation of the cluster composition is difficult in this strategy due to the ill-defined nature of many cluster assembly reactions.[42–50]

Strategies involving the manipulation of preformed clusters are potentially more generalizable. One approach entails the excision of a metal from the cluster to generate a voided cluster with an open metal binding site. This approach has been demonstrated in biological Fe–S clusters through oxidative degradation of a [Fe_4S_4] cluster to [Fe_3S_4], followed by heterometal reconstitution.[51–54] Previously, extensions of this strategy to synthetic clusters have utilized supporting ligands that mimic the (*pseudo*) 3:1 site-differentiation pattern of those protein environments and stabilize the voided cluster (to avoid decomposition pathways[55]). Notably, Holm demonstrated that a single Fe center could be excised from [$Fe_4S_4(LS_3)Cl$] (LS_3 = 1,3,5-tris((4,6-dimethyl-3-mercaptophenyl)thio)-2,4,6-tris(*p*-tolylthio)benzene(3–)) by treatment with a chelator.[56,57] The resulting [Fe_3S_4] cluster could then be reconstituted with a variety of heterometals.[55,56,58,59]

We recently demonstrated that treating the 3:1 site-differentiated cluster [$Fe_4S_4(IMes)_3Cl$] (IMes = 1,3-dimesitylimidazol-2-ylidene) with excess chelator produced the stable voided cluster, [$Fe_3S_4(IMes)_3$].[60] We hypothesized that our [Fe_3S_4] cluster could be reconstituted with other transition-metals to yield site-differentiated heterobimetallic [MFe_3S_4] clusters. Compared to the trithiolate ligand platform, LS_3, employed by Holm, the three IMes ligands in [$MFe_3S_4(IMes)_3$] clusters provide additional steric protection and reduce the molecular charge,[61] enabling greater synthetic versatility.

In this chapter, we sought to outline the underlying factors of heterometal substitution that impact the electronic structure and charge distribution within the clusters and how that may relate to their biologically relevant reactivity. As such, we targeted Co substituted analogs of our recently reported [$Fe_4S_4(IMes)_3(CO)$] (Figure 4.2).[62] Here we extended the site-differentiation methodology our lab developed for [Fe_4S_4] clusters to [Co_4S_4] clusters to gain access to all four metal substitution patterns within 3:1 symmetry (Figure 4.2).[61,63]. Specifically, our approach employs bulky IMes ligands to chemically differentiated the cluster subsites for site-selective metal excision and reconstitution from [$Fe_4S_4(IMes)_3Cl$] and [$Co_4S_4(IMes)_3Cl$]. The impact of heterometal substitution on the properties of the clusters, in particular the carbonyl adducts, with respect to the homometallic variants is discussed.

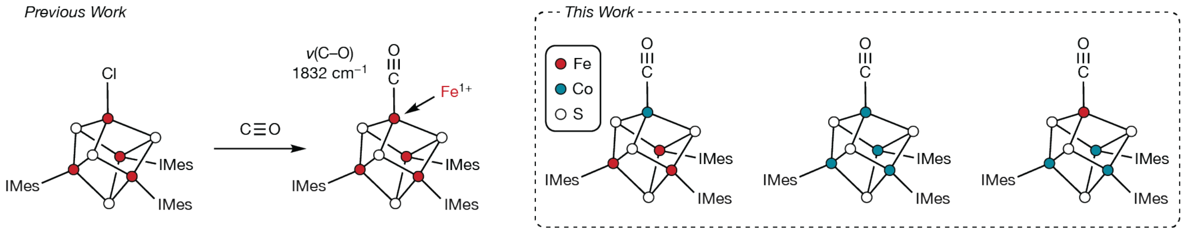

Figure 4.2. (*left*) Previous work from our lab demonstrating intracluster redox disproportionation to access monovalent Fe upon binding CO. (*right*) This work targets heterobimetallic Fe and Co clusters to investigate the role of cluster composition and metal atom substitution on cluster properties.

Synthesis of Fe/Co–S clusters

Recently, our lab demonstrated that the unique Fe-site of the site-differentiated cluster $[Fe_4S_4(IMes)_3Cl]^+$ could be selectively excised by reaction with potassium hydrotris(1-pyrazolyl)borate (KTp) to yield the voided cubane $[Fe_3S_4(IMes)_3]$ through the intermediacy of the unstable K-substituted cluster $[KFe_3S_4(IMes)_3][PF_6]$.[60] Because of the poor stability of $[KFe_3S_4(IMes)_3][PF_6]$ with respect to loss of KPF_6, we targeted the thallium-substituted analogue, $[TlFe_3S_4(IMes)_3][PF_6]$, which we anticipated would display greater stability owing to the favorable interactions between the soft Tl and soft S ions.

Addition of a slight excess of TlTp to $[Fe_4S_4(IMes)_3Cl][PF_6]$ gave $[TlFe_3S_4(IMes)_3][PF_6]$ and 1 equiv Tp_2Fe, indicated by the ^1H NMR spectrum of the crude reaction mixture. The identity of $[TlFe_3S_4(IMes)_3][PF_6]$ was confirmed by single crystal XRD and ^1H NMR spectroscopy (Figure 4.3b and Figure S4.1). The Tl^{1+} ion occupied the unique site with nearly identical Tl–S bonds to each of the three bridging S ligands (2.868(1) Å on average). Long Tl–arene distances (4.757(3) Å at the shortest) indicated little to no bonding to the mesityl π-system. Compared to $[KFe_3S_4(IMes)_3]^+$, the average Fe–(μ_2-S) distances of the $[Fe_3S_4(IMes)_3]$ fragment of $[TlFe_3S_4(IMes)_3]^+$ were elongated (2.260(2) Å vs 2.237(1) Å), likely the result of greater covalency of the Tl–S bonds.

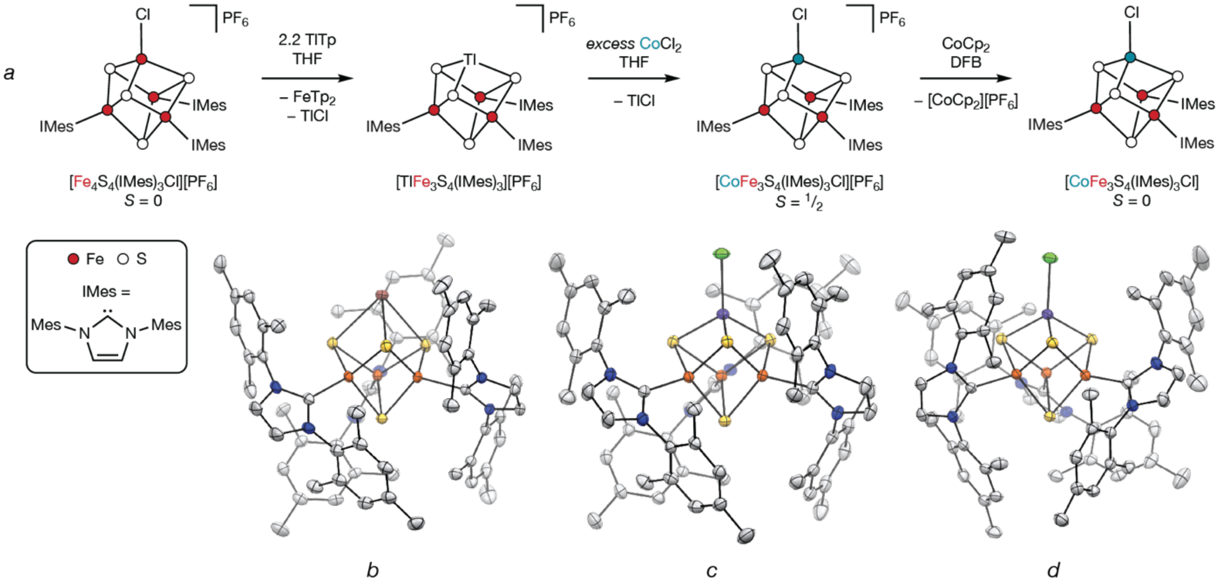

Figure 4.3. (*a*) Synthesis of $[Fe_4S_4(IMes)_3Cl][PF_6]$, $[TlFe_3S_4(IMes)_3][PF_6]$, $[CoFe_3S_4(IMes)_3Cl][PF_6]$, and $[CoFe_3S_4(IMes)_3Cl]$. Abbreviations: Tp, hydrotris(1-pyrazolyl)borate; Mes, 2,4,6-trimethylphenyl. (*b*–*d*) Thermal ellipsoid plots (50%) of $[TlFe_3S_4(IMes)_3][BAr^F_4]$, $[CoFe_3S_4(IMes)_3Cl][BAr^F_4]$, and $[CoFe_3S_4(IMes)_3Cl]$, respectively. Hydrogen atoms, counter ions, and solvent molecules omitted for clarity. Color scheme: Fe (red-orange), Co (purple), S (yellow), Tl (brown), Cl (green), N (blue), C (grey). Abbreviations: BAr^F_4, tetrakis(3,5-bis(trifluoromethyl)phenyl)borate.

Addition of $CoCl_2$ as a slurry in THF to a solution of $[TlFe_3S_4(IMes)_3][PF_6]$ quickly produced $[CoFe_3S_4(IMes)_3Cl][PF_6]$, as indicated by a color change from brown-black to green-black, and solid TlCl (Figure 4.3). The identity of $[CoFe_3S_4(IMes)_3Cl][PF_6]$ was confirmed by single crystal XRD (Figure 4.3c). The ^1H NMR spectrum of $[CoFe_3S_4(IMes)_3Cl][PF_6]$ showed a single, highly

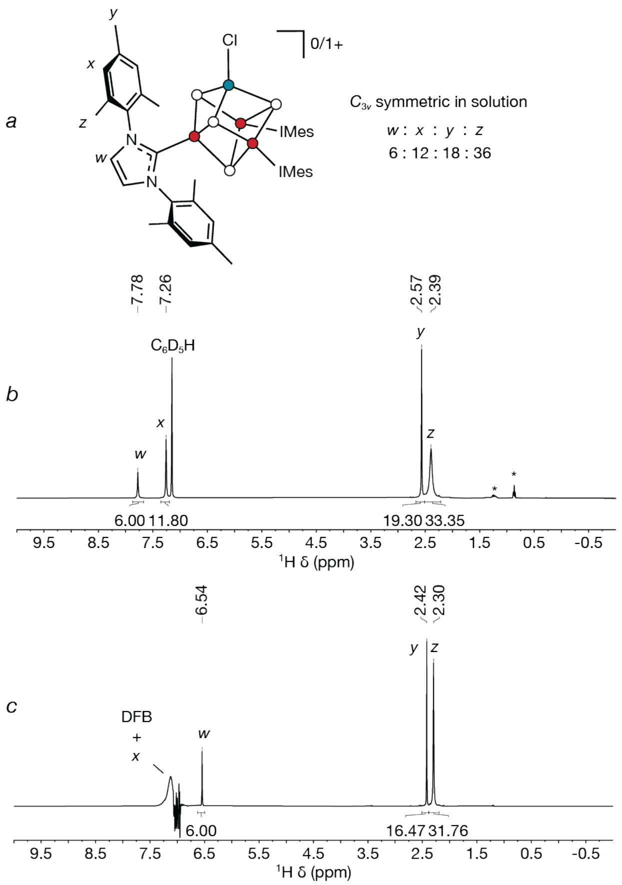

Figure 4.4. (*a*) ^{1}H NMR peak assignment key. (*b*) ^{1}H NMR spectrum of $[CoFe_3S_4(IMes)_3Cl]$ in C_6D_6 (298 K, 400 MHz; * = pentane). (*c*) Solvent-suppressed ^{1}H NMR spectrum of $[CoFe_3S_4(IMes)_3Cl][PF_6]$ in DFB (298 K, 500 MHz).

symmetric species. The solution C_{3v} symmetry of the compound was evidence that there was no scrambling between the Fe and Co ions (Figure 4.4). Additionally, re-refinement of the XRD dataset with Fe in place of Co or Co in place of any of the three Fe sites resulted in poorer refinement statistics. Reduction of $[CoFe_3S_4(IMes)_3Cl][PF_6]$ with cobaltocene ($CoCp_2$) quantitatively provided $[CoFe_3S_4(IMes)_3Cl]$, isolated as a green-black microcrystalline solid (Figure 4.3). Single crystal XRD and ^{1}H NMR of $[CoFe_3S_4(IMes)_3Cl]$ (Figure 4.3d and Figure 4.4) indicated that the Co remained in the unique metal site, again with no metal ion scrambling. The ground spin states of $[CoFe_3S_4(IMes)_3Cl]$ (S = ½) and $[CoFe_3S_4(IMes)_3Cl]^+$ (S = 0) were established by SQUID magnetometry (Figure S4.13 and Figure S4.14).

Due to the instability of the all-ferrous $[Fe_4S_4]$ clusters, Holm and coworkers targeted $[Co_4S_4(P^iPr_3)_4]$ and $[Co_4S_4(I^iPr^{Me})_4]$ (I^iPr^{Me} = 1,3-diisopropyl-4,5-dimethylimidazol-2-ylidene).[64] It was concluded that high-spin Co^{2+} ions of these clusters were coupled via an identical scheme hypothesized for $[Fe_4S_4(P^iPr_3)_4]$ and $[Fe_4S_4(I^iPr^{Me})_4]$. Recently, the $[Co_4S_4]$ core was investigated by Bejger and coworkers as a component for redox active organometallic polymers.[65] To the best of our knowledge, no site-differentiated $[Co_4S_4]$ clusters have been reported previously.

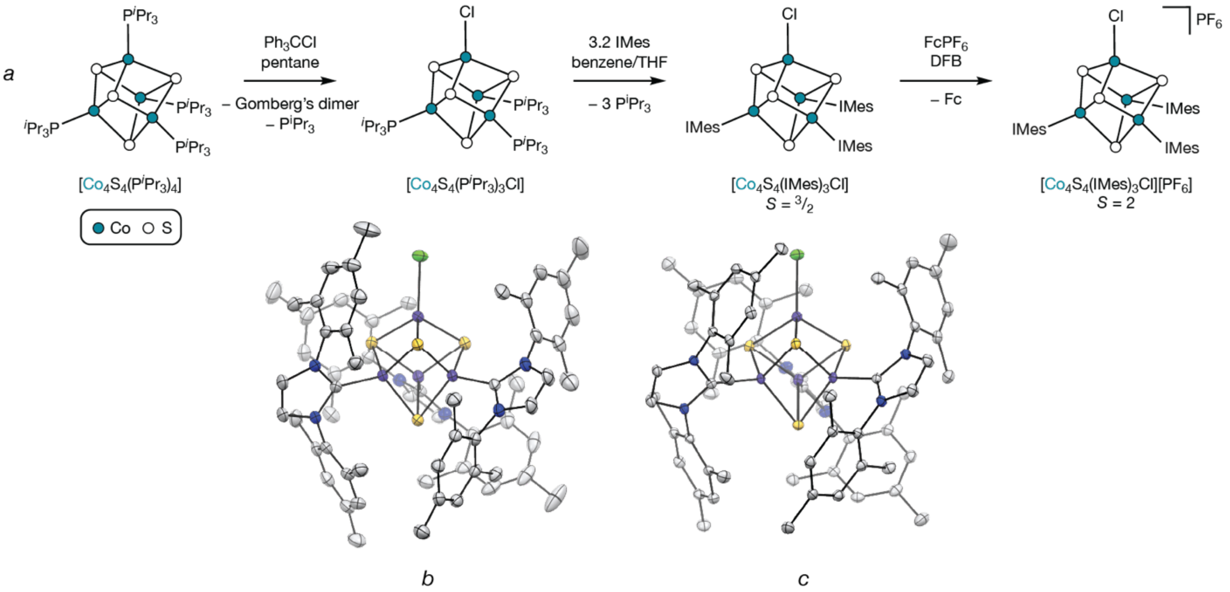

Figure 4.5. (*a*) Synthesis of $[Co_4S_4(IMes)_3Cl]$ and $[Co_4S_4(IMes)_3Cl][PF_6]$. (*b, c*) Thermal ellipsoid plots (50%) of $[Co_4S_4(IMes)_3Cl]$ and $[Co_4S_4(IMes)_3Cl][PF_6]$, respectively. Hydrogen atoms, counter ions, and solvent molecules omitted for clarity. Color scheme: Co (purple), S (yellow), Cl (green), N (blue), C (grey).

We found that treatment of $[Co_4S_4(P^iPr_3)_4]$ with trityl chloride (Ph_3CCl) in pentane gave the one-electron oxidized, site-differentiated cluster $[Co_4S_4(P^iPr_3)_3Cl]$ as a brown-black solution in pentane (Figure 4.5). Addition of excess IMes in benzene selectively produced $[Co_4S_4(IMes)_3Cl]$. $[Co_4S_4(IMes)_3Cl]$ was isolated as a brown-black microcrystalline solid and had a $S = 3/2$ ground spin state as established by SQUID magnetometry (Figure S4.15). Oxidation of $[Co_4S_4(IMes)_3Cl]$ with $FcPF_6$ quantitatively yielded $[Co_4S_4(IMes)_3Cl][PF_6]$ as a black microcrystalline solid. $[Co_4S_4(IMes)_3Cl]^+$ had a $S = 2$ ground spin state as established by SQUID magnetometry (Figure S4.16).

We hypothesized that the analogous $[FeCo_3S_4(IMes)_3Cl]$ cluster could be accessed via heterometal substitution (Figure 4.6). Upon addition of a slight excess (2.2 equiv) of TlTp to $[Co_4S_4(IMes)_3Cl][PF_6]$ in THF, TlCl precipitated as a colorless solid. ^1H NMR of the crude filtered solution showed a new cluster species with resonances tentatively assigned as bound Tp (Figure S4.6), little to no $CoTp_2$, as well as approximately 1.2 equiv of TlTp. This new species was likely $[Co_4S_4(IMes)_3Tp][PF_6]$. Concentration of this solution to dryness *in vacuo*, followed by addition of Et_2O resulted in further reaction, indicated by the formation of a yellow-brown, Et_2O-soluble mixture confirmed to contain $CoTp_2$ by ^1H NMR. After washing with additional Et_2O, the remaining Et_2O-insoluble, black solids were collected, and a new ^1H NMR spectrum was obtained (Figure S4.7). The product, $[TlCo_3S_4(IMes)_3][PF_6]$, was crystallized from DFB with Et_2O (Figure 4.6b). Unlike $[TlFe_3S_4(IMes)_3]^+$, the solid-state structure of $[TlCo_3S_4(IMes)_3]^+$ displayed highly asymmetric Tl–S distances (2.525(5) Å, 3.376(4) Å, and 3.029(1) Å) likely reflecting reduced donicity of the S ligands to Tl due to the greater electronegativity of Co with respect to Fe. Perhaps a result of the poorer donor strength of the S ligands, the Tl–arene distances (3.266(9) Å, 3.582(4) Å, and 3.66(2) Å) were notably contracted with respect to $[TlFe_3S_4(IMes)_3]^+$.

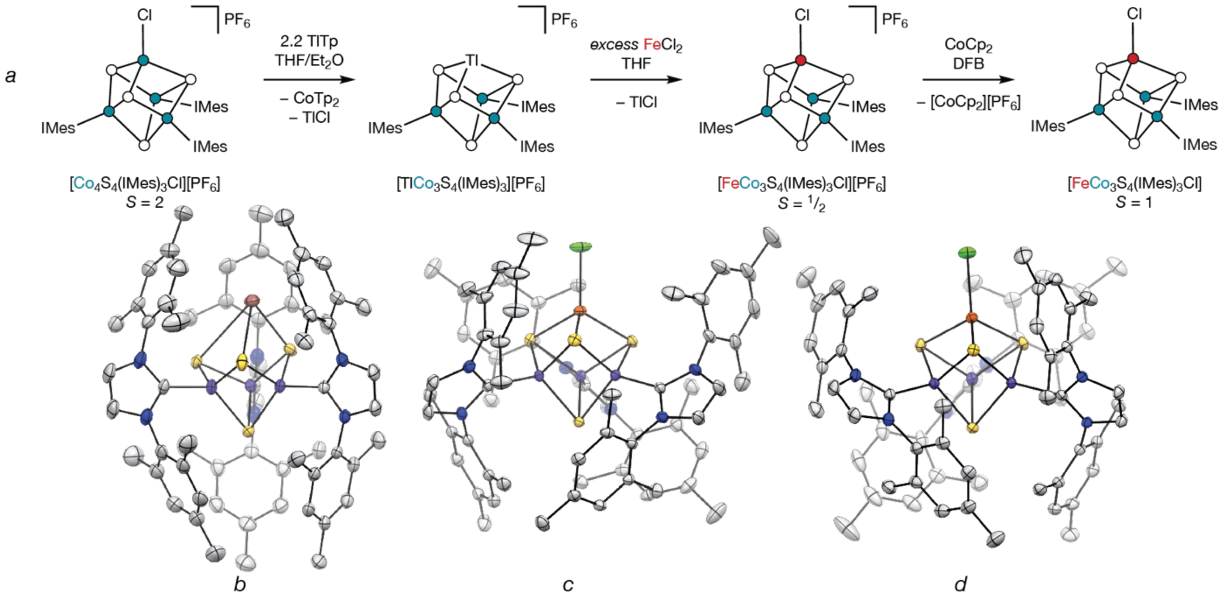

Figure 4.6. (*a*) Synthesis of $[Co_4S_4(IMes)_3Cl][PF_6]$, $[TlCo_3S_4(IMes)_3][PF_6]$, $[FeCo_3S_4(IMes)_3Cl][PF_6]$, and $[FeCo_3S_4(IMes)_3Cl]$. (*b–d*) Thermal ellipsoid plots (50%) of $[TlCo_3S_4(IMes)_3][PF_6]$, $[FeCo_3S_4(IMes)_3Cl][PF_6]$, and $[FeCo_3S_4(IMes)_3Cl]$, respectively. Hydrogen atoms, counter ions, and solvent molecules omitted for clarity. Color scheme: Fe (red-orange), Co (purple), S (yellow), Tl (brown), Cl (green), N (blue), C (grey).

$[FeCo_3S_4(IMes)_3Cl][PF_6]$ was obtained following a similar procedure for $[CoFe_3S_4(IMes)_3Cl][PF_6]$: excess $FeCl_2$ and $[TlCo_3S_4(IMes)_3][PF_6]$ were combined in THF to yield $[FeCo_3S_4(IMes)_3Cl][PF_6]$, indicated by a color change from green-black to brown-black, and precipitation of solid TlCl (Figure 4.6). Reduction of $[FeCo_3S_4(IMes)_3Cl][PF_6]$ with $CoCp_2$ gave $[FeCo_3S_4(IMes)_3Cl]$. The C_{3v} symmetry revealed in the ^1H NMR spectra of $[FeCo_3S_4(IMes)_3Cl][PF_6]$ and $[FeCo_3S_4(IMes)_3Cl]$ confirmed that no scrambling of Co and Fe had occurred (Figure 4.7). The ground spin states of $[FeCo_3S_4(IMes)_3Cl]^+$ ($S = ½$) and $[FeCo_3S_4(IMes)_3Cl]$ ($S = 1$) were established by SQUID magnetometry (Figure S4.17 and Figure S4.18).

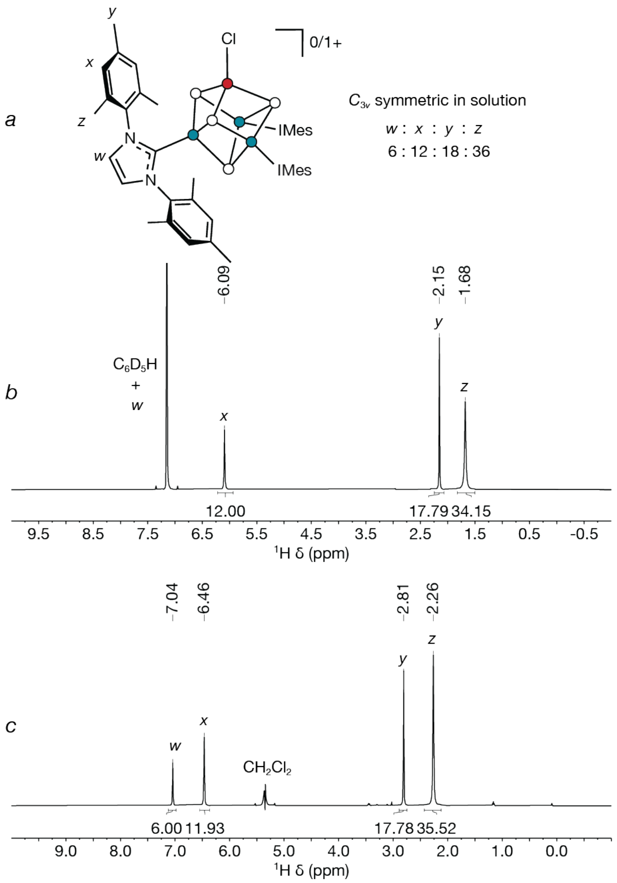

Figure 4.7. (*a*) ^{1}H NMR peak assignment key. (*b*) ^{1}H NMR spectrum of [$FeCo_3S_4(IMes)_3Cl$] in C_6D_6 (298 K, 400 MHz). (*c*) Solvent-suppressed ^{1}H NMR spectrum of [$FeCo_3S_4(IMes)_3Cl$][PF_6] in CH_2Cl_2 (298 K, 500 MHz).

Evidence for low-valent Fe and Co in CO-bound clusters

As previously discussed, the low C–O stretching frequency observed for [$Fe_4S_4(IMes)_3(CO)$] (ν(C–O) = 1832 cm^{-1}) is incompatible with the canonical formulation of [Fe_4S_4]^0 clusters, specifically their being composed of high-spin Fe^{2+} centers. Instead, the extent of C–O bond weakening was more reminiscent of (and in many cases significantly greater than) that observed for mononuclear Fe^{1+}–CO complexes (typical values for ν(C–O) can range between 1850 and 1907 cm^{-1}).[66–71] This observation, combined with the tetrahedral geometry of the Fe_{CO} site and Mössbauer spectroscopic analysis of the three Fe_{IMes} sites, ruled out the possibility of a high-spin Fe^{2+}–CO center and instead pointed to an $Fe^{1+}{}_{CO}$ site, where the low-valent site was generated upon intracluster electron transfer from the NHC-bound Fe sites.[62]

The previously reported cluster [$Fe_4S_4(IMes)_3(CO)$] was prepared by reduction of [$Fe_4S_4(IMes)_3Cl$] with Ti(N[^{t}Bu]Ar)$_3$ (Ar = 3,5-dimethylphenyl).[62] Application of this protocol to [$CoFe_3S_4(IMes)_3Cl$], [$Co_4S_4(IMes)_3Cl$], and [$FeCo_3S_4(IMes)_3Cl$] similarly yielded [$CoFe_3S_4(IMes)_3(CO)$], [$Co_4S_4(IMes)_3(CO)$], and [$FeCo_3S_4(IMes)_3(CO)$], respectively (Figure 4.8). The ground spin states of [$Fe_4S_4(IMes)_3(CO)$], [$CoFe_3S_4(IMes)_3(CO)$], [$Co_4S_4(IMes)_3(CO)$], and [$FeCo_3S_4(IMes)_3(CO)$] are S = 2, ½, 3, and ⁵⁄₂, respectively, as determined from SQUID magnetometry (Figure S4.19–Figure S4.21). Each cluster has solution C_{3v} symmetry as revealed by ^{1}H NMR spectroscopy, once again showing that the heterometallic clusters have not undergone any metal ion scrambling. A comparative analysis of these isostructural CO complexes is now undertaken.

Regarding the three novel CO-bound clusters reported herein, we formulated a few hypotheses about how metal-ion substitution would affect the degree of C–O bond weaking. First, we expected that replacement of the supporting Fe ions with Co (*i.e.*, by comparing [$Fe_4S_4(IMes)_3(CO)$] and [$FeCo_3S_4(IMes)_3(CO)$], or [$CoFe_3S_4(IMes)_3(CO)$] and [$Co_4S_4(IMes)_3(CO)$]) would attenuate the degree of C–O bond weakening as a result of the greater electronegativity of Co with respect to Fe; taking this logic to the extreme, the higher electronegativity of Co could even preclude the intramolecular charge transfer required to generate a low-valent M_{CO} site. Second, we anticipated that substitution of the M_{CO} site for Co (*i.e.*, by comparing [$Fe_4S_4(IMes)_3(CO)$] and [$CoFe_3S_4(IMes)_3(CO)$], or [$FeCo_3S_4(IMes)_3(CO)$] and [$Co_4S_4(IMes)_3(CO)$]) would also result in poorer C–O bond weakening for the same reason.

An interesting and related consideration is the electron count at each M_{CO} site. For the Fe_{CO} site in [$Fe_4S_4(IMes)_3(CO)$], the substantial C–O bond weakening was only observed because of the cluster's ability to access configurations in which the Fe_{CO} site is d^7 (assuming this site maintains a high spin state, as was supported by structural and computational analyses).[62] However, Co^{2+} is d^7, and thus the requirement of obtaining a $d \geq 7$ electron count is already met in the absence of adopting a locally low-valent configuration.

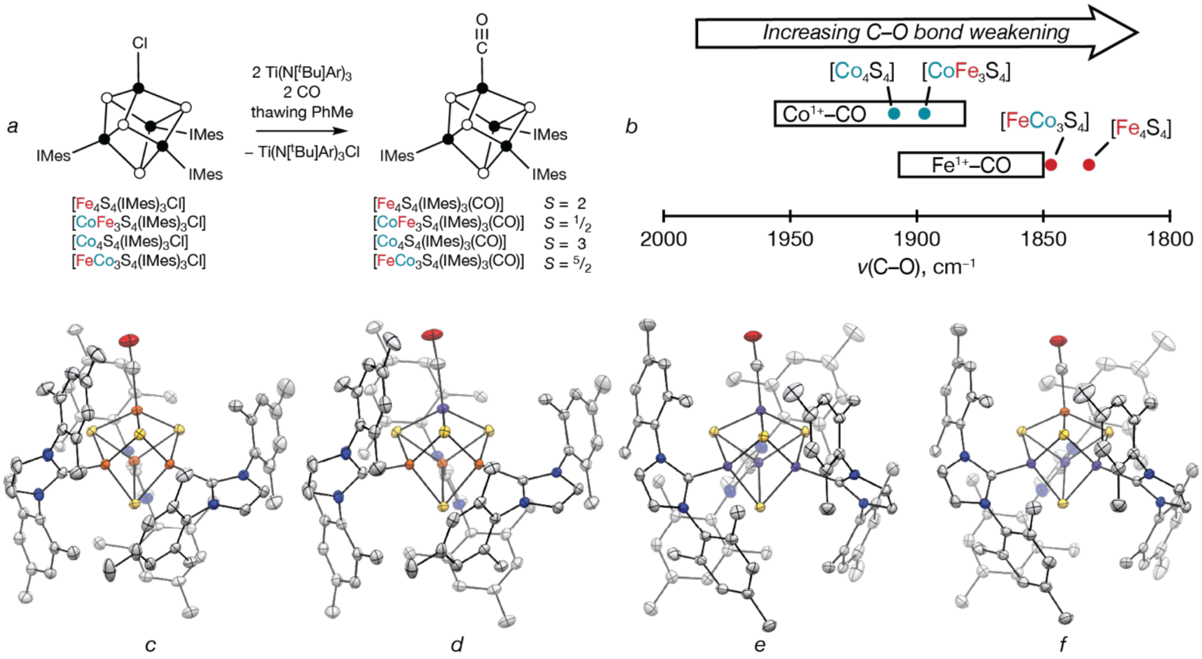

Figure 4.8. (*a*) Synthesis of carbonyl adducts $[Fe_4S_4(IMes)_3(CO)]$, $[CoFe_3S_4(IMes)_3(CO)]$, $[Co_4S_4(IMes)_3(CO)]$, and $[FeCo_3S_4(IMes)_3(CO)]$. Abbreviations: Ar, 3,5-dimethylphenyl. (*b*) C–O stretching frequencies of $[Fe_4S_4(IMes)_3(CO)]$, $[CoFe_3S_4(IMes)_3(CO)]$, $[Co_4S_4(IMes)_3(CO)]$, and $[FeCo_3S_4(IMes)_3(CO)]$ compared to a range of C–O stretching frequencies of mononuclear Fe^{1+}–CO and Co^{1+}–CO complexes from the literature. Vertical offset between Fe–CO and Co–CO complexes for clarity. (*c*–*f*) Thermal ellipsoid plots (50%) of $[Fe_4S_4(IMes)_3(CO)]$, $[CoFe_3S_4(IMes)_3(CO)]$, $[Co_4S_4(IMes)_3(CO)]$, and $[FeCo_3S_4(IMes)_3(CO)]$, respectively. Hydrogen atoms and solvent molecules omitted for clarity. Color scheme: Fe (red-orange), Co (purple), S (yellow), O (red), N (blue), C (grey).

Given these considerations, we first set out to evaluate valence of the M_{CO} sites in the three novel carbonylated clusters reported herein. Our approach was to compare the C–O stretching frequencies with those of $[Fe_4S_4(IMes)_3(CO)]$ and mononuclear Fe– and Co–CO complexes, whose valences either have already been deduced or are trivial to establish.

The IR spectra of $[CoFe_3S_4(IMes)_3(CO)]$, $[Co_4S_4(IMes)_3(CO)]$, and $[FeCo_3S_4(IMes)_3(CO)]$ are presented in Figure S4.28–Figure S4.30 and plotted in Figure 4.8b. A similar degree of C–O bond weakening was observed in $[FeCo_3S_4(IMes)_3(CO)]$ (1847 cm^{-1}) as for $[Fe_4S_4(IMes)_3(CO)]$ (1832 cm^{-1}), consistent with the heterometallic cluster likewise featuring an $Fe^{1+}{}_{CO}$ site, and likewise generated via valence disproportionation. The modestly lower C–O stretching frequency for the heterometallic cluster also showed that substitution of the supporting Fe centers with Co attenuates C–O bond weakening as a result of the greater electronegativity of Co with respect to Fe. Thus, even though the electron count at the unique Fe was likely the same for both clusters, the donicity of the sulfides was attenuated in $[FeCo_3S_4(IMes)_3(CO)]$, leading to poorer C–O bond weakening.

Tetrahedral, Co^{1+}–CO mononuclear complexes have stretching frequencies in the range of 1881–1956 cm^{-1} (Figure 4.8b).[72–75] The IR spectra of $[CoFe_3S_4(IMes)_3(CO)]$ (Figure S4.28) and $[Co_4S_4(IMes)_3(CO)]$ (Figure S4.29) showed ν(C–O) = 1897 cm^{-1} and 1909 cm^{-1}, respectively. These data reflected strong C–O bond weakening in both $[CoFe_3S_4(IMes)_3(CO)]$ and $[Co_4S_4(IMes)_3(CO)]$, consistent with $Co^{1+}{}_{CO}$ and intracluster electron transfer from the supporting metals. We also favored a $Co^{1+}{}_{CO}$ formulation over a $Co^{2+}{}_{CO}$ formulation in part because, to the best of our knowledge, no mononuclear, high-spin Co^{2+}–CO have been reported. We therefore surmised that, despite having a proper electron count for strong Co–CO backbonding, high-spin Co^{2+} is not a sufficiently strong π-base to allow for strong CO binding and activation. The values of *v*(C–O) for $[CoFe_3S_4(IMes)_3(CO)]$ and $[Co_4S_4(IMes)_3(CO)]$ were remarkably similar to those of the previously reported bimetallic clusters $[CoM_3S_4(Cp')_3(CO)]$ (M = Cr, Mo, W; Cp' = methylcyclopentadienide; 1900 cm^{-1}, 1903 cm^{-1}, and 1881 cm^{-1}, respectively), suggesting that each contains a $Co^{1+}{}_{CO}$ site.[76–80] Furthermore, these findings revealed a similar increase in C–O stretching frequency from $[CoFe_3S_4(IMes)_3(CO)]$ to $[Co_4S_4(IMes)_3(CO)]$ as observed between $[Fe_4S_4(IMes)_3(CO)]$ and $[FeCo_3S_4(IMes)_3(CO)]$ resulting from the identity of the supporting metal ions.

The evidence suggests that the extent of C–O bond weakening is primarily dictated by the identity of the metal to which CO is bound (Fe or Co). The difference between *v*(C–O) for Fe vs Co was *ca.* 60 cm^{-1} for $[Fe_4S_4(IMes)_3(CO)]$ vs $[CoFe_3S_4(IMes)_3(CO)]$ and $[FeCo_3S_4(IMes)_3(CO)]$ vs $[Co_4S_4(IMes)_3(CO)]$. That this difference was only marginally smaller in magnitude to the difference between two structurally similar mononuclear Fe^{1+} and Co^{1+} carbonyl complexes—$[{}^{Ph}Tp^{tBu}Fe(CO)]$ (1863 cm^{-1})[81] vs $[Tp^{Np}Co(CO)]$ (1950 cm^{-1}),[72] a difference of 87 cm^{-1}—added support for monovalent electronic configurations upon CO binding in all four clusters.

The intracluster charge transfer attendant with CO binding was evident in the solid-state structure of $[Fe_4S_4(IMes)_3(CO)]$. Compared to the all-ferrous cluster $[Fe_4S_4(I^iPr^{Me})_4]$, for which the valences (Fe^{2+}) are unambiguous, the average Fe_{NHC}–S and Fe_{NHC}–C bonds of $[Fe_4S_4(IMes)_3(CO)]$ were contracted (Table 4.1). Given the IR evidence of $Fe^{1+}{}_{CO}$ and $Co^{1+}{}_{CO}$ in our three novel carbonylated clusters, we anticipated similar evidence for charge depletion at the supporting metal sites from their solid-state structures.

Table 4.1. Summary of average bond distances of CO-bound clusters compared to homoleptic tetra-NHC clusters reported previously.[64,82] Standard uncertainties for average bond distances are estimated as the root of the sum of the squares of the individual standard uncertainties for each bond.

	M_{NHC} (avg.)			M_{CO} (avg.)		
	M–S (Å)	M–C (Å)	M_{NHC}–M_{NHC} (Å)	M–S (Å)	M–C (Å)	M_{CO}–M_{NHC} (Å)
$[Fe_4S_4(I^iPr^{Me})_4]^a$	2.330(3)	2.109(5)	2.681(1)	—	—	—
$[Fe_4S_4(IMes)_3(CO)]^b$	2.280(2)	2.053(2)	2.669(1)	2.259(1)	1.772(2)	2.665(1)
$[CoFe_3S_4(IMes)_3(CO)]$	2.269(2)	2.037(2)	2.697(1)	2.259(1)	1.755(1)	2.663(1)
$[Co_4S_4(I^iPr^{Me})_4]^c$	2.254(3)	1.985(5)	2.691(2)	—	—	—
$[Co_4S_4(IMes)_3(CO)]$	2.228(2)	1.953(2)	2.637(1)	2.228(1)	1.763(1)	2.622(1)
$[FeCo_3S_4(IMes)_3(CO)]$	2.234(2)	1.963(2)	2.652(1)	2.208(1)	1.761(2)	2.605(1)

[a] reference [82]. [b] reference [62]. [c] reference [64].

All four CO-bound clusters crystallized in the $P2_1/n$ space group with essentially identical unit cells and one cluster in the asymmetric unit (Figure 4.8). Considering first $[CoFe_3S_4(IMes)_3(CO)]$, formally the substitution of $Fe^{1+}{}_{CO}$ for $Co^{1+}{}_{CO}$, we observed average Fe_{NHC}–S and Fe_{NHC}–C bonds of 2.260(2) Å and 2.037(2) Å, respectively. Compared to $[Fe_4S_4(IMes)_3(CO)]$, $[CoFe_3S_4(IMes)_3(CO)]$ showed a greater contraction at the supporting Fe sites. This is likely the due to the greater electronegativity of Co attenuating the donicity of the bridging S ligands.

As discussed previously, reduced C–O bond weakening was observed when the supporting metals were substituted with Co (*i.e.,* [Fe$_4$S$_4$(IMes)$_3$(CO))] vs [FeCo$_3$S$_4$(IMes)$_3$(CO)], or [CoFe$_3$S$_4$(IMes)$_3$(CO)] vs [Co$_4$S$_4$(IMes)$_3$(CO)]). Here we make the comparison between the our two Co-rich carbonyl adducts, [FeCo$_3$S$_4$(IMes)$_3$(CO)] and [Co$_4$S$_4$(IMes)$_3$(CO)], and the homoleptic cluster, [Co$_4$S$_4$(I^{i}Pr$^{\text{Me}}$)$_4$] in the same charge state.[64]

As summarized in Table 4.1 and Figure 4.9, the average Co$_{\text{NHC}}$–S distances of [Co$_4$S$_4$(IMes)$_3$(CO)] and [FeCo$_3$S$_4$(IMes)$_3$(CO)] (2.228(2) Å and 2.234(2) Å) were shortened with respect to [Co$_4$S$_4$(I^{i}Pr$^{\text{Me}}$)$_4$] (2.254(3) Å). Similarly, the Co$_{\text{NHC}}$–C bond distances were 1.953(2) Å and 1.963(2) Å for [Co$_4$S$_4$(IMes)$_3$(CO)] and [FeCo$_3$S$_4$(IMes)$_3$(CO)] with respect to 1.985(5) Å in [Co$_4$S$_4$(I^{i}Pr$^{\text{Me}}$)$_4$]. The contraction of the bonds in the [Fe$_3$S$_4$(IMes)$_3$] and (to a lesser extent) the [Co$_3$S$_4$(IMes)$_3$] subclusters compared to the homoleptic clusters [Fe$_4$S$_4$(I^{i}Pr$^{\text{Me}}$)$_4$] and [Co$_4$S$_4$(I^{i}Pr$^{\text{Me}}$)$_4$] reflected the charge depletion at these supporting metal sites necessary to access low-valent electronic configurations at the CO-bound Fe and Co sites.

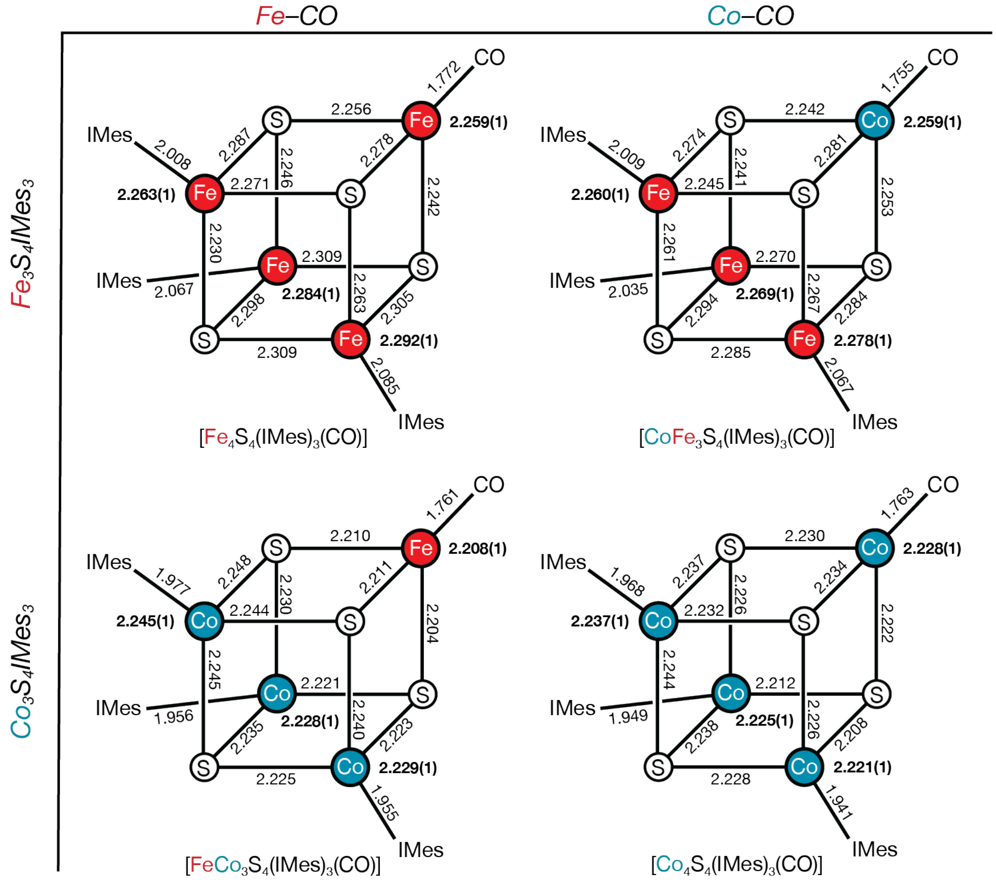

Figure 4.9. Schematics of [Fe$_4$S$_4$(IMes)$_3$(CO)] (*upper left*), [CoFe$_3$S$_4$(IMes)$_3$(CO)] (*upper right*), [Co$_4$S$_4$(IMes)$_3$(CO)] (*bottom right*), and [FeCo$_3$S$_4$(IMes)$_3$(CO)] (*bottom left*) depicting the bond distances in Å. Standard uncertainties are omitted for clarity. Average M–S bond distances for each site are provided in bold. Standard uncertainties for average bond distances are estimated as the root of the sum of the squares of the individual standard uncertainties for each bond.

As discussed above, we hypothesized that the poorer C–O bond weakening in [FeCo$_3$S$_4$(IMes)$_3$(CO)] vs [Fe$_4$S$_4$(IMes)$_3$(CO)] and [Co$_4$S$_4$(IMes)$_3$(CO)] vs [CoFe$_3$S$_4$(IMes)$_3$(CO)] was due to a reduction in S donicity at the CO-bound site due to the higher electronegativity of Co compared to Fe. This was manifest in the solid-state structure as a contraction in the M_{CO}–S bonds in both $[FeCo_3S_4(IMes)_3(CO)]$ and $[Co_4S_4(IMes)_3(CO)]$ relative to $[Fe_4S_4(IMes)_3(CO)]$ and $[CoFe_3S_4(IMes)_3(CO)]$, respectively (Table 4.1 and Figure 4.9). The average Fe_{CO}–S bond length in $[FeCo_3S_4(IMes)_3(CO)]$ (2.208(1) Å) was contracted relative to that of $[Fe_4S_4(IMes)_3(CO)]$ (2.259(1) Å). The average Co_{CO}–S bond in $[CoFe_3S_4(IMes)_3(CO)]$ was 2.259(1) Å compared to 2.228(1) Å in $[Co_4S_4(IMes)_3(CO)]$. The more electronegative Co sites of the $[Co_3S_4(IMes)_3]$ subcluster (relative to $[Fe_3S_4(IMes)_3]$) reduced the donicity of the S ligands to the M–CO fragment. This reduced donicity of the supporting S ligands at the CO-bound site lessened the degree of π-backbonding to CO by low-valent Co^{1+} or Fe^{1+} in $[Co_4S_4(IMes)_3(CO)]$ and $[FeCo_3S_4(IMes)_3(CO)]$ compared to $[CoFe_3S_4(IMes)_3(CO)]$ and $[Fe_4S_4(IMes)_3(CO)]$.

The structure of $[Fe_4S_4(IMes)_3(CO)]$ showed a tetragonal compression indicative of pairwise coupling as discussed for the Cl-bound clusters (*vide infra*). Although a tetragonal distortion is not evident for $[CoFe_3S_4(IMes)_3(CO)]$, $[Co_4S_4(IMes)_3(CO)]$, nor $[FeCo_3S_4(IMes)_3(CO)]$, this does not rule out the possibility of exchange-coupling. Given the marked similarities in the spectroscopic and structural data of these clusters thus far, we tentatively propose a pairwise coupling scheme for our Co-substituted carbonylated clusters identical to $[Fe_4S_4(IMes)_3(CO)]$.[62] Computational studies to evaluate this proposal are in progress.

In addition to the structural evidence for the oxidation of the supporting Fe_{NHC} sites, we employed ^{57}Fe Mössbauer spectroscopy to evaluate our proposed Fe valence assignments. ^{57}Fe Mössbauer spectroscopy is a powerful technique in Fe–S cluster chemistry that provides information about Fe coordination number, valence, and Fe–ligand covalency. For ligands whose donor properties substantially outweigh their acceptor properties (*e.g.*, sulfides, which are strong π-donors, and NHCs, which are strong σ donors and weak π acceptors), the isomer shift (δ) is inversely related to the Fe valence and Fe–ligand covalency. For example, the average isomer shift of the Fe_{NHC} sites in $[CoFe_3S_4(IMes)_3Cl]$ (δ_{avg} = 0.42 mm s^{-1}) decreases upon 1e^- oxidation to $[CoFe_3S_4(IMes)_3Cl]^+$ (δ_{avg} = 0.30 mm s^{-1}). Similarly, the isomer shift of the Fe_{Cl} site in $[FeCo_3S_4(IMes)_3Cl]$ (δ_{avg} = 0.54 mm s^{-1}) decreases to δ_{avg} = 0.47 mm s^{-1} in $[FeCo_3S_4(IMes)_3Cl]^+$.

However, for strongly π-acidic ligands like CO, the Fe valence and Fe–CO covalency have opposing impacts on the isomer shift (*i.e.*, Fe–CO covalency increases due to greater π-backbonding with decreasing Fe valence), precluding unambiguous assignment of the Fe valence for the CO-bound sites.[62,83] The Mössbauer spectrum of $[Fe_4S_4(IMes)_3(CO)]$ has been discussed previously and the values are reproduced here in Table 4.2.[62] The average isomer shift of the Fe–NHC sites in $[CoFe_3S_4(IMes)_3(CO)]$ was 0.47 mm s^{-1}, nearly identical to that of $[Fe_4S_4(IMes)_3(CO)]$, and indicative of the oxidation of these sites with respect to the Fe^{2+}_{NHC} sites of $[Fe_4S_4(I^iPr^{Me})_4]$. For $[Fe_4S_4(IMes)_3(CO)]$ an average valence of $Fe^{2.25+}$ was concluded for the NHC-bound sites—by comparison to $[Fe_4S_4(I^iPr^{Me})_4]$ and $[Fe_4S_4(I^iPr^{Me})_4]^+$—leaving the Fe_{CO} site with a computed valence of $Fe^{1.25+}$.[62] Given that the average isomer shift of $[CoFe_3S_4(IMes)_3(CO)]$ was nearly identical, we draw the same conclusion for this cluster: $Fe^{2.25+}_{NHC}$ and $Co^{1.25+}_{CO}$.

Table 4.2. Mössbauer parameters (80 K) for [$Fe_4S_4(IMes)_3(CO)$], [$CoFe_3S_4(IMes)_3(CO)$], [$FeCo_3S_4(IMes)_3(CO)$], and [$Fe_4S_4(I^iPr^{Me})_4$].

	Fe_{NHC}		Fe_{CO}	
	δ_{avg} (mm s^{-1})	$\lvert\Delta E_Q\rvert_{avg}$ (mm s^{-1})	δ (mm s^{-1})	$\lvert\Delta E_Q\rvert$ (mm s^{-1})
[$Fe_4S_4(I^iPr^{Me})_4$][a]	0.60	1.97	—	—
[$Fe_4S_4(IMes)_3(CO)$][b]	0.48	1.34	0.32	2.41
[$CoFe_3S_4(IMes)_3(CO)$]	0.47	1.36	—	—
[$FeCo_3S_4(IMes)_3(CO)$]	—	—	0.20	1.99

[a] reference [82]. [b] reference [62]

As discussed above, the conflicting trends in isomer shift for Fe valence and Fe–CO covalency prevented assignment of the Fe–CO valence directly from the Mössbauer parameters of this site. That said, the lower isomer shift of Fe–CO in [$FeCo_3S_4(IMes)_3(CO)$] (δ = 0.20 mm s^{-1}) relative to [$Fe_4S_4(IMes)_3(CO)$] (δ = 0.32 mm s^{-1}) was consistent with the contracted Fe–S bonds (Table 4.2).[83]

The above spectroscopic and structural analyses concluded low-valent $Fe^{1+}{}_{CO}$ and $Co^{1+}{}_{CO}$ were accessed upon CO binding in all four clusters. Furthermore, the degree of C–O bond weakening was dictated primarily by the identity of M_{CO} and secondarily by the identity of M_{NHC}. Interestingly, the electrochemical properties, namely the redox potentials, of the clusters are grouped not by M_{CO}, but by M_{NHC}.

We anticipated that the redox potentials of the clusters would trend with cluster composition such that increasing Co content in the cluster core would yield more positive redox potentials. Our hypothesis was supported by previous findings, including the observed anodic shift of the 1+/0 potentials of [$Co_4S_4(I^iPr^{Me})_4$] vs [$Fe_4S_4(I^iPr^{Me})_4$], as well as previously reported heterometal substituted Fe–S clusters.[64,82] The series [$MFe_3S_4(SMes)_4$]$^{2-/3-}$ (M = Fe, Co, Ni) showed reversible [MFe_3S_4]$^{2+/1+}$ couples in the order M = Fe (−1.20 V) < Co (−0.95 V) < Ni (−0.90 V vs SCE).[55,58,59] The trend was extended to Cu in the series [$(Ph_3P)MFe_3S_4(LS_3)$]$^{2-/3-}$ (M = Co, Ni, Cu; LS_3 = 1,3,5-tris((4,6-dimethyl-3-mercaptophenyl)thio)-2,4,6-tris(*p*-tolylthio)benzene(3−)) giving the order: (Fe) < Co (−1.57 V) < Ni (−1.45 V) < Cu (−1.35 V vs SCE) for the [MFe_3S_4]$^{1+/0}$ couple.[55,58,59]

The cyclic voltammogram (CV) of [$CoFe_3S_4(IMes)_3(CO)$] would then be expected to show redox potentials shifted to more positive values compared to [$Fe_4S_4(IMes)_3(CO)$]. The CV of [$CoFe_3S_4(IMes)_3(CO)$] exhibited a reversible oxidation at −1.55 V (vs Fc/Fc^+) corresponding to the [M_4S_4]$^{1+/0}$ couple (Table 4.6 and Figure 4.10). That this couple occurred at nearly identical potential to that of [$Fe_4S_4(IMes)_3(CO)$] (−1.54 V) suggested that the greatest change in electron density upon oxidation occurred at the [$Fe_3S_4(IMes)_3$] subcluster with little to no involvement of the M–CO fragment.

The same redox couple was observed at −1.25 V and −1.29 V for [$Co_4S_4(IMes)_3(CO)$] and [$FeCo_3S_4(IMes)_3(CO)$], respectively. Between these two Co-rich clusters, the redox potential of this couple trended as expected (*i.e.,* substitution of a Co with Fe resulted in a more negative redox potential). However, this *ca.* 40 mV shift between these two clusters was small in comparison to the difference between [$Fe_4S_4(IMes)_3(CO)$] and [$FeCo_3S_4(IMes)_3(CO)$] (*ca.* 250 mV), or [$CoFe_3S_4(IMes)_3(CO)$] and [$Co_4S_4(IMes)_3(CO)$] (*ca.* 300 mV). Given these observations, we concluded that the 1+/0 redox couple of these four carbonylated clusters are localized to the $[M_3S_4(IMes)_3]$ subclusters.

Table 4.3. Summary of redox potentials (vs Fc/Fc^+) of carbonylated clusters according to core charge state. Italics indicate electrochemically irreversible redox couples.

	Core composition	$E_{1/2}$ (V vs Fc/Fc^+)	
		$[M_4S_4]^{0/1-}$	$[M_4S_4]^{1+/0}$
$[Fe_4S_4(IMes)_3(CO)]^a$	$[Fe_4S_4]$	*−2.59*	−1.54
$[CoFe_3S_4(IMes)_3(CO)]^a$	$[CoFe_3S_4]$	*−2.53*	−1.55
$[Co_4S_4(IMes)_3(CO)]^a$	$[Co_4S_4]$	−2.41	−1.25
$[FeCo_3S_4(IMes)_3(CO)]^a$	$[FeCo_3S_4]$	−2.24	−1.29

[a] in *o*-DFB with $[Pr_4N][BAr^F_4]$.

The CV of $[Co_4S_4(IMes)_3(CO)]$ and $[FeCo_3S_4(IMes)_3(CO)]$ also showed a reversible reduction to $[Co_4S_4(IMes)_3(CO)]^-$ and $[FeCo_3S_4(IMes)_3(CO)]^-$ at −2.41 V and −2.24 V. This couple is observed in the CV of both $[Fe_4S_4(IMes)_3(CO)]$ (−2.59 V) and $[CoFe_3S_4(IMes)_3(CO)]$ (−2.53 V) but is less reversible.

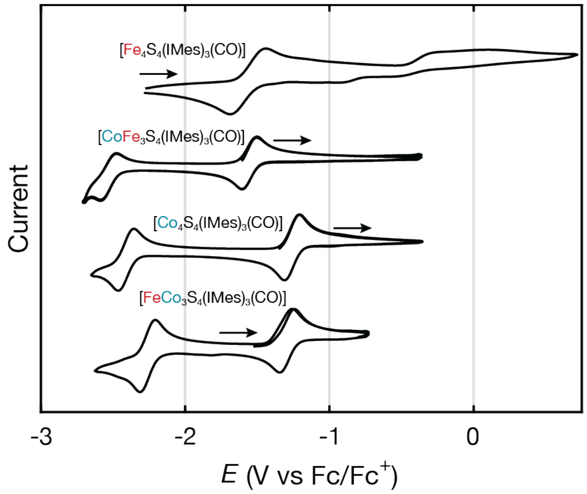

Figure 4.10. CV plot of $[Fe_4S_4(IMes)_3(CO)]$,[62] $[CoFe_3S_4(IMes)_3(CO)]$, $[Co_4S_4(IMes)_3(CO)]$, and $[FeCo_3S_4(IMes)_3(CO)]$ (2 mM; *top to bottom, respectively*) at 200 mV/s in DFB with $[^nPr_4N][BAr^F_4]$ (0.2 M) as electrolyte. The cell consisted of a glassy carbon working electrode, a Ag wire auxiliary electrode, and a Ag wire *pseudo*-reference electrode.

Comparative analysis of Cl-bound hetero- and homometallic clusters

We now examine the Cl-bound clusters to establish the impact of the metal-ion composition on the clusters' geometric and electronic structures. We anticipated the greater electronegativity of Co would produce shorter Co–S bonds compared to Fe, but that we would otherwise largely observe structural trends identical to the all-Fe clusters. $[Fe_4S_4]$ clusters often display tetragonal compression or elongation along four of the twelve core Fe–S bonds, reflective of the pairwise exchange-coupling of the Fe ions that maximize antiferromagnetic coupling to arrive at the observed spin states of the clusters.[84] This distortion was evident in the structures of $[Fe_4S_4(IMes)_3Cl]$ and $[Fe_4S_4(IMes)_3Cl]^+$, both of which were reported previously.[60,61] However, we note at the outset that, although many clusters exhibit nearly three-fold symmetry, no cluster crystallized on a three-fold axis or any other special position.

To our surprise, the solid-state structure of $[CoFe_3S_4(IMes)_3Cl]^+$ showed no evidence of a tetragonal distortion, and instead the core showed *pseudo*-C_3 symmetry (Figure 4.11). The average Fe_{NHC}–S bonds to the three μ_3-S ligands that bridge Fe and Co were short (2.206(2) Å) compared to the average Fe_{NHC}–S bonds to the μ_3-S ligand that bridges the three Fe_{NHC} sites (2.229(2) Å), possibly the result of the greater electronegativity of Co compared to Fe. Furthermore, the three Co_{Cl}–S bonds were nearly identical, lacking any significant distortion along a particular axis.

Upon reduction a clear tetragonal compression became apparent in the structure of $[CoFe_3S_4(IMes)_3Cl]$ (Figure 4.3b and Figure 4.12), suggesting that the pairwise exchange-coupling typical of $[Fe_4S_4]$ clusters was similarly present in $[CoFe_3S_4(IMes)_3Cl]$. This proposal was also consistent with the $S = 0$ ground spin state observed by SQUID magnetometry (Figure S4.14). SQUID magnetometry of $[CoFe_3S_4(IMes)_3Cl]^+$ and $[FeCo_3S_4(IMes)_3Cl]^+$ supported ground spin state assignments of $S = ½$ for both (Figure S4.13 and Figure S4.17), which may also reflect pairwise exchange-coupling between the Fe and Co ions despite the absence of tetragonal distortions in their solid-state structures.

With the exception of $[FeCo_3S_4(IMes)_3Cl]^+$, the ground spin-states of the Co-rich clusters $[Co_4S_4(IMes)_3Cl]$ ($S = 3/2$), $[Co_4S_4(IMes)_3Cl]^+$ ($S = 2$), and $[FeCo_3S_4(IMes)_3Cl]$ ($S = 1$) were inconsistent with the straightforward, non-spin-canted pairwise coupling schemes typical of $[Fe_4S_4]$ clusters (*vide supra*; Figure S4.15, Figure S4.16, and Figure S4.18). The solid-state structures of $[Co_4S_4(IMes)_3Cl]$, $[Co_4S_4(IMes)_3Cl]^+$, and $[FeCo_3S_4(IMes)_3Cl]$ lack tetragonal distortions along any M–S bond axes (Figure 4.11 and Figure 4.12). It is important to note, however, that not all $[Fe_4S_4]$ clusters display clear tetragonal distortions in their solid-state structures, and the absence of such distortions are not unequivocal evidence of the absence of pairwise coupling.[84–86]

The ground spin states for two $[CoFe_3S_4]$ clusters have been reported previously: $[CoFe_3S_4(PPh_3)(LS_3)]^{2-}$ ($[CoFe_3S_4]^{1+}$, $S = ½$) and $[CoFe_3S_4(SMes)_4]^{2-}$ ($[CoFe_3S_4]^{2+}$, $S = 1$).[55,59] These ground spin states were rationalized via antiparallel alignment of a high-spin Co^{2+} ($S = 3/2$) ion and $[Fe_3S_4]^{0,1-}$ ($S = 2, 5/2$), respectively. At parity of cluster charge our $[CoFe_3S_4]$ clusters were shown to possess identical ground spin states and we therefore concluded similar coupling patterns. However, this formulation assumed that oxidation of $[CoFe_3S_4]^{1+}$ to $[CoFe_3S_4]^{2+}$ was localized to the $[Fe_3S_4]$ fragment, but structural characterization of these clusters was limited. Crystals of suitable quality for structure determination of clusters site-differentiated by the trithiolate ligand platform (LS_3^{3-}) could not be obtained. The homoleptic cluster was structurally characterized, but the Co and Fe ions were disordered equally among the four cluster sites.

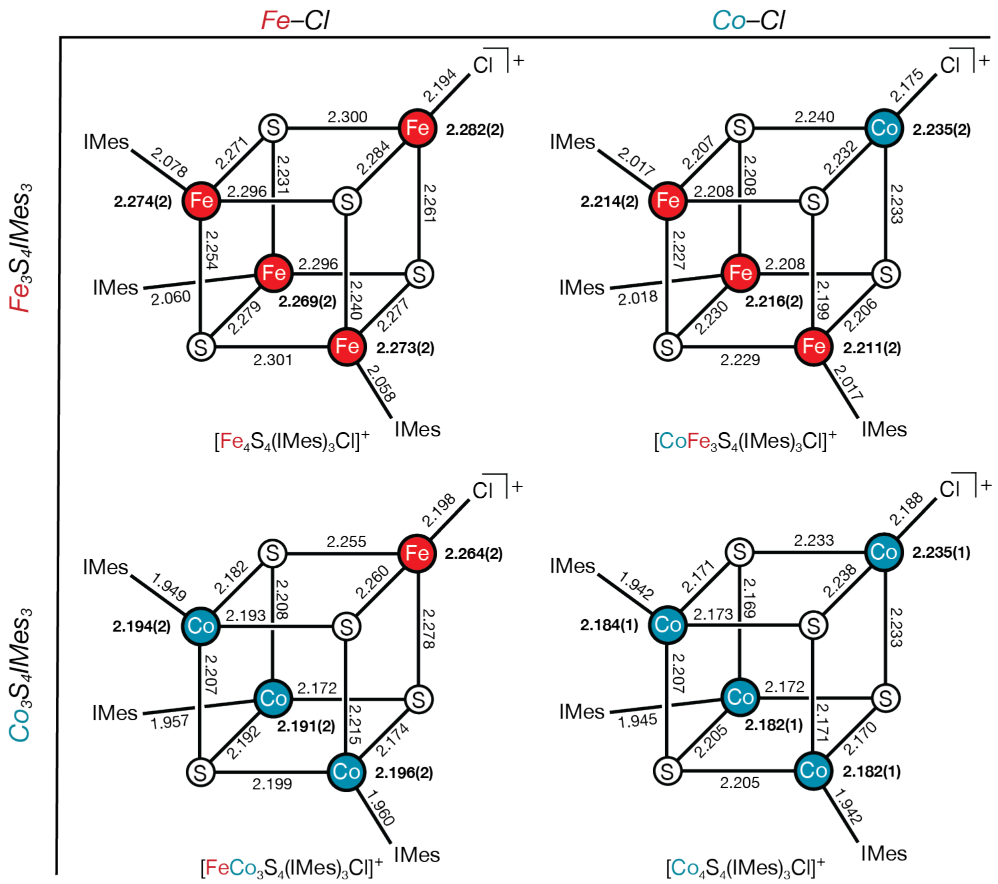

Figure 4.11. Schematics of $[Fe_4S_4(IMes)_3Cl]^+$ (*upper left*), $[CoFe_3S_4(IMes)_3\ Cl]^+$ (*upper right*), $[Co_4S_4(IMes)_3\ Cl]^+$ (*bottom right*), and $[FeCo_3S_4(IMes)_3\ Cl]^+$ (*bottom left*) depicting the bond distances in Å. Standard uncertainties are omitted for clarity. Average M–S bond distances for each site are provided in bold. Standard uncertainties for average bond distances are estimated as the root of the sum of the squares of the individual standard uncertainties for each bond.

Analysis of our reduced and oxidized $[CoFe_3S_4]$ clusters revealed comparable redox induced structural changes at both the Co_{Cl} and Fe_{NHC} sites, suggesting that both the Co–Cl and $[Fe_3S_4(IMes)_3]$ fragments participated in redox chemistry (Table 4.4). Furthermore, the oxidized cluster ($[CoFe_3S_4(IMes)_3Cl]^+$) and the Co-rich clusters ($[Co_4S_4(IMes)_3Cl]^{0,1+}$ and $[FeCo_3S_4(IMes)_3Cl]^{0,1+}$) were contracted compared to $[CoFe_3S_4(IMes)_3Cl]$ and the all-Fe clusters (both reduced and oxidized; Table 4.5). We speculate that the electronic structure of the Co-substituted cluster, as well as the $[MCo_3S_4]$ (M = Fe, Co) clusters, may be more delocalized than typical Fe–S clusters.

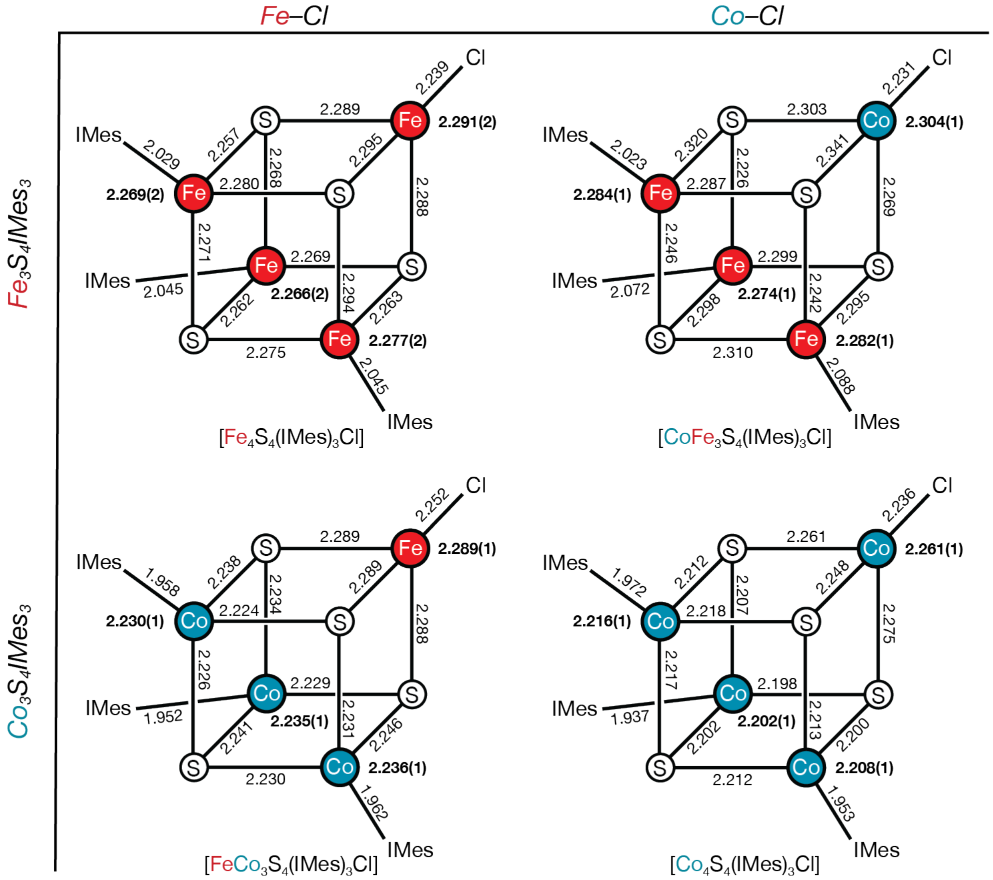

Figure 4.12. Schematics of $[Fe_4S_4(IMes)_3Cl]$ (*upper left*), $[CoFe_3S_4(IMes)_3Cl]$ (*upper right*), $[Co_4S_4(IMes)_3Cl]$ (*bottom right*), and $[FeCo_3S_4(IMes)_3Cl]$ (*bottom left*) depicting the bond distances in Å. Standard uncertainties are omitted for clarity. Average M–S bond distances for each site are provided in bold. Standard uncertainties for average bond distances are estimated as the root of the sum of the squares of the individual standard uncertainties for each bond.

In addition to the structural evidence for redox participation of the Co_{Cl} site, we deduced the metal atom charges by comparison of the Mössbauer isomer shifts of the Fe_{NHC} sites in the reduced and oxidized clusters. Although not directly comparable to previously reported $[CoFe_3S_4]$ clusters due to differences in terminal ligation, the average isomer shifts of the Fe_{NHC} sites in $[CoFe_3S_4(IMes)_3Cl]$ ($\delta_{avg} = 0.422$ mm s^{-1}) and $[CoFe_3S_4(IMes)_3Cl]^+$ ($\delta_{avg} = 0.295$ mm s^{-1}) differed by *ca.* 0.127 mm s^{-1} (Figure S4.31 and Table S4.1). This decrease in the average isomer shift indicated oxidation of each Fe_{NHC} site by 0.25 e$^-$ corresponding to 3 × $Fe^{2.5+}_{NHC}$ and 1 × $Co^{2.5+}_{Cl}$ for $[CoFe_3S_4(IMes)_3Cl]^+$.[62] The isomer shift of the Fe_{Cl} site of $[FeCo_3S_4(IMes)_3Cl]$ (0.542 mm s^{-1}) also decreased upon oxidation to $[FeCo_3S_4(IMes)_3Cl]^+$ (0.472 mm s^{-1}).

Table 4.4. Summary of average bond distances of Cl-bound clusters. Standard uncertainties for average bond distances are estimated as the root of the sum of the squares of the individual standard uncertainties for each bond.

	M_{NHC} (avg.)			M_{Cl} (avg.)		
	M–S (Å)	M–C (Å)	M_{NHC}–M_{NHC} (Å)	M–S (Å)	M–Cl (Å)	M_{Cl}–M_{NHC} (Å)
$[Fe_4S_4(IMes)_3Cl]$[a]	2.271(5)	2.035(9)	2.713(9)	2.290(2)	2.234(2)	2.686(4)
$[Fe_4S_4(IMes)_3Cl]^{+}$[b]	2.271(4)	2.063(9)	2.720(2)	2.285(2)	2.194(1)	2.714(2)
$[CoFe_3S_4(IMes)_3Cl]$	2.280(2)	2.061(3)	2.698(1)	2.304(1)	2.231(1)	2.789(1)
$[CoFe_3S_4(IMes)_3Cl]^{+}$	2.214(3)	2.017(2)	2.650(2)	2.235(2)	2.175(1)	2.684(1)
$[Co_4S_4(IMes)_3Cl]$	2.209(2)	1.955(3)	2.626(1)	2.261(1)	2.236(1)	2.696(1)
$[Co_4S_4(IMes)_3Cl]^{+}$	2.183(2)	1.943(2)	2.578(1)	2.235(1)	2.188(1)	2.684(1)
$[FeCo_3S_4(IMes)_3Cl]$	2.233(2)	1.957(3)	2.678(1)	2.289(1)	2.252(1)	2.714(1)
$[FeCo_3S_4(IMes)_3Cl]^{+}$	2.194(3)	1.956(5)	2.625(1)	2.264(2)	2.198(1)	2.694(1)

[a] reference [61]. [b] reference [60].

Table 4.5. Summary of core structural comparisons of Cl-bound clusters.

	$V(M_4)$, (Å^3)	$V(S_4)$, (Å^3)	$V(M_4S_4)$, (Å^3)
$[Fe_4S_4(IMes)_3Cl]$	2.32	5.53	9.29
$[Fe_4S_4(IMes)_3Cl]^{+}$	2.36	5.47	9.38
$[CoFe_3S_4(IMes)_3Cl]$	2.44	5.51	9.60
$[CoFe_3S_4(IMes)_3Cl]^{+}$	2.23	5.04	8.79
$[Co_4S_4(IMes)_3Cl]$	2.22	5.08	8.77
$[Co_4S_4(IMes)_3Cl]^{+}$	2.14	4.90	8.47
$[FeCo_3S_4(IMes)_3Cl]$	2.31	5.25	9.11
$[FeCo_3S_4(IMes)_3Cl]^{+}$	2.21	4.98	8.71

To further examine explore the effect of Co-substitution on the redox properties of these Cl-bound clusters, the voltammograms of $[Fe_4S_4(IMes)_3Cl]$, $[CoFe_3S_4(IMes)_3Cl]$, $[Co_4S_4(IMes)_3Cl]$, and $[FeCo_3S_4(IMes)_3Cl]$ were collected (Table 4.6 and Figure 4.13). Each voltammogram showed two reversible oxidation events corresponding to the 1+/0 ($[M'M_3S_4]^{2+/1+}$) and 2+/1+ ($[M'M_3S_4]^{3+/2+}$) couples; the $E_{1/2}$ values are collected in Table 4.6. Compared to the all-Fe cluster, the 2+/1+ (+0.381 V) and 1+/0 (−0.890 V) couples are shifted positively by *ca.* 40 mV and 310 mV, respectively. We therefore anticipated that each Co substituted into the core would result in a *ca.* 80 mV positive shift in the potential of the 1+/0 couples compared to the all-Fe cluster, and minimal positive shifts in the 2+/1+ couple. Substitution of the apical Fe site in $[Fe_4S_4(IMes)_3Cl]$ with Co to give $[CoFe_3S_4(IMes)_3Cl]$ resulted in a *ca.* 140 mV positive shift of the $[M'M_3S_4]^{2+/1+}$ couple, much greater than expected.

Compared to the all-Co cluster, we anticipated that substitution of one Co ion with Fe would produce a shift in the redox potentials to more negative values. In the CV of $[FeCo_3S_4(IMes)_3Cl]$, the 2+/1+ and 1+/0 couples occur at +434 mV and −837 mV, respectively. That a positive shift in the redox potentials was observed suggested that these Co-rich clusters ($[Co_4S_4]$ and $[FeCo_3S_4]$) possess electronic structures that are considerably different from $[Fe_4S_4]$ clusters. We speculated that for many of these compounds, more delocalized electronic structure pictures may be warranted; computational studies to assess this possibility are underway.

Table 4.6. Summary of redox potentials (vs Fc/Fc$^+$) of Cl-bound clusters according to core charge state.

	Core composition	$E_{1/2}$ (V vs Fc/Fc$^+$)	
		$[M_4S_4]^{2+/1+}$	$[M_4S_4]^{3+/2+}$
$[Fe_4S_4(IMes)_3Cl]^{a,b}$	$[Fe_4S_4]$	−1.203	+0.341
$[CoFe_3S_4(IMes)_3Cl]^{b}$	$[CoFe_3S_4]$	−1.062	+0.302
$[Co_4S_4(IMes)_3Cl]^{b}$	$[Co_4S_4]$	−0.890	+0.381
$[FeCo_3S_4(IMes)_3Cl]^{b}$	$[FeCo_3S_4]$	−0.837	+0.434

[a] reference [62]. [b] in DFB with $[Bu_4N][PF_6]$.

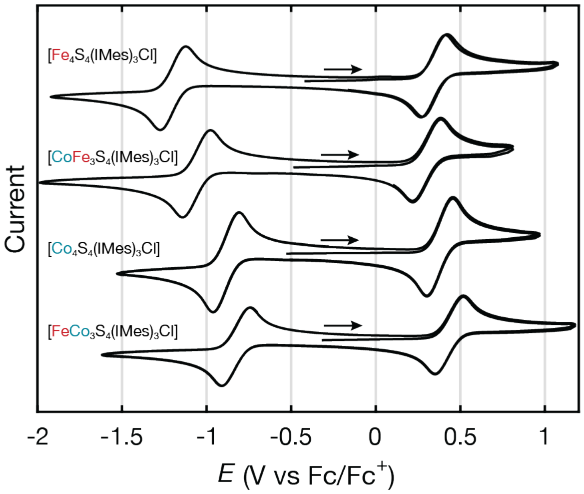

Figure 4.13. CV plot of $[Fe_4S_4(IMes)_3Cl]$, $[CoFe_3S_4(IMes)_3Cl]$, $[Co_4S_4(IMes)_3Cl]$, and $[FeCo_3S_4(IMes)_3Cl]$ (5 mM; *top to bottom, respectively*) at 200 mV/s in DFB with $[^nBu_4N][PF_6]$ (0.5 M) as electrolyte. The cell consisted of a glassy carbon working electrode, a Ag wire auxiliary electrode, and a Ag wire *pseudo*-reference electrode.

Conclusions

In conclusion, we have shown that the 3:1 site-differentiation pattern enforced by sterically encumbering IMes ligands allows for targeted heterometal substitution using $CoCl_2$ and $FeCl_2$ through the intermediacy of Tl-substituted $[Fe_3S_4(IMes)_3]$ and $[Co_3S_4(IMes)_3]$ clusters, respectively. The impact of core metal substitution with Fe and Co on the properties of these clusters, in particular their degree of CO activation, was investigated through structural, spectroscopic, magnetochemical, and electrochemical methods. We have shown that low-valent Fe^{1+} and Co^{1+} electronic configurations are accessed through intracluster charge transfer upon CO binding for all four core metal atom compositions. We observed that the degree of C–O bond weakening was primarily dictated by the identity of the CO-bound metal, and to a lesser extent by the identity of the supporting metal atoms.

Experimental details and supplemental information

General Considerations

Unless otherwise noted, all manipulations were performed under an atmosphere of purified N_2 in an LC Technologies model LC-1 glovebox or using standard Schlenk techniques. Glassware was dried in an oven at 160 °C prior to use. Molecular sieves (3 Å) and Celite® were activated/dried by heating to 250 °C under vacuum overnight and stored in the glovebox. Filtrations were performed using either fritted glass funnels or pipette filters plugged with oven-dried glass microfiber filter paper. Unless otherwise stated, all reagents and solvents were obtained from commercial suppliers and used as received. Benzene, toluene, pentane, diethyl ether, and CH_2Cl_2 were degassed by sparging with Ar and dried by passing through columns packed with alumina and Q5.[87] THF was dried/deoxygenated over Na benzophenone ketyl and distilled under N_2. *Ortho*-difluorobenzene was distilled from CaH_2. C_6D_6 was degassed by three freeze-pump-thaw cycles. All solvents were stored over activated 3 Å molecular sieves in the glovebox for at least 12 h prior to use. IMes,[88,89] TlTp,[90] $[Co_4S_4(P^iPr_3)_4]$,[64] $[Fe_4S_4(IMes)_3Cl][PF_6]$,[60] $FcPF_6$,[91] and $Ti(N\{^tBu\}Ar)_3$[92] were prepared according to literature procedures. Abbreviations: *ortho*-difluorobenzene (DFB); room temperature (RT).

Statement on compound purity

In accordance with the recommendation of the *Organometallics* editorial board,[93] we provide a statement on how we evaluated the purity of the novel compounds reported herein. The purity of the novel clusters reported herein was established primarily by ^1H NMR spectroscopy. Additionally, all compounds as-prepared are freely soluble in organic solvents, precluding the presence of NMR-silent, insoluble species. The novel clusters reported herein were analyzed for their C, H, and N content by elemental analysis. Most values match the theoretical values within experimental error; deviations may be due to the presence of organic solvent in the lattice or incomplete combustion, as has been observed for other members of this class of molecules[94,95] and in other contexts.[96] $[TlFe_3S_4(IMes)_3][PF_6]$ and $[TlCo_3S_4(IMes)_3][PF_6]$ were not analyzed by elemental analysis due to the toxicity of Tl.

Spectroscopy and other characterization techniques

^1H NMR spectra were collected on Bruker Avance 400 MHz or Neo 500 MHz spectrometers. Chemical shifts are reported relative to tetramethylsilane using residual solvent as an internal standard. Solvent suppression for NMR in protonated solvents was carried out using WET solvent suppression.[97] UV/visible spectra were recorded on a Cary 50 spectrophotometer. FT-IR spectra were recorded in the glovebox as powders or thin films prepared by evaporation of DCM solutions using a Bruker Alpha Platinum attenuated total reflection (ATR) spectrometer operating at 2 cm^{-1} resolution. Elemental analysis was performed by Midwest Microlab (Indianapolis, IN). Simulations were performed using EasySpin[98] (5.2.21) in Matlab (R2022b). UV-vis spectra were recorded on a Cary 60 spectrometer. Zero-field 80 K ^{57}Fe Mössbauer spectra were measured with a SEE co. MS3 W301 constant-acceleration spectrometer. Variable temperature (5–200 K) zero-field 57Fe Mössbauer spectra were measured with a SEE co. W302 constant-acceleration spectrometer. Isomer shifts are quoted relative to α-Fe foil at room temperature; Mössbauer spectra were simulated with WMOSS v.4.[99] SQUID data was collected on a Quantum Design MPMS3

SQUID magnetometer in the range of 2–300 K with a 0.5 T applied field. X-ray structural determinations were performed at the MIT diffraction facility using a Bruker X8 diffractometer with an APEX II CCD detector or a Bruker D8 Venture diffractometer with a Photon2 CPAD detector. Diffraction data was collected, integrated, and corrected for absorption using Bruker APEX3 software and its associated modules (SAINT, SADABS, TWINABS). Structural solutions and refinements (on F^2) were carried out using SHELXT and SHELXL-2018 in ShelXle.[100] Ellipsoid plots and figures were made using Mercury. Cyclic voltammetry (CV) experiments were performed using a GAMRY Reference 600 potentiostat. The cell consisted of a glassy carbon working electrode, a Ag wire auxiliary electrode, and a Ag wire pseudo-reference electrode. For [Co_4S_4(IMes)$_3$Cl], [$CoFe_3S_4$(IMes)$_3$Cl], and [$FeCo_3S_4$(IMes)$_3$Cl], the 1+/2+ pair was referenced to the Fc/Fc$^+$ peak in an analyte solution in the presence of Fc. Then in the working CV without Fc, we utilized the 1+/2+ pair to internally reference the remaining peaks at different scan rates. For [Co_4S_4(IMes)$_3$(CO)], [$CoFe_3S_4$(IMes)$_3$(CO)], and [$FeCo_3S_4$(IMes)$_3$(CO)], the 0/1+ pair was referenced to the Cp_2Co/Cp_2Co^+ peak in an analyte solution in the presence of Cp_2Co. Then in the working CV without Cp_2Co, we utilized the 0/1+ pair to internally reference the remaining peaks at different scan rates.

Synthetic procedures

[$TlFe_3S_4$(IMes)$_3$][PF_6]

TlTp (371.2 mg, 0.8889 mmol) in THF (2 mL) was added dropwise to a stirring slurry of [Fe_4S_4(IMes)$_3$Cl][PF_6] (600.4 mg, 0.4154 mmol) in THF (16 mL). After 1 h, the solution was filtered through Celite and concentrated to 5 mL *in vacuo*. The product was precipitated by addition of Et_2O (10 mL). The mother liquor was decanted, and the remaining solids washed with benzene (2 × 5 mL). The solids were extracted with DFB (5 mL) and filtered through Celite. The filtrate was concentrated *in vacuo* to 3 mL, then layered with ether (12 mL). The product was obtained as a black crystalline solid (549.7 mg, 85 % yield). Crystals for structure determination were obtained by layering pentane onto a saturated solution of [$TlFe_3S_4$(IMes)$_3$][BAr^F_4] in Et_2O. ^{1}H NMR (DFB, 400 MHz, 298 K): δ (ppm) 10.20 (s, 6H, Im-H), 3.67 (s, 36H, *o*-Me), 2.98 (s, 18H, *p*-Me).

[$CoFe_3S_4$(IMes)$_3$Cl][PF_6]

$CoCl_2$ (74.0 mg, 0.5699 mmol) was stirred in THF (1 mL) for 1 h. The $CoCl_2$ slurry was then added dropwise to a stirring slurry of [$TlFe_3S_4$(IMes)$_3$][PF_6] (549.7 mg, 0.4154 mmol) in THF (30 mL). After 30 min, the solution was filtered through Celite. DFB (10 mL) was used to wash some black solids that were collected by filtration into the filtrate. The filtrate was concentrated to dryness *in vacuo*, then washed with Et_2O (3 × 5 mL). The solids were extracted with DFB (15 mL), filtered through Celite, and concentrated *in vacuo* to 5 mL. The product was precipitated following addition of Et_2O (10 mL). The product was isolated as a black crystalline solid (451.1 mg, 88% yield). Crystals for structure determination were obtained by layering pentane onto a saturated solution of [$CoFe_3S_4$(IMes)$_3$Cl][BAr^F_4] in Et_2O. ^{1}H NMR (DFB, 500 MHz, 298 K): δ (ppm) 6.53 (s, 6H, Im-H), 2.40 (s, 18H, *p*-Me), 2.28 (s, 36H, *o*-Me). Anal. Found (Calc.): C, 52.38% (52.24%); H, 5.01% (5.01%); N, 5.65% (5.80%).

[$CoFe_3S_4(IMes)_3Cl$]

Cp_2Co (43.4 mg, 0.2295 mmol) in DFB (1 mL) was added dropwise to a stirring solution of [$CoFe_3S_4(IMes)_3Cl$][PF_6] (349.9 mg, 0.2416 mmol) in DFB (8 mL). After 10 min, the solution was filtered through Celite and concentrated to dryness *in vacuo*. The solids were triturated with pentane (2 mL), then dried. The product was extracted with benzene (8 mL), filtered through Celite, and concentrated to 5 mL. The solution was layered with pentane (15 mL) overnight. The product was obtained as black needles (290.8 mg, 97%). Crystals for structure determination were obtained by diffusion of pentane onto a saturated benzene solution at RT. ^1H NMR (C_6D_6, 400 MHz, 298 K): δ (ppm) 7.78 (s, 6H, Im-H), 7.26 (s, 12H, *m*-H), 2.57 (s, 18H, *p*-Me), 2.39 (s, 36H, *o*-Me). Anal. Found (Calc.): C, 57.98% (58.05%); H, 5.48% (5.57%); N, 6.34% (6.45%).

[$Co_4S_4(IMes)_3Cl$]

Solid trityl chloride (539.2 mg, 1.934 mmol) was slowly added to a stirring slurry of [$Co_4S_4(P^iPr_3)_4$] (2.0402 g, 2.0302 mmol) in pentane (30 mL). The mixture was stirred overnight at RT. The solids were collected by filtration and washed with copious pentane (80 mL) until the flowthrough was colorless. The solids were extracted with benzene (130 mL), filtered through Celite, and concentrated to dryness *in vacuo*. The 1.4432 g of amorphous black solids, assigned as [$Co_4S_4(P^iPr_3)_3Cl$], were dissolved in benzene (70 mL). IMes (1.6610 g, 5.4559 mmol) in benzene (5 mL) was added with stirring. The mixture was stirred for 3 h at RT, then concentrated to dryness *in vacuo*. The resulting solids were washed with pentane (4 × 10 mL) to remove P^iPr_3. The remaining black solids were dissolved in THF (120 mL) and additional IMes (570.0 mg, 1.872 mmol) was added. After stirring for 1 h, the solution was filtered through Celite. The filtrate was concentrated *in vacuo* to 75 mL and layered with pentane (100 mL) at −30 °C. The product was obtained as black needles (899.2 mg, 34%). Crystals for structure determination were obtained by layering a saturated benzene solution with pentane. ^1H NMR (DFB, 400 MHz, 298 K): δ (ppm) 8.46 (s, 6H, Im-H), 6.04 (s, 12H, *m*-H), 2.89 (s, 18H, *p*-Me), 1.82 (s, 36H, *o*-Me). Anal. Found (Calc.): C, 57.54% (57.64%); H, 6.17% (5.53%); N, 6.41% (6.40%).

[$Co_4S_4(IMes)_3Cl$][PF_6]

$FcPF_6$ (214.0 mg, 0.6465 mmol) in DFB (4 mL) was added dropwise to a stirring solution of [$Co_4S_4(IMes)_3Cl$] (892.9 mg, 0.6802 mmol) in DFB (30 mL). After 30 min, the solution was filtered through Celite. The filtrate was concentrated *in vacuo* to 10 mL. The product was precipitated by addition of Et_2O (20 mL). The resulting solids were washed with additional Et_2O (3 × 5 mL). The product was obtained as a black crystalline solid (941.4 mg, 100%). Crystals for structure determination were obtained by layering a saturated CH_2Cl_2 solution with pentane. ^1H NMR (DFB, 500 MHz, 298 K): δ (ppm) 6.03 (s, 12H, *m*-H), 5.53 (s, 6H, Im-H), 3.40 (s, 36H, *o*-Me), 3.14 (s, 18H, *p*-Me). Anal. Found (Calc.): C, 47.52% (51.91%); H, 5.02% (4.98%); N, 5.12% (5.77%).

[$TlCo_3S_4(IMes)_3$][PF_6]

TlTp (300.7 mg, 0.7204 mmol) in THF (1 mL) was added to a stirring slurry of [$Co_4S_4(IMes)_3Cl$][PF_6] (498.8 mg, 0.3422 mmol) in THF (20 mL). After 30 min, the solution was filtered through Celite, and the filtrate concentrated to dryness *in vacuo*. The resulting solids were then suspended in Et$_2$O (10 mL) and stirred for 15 min, during which time the solution began to turn slightly yellow. The solution was decanted. Additional Et$_2$O (10 mL) was added, and the mixture stirred for another 15 min. This process was repeated twice more, discarding the Et$_2$O each time. Finally, the residual, Et$_2$O insoluble, black solids were extracted with THF (10 mL), and the solution filtered through Celite. The filtrate was concentrated *in vacuo* to 5 mL, then layered with pentane (15 mL) at −30 °C. The product was obtained as a black crystalline solid (442.0 mg, 82%). Crystals for structure determination were obtained by layering a saturated THF solution with Et$_2$O at −35 °C. ^{1}H NMR (DFB, 400 MHz, 298 K): δ (ppm) 6.12 (s, 6H, Im-H), 5.94 (s, 12H, *m*-H), 2.41 (s, 36H, *o*-Me), 2.01 (s, 18H, *p*-Me).

[FeCo$_3$S$_4$(IMes)$_3$Cl][PF$_6$]

FeCl$_2$ (41.1 mg, 0.3243 mmol) was stirred in THF (1.5 mL) for 1 h. The FeCl$_2$ slurry was added dropwise to a stirring slurry of [TlCo$_3$S$_4$(IMes)$_3$][PF$_6$] (300.2 mg, 0.1915 mmol) in THF (15 mL). After 15 min, the solution was filtered through Celite, and the filtrate concentrated to 5 mL *in vacuo*. The product was precipitated by addition of Et$_2$O (15 mL). The resulting black solids were washed with Et$_2$O (3 × 5 mL), then extracted with DFB (6 mL) and filtered through Celite. The solution as concentrated *in vacuo* to 3 mL, then layered with Et$_2$O (15 mL) at −30 °C. The product was obtained as black needles (234.6 mg, 84%). Crystals for structure determination were obtained by layering a saturated DFB solution with Et$_2$O at −30 °C. ^{1}H NMR (DFB, 400 MHz, 298 K): δ (ppm) 6.44 (s, 12H, *m*-H), 2.81 (s, 18H, *p*-Me), 2.35 (s, 36H, *o*-Me). Anal. Found (Calc.): C, 51.52% (52.02%); H, 5.06% (4.99%); N, 5.62% (5.78%).

[FeCo$_3$S$_4$(IMes)$_3$Cl]

Cp$_2$Co (24.7 mg, 0.1306 mmol) in DFB (1 mL) was added dropwise to a stirring solution of [FeCo$_3$S$_4$(IMes)$_3$Cl][PF$_6$] (200.5 mg, 0.1378 mmol) in DFB (5 mL). After 10 min, the solution was filtered through Celite and concentrated to dryness *in vacuo*. The solids were triturated with pentane (2 mL), then dried. The product was extracted with benzene (8 mL), filtered through Celite, and concentrated to 5 mL. The solution was layered with pentane (15 mL) overnight. The product was obtained as black needles (162.3 mg, 95%). Crystals for structure determination were obtained by diffusion of pentane onto a saturated benzene solution at RT. ^{1}H NMR (C$_6$D$_6$, 400 MHz, 298 K): δ (ppm) 6.09 (s, 12H, *m*-H), 2.15 (s, 18H, *p*-Me), 1.68 (s, 36H, *o*-Me). Anal. Found (Calc.): C, 57.63% (57.78%); H, 5.36% (5.54%); N, 6.47% (6.42%).

[CoFe$_3$S$_4$(IMes)$_3$(CO)]

In a 50 mL Schlenk flask, [CoFe$_3$S$_4$(IMes)$_3$Cl] (200.0 mg, 0.1534 mmol) in toluene (6 mL) was frozen in a liquid N$_2$ cooled cold-well. Separately, Ti(N{^{t}Bu}Ar)$_3$ (176.9 mg, 0.3067 mmol) in toluene (6 mL) was cooled to near freezing. This chilled solution was then carefully layered onto the [CoFe$_3$S$_4$(IMes)$_3$Cl] solution without mixing. With both solutions frozen, the flask was sealed with a rubber septum and wire. Outside the glovebox, the flask was kept frozen in liquid N$_2$ while the headspace was evacuated *in vacuo*. Using a 10 mL gas-tight syringe with hypodermic needle, CO (7.5 mL) was added to the still frozen, layered solutions. The mixture was allowed to thaw to RT with vigorous stirring and shaking. After 5 min, the flask was returned to the glovebox, and the solution was filtered through Celite. The filtrate was concentrated to dryness *in vacuo*, then the residual solids were washed with copious pentane (5 × 4 mL) until the pentane solution was nearly colorless. The remaining black solids were extracted with Et_2O (6 mL). The solution was filtered through Celite. The filtrate was concentrated *in vacuo* to 3 mL, then layered with pentane (10 mL) at −30 °C. The product was obtained as black crystalline solids (140.3 mg, 71%). Crystals for structure determination were obtained by layering a saturated Et_2O solution with pentane at −30 °C. ^1H NMR (C_6D_6, 400 MHz, 298 K): δ (ppm) 8.49 (s, 6H, Im-H), 7.37 (s, 12H, *m*-H), 2.67 (s, 18H, *p*-Me), 2.60 (s, 36H, *o*-Me). Anal. Found (Calc.): C, 59.54% (59.31%); H, 5.73% (5.60%); N, 6.61% (6.48%).

[$Co_4S_4(IMes)_3(CO)$]

In a 50 mL Schlenk flask, [$Co_4S_4(IMes)_3Cl$] (117.1 mg, 0.0892 mmol) in toluene (3 mL) was frozen in a liquid N_2 cooled cold-well. Separately, Ti(N{^{t}Bu}Ar)$_3$ (102.8 mg, 0.1782 mmol) in toluene (3 mL) was cooled to near freezing. This chilled solution was then carefully layered onto the [$Co_4S_4(IMes)_3Cl$] solution without mixing. With both solutions frozen, the flask was sealed with a rubber septum and wire. Outside the glovebox, the flask was kept frozen in liquid N_2 while the headspace was evacuated *in vacuo*. Using a 6 mL gas-tight syringe with hypodermic needle, CO (4.35 mL) was added to the still frozen, layered solutions. The mixture was allowed to thaw to RT with vigorous stirring and shaking. After 5 min, the flask was returned to the glovebox, and the solution was filtered through Celite. The filtrate was concentrated to dryness *in vacuo*, then the residual solids were washed with copious pentane (5 × 4 mL) until the pentane solution was nearly colorless. The remaining black solids were extracted with Et_2O (3 mL). The solution was filtered through Celite. The filtrate was concentrated *in vacuo* to 1.5 mL, then layered with pentane (6 mL) at −30 °C. The product was obtained as black crystalline solids (81.0 mg, 69%). Crystals for structure determination were obtained by layering a saturated Et_2O solution with pentane at −30 °C. ^1H NMR (C_6D_6, 400 MHz, 298 K): δ (ppm) 14.31 (s, 6H, Im-H), 7.06 (s, 12H, *m*-H), 4.72 (s, 18H, *p*-Me), 2.51 (s, 36H, *o*-Me). Anal. Found (Calc.): C, 56.94% (58.89%); H, 5.76% (5.56%); N, 6.33% (6.44%).

[$FeCo_3S_4(IMes)_3(CO)$]

In a 50 mL Schlenk flask, [$FeCo_3S_4(IMes)_3Cl$] (177.0 mg, 0.1351 mmol) in toluene (6 mL) was frozen in a liquid N_2 cooled cold-well. Separately, Ti(N{^{t}Bu}Ar)$_3$ (155.9 mg, 0.2703 mmol) in toluene (6 mL) was cooled to near freezing. This chilled solution was then carefully layered onto the [$FeCo_3S_4(IMes)_3Cl$] solution without mixing. With both solutions frozen, the flask was sealed with a rubber septum and wire. Outside the glovebox, the flask was kept frozen in liquid N_2 while the headspace was evacuated *in vacuo*. Using a 10 mL gas-tight syringe with hypodermic needle, CO (7.5 mL) was added to the still frozen, layered solutions. The mixture was allowed to thaw to RT with vigorous stirring and shaking. After 5 min, the flask was returned to the glovebox, and the solution was filtered through Celite. The filtrate was concentrated to dryness *in vacuo*, then the residual solids were washed with copious pentane (5 × 4 mL) until the pentane solution was nearly colorless. The remaining black solids were extracted with Et_2O (6 mL). The solution was filtered through Celite. The filtrate was concentrated *in vacuo* to 3 mL, then layered with pentane (10 mL) at −30 °C. The product was obtained as black crystalline solids (96.4 mg, 55%). Crystals for structure determination were obtained by layering a saturated Et_2O solution with pentane at −30 °C. ^1H NMR (C_6D_6, 500 MHz, 298 K): δ (ppm) 14.92 (s, 6H, Im-H), 6.70 (s, 12H, *m*-H), 3.20 (s, 18H, *p*-Me), 2.92 (s, 36H, *o*-Me). Anal. Found (Calc.): C, 57.17% (59.03%); H, 6.00% (5.77%); N, 6.42% (6.45%).

Spectroscopic and magnetochemical data

^{1}H NMR spectra

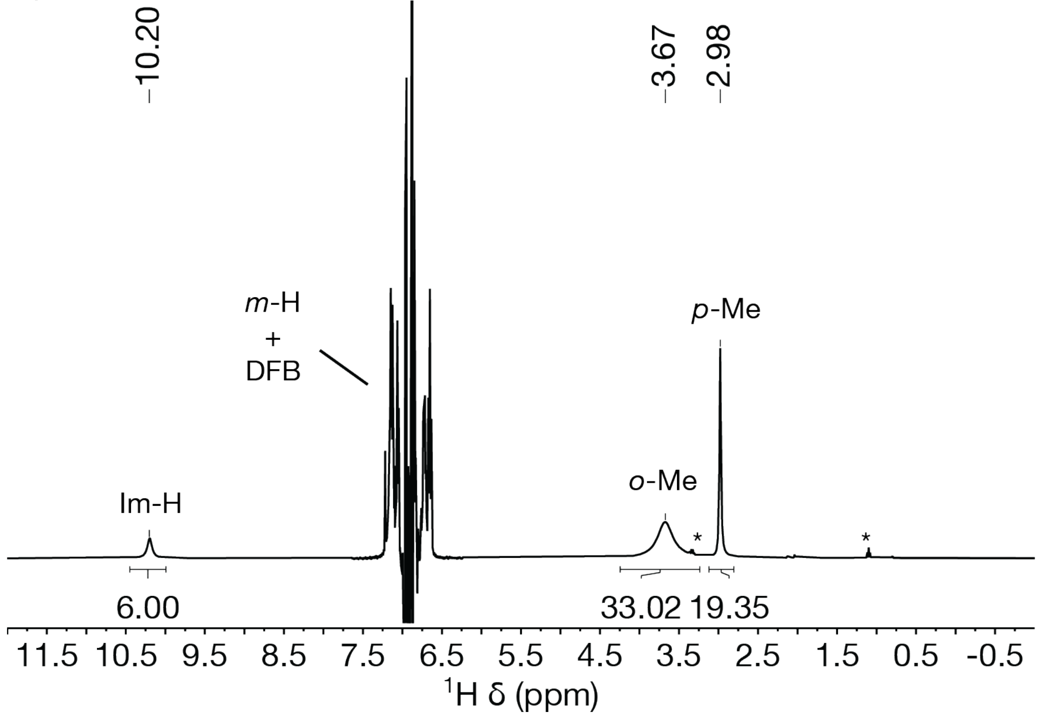

Figure S4.1. Solvent-suppressed ^{1}H NMR of [$TlFe_3S_4(IMes)_3$][PF_6] in DFB (400 MHz, 298 K; * = Et_2O). The *meta*-H of IMes ligands of [$TlFe_3S_4(IMes)_3$][PF_6] are obscured by solvent-suppressed DFB peaks.

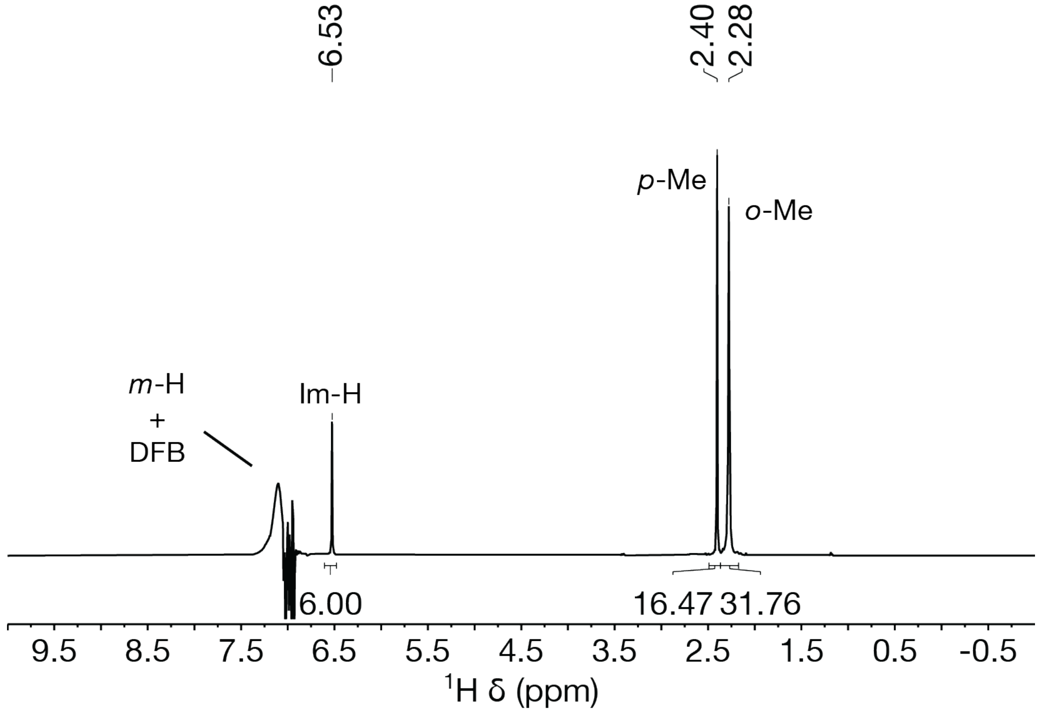

Figure S4.2. Solvent-suppressed ^{1}H NMR of [$CoFe_3S_4(IMes)_3Cl$][PF_6] in DFB (500 MHz, 298 K). The *meta*-H of IMes ligands of [$CoFe_3S_4(IMes)_3Cl$][PF_6] are obscured by solvent-suppressed DFB peaks.

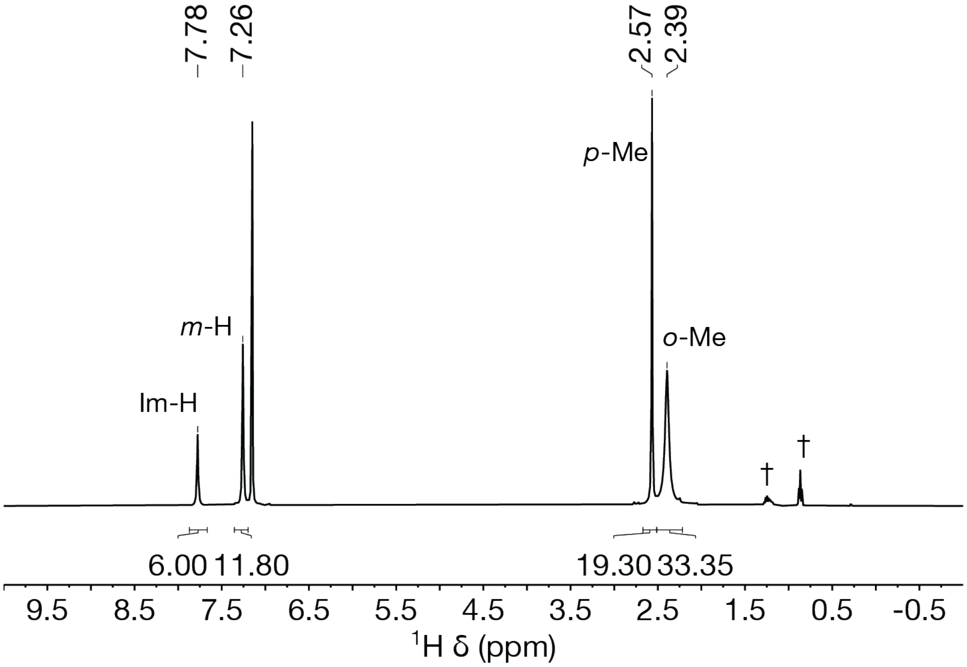

Figure S4.3. ^{1}H NMR of [$CoFe_3S_4(IMes)_3Cl$] in C_6D_6 (400 MHz, 298 K; † = pentane).

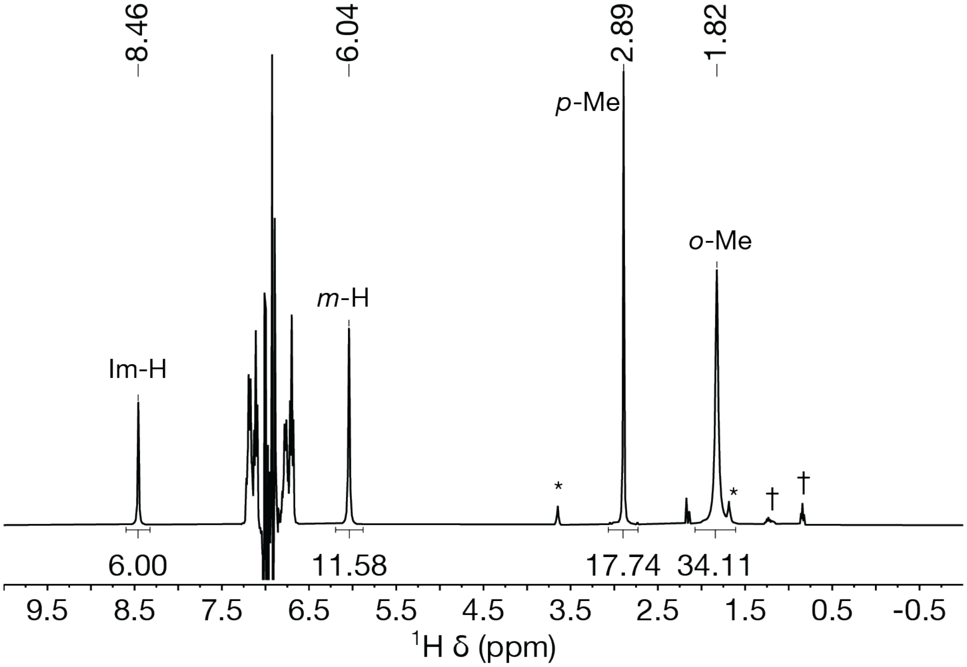

Figure S4.4. Solvent-suppressed ^{1}H NMR of [$Co_4S_4(IMes)_3Cl$] in DFB (400 MHz, 298 K; * = Et_2O, † = pentane).

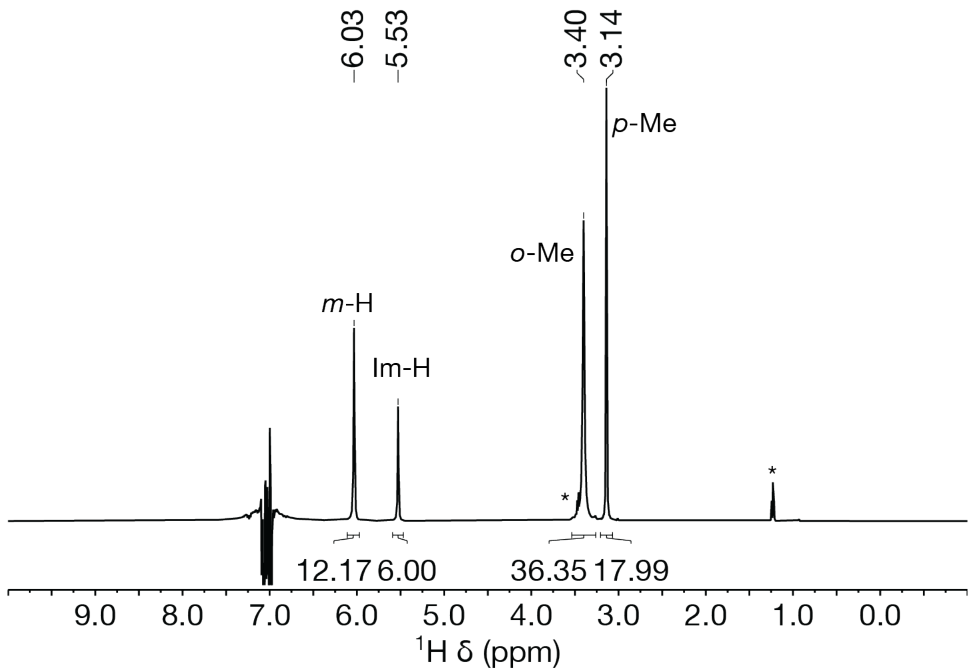

Figure S4.5. Solvent-suppressed ^{1}H NMR of $[Co_4S_4(IMes)_3Cl][PF_6]$ in DFB (500 MHz, 298 K; * = Et_2O).

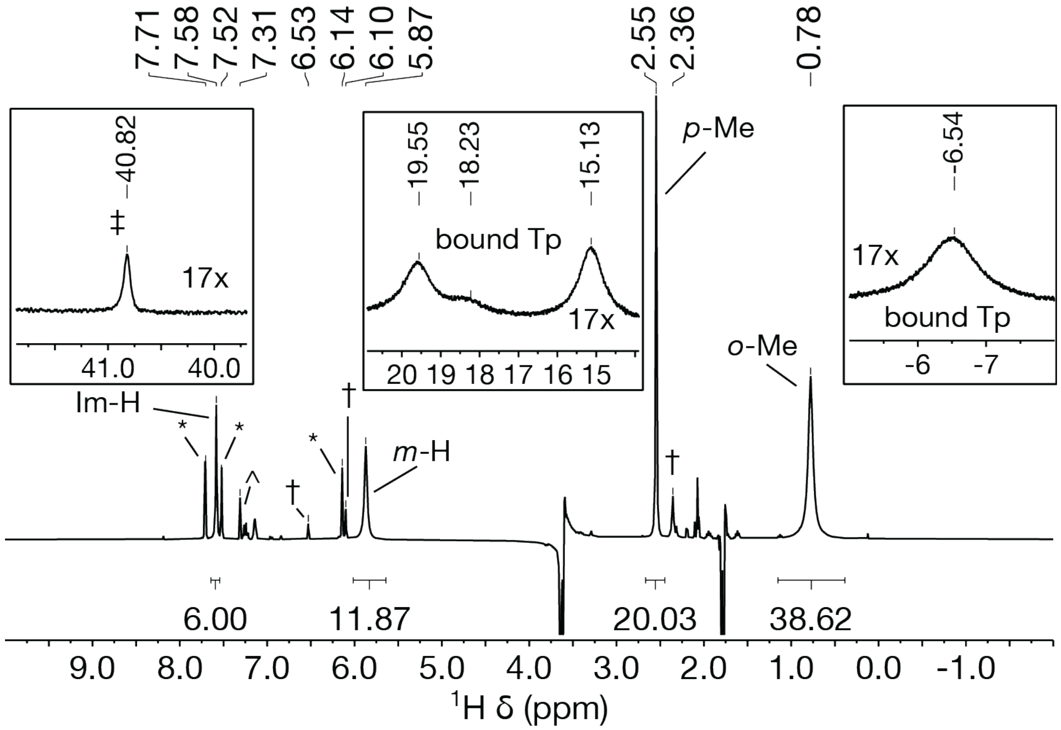

Figure S4.6. Solvent-suppressed ^{1}H NMR of crude reaction mixture following addition of TlTp to $[Co_4S_4(IMes)_3Cl][PF_6]$ in THF (400 MHz, 298 K; * = TlTp, † = $[TlCo_3S_4(IMes)_3][PF_6]$, ‡ = $CoTp_2$, ^ = PhH).

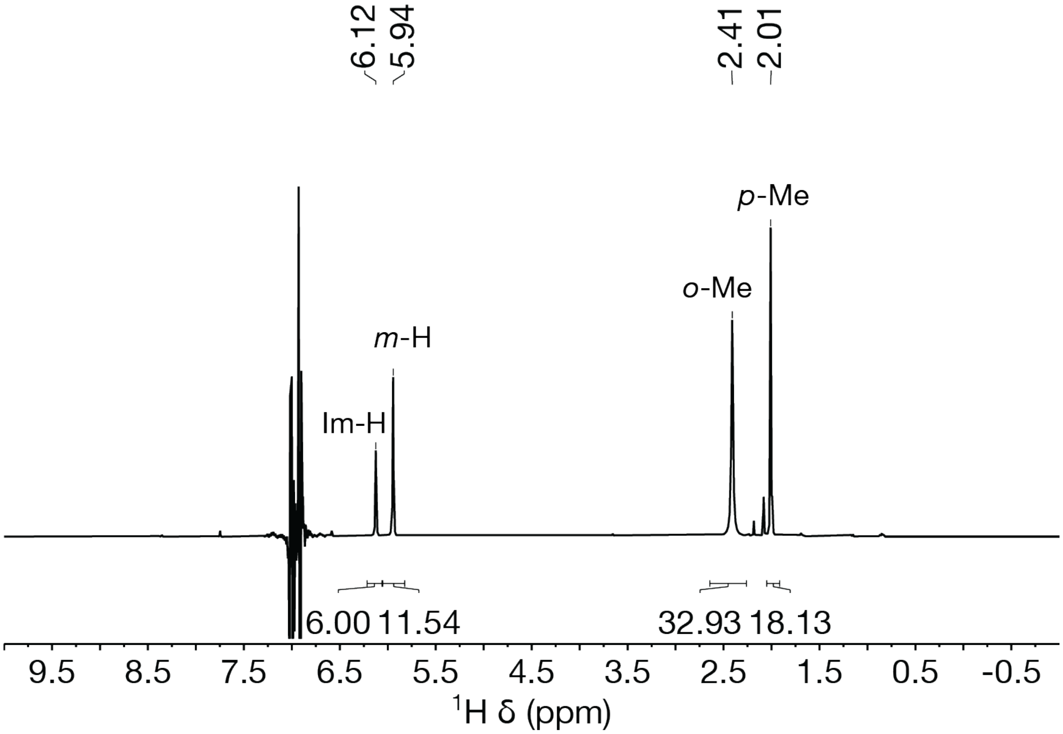

Figure S4.7. Solvent-suppressed ^{1}H NMR of [$TlCo_3S_4(IMes)_3$][PF_6] in DFB (400 MHz, 298 K).

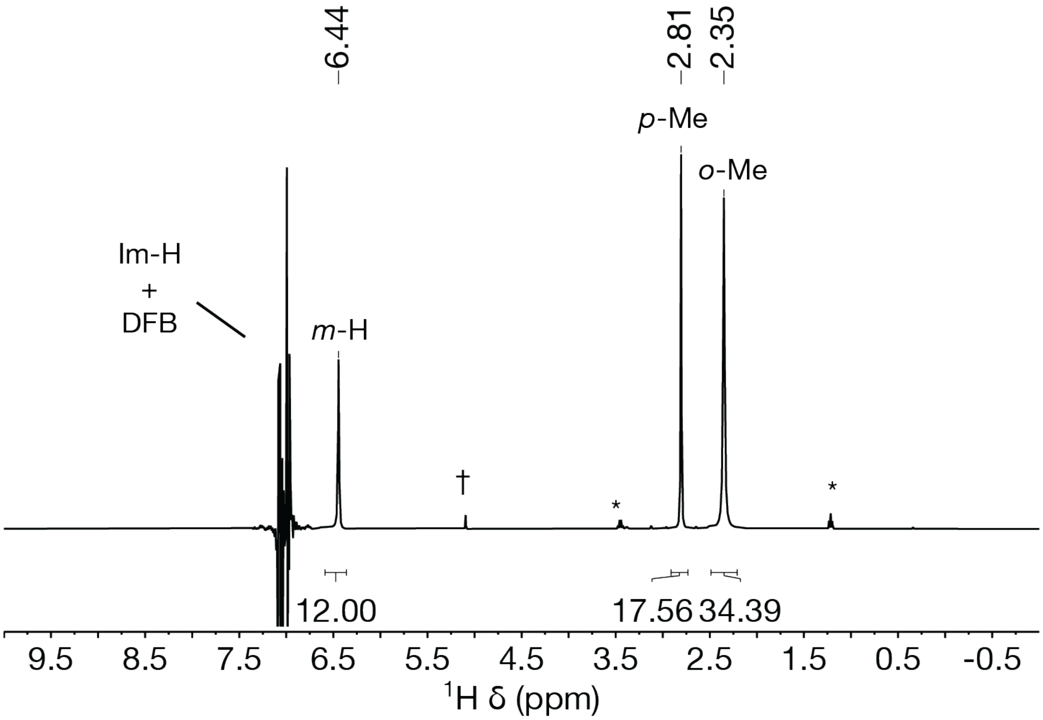

Figure S4.8. Solvent-suppressed ^{1}H NMR of [$FeCo_3S_4(IMes)_3Cl$][PF_6] in DFB (400 MHz, 298 K; * = CH_2Cl_2, † = Et_2O). Im-H of IMes ligands of [$FeCo_3S_4(IMes)_3Cl$][PF_6] are obscured by solvent-suppressed DFB peaks.

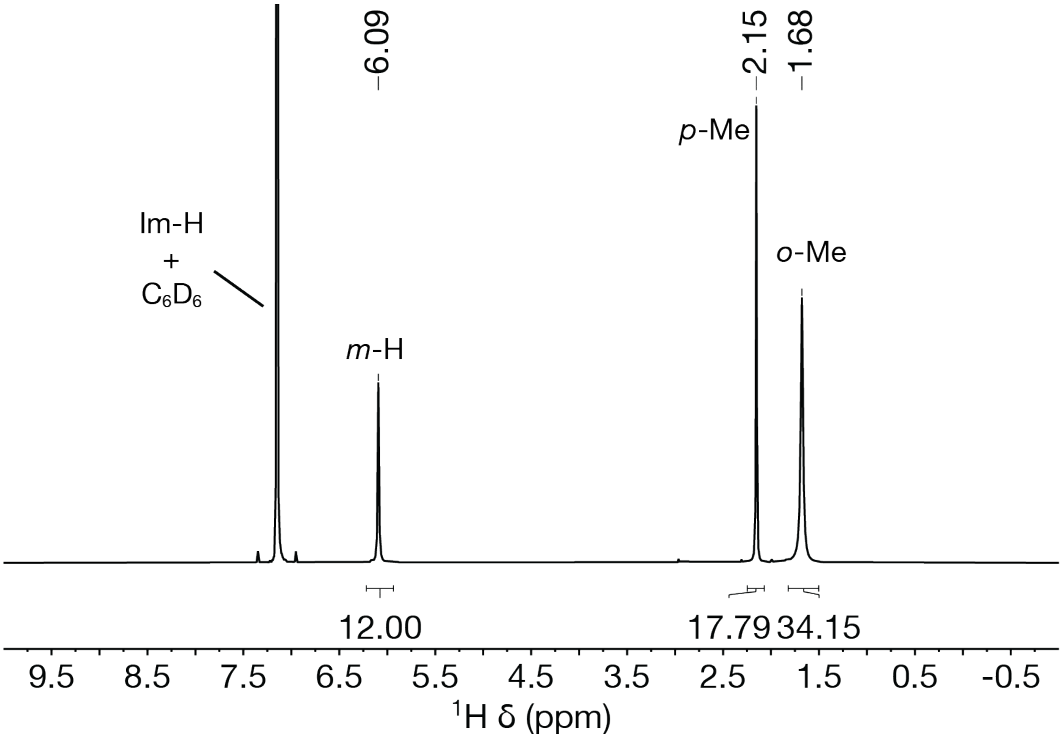

Figure S4.9. ^{1}H NMR of [$FeCo_3S_4(IMes)_3Cl$] in C_6D_6 (400 MHz, 298 K). Im-H of IMes ligands of [$FeCo_3S_4(IMes)_3Cl$] are obscured by the C_6D_6 peak.

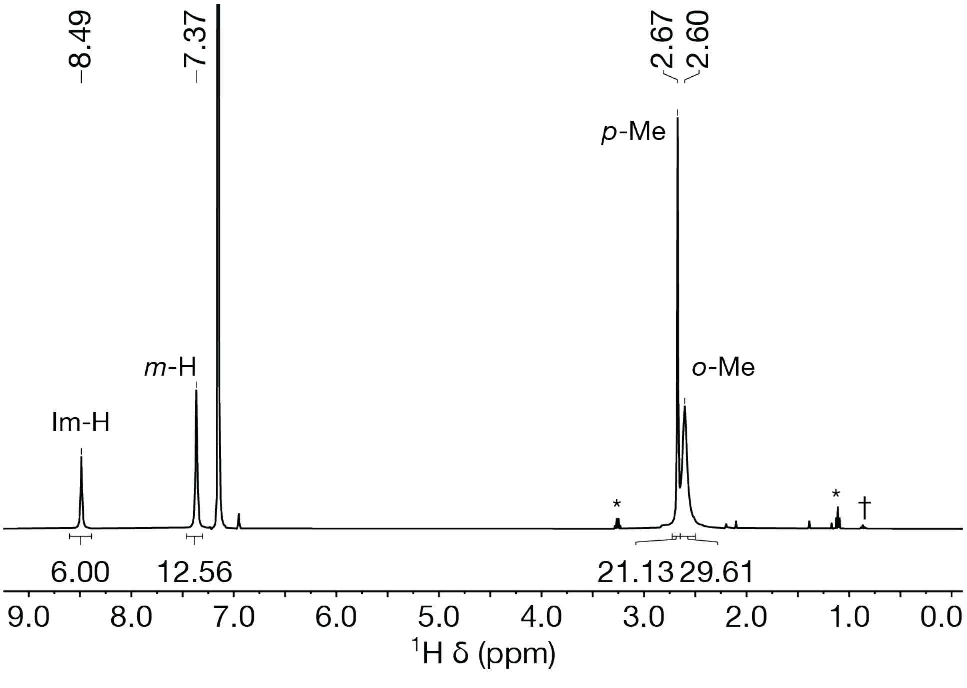

Figure S4.10. ^{1}H NMR of [$CoFe_3S_4(IMes)_3(CO)$] in C_6D_6 (400 MHz, 298 K; * = Et_2O, † = pentane).

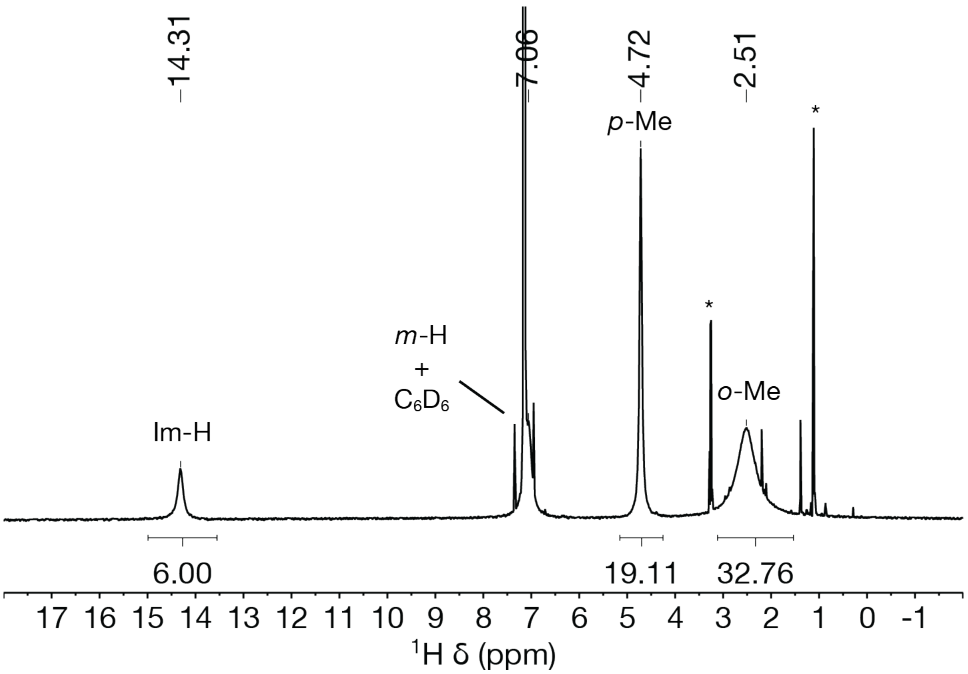

Figure S4.11. ^{1}H NMR of [$Co_4S_4(IMes)_3(CO)$] in C_6D_6 (400 MHz, 298 K; * = Et_2O). Im-H of IMes ligands of [$Co_4S_4(IMes)_3(CO)$] are obscured by the C_6D_6 peak.

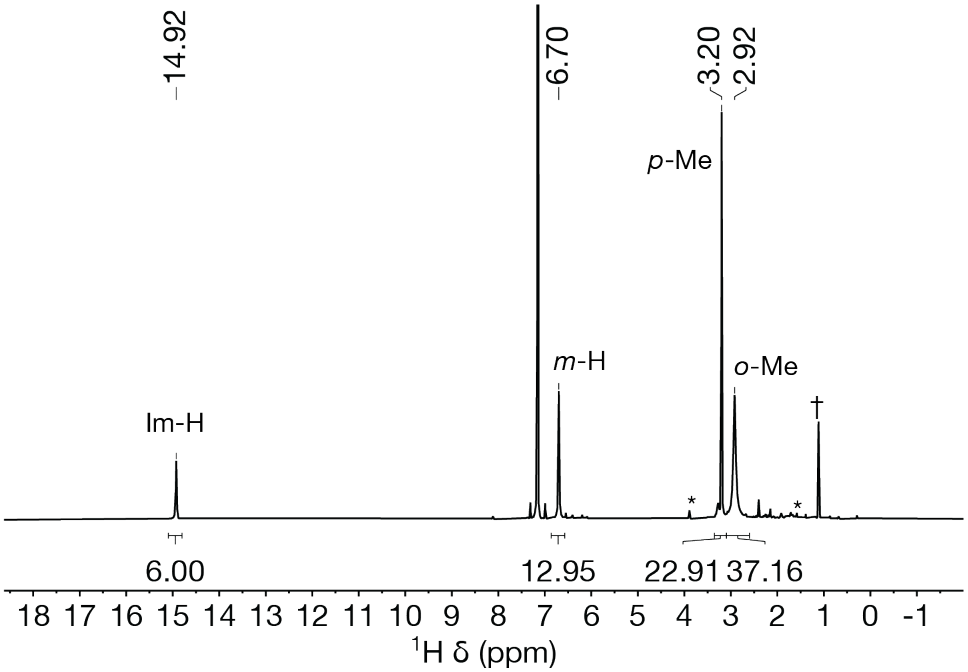

Figure S4.12. ^{1}H NMR of [$FeCo_3S_4(IMes)_3(CO)$] in C_6D_6 (500 MHz, 298 K; * = Et_2O, † = pentane).

SQUID magnetometry

The samples were prepared in the glovebox by loading microcrystalline solids into a polycarbonate gel capsule followed by immobilizing the sample by melting eicosane into the sample. Data are corrected for diamagnetic contributions using Pascal's constants.[101]

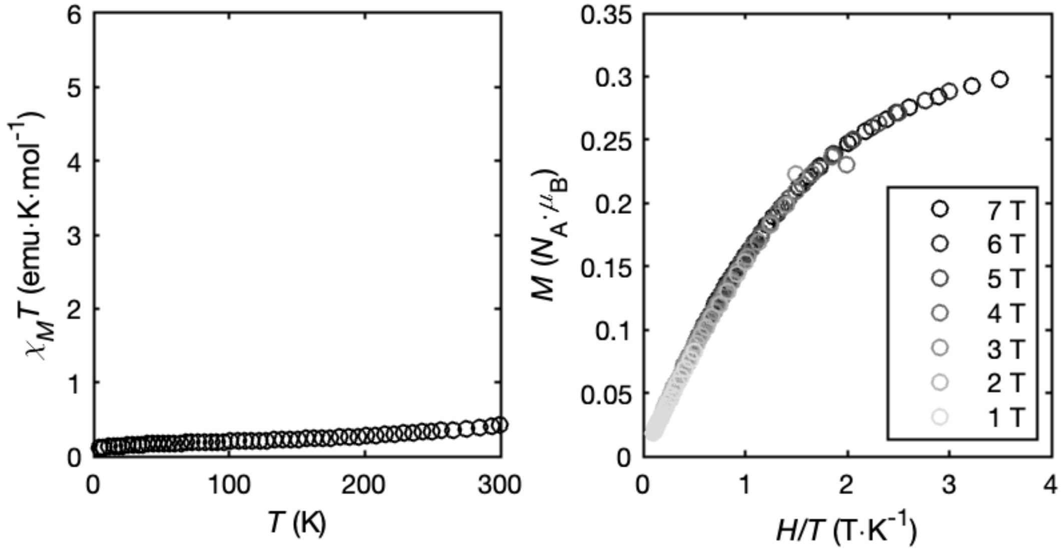

Figure S4.13. (*left*) SQUID magnetometry data (χ_MT vs. T) for [CoFe$_3$S$_4$(IMes)$_3$Cl][PF$_6$] collected at a field of 0.5 T. Data are corrected for diamagnetic contributions using Pascal's constants. The values of χ_MT at low temperature (*ca.* 0.17 emu K mol^{-1}) are close to the expected value for an S = ½ system (ca. 0.38 emu K mol^{-1}). The increase in χ_MT with increasing temperature may be attributed to temperature independent paramagnetism (TIP) or population of excited states. (*right*) Reduced magnetization curves collected from 1–7 T and 2–10 K. Overlaying curves is characteristic of S = ½ systems.

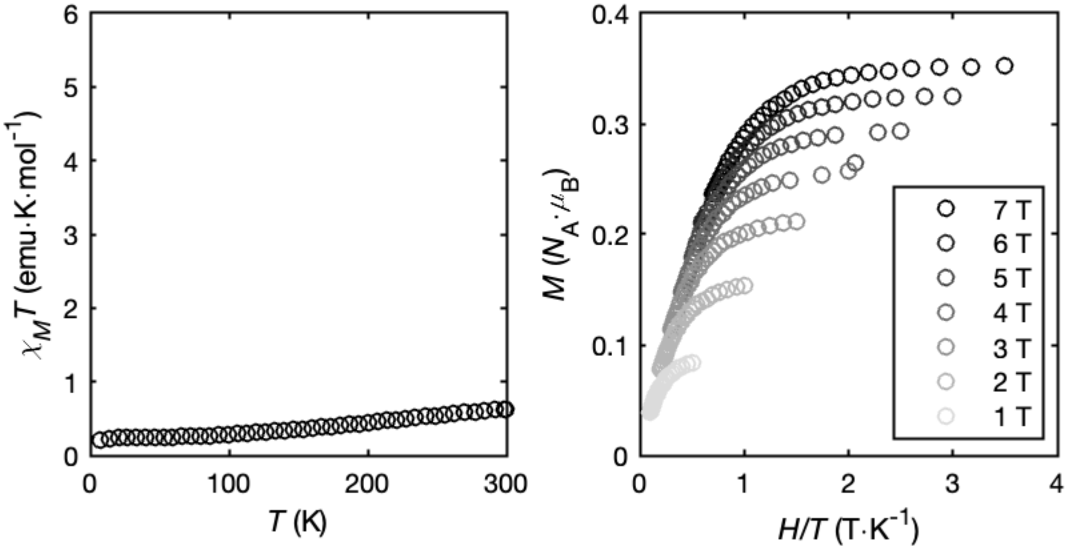

Figure S4.14. (*left*) SQUID magnetometry data (χ_MT vs. T) for [CoFe$_3$S$_4$(IMes)$_3$Cl] collected at a field of 0.5 T. Data are corrected for diamagnetic contributions using Pascal's constants. The values of χ_MT at low temperature (*ca.* 0.25 emu K mol^{-1}) are close to the expected value for an S = 0 system. The increase in χ_MT with increasing temperature may be attributed to temperature independent paramagnetism (TIP) or population of excited states. (*right*) Reduced magnetization curves collected from 1–7 T and 2–10 K.

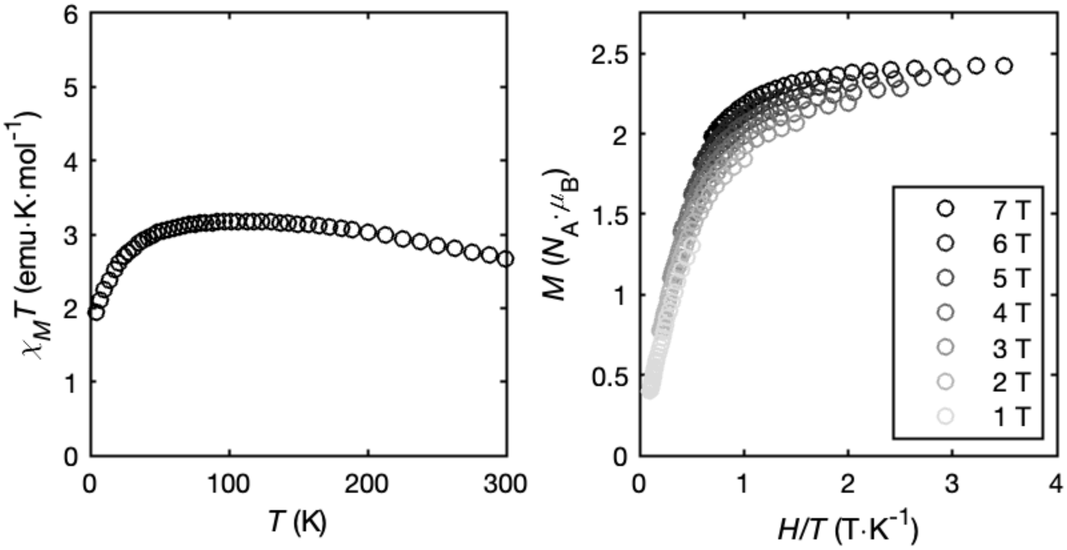

Figure S4.15. (*left*) SQUID magnetometry data (χ_MT vs. T) for [Co_4S_4(IMes)$_3$Cl] collected at a field of 0.5 T. Data are corrected for diamagnetic contributions using Pascal's constants. The values of χ_MT at low temperature (*ca.* 1.7 emu K mol^{-1}) are close to the expected value for an $S = \frac{3}{2}$ system (*ca.* 1.8 emu K mol^{-1}). The decrease in χ_MT with increasing temperature (>100 K) may be attributed to antiferromagnetic coupling within the cluster or population of excited states. (*right*) Reduced magnetization curves collected from 1–7 T and 2–10 K.

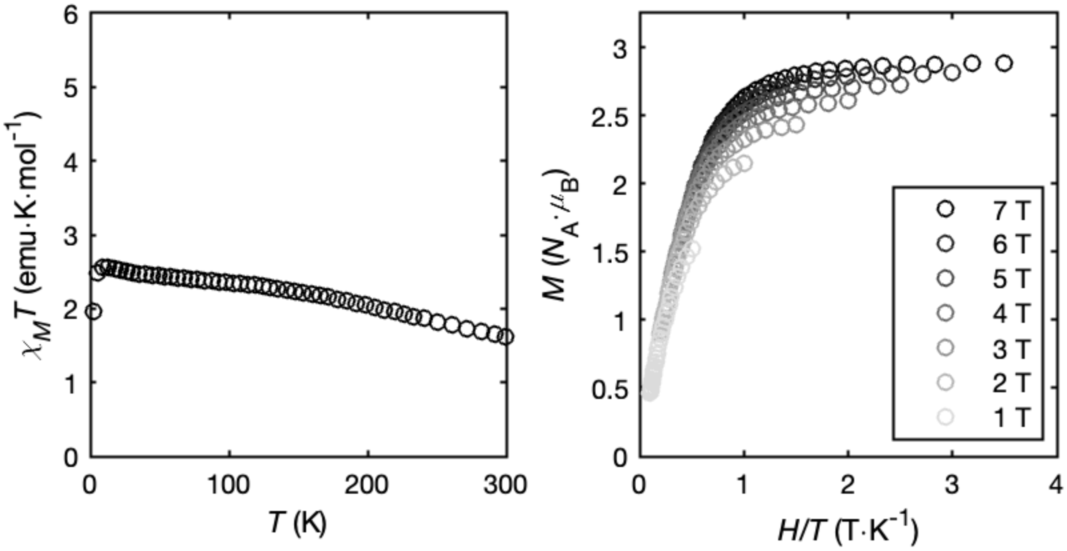

Figure S4.16. (*left*) SQUID magnetometry data (χ_MT vs. T) for [Co_4S_4(IMes)$_3$Cl][PF_6] collected at a field of 0.5 T. Data are corrected for diamagnetic contributions using Pascal's constants. The values of χ_MT at low temperature (*ca.* 2.5 emu K mol^{-1}) are close to the expected value for an $S = 2$ system (*ca.* 3.0 emu K mol^{-1}). The decrease in χ_MT with increasing temperature may be attributed to antiferromagnetic coupling within the cluster or population of excited states. (*right*) Reduced magnetization curves collected from 1–7 T and 2–10 K.

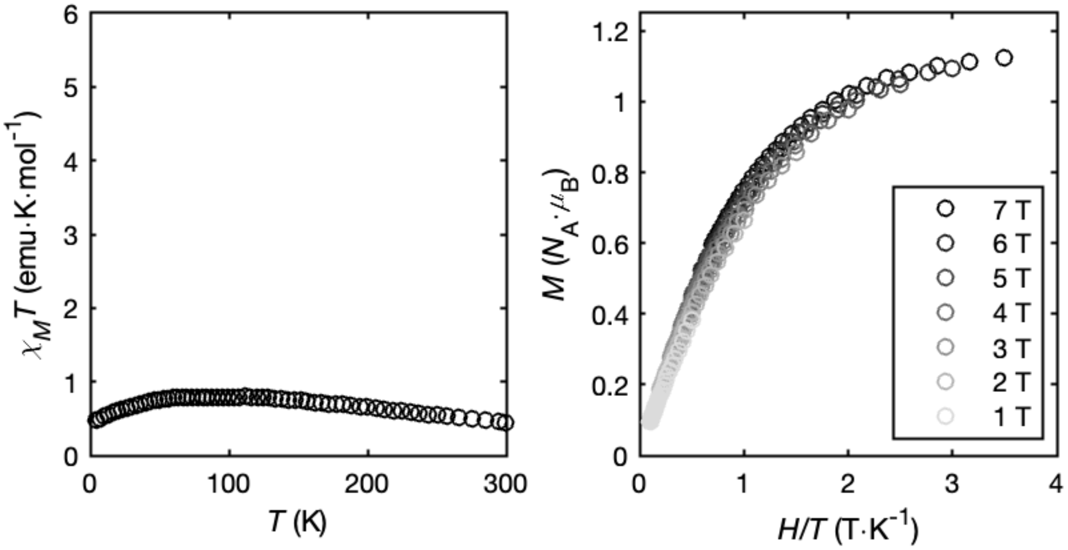

Figure S4.17. (*left*) SQUID magnetometry data (χ_MT vs. T) for [$FeCo_3S_4(IMes)_3Cl$][PF_6] collected at a field of 0.5 T. Data are corrected for diamagnetic contributions using Pascal's constants. The values of χ_MT at low temperature (*ca*. 0.4 emu K mol^{-1}) are close to the expected value for an $S = ½$ system (*ca*. 0.38 emu K mol^{-1}). The decrease in χ_MT with increasing temperature (>100 K) may be attributed to antiferromagnetic coupling within the cluster or population of excited states. (*right*) Reduced magnetization curves collected from 1–7 T and 2–10 K. Overlaying curves is characteristic of $S = ½$ systems.

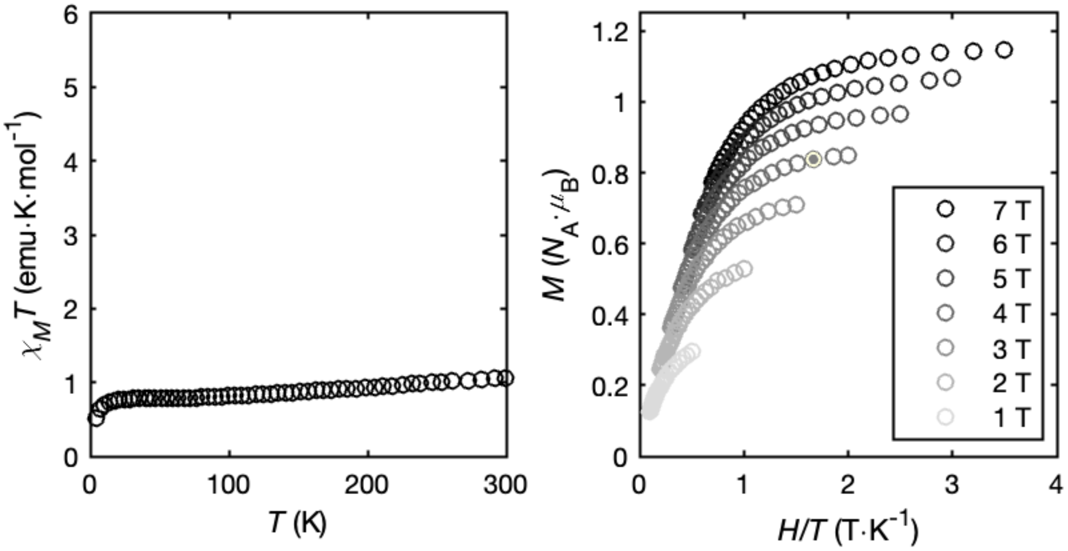

Figure S4.18. (*left*) SQUID magnetometry data (χ_MT vs. T) for [$FeCo_3S_4(IMes)_3Cl$] collected at a field of 0.5 T. Data are corrected for diamagnetic contributions using Pascal's constants. The values of χ_MT at low temperature (*ca*. 0.7 emu K mol^{-1}) are close to the expected value for an $S = 1$ system (*ca*. 1.0 emu K mol^{-1}). The increase in χ_MT with increasing temperature may be attributed to temperature independent paramagnetism (TIP) or population of excited states. (*right*) Reduced magnetization curves collected from 1–7 T and 2–10 K.

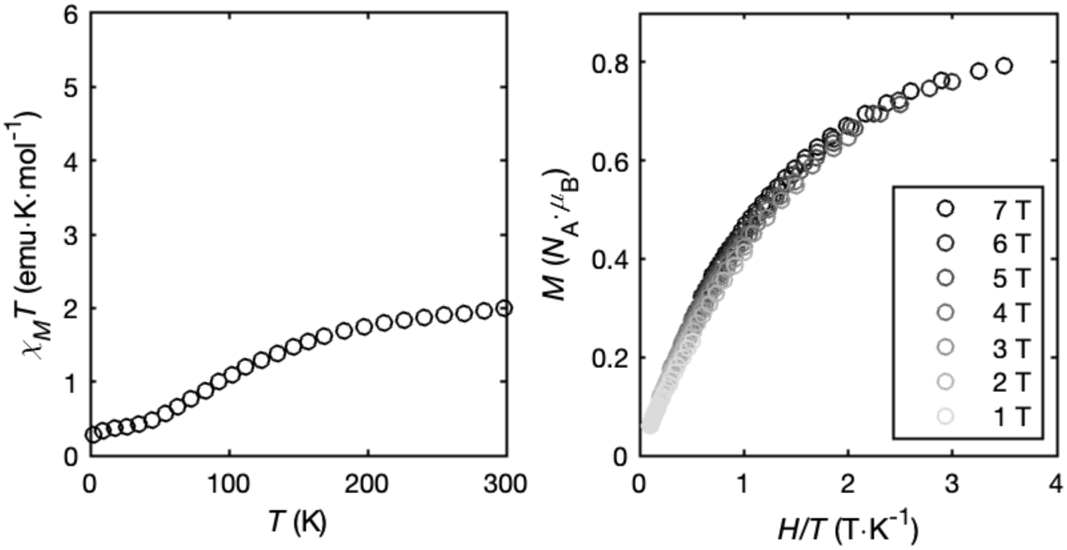

Figure S4.19. (*left*) SQUID magnetometry data (χ_MT vs. T) for [$CoFe_3S_4(IMes)_3(CO)$] collected at a field of 0.5 T. Data are corrected for diamagnetic contributions using Pascal's constants. The values of χ_MT at low temperature (*ca.* 0.34 emu K mol^{-1}) are close to the expected value for an $S = ½$ system (*ca.* 0.38 emu K mol^{-1}). The increase in χ_MT with increasing temperature may be attributed to temperature independent paramagnetism (TIP) or population of excited states. (*right*) Reduced magnetization curves collected from 1–7 T and 2–10 K. Overlaying curves is characteristic of $S = ½$ systems.

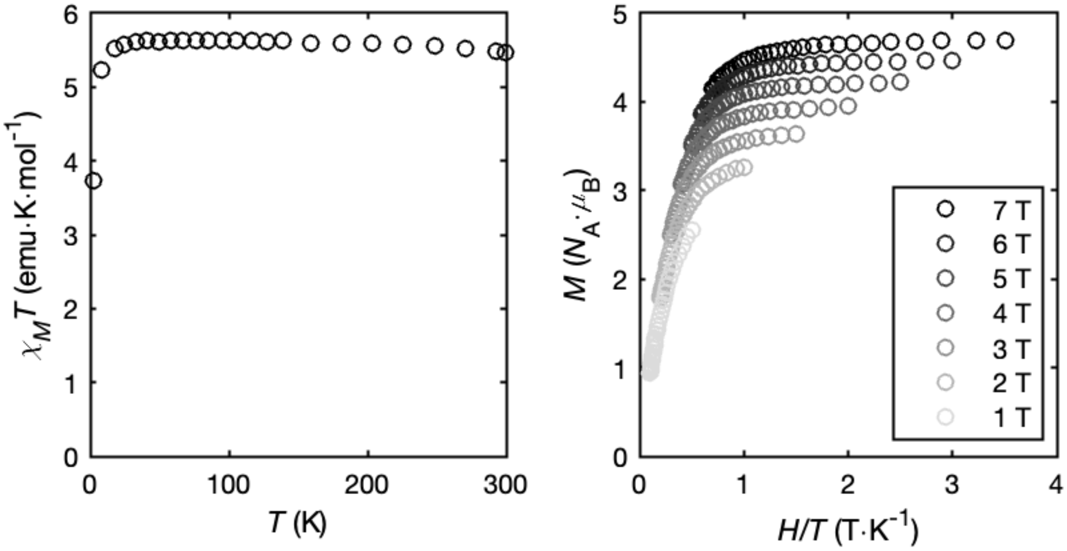

Figure S4.20. (*left*) SQUID magnetometry data (χ_MT vs. T) for [$Co_4S_4(IMes)_3(CO)$] collected at a field of 0.5 T. Data are corrected for diamagnetic contributions using Pascal's constants. The values of χ_MT at low temperature (*ca.* 5.6 emu K mol^{-1}) are close to the expected value for an $S = 3$ system (*ca.* 6.0 emu K mol^{-1}). (*right*) Reduced magnetization curves collected from 1–7 T and 2–10 K.

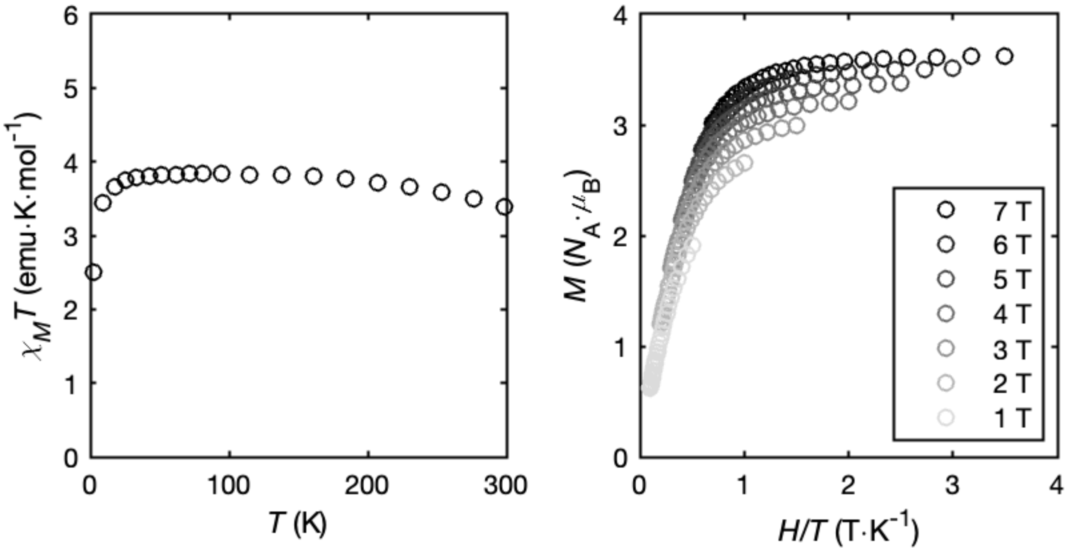

Figure S4.21. (*left*) SQUID magnetometry data (χ_MT vs. T) for [$FeCo_3S_4(IMes)_3(CO)$] collected at a field of 0.5 T. Data are corrected for diamagnetic contributions using Pascal's constants. The values of χ_MT at low temperature (*ca*. 3.8 emu K mol^{-1}) are close to the expected value for an $S = \frac{5}{2}$ system (*ca*. 4.4 emu K mol^{-1}). The decrease in χ_MT with increasing temperature (>100 K) may be attributed to antiferromagnetic coupling within the cluster or population of excited states. (*right*) Reduced magnetization curves collected from 1–7 T and 2–10 K.

IR spectra

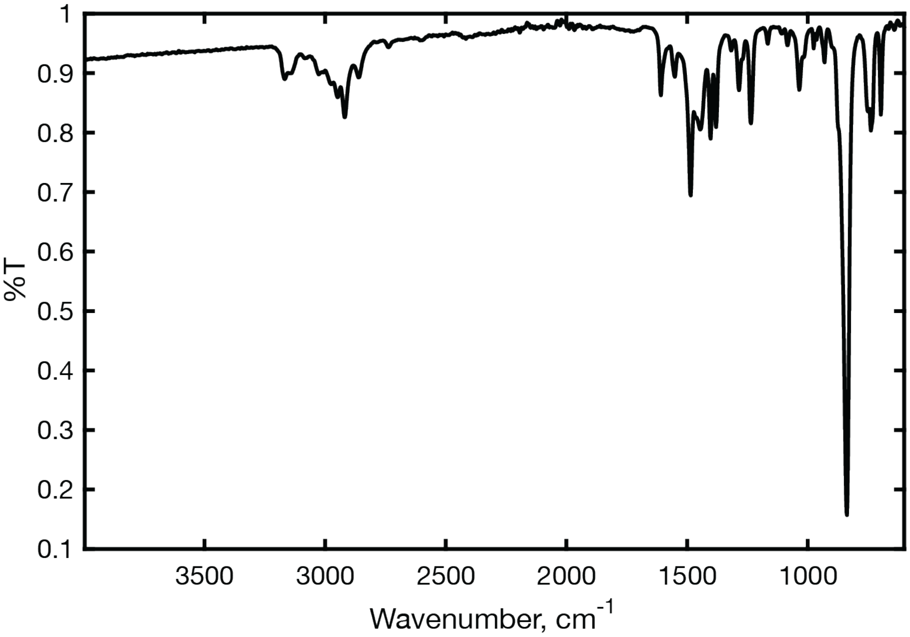

Figure S4.22. Thin film FT-IR spectrum of [$CoFe_3S_4(IMes)_3Cl$][PF_6].

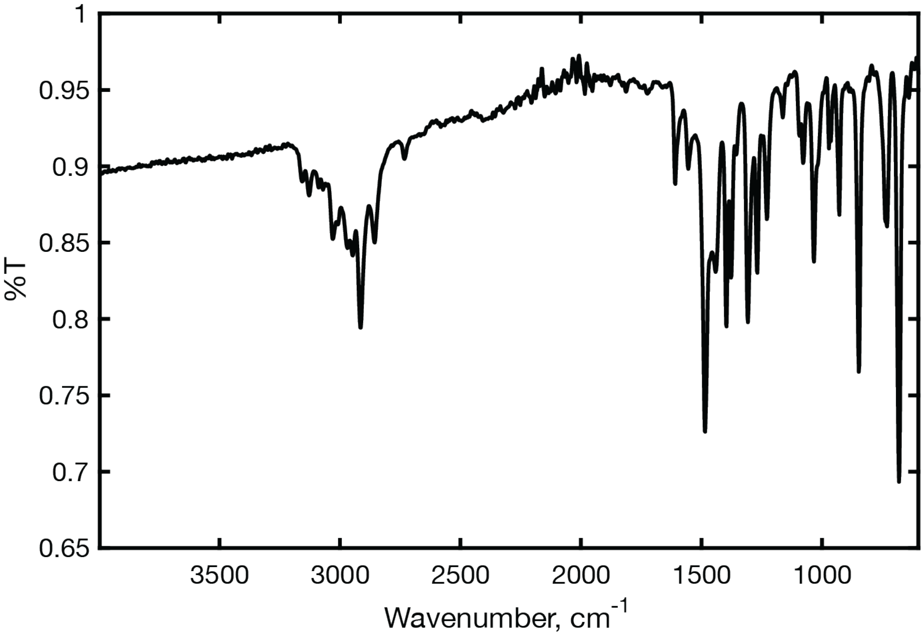

Figure S4.23. Thin film FT-IR spectrum of [$CoFe_3S_4(IMes)_3Cl$].

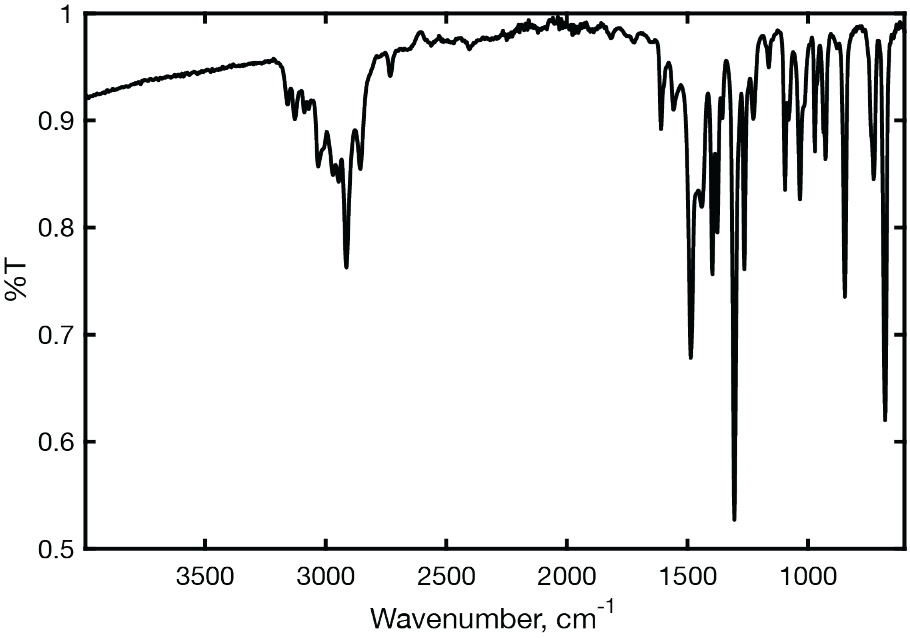

Figure S4.24. Thin film FT-IR spectrum of [$Co_4S_4(IMes)_3Cl$].

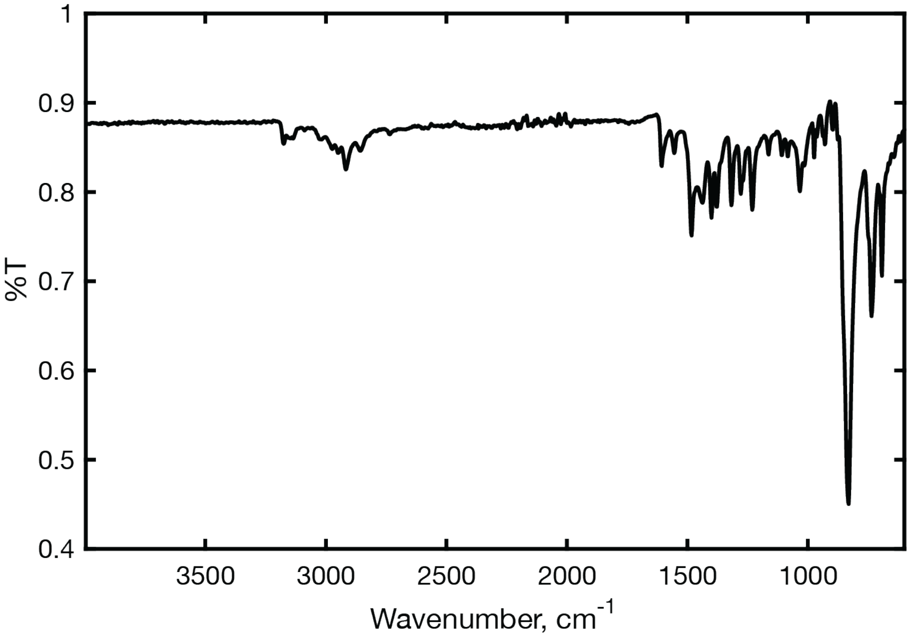

Figure S4.25. Thin film FT-IR spectrum of [$Co_4S_4(IMes)_3Cl$][PF_6].

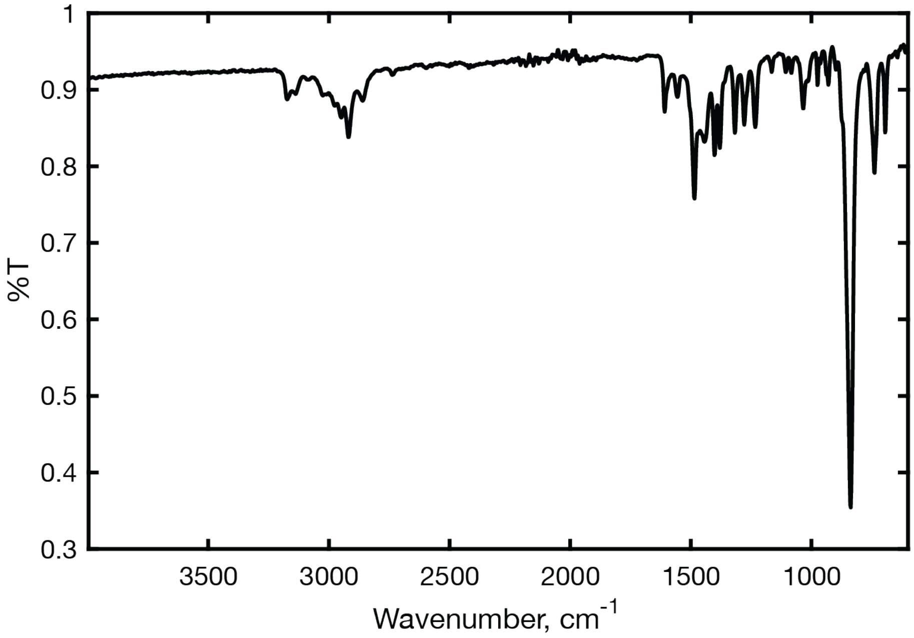

Figure S4.26. Thin film FT-IR spectrum of [$FeCo_3S_4(IMes)_3Cl$][PF_6].

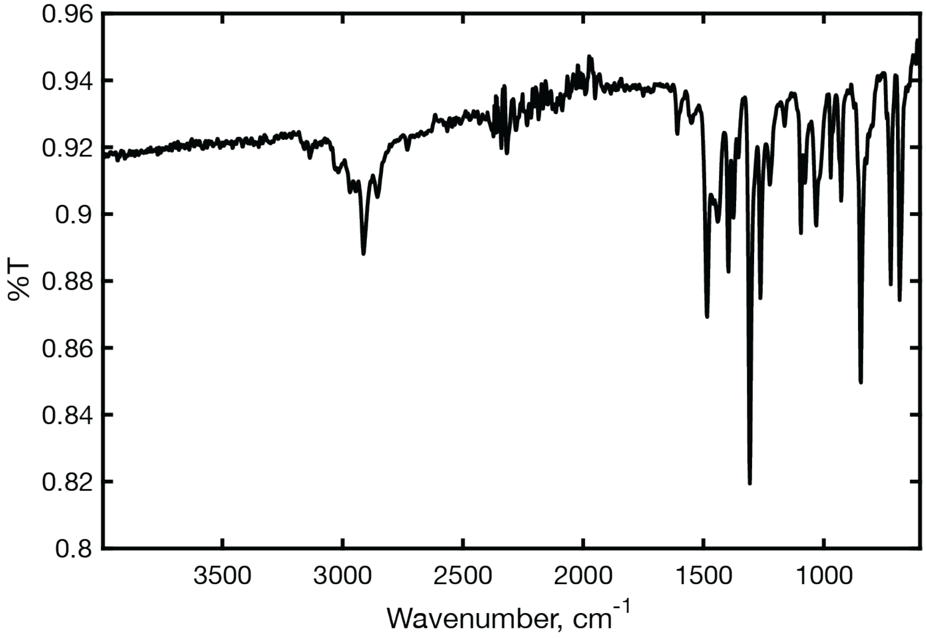

Figure S4.27. Thin film FT-IR spectrum of [$FeCo_3S_4(IMes)_3Cl$].

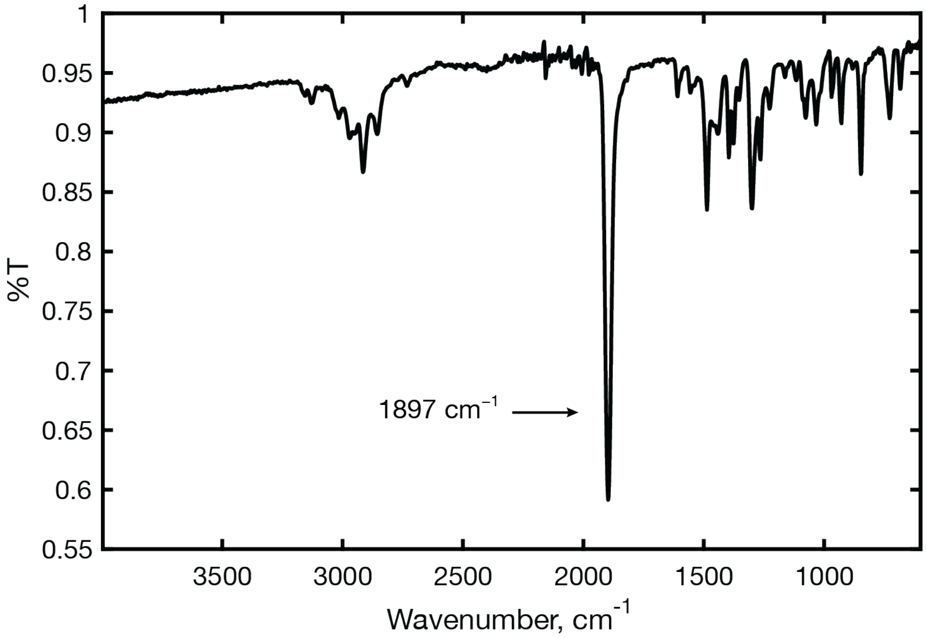

Figure S4.28. Thin film FT-IR spectrum of [$CoFe_3S_4(IMes)_3(CO)$].

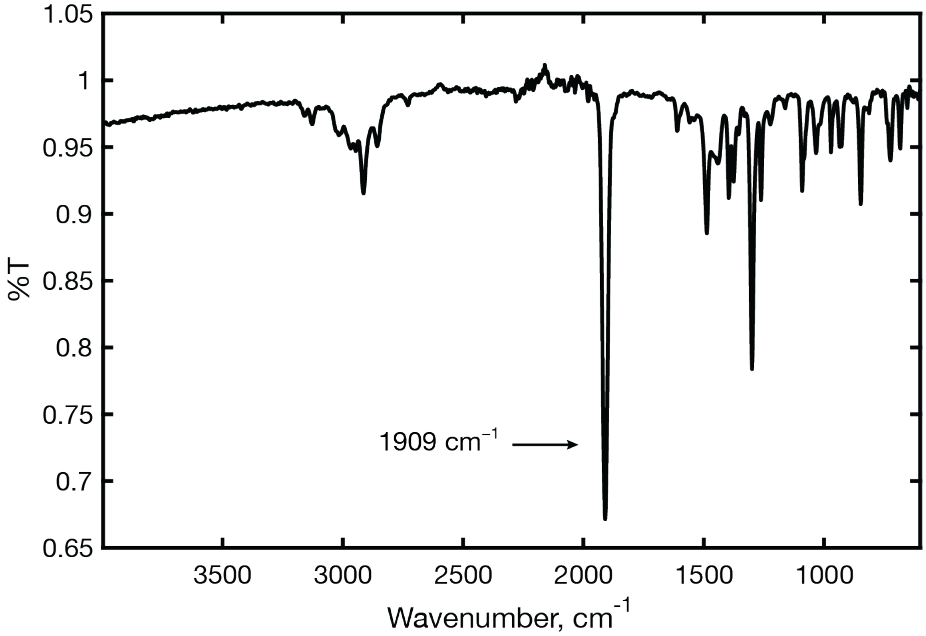

Figure S4.29. Thin film FT-IR spectrum of [$Co_4S_4(IMes)_3(CO)$].

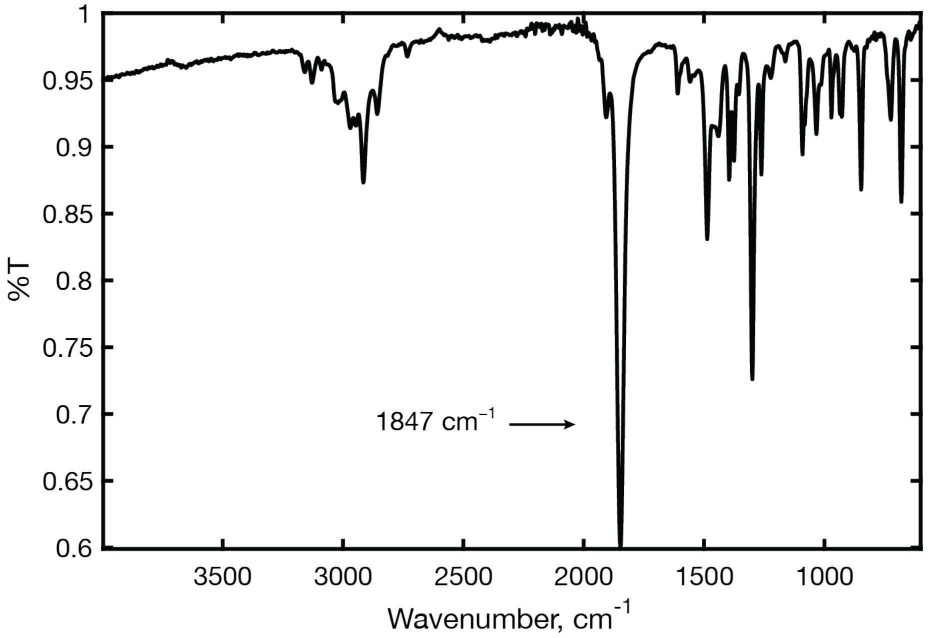

Figure S4.30. Thin film FT-IR spectrum of [$FeCo_3S_4(IMes)_3(CO)$].

Mössbauer spectra

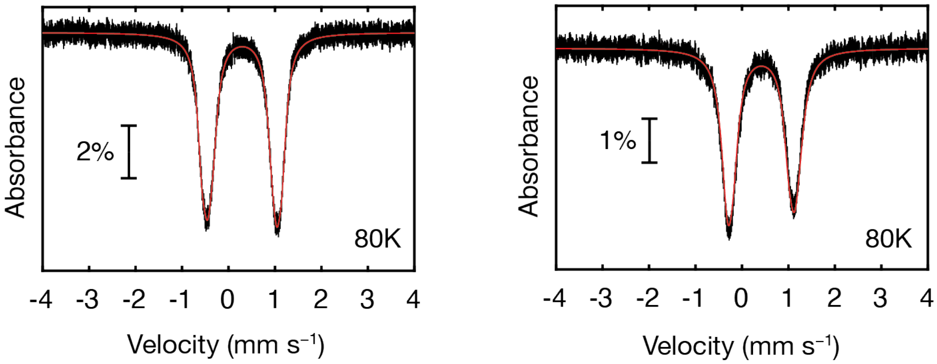

Figure S4.31. Mössbauer spectra (vertical lines) of [$CoFe_3S_4(IMes)_3Cl$][PF_6] (*left*) and [$CoFe_3S_4(IMes)_3Cl$] (*right*) at 80 K. Total simulations (red traces) using parameters in Table S4.1.

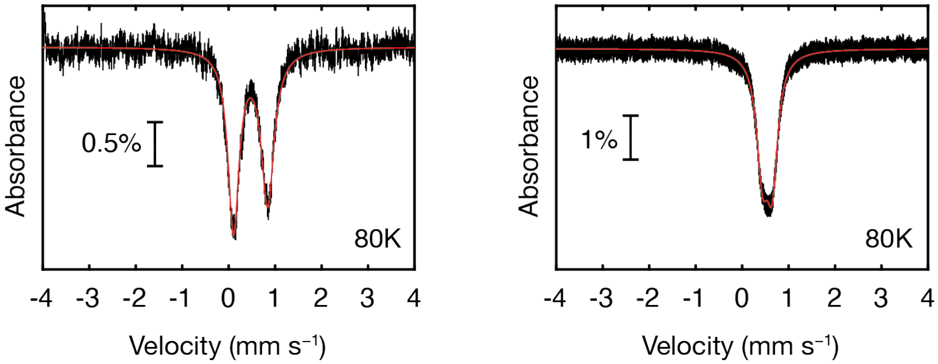

Figure S4.32. Mössbauer spectra (vertical lines) of [$FeCo_3S_4(IMes)_3Cl$][PF_6] (*left*) and [$FeCo_3S_4(IMes)_3Cl$] (*right*) at 80 K. Total simulations (red traces) using parameters in Table S4.1.

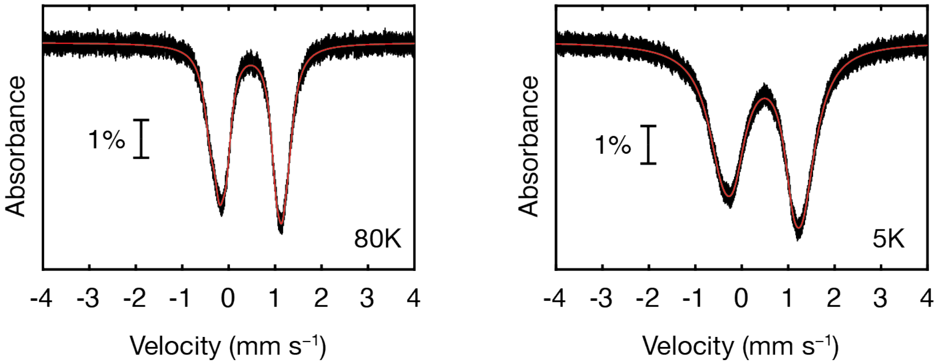

Figure S4.33. Mössbauer spectra (vertical lines) of [$CoFe_3S_4(IMes)_3(CO)$] at 80 K (*left*) and 5 K (*right*). Total simulations (red traces) using parameters in Table S4.1.

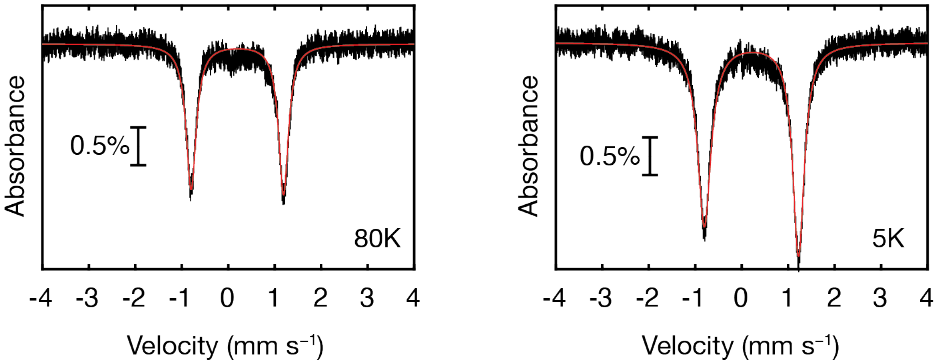

Figure S4.34. Mössbauer spectra (vertical lines) of $[FeCo_3S_4(IMes)_3(CO)]$ at 80 K (*left*) and 5 K (*right*). Total simulations (red traces) using parameters in Table S4.1.

Table S4.1. Fit parameters for Mössbauer spectra in Figure S4.31–Figure S4.34.[a]

Compound		δ (mm s^{-1})	$\lvert\Delta E_Q\rvert$ (mm s^{-1})	Γ (mm s^{-1})
$[CoFe_3S_4(IMes)_3Cl]^+$ (80 K)	Site 1	0.291	1.718	0.235
	Site 2	0.295	1.494	0.229
	Site 3	0.300	1.285	0.273
	Avg δ	**0.295**	—	—
$[CoFe_3S_4(IMes)_3Cl]$ (80 K)	Site 1	0.442	1.565	0.351
	Site 2	0.414	1.429	0.263
	Site 3	0.410	1.197	0.286
	Avg δ	**0.422**	—	—
$[FeCo_3S_4(IMes)_3Cl]^+$ (80 K)	**Site 1**	**0.472**	0.734	L: 0.287 R: 0.338
$[FeCo_3S_4(IMes)_3Cl]$ (80 K)	**Site 1**	**0.542**	0.209	L: 0.305 R: 0.288
$[CoFe_3S_4(IMes)_3(CO)]$ (80 K)	Site 1	0.472	1.344	0.264
	Site 2	0.442	1.662	0.344
	Site 3	0.482	1.069	0.276
	Avg δ	**0.465**	—	—
$[CoFe_3S_4(IMes)_3(CO)]$ (5 K)	Site 1	0.377	1.453	L: 1.000 R: 0.487
	Site 2	0.431	1.746	L: 0.710 R: 0.527
	Site 3	0.635	1.610	L: 0.620 R: 0.830
	Avg δ	**0.481**	—	—
$[FeCo_3S_4(IMes)_3(CO)]$ (80 K)	**Site 1**	**0.197**	1.988	L: 0.265 R: 0.256
$[FeCo_3S_4(IMes)_3(CO)]$ (5 K)	**Site 1**	**0.209**	2.026	L: 0.350 R: 0.301

[a] Note that the parameters for the individual quadrupole doublets are not physically meaningful for clusters with multiple Fe sites because the spectra cannot be fit by a unique, reliable simulation.

X-ray refinement details

[$TlFe_3S_4(IMes)_3$][$BAr^F{}_4$]: Crystallized in the monoclinic, noncentrosymmetric space group *Cc* with one molecule in the asymmetric unit and as an inversion twin; the twinning was modelled with a BASF parameter of 0.28. The solvent in the lattice was a mixture of DFB and pentane disordered in a 61:39 ratio. Additionally, four CF_3 groups of the [$BAr^F{}_4$] anion were disorded by rotation. The molecule crystallized as an inversion twin, which was modelled with a BASF parameter of 0.28.

[$CoFe_3S_4(IMes)_3Cl$][$BAr^F{}_4$]: Crystallizes in the orthorhombic, centrosymmetric space group *Pbca* with one cluster and one $BAr^F{}_4{}^-$ anion in the asymmetric unit. Rotational disorder in the F atoms of two CF_3 moieties of the counterion were refined in ratios of 83:17 and 49:51, respectively. *PLATON* SQUEEZE[102] was used to omit additional disordered solvent molecules that could not be satisfactorily refined.

[$CoFe_3S_4(IMes)_3Cl$]: Crystallizes in the monoclinic, centrosymmetric space group $P2_1/n$ with one cluster in the asymmetric unit. A benzene solvent molecule is disordered over two positions, one of which resides on a special position. *PLATON* SQUEEZE[102] was used to omit additional disordered solvent molecules that could not be satisfactorily refined.

[$Co_4S_4(IMes)_3Cl$]: Crystallizes in the monoclinic, centrosymmetric space group $P2_1/n$ with one cluster in the asymmetric unit. Disordered benzene and pentane solvent molecules were unable to be satisfactorily refined and were omitted using *PLATON* SQUEEZE.[102]

[$Co_4S_4(IMes)_3Cl$][PF_6]: Crystallizes in the monoclinic, centrosymmetric space group $P2_1/c$ with one cluster, one $PF_6{}^-$ anion, and two CH_2Cl_2 solvent molecules in the asymmetric unit.

[$TlCo_3S_4(IMes)_3$][PF_6]: Crystallizes in the monoclinic, centrosymmetric space group $P2_1/n$ with one cluster and one $PF_6{}^-$ anion in the asymmetric unit. The cluster shows whole molecule disordered related by a mirror plane in the Co_3 plane (the Co atoms are not disordered). The whole molecule disorder was refined in an 83:17 ratio. Within the major component, two of the μ_3-S ligands and the Tl atom are disordered in a nearly 1:1 ratio. One of the IMes ligands is also disordered as part of the whole molecule disorder and the additional disorder within the major component. Finally, the $PF_6{}^-$ is also disordered over three positions due to whole molecule disorder and disorder in the major component. Reflections with estimated standard deviations > 10 were omitted from the final dataset.

[$FeCo_3S_4(IMes)_3Cl$][PF_6]: Crystallizes in the monoclinic, centrosymmetric space group $P2_1/n$ with one cluster, one $PF_6{}^-$ anion, and one Et_2O solvent molecule in the asymmetric unit. The cluster and counterion show whole molecule disorder over three positions via translation along a single direction refined in a 97:1.5:1.5 ratio. Only the heavy atoms were observed in the minor components and all atoms in the minor components were refined isotropically. The Et_2O solvent molecule is disordered over three positions in a 47:33:20 ratio. Reflections with estimated standard deviations > 10 were omitted from the final dataset.

[$FeCo_3S_4(IMes)_3Cl$]: Crystallizes in the monoclinic, centrosymmetric space group $P2_1/c$ with one cluster and one benzene solvent molecule in the asymmetric unit. One mesityl group of one IMes

ligand is disordered over two positions in a 76:24 ratio. The benzene solvent molecule is similarly disordered over two positions in a 71:29 ratio. Three reflections with estimated standard deviations > 10 were omitted from the final dataset.

[$CoFe_3S_4(IMes)_3(CO)$]: Crystallizes in the monoclinic, centrosymmetric space group $P2_1/c$ with one cluster in the asymmetric unit. Disordered pentane and Et_2O solvent molecules could not be satisfactorily refined and were omitted using *PLATON* SQUEEZE.[102]

[$Co_4S_4(IMes)_3(CO)$]: Crystallizes in the monoclinic, centrosymmetric space group $P2_1/c$ with one cluster in the asymmetric unit. Disordered pentane and Et_2O solvent molecules could not be satisfactorily refined and were omitted using *PLATON* SQUEEZE.[102]

[$FeCo_3S_4(IMes)_3(CO)$]: Crystallizes in the monoclinic, centrosymmetric space group $P2_1/c$ with one cluster in the asymmetric unit. Disordered pentane and Et_2O solvent molecules could not be satisfactorily refined and were omitted using *PLATON* SQUEEZE.[102]

Table S4.2. Crystallographic data for $[\mathrm{TlFe_3S_4(IMes)_3}][\mathrm{BAr^F{}_4}]$ and $[\mathrm{CoFe_3S_4(IMes)_3Cl}][\mathrm{BAr^F{}_4}]$.

	$[\mathrm{TlFe_3S_4(IMes)_3}][\mathrm{BAr^F{}_4}]$	$[\mathrm{CoFe_3S_4(IMes)_3Cl}][\mathrm{BAr^F{}_4}]$
CCDC deposition number		
Empirical formula	$\mathrm{C_{50.30}H_{45.57}B_{0.50}F_{12.64}Fe_{1.50}N_3S_2Tl_{0.50}}$	$\mathrm{C_{95}H_{84}BClCoF_{24}Fe_3N_6S_4}$
Color, habit	Brown, block	Black, block
Formula weight	1187.80	2166.66
T [K]	100(2)	100(2)
λ [Å]	0.71073	0.71073
Crystal system	Monoclinic	Monoclinic
Space group	*Cc*	*Pbca*
a [Å]	24.1210(11)	21.7961(4)
b [Å]	22.1621(9)	21.4334(4)
c [Å]	20.6243(8)	44.6379(15)
α [°]	90	90
β [°]	111.694(2)	90
γ [°]	90	90
V [Å^3]	10244.3(8)	20853.2(9)
Z	8	8
d_{calc} [g cm^{-1}]	1.540	1.280
Radiation type	Mo K_α	Mo K_α
μ [mm^{-1}]	2.161	0.759
$F(000)$	4769	8824
Crystal size [mm^3]	0.534 × 0.238 × 0.186	0.357 × 0.163 × 0.133
θ range for data collection [°]	1.292–33.233	1.306–35.025
Miller index ranges	$-37 \leq h \leq 37$	$-35 \leq h \leq 35$
	$-34 \leq k \leq 34$	$-34 \leq k \leq 34$
	$-31 \leq l \leq 31$	$-71 \leq l \leq 71$
Reflections collected	405141	1417072
Independent reflections	39153 ($R_{\mathrm{int}} = 0.0526$)	45902 ($R_{\mathrm{int}} = 0.0734$)
Completeness to $\theta = 25.242°$ [%]	100.0	100.0
Absorption correction	Semi-empirical from equivalents	Semi-empirical from equivalents
Refinement method	Full-matrix least-squares on F^2	Full-matrix least-squares on F^2
Data / restraints / parameters	39153 / 3 / 1458	45902 / 114 / 1291
Goodness-of-fit on F^2	1.027	1.024
Final R indices ($I > 2\sigma(I)$)	$R_1 = 0.0284$, $wR_2 = 0.0685$	$R_1 = 0.0380$, $wR_2 = 0.0883$
R indices (all data)	$R_1 = 0.0336$, $wR_2 = 0.0713$	$R_1 = 0.0585$, $wR_2 = 0.1001$
$\Delta\rho_{\mathrm{max}}$, $\Delta\rho_{\mathrm{min}}$ [e Å^{-3}]	1.739, −1.620	0.828, −0.849

Table S4.3. Crystallographic data for [$CoFe_3S_4(IMes)_3Cl$] and [$Co_4S_4(IMes)_3Cl$].

	[$CoFe_3S_4(IMes)_3Cl$]	[$Co_4S_4(IMes)_3Cl$]
CCDC deposition number		
Empirical formula	$C_{68.61}H_{77.61}ClCoFe_3N_6S_4$	$C_{63}H_{72}ClCo_4N_6S_4$
Color, habit	Brown, block	Black, block
Formula weight	1376.47	1312.67
T [K]	100(2)	100(2)
λ [Å]	0.71073	0.71073
Crystal system	Monoclinic	Monoclinic
Space group	$P2_1/n$	$P2_1/n$
a [Å]	15.2425(4)	15.0531(14)
b [Å]	24.8444(6)	24.789(2)
c [Å]	19.7321(5)	19.8082(19)
α [°]	90	90
β [°]	102.4110(10)	101.859(4)
γ [°]	90	90
V [Å^3]	7297.7(3)	7233.7(12)
Z	4	4
d_{calc} [g cm^{-1}]	1.253	1.205
Radiation type	Mo K_α	Mo K_α
μ [mm^{-1}]	1.000	1.091
$F(000)$	2869	2724
Crystal size [mm^3]	0.440 × 0.430 × 0.250	0.330 × 0.320 × 0.250
θ range for data collection [°]	1.337–33.223	1.555–30.508
Miller index ranges	$-23 \leq h \leq 23$ $-38 \leq k \leq 37$ $-30 \leq l \leq 29$	$-21 \leq h \leq 21$ $-35 \leq k \leq 35$ $-28 \leq l \leq 28$
Reflections collected	451979	504756
Independent reflections	27937 (R_{int} = 0.0582)	22108 (R_{int} = 0.1107)
Completeness to θ = 25.242° [%]	100.0	100.0
Absorption correction	Semi-empirical from equivalents	Semi-empirical from equivalents
Refinement method	Full-matrix least-squares on F^2	Full-matrix least-squares on F^2
Data / restraints / parameters	27937 / 1264 / 804	22108 / 1165 / 721
Goodness-of-fit on F^2	1.064	1.054
Final R indices ($I > 2\sigma(I)$)	$R_1 = 0.0384$, $wR_2 = 0.0916$	$R_1 = 0.0333$, $wR_2 = 0.0827$
R indices (all data)	$R_1 = 0.0635$, $wR_2 = 0.1035$	$R_1 = 0.0491$, $wR_2 = 0.0883$
$\Delta\rho_{max}$, $\Delta\rho_{min}$ [e Å^{-3}]	0.837, −0.694	0.553, −0.551

Table S4.4. Crystallographic data for [$Co_4S_4(IMes)_3Cl$][PF_6] and [$TlCo_3S_4(IMes)_3$][PF_6].

	[$Co_4S_4(IMes)_3Cl$][PF_6]	[$TlCo_3S_4(IMes)_3$][PF_6]
CCDC deposition number		
Empirical formula	$C_{65}H_{76}Cl_5Co_4F_6N_6PS_4$	$C_{63.15}H_{72.19}Co_3F_{6.02}N_6PS_{3.98}Tl_{0.99}$
Color, habit	Brown, block	Black, block
Formula weight	1627.49	1567.39
T [K]	100(2)	100(2)
λ [Å]	0.71073	0.71073
Crystal system	Monoclinic	Monoclinic
Space group	$P2_1/c$	$P2_1/n$
a [Å]	18.1012(9)	20.4706(11)
b [Å]	19.7701(10)	13.3357(6)
c [Å]	20.6538(9)	24.5221(13)
α [°]	90	90
β [°]	99.204(2)	104.946
γ [°]	90	90
V [Å^3]	7296.1(6)	6467.8(6)
Z	4	4
d_{calc} [g cm^{-1}]	1.482	1.610
Radiation type	Mo K_α	Mo K_α
μ [mm^{-1}]	01.271	3.429
F(000)	3336	3149
Crystal size [mm^3]	0.295 × 0.195 × 0.185	0.265 × 0.115 × 0.025
θ range for data collection [°]	1.435–32.646	1.502–31.054
Miller index ranges	$-27 \le h \le 27$ $-29 \le k \le 29$ $-31 \le l \le 30$	$-29 \le h \le 29$ $-19 \le k \le 19$ $-35 \le l \le 35$
Reflections collected	506385	480327
Independent reflections	26693 (R_{int} = 0.0730)	20681 (R_{int} = 0.0517)
Completeness to θ = 25.242° [%]	100.0	99.8
Absorption correction	Semi-empirical from equivalents	Semi-empirical from equivalents
Refinement method	Full-matrix least-squares on F^2	Full-matrix least-squares on F^2
Data / restraints / parameters	26693 / 1296 / 838	20681 / 5138 / 1376
Goodness-of-fit on F^2	1.031	1.231
Final R indices ($I > 2\sigma(I)$)	$R_1 = 0.0340$, $wR_2 = 0.0750$	$R_1 = 0.0488$, $wR_2 = 0.1040$
R indices (all data)	$R_1 = 0.0538$, $wR_2 = 0.0824$	$R_1 = 0.0606$, $wR_2 = 0.1082$
$\Delta\rho_{max}$, $\Delta\rho_{min}$ [e Å^{-3}]	0.719, −0.863	0.844, −1.220

Table S4.5. Crystallographic data for [$FeCo_3S_4(IMes)_3Cl$][PF_6] and [$FeCo_3S_4(IMes)_3Cl$].

	[$FeCo_3S_4(IMes)_3Cl$][PF_6]	[$FeCo_3S_4(IMes)_3Cl$]
CCDC deposition number		
Empirical formula	$C_{65.92}H_{80.05}Cl_{1.01}Co_{3.04}F_{5.90}Fe_{1.01}N_{5.90}O_{0.99}P_{1.01}S_{4.06}$	$C_{69}H_{78.24}ClCo_3FeN_6S_4$
Color, habit	Brown, block	Black, block
Formula weight	1516.41	1387.95
T [K]	100(2)	100(2)
λ [Å]	0.71073	0.71073
Crystal system	Triclinic	Monoclinic
Space group	$P-1$	$P2_1/c$
a [Å]	13.6545(5)	12.9197(3)
b [Å]	13.7068(6)	13.7654(4)
c [Å]	20.0133(8)	38.5876(11)
α [°]	79.704(2)	90
β [°]	77.525(2)	96.9570(10)
γ [°]	78.540(2)	90
V [Å^3]	3548.0(3)	6812.1(3)
Z	2	4
d_{calc} [g cm^{-1}]	1.419	1.353
Radiation type	Mo K_α	Mo K_α
μ [mm^{-1}]	1.142	1.132
F(000)	1568	2889
Crystal size [mm^3]	0.168 × 0.125 × 0.081	0.180 × 0.085 × 0.040
θ range for data collection [°]	1.531–33.326	1.572–31.539
Miller index ranges	$-20 \leq h \leq 21$ $-21 \leq k \leq 21$ $-30 \leq l \leq 30$	$-14 \leq h \leq 19$ $-20 \leq k \leq 20$ $-56 \leq l \leq 56$
Reflections collected	247571	345947
Independent reflections	27174 (R_{int} = 0.0606)	22723 (R_{int} = 0.0665)
Completeness to θ = 25.242° [%]	99.7	100.0
Absorption correction	Semi-empirical from equivalents	Semi-empirical from equivalents
Refinement method	Full-matrix least-squares on F^2	Full-matrix least-squares on F^2
Data / restraints / parameters	27174 / 1887 / 945	22723 / 1770 / 917
Goodness-of-fit on F^2	1.139	1.069
Final R indices ($I > 2\sigma(I)$)	R_1 = 0.0588, wR_2 = 0.1302	R_1 = 0.0343, wR_2 = 0.0.691
R indices (all data)	R_1 = 0.0774, wR_2 = 0.1379	R_1 = 0.0533, wR_2 = 0.0.775
$\Delta\rho_{max}$, $\Delta\rho_{min}$ [e Å^{-3}]	1.049, −0.598	0.784, −0.460

Table S4.6. Crystallographic data for [$CoFe_3S_4(IMes)_3(CO)$] and [$Co_4S_4(IMes)_3(CO)$].

	[$CoFe_3S_4(IMes)_3(CO)$]	[$Co_4S_4(IMes)_3(CO)$]
CCDC deposition number		
Empirical formula	$C_{64}H_{72}CoFe_3N_6OS_4$	$C_{64}H_{72}Co_4N_6OS_4$
Color, habit	Brown, block	Black, block
Formula weight	1295.99	1305.23
T [K]	100(2)	100(2)
λ [Å]	0.71073	0.71073
Crystal system	Monoclinic	Monoclinic
Space group	$P2_1/n$	$P2_1/n$
a [Å]	15.2371(5)	15.0962(5)
b [Å]	24.7531(8)	24.6445(7)
c [Å]	19.8098(6)	19.9063(6)
α [°]	90	90
β [°]	102.3700(10)	101.8150(10)
γ [°]	90	90
V [Å^3]	7298.1(4)	7249.0(4)
Z	4	4
d_{calc} [g cm^{-1}]	1.180	1.196
Radiation type	Mo K_α	Mo K_α
μ [mm^{-1}]	0.961	1.054
F(000)	2700	2712
Crystal size [mm^3]	0.458 × 0.154 × 0.135	0.520 × 0.480 × 0.250
θ range for data collection [°]	1.336–34.431	1.332–33.211
Miller index ranges	$-24 \leq h \leq 24$ $-39 \leq k \leq 39$ $-31 \leq l \leq 31$	$-23 \leq h \leq 23$ $-37 \leq k \leq 37$ $-30 \leq l \leq 30$
Reflections collected	434531	532208
Independent reflections	30702 (R_{int} = 0.0625)	27755 (R_{int} = 0.0474)
Completeness to θ = 25.242° [%]	100.0	100.0
Absorption correction	Semi-empirical from equivalents	Semi-empirical from equivalents
Refinement method	Full-matrix least-squares on F^2	Full-matrix least-squares on F^2
Data / restraints / parameters	30702 / 0 / 731	27755 / 0 / 730
Goodness-of-fit on F^2	1.032	1.044
Final R indices ($I > 2\sigma(I)$)	R_1 = 0.0333, wR_2 = 0.0790	R_1 = 0.0280, wR_2 = 0.0687
R indices (all data)	R_1 = 0.0475, wR_2 = 0.0866	R_1 = 0.0363, wR_2 = 0.0726
$\Delta\rho_{max}$, $\Delta\rho_{min}$ [e Å^{-3}]	0.677, −0.653	0.460, −0.503

Table S4.7. Crystallographic data for [$FeCo_3S_4(IMes)_3(CO)$].

	[$FeCo_3S_4(IMes)_3(CO)$]
CCDC deposition number	
Empirical formula	$C_{64}H_{72}Co_3FeN_6OS_4$
Color, habit	Brown, block
Formula weight	1302.15
T [K]	100(2)
λ [Å]	0.71073
Crystal system	Monoclinic
Space group	$P2_1/n$
a [Å]	15.0660(10)
b [Å]	24.6438(15)
c [Å]	19.8611(13)
α [°]	90
β [°]	101.925(2)
γ [°]	90
V [Å^3]	7215.0(8)
Z	4
d_{calc} [g cm^{-1}]	1.199
Radiation type	Mo K_α
μ [mm^{-1}]	1.030
$F(000)$	2708
Crystal size [mm^3]	0.225 × 0.160 × 0.110
θ range for data collection [°]	1.334–31.050
Miller index ranges	$-21 \leq h \leq 21$ $-35 \leq k \leq 35$ $-28 \leq l \leq 28$
Reflections collected	367016
Independent reflections	23074 (R_{int} = 0.0515)
Completeness to θ = 25.242° [%]	100.0
Absorption correction	Semi-empirical from equivalents
Refinement method	Full-matrix least-squares on F^2
Data / restraints / parameters	23074 / 0 / 730
Goodness-of-fit on F^2	1.035
Final R indices ($I > 2\sigma(I)$)	$R_1 = 0.0287$, $wR_2 = 0.0687$
R indices (all data)	$R_1 = 0.0404$, $wR_2 = 0.0737$
$\Delta\rho_{max}$, $\Delta\rho_{min}$ [e Å^{-3}]	0.418, −0.302

References

(1) Johnson, D. C.; Dean, D. R.; Smith, A. D.; Johnson, M. K. Structure, Function, and Formation of Biological Iron-Sulfur Clusters. *Annu. Rev. Biochem.* **2005**, *74* (1), 247–281.

(2) Lill, R. Function and Biogenesis of Iron–Sulphur Proteins. *Nature* **2009**, *460* (7257), 831–838.

(3) Burgess, B. K.; Lowe, D. J. Mechanism of Molybdenum Nitrogenase. *Chem. Rev.* **1996**, *96* (7), 2983–3012.

(4) Howard, J. B. Rees., DC, Structural Basis of Biological Nitrogen Fixation. *Chem Rev* **1996**, *96*, 2965–2982.

(5) Dos Santos, P. C.; Igarashi, R. Y.; Lee, H.-I.; Hoffman, B. M.; Seefeldt, L. C.; Dean, D. R. Substrate Interactions with the Nitrogenase Active Site. *Acc. Chem. Res.* **2005**, *38* (3), 208–214.

(6) Hoffman, B. M.; Dean, D. R.; Seefeldt, L. C. Climbing Nitrogenase: Toward a Mechanism of Enzymatic Nitrogen Fixation. *Acc. Chem. Res.* **2009**, *42* (5), 609–619.

(7) Eady, R. R. Structure−Function Relationships of Alternative Nitrogenases. *Chem. Rev.* **1996**, *96* (7), 3013–3030.

(8) Hu, Y.; Lee, C. C.; Ribbe, M. W. Vanadium Nitrogenase: A Two-Hit Wonder? *Dalton Trans.* **2012**, *41* (4), 1118–1127.

(9) Umena, Y.; Kawakami, K.; Shen, J.-R.; Kamiya, N. Crystal Structure of Oxygen-Evolving Photosystem II at a Resolution of 1.9 Å. *Nature* **2011**, *473* (7345), 55–60.

(10) Rhee, K.-H.; Morris, E. P.; Barber, J.; Kühlbrandt, W. Three-Dimensional Structure of the Plant Photosystem II Reaction Centre at 8 Å Resolution. *Nature* **1998**, *396* (6708), 283–286.

(11) Hoffman, B. M.; Lukoyanov, D.; Yang, Z.-Y.; Dean, D. R.; Seefeldt, L. C. Mechanism of Nitrogen Fixation by Nitrogenase: The Next Stage. *Chem. Rev.* **2014**, *114* (8), 4041–4062.

(12) Can, M.; Armstrong, F. A.; Ragsdale, S. W. Structure, Function, and Mechanism of the Nickel Metalloenzymes, CO Dehydrogenase, and Acetyl-CoA Synthase. *Chem. Rev.* **2014**, *114* (8), 4149–4174.

(13) Tsui, E. Y.; Kanady, J. S.; Agapie, T. Synthetic Cluster Models of Biological and Heterogeneous Manganese Catalysts for O_2 Evolution. *Inorg. Chem.* **2013**, *52* (24), 13833–13848.

(14) Kanady, J. S.; Lin, P.-H.; Carsch, K. M.; Nielsen, R. J.; Takase, M. K.; Goddard, W. A. I.; Agapie, T. Toward Models for the Full Oxygen-Evolving Complex of Photosystem II by Ligand Coordination To Lower the Symmetry of the Mn_3CaO_4 Cubane: Demonstration

That Electronic Effects Facilitate Binding of a Fifth Metal. *J. Am. Chem. Soc.* **2014**, *136* (41), 14373–14376.

(15) Jasniewski, A. J.; Lee, C. C.; Ribbe, M. W.; Hu, Y. Reactivity, Mechanism, and Assembly of the Alternative Nitrogenases. *Chem. Rev.* **2020**, *120* (12), 5107–5157.

(16) Burén, S.; Jiménez-Vicente, E.; Echavarri-Erasun, C.; Rubio, L. M. Biosynthesis of Nitrogenase Cofactors. *Chem. Rev.* **2020**, *120* (12), 4921–4968.

(17) Wittenborn, E. C.; Merrouch, M.; Ueda, C.; Fradale, L.; Léger, C.; Fourmond, V.; Pandelia, M.-E.; Dementin, S.; Drennan, C. L. Redox-Dependent Rearrangements of the NiFeS Cluster of Carbon Monoxide Dehydrogenase. *eLife* **2018**, *7*, e39451.

(18) Alfano, M.; Cavazza, C. Structure, Function, and Biosynthesis of Nickel-Dependent Enzymes. *Protein Sci.* **2020**, *29* (5), 1071–1089.

(19) Dobbek, H.; Svetlitchnyi, V.; Gremer, L.; Huber, R.; Meyer, O. Crystal Structure of a Carbon Monoxide Dehydrogenase Reveals a [Ni-4Fe-5S] Cluster. *Science* **2001**, *293*

(20) Chen, J.; Huang, S.; Seravalli, J.; Gutzman, Howard; Swartz, D. J.; Ragsdale, S. W.; Bagley, K. A. Infrared Studies of Carbon Monoxide Binding to Carbon Monoxide Dehydrogenase/Acetyl-CoA Synthase from Moorella Thermoacetica. *Biochemistry* **2003**, *42* (50), 14822–14830.

(21) Ha, S.-W.; Korbas, M.; Klepsch, M.; Meyer-Klaucke, W.; Meyer, O.; Svetlitchnyi, V. Interaction of Potassium Cyanide with the [Ni-4Fe-5S] Active Site Cluster of CO Dehydrogenase from Carboxydothermus Hydrogenoformans. *J. Biol. Chem.* **2007**, *282* (14), 10639–10646.

(22) Rodriguez, J. A.; Goodman, D. W. The Nature of the Metal-Metal Bond in Bimetallic Surfaces. *Science* **1992**, *257* (5072), 897–903.

(23) Burke, M. S.; Kast, M. G.; Trotochaud, L.; Smith, A. M.; Boettcher, S. W. Cobalt–Iron (Oxy)Hydroxide Oxygen Evolution Electrocatalysts: The Role of Structure and Composition on Activity, Stability, and Mechanism. *J. Am. Chem. Soc.* **2015**, *137* (10), 3638–3648.

(24) Trotochaud, L.; Young, S. L.; Ranney, J. K.; Boettcher, S. W. Nickel–Iron Oxyhydroxide Oxygen-Evolution Electrocatalysts: The Role of Intentional and Incidental Iron Incorporation. *J. Am. Chem. Soc.* **2014**, *136* (18), 6744–6753.

(25) Song, F.; Hu, X. Ultrathin Cobalt–Manganese Layered Double Hydroxide Is an Efficient Oxygen Evolution Catalyst. *J. Am. Chem. Soc.* **2014**, *136* (47), 16481–16484.

(26) Nguyen, A. I.; Suess, D. L. M.; Darago, L. E.; Oyala, P. H.; Levine, D. S.; Ziegler, M. S.; Britt, R. D.; Tilley, T. D. Manganese–Cobalt Oxido Cubanes Relevant to Manganese-Doped Water Oxidation Catalysts. *J. Am. Chem. Soc.* **2017**, *139* (15), 5579–5587.

(27) Li, D.; Baydoun, H.; Verani, C. N.; Brock, S. L. Efficient Water Oxidation Using CoMnP Nanoparticles. *J. Am. Chem. Soc.* **2016**, *138* (12), 4006–4009.

(28) Rees, J. A.; Bjornsson, R.; Kowalska, J. K.; Lima, F. A.; Schlesier, J.; Sippel, D.; Weyhermüller, T.; Einsle, O.; Kovacs, J. A.; DeBeer, S. Comparative Electronic Structures of Nitrogenase FeMoco and FeVco. *Dalton Trans.* **2017**, *46* (8), 2445–2455.

(29) Yeuk-Wah Hung, S.; Wong, W.-T. Synthesis and Characterization of High-Nuclearity Osmium–Rhodium Mixed-Metal Carbonyl Clusters; Molecular and Crystal Structures of $[Os_{12}Rh_9(CO)_{44}(\mu_3\text{-}Cl)]\cdot 2CH_2Cl_2$ and $[Os_4Rh_3(\mu_3\text{-}H)(CO)_{14}(\mu_3\text{-}CO)(\eta^4\text{-}C_7H_8)_2]$. *Chem. Commun.* **1997**, No. 21, 2099–2100.

(30) Adams, R. D.; Barnard, T. S.; Li, Z.; Wu, W.; Yamamoto, J. Catalytic Hydrogenation of Diphenylacetylene by a Layer-Segregated Platinum-Ruthenium Cluster Complex. *J. Am. Chem. Soc.* **1994**, *116* (20), 9103–9113.

(31) Hernandez-Molina, R.; Sokolov, M. N.; Sykes, A. G. Behavioral Patterns of Heterometallic Cuboidal Derivatives of $[M_3Q_4(H_2O)_9]^{4+}$ (M = Mo, W; Q = S, Se). *Acc. Chem. Res.* **2001**, *34* (3), 223–230.

(32) Holm, R. H. Trinuclear Cuboidal and Heterometallic Cubane-Type Iron–Sulfur Clusters: New Structural and Reactivity Themes in Chemistry and Biology. In *Advances in inorganic chemistry*; Elsevier, 1992; Vol. 38, pp 1–71.

(33) Johnson, M. K.; Duderstadt, R. E.; Duin, E. C. Biological and Synthetic $[Fe_3S_4]$ Clusters. In *Advances in Inorganic Chemistry*; Elsevier, 1999; Vol. 47, pp 1–82.

(34) Eames, E. V.; Hernández Sánchez, R.; Betley, T. A. Metal Atom Lability in Polynuclear Complexes. *Inorg. Chem.* **2013**, *52* (9), 5006–5012.

(35) Powers, T. M.; Gu, N. X.; Fout, A. R.; Baldwin, A. M.; Hernández Sánchez, R.; Alfonso, D. M.; Chen, Y.-S.; Zheng, S.-L.; Betley, T. A. Synthesis of Open-Shell, Bimetallic Mn/Fe Trinuclear Clusters. *J. Am. Chem. Soc.* **2013**, *135* (38), 14448–14458.

(36) Beissel, T.; Birkelbach, F.; Bill, E.; Glaser, T.; Kesting, F.; Krebs, C.; Weyhermüller, T.; Wieghardt, K.; Butzlaff, C.; Trautwein, A. X. Exchange and Double-Exchange Phenomena in Linear Homo-and Heterotrinuclear Nickel (II, III, IV) Complexes Containing Six μ_2-Phenolato or μ_2-Thiophenolato Bridging Ligands. *J. Am. Chem. Soc.* **1996**, *118* (49), 12376–12390.

(37) Glaser, T.; Kesting, F.; Beissel, T.; Bill, E.; Weyhermüller, T.; Meyer-Klaucke, W.; Wieghardt, K. Spin-Dependent Delocalization in Three Isostructural Complexes $[LFeNiFeL]^{2+/3+/4+}$ (L = 1, 4, 7-(4-Tert-Butyl-2-Mercaptobenzyl)-1, 4, 7-Triazacyclononane). *Inorg. Chem.* **1999**, *38* (4), 722–732.

(38) Amtawong, J.; Skjelstad, B. B.; Handford, R. C.; Suslick, B. A.; Balcells, D.; Tilley, T. D. C–H Activation by $RuCo_3O_4$ Oxo Cubanes: Effects of Oxyl Radical Character and Metal–Metal Cooperativity. *J. Am. Chem. Soc.* **2021**, *143* (31), 12108–12119.

(39) Tsui, E. Y.; Agapie, T. Reduction Potentials of Heterometallic Manganese–Oxido Cubane Complexes Modulated by Redox-Inactive Metals. *Proc. Natl. Acad. Sci.* **2013**, *110* (25), 10084–10088.

(40) Carsch, K. M.; de Ruiter, G.; Agapie, T. Intramolecular C–H and C–F Bond Oxygenation by Site-Differentiated Tetranuclear Manganese Models of the OEC. *Inorg. Chem.* **2017**, *56* (15), 9044–9054.

(41) de Ruiter, G.; Carsch, K. M.; Gul, S.; Chatterjee, R.; Thompson, N. B.; Takase, M. K.; Yano, J.; Agapie, T. Accelerated Oxygen Atom Transfer and C−H Bond Oxygenation by Remote Redox Changes in Fe_3Mn-Iodosobenzene Adducts. *Angew. Chem. Int. Ed.* **2017**, *56* (17), 4772–4776.

(42) Clegg, W.; Elsegood, M. R.; Errington, R. J.; Havelock, J. Alkoxide Hydrolysis as a Route to Early Transition-Metal Polyoxometalates: Synthesis and Crystal Structures of Heteronuclear Hexametalate Derivatives. *J. Chem. Soc. Dalton Trans.* **1996**, No. 5, 681–690.

(43) Wei, Y.; Lu, M.; Cheung, C. F.; Barnes, C. L.; Peng, Z. Functionalization of $[MoW_5O_{19}]^{2-}$ with Aromatic Amines: Synthesis of the First Arylimido Derivatives of Mixed-Metal Polyoxometalates. *Inorg. Chem.* **2001**, *40* (22), 5489–5490.

(44) Tulsky, E. G.; Long, J. R. Heterometal Substitution in the Dimensional Reduction of Cluster Frameworks: Synthesis of Soluble $[Re_{6-n}Os_nSe_8Cl_6]^{(4-n)-}$ (n = 1−3) Cluster-Containing Solids. *Inorg. Chem.* **2001**, *40* (27), 6990–7002.

(45) Kovacs, J. A.; Holm, R. H. Heterometallic Clusters: Synthesis and Reactions of Vanadium-Iron-Sulfur Single-and Double-Cubane Clusters and the Structure of $[V_2Fe_6S_8Cl_4(C_2H_4S_2)_2]^{4-}$. *Inorg. Chem.* **1987**, *26* (5), 702–711.

(46) Ciurli, S.; Carney, M. J.; Holm, R. H.; Papaefthymiou, G. C. Stability Range of Heterometal Cubane-Type Clusters MFe_3S_4: Assembly of Double-Cubane Clusters with the Rhenium-Iron-Sulfur $ReFe_3S_4$ Core. *Inorg. Chem.* **1989**, *28* (14), 2696–2698.

(47) Cen, W.; Lee, S. C.; Li, J.; MacDonnell, F. M.; Holm, R. H. Heterometal Dependence of Electron Distributions and Redox Potentials in Clusters with Cubane-Type $[MFe_3S_4]^{2-}$ Cores. *J. Am. Chem. Soc.* **1993**, *115* (21), 9515–9523.

(48) Preetz, W.; Harder, K. Trennung Und Charakterisierung Der Metallgemischten Cluster $[(Nb_nTa_{6-n})Cl]^{2+}$, n = 0–6. *Z. Für Anorg. Allg. Chem.* **1991**, *597* (1), 163–172.

(49) Brückner, P.; Peters, G.; Preetz, W. Darstellung, ^{19}F-NMR-Spektroskopischer Nachweis Und Untersuchung Zur Bildung Der Metallgemischten Clusteranionen $[(Mo_{6-n}W_nCl)F]^{2-}$, n = 0−6. *Z. Für Anorg. Allg. Chem.* **1994**, *620* (10), 1669–1677.

(50) Naumov, N. G.; Brylev, K. A.; Mironov, Y. V.; Virovets, A. V.; Fenske, D.; Fedorov, V. E. Synthesis and Structures of New Octahedral Water-Soluble Heterometal Rhenium–Molybdenum Clusters. *Polyhedron* **2004**, *23* (4), 599–603.

(51) Moura, I.; Moura, J. J.; Munck, E.; Papaefthymiou, V.; LeGall, J. Evidence for the Formation of a Cobalt-Iron-Sulfur ($CoFe_3S_4$) Cluster in Desulfovibrio Gigas Ferredoxin II. *J. Am. Chem. Soc.* **1986**, *108* (2), 349–351.

(52) Conover, R. C.; Park, J. B.; Adams, M. W.; Johnson, M. K. Formation and Properties of an Iron-Nickel Sulfide ($NiFe_3S_4$) Cluster in Pyrococcus Furiosus Ferredoxin. *J. Am. Chem. Soc.* **1990**, *112* (11), 4562–4564.

(53) Surerus, K. K.; Munck, E.; Moura, I.; Moura, J. J.; LeGall, J. Evidence for the Formation of a $ZnFe_3S_4$ Cluster in Desulfovibrio Gigas Ferredoxin II. *J. Am. Chem. Soc.* **1987**, *109* (12), 3805–3807.

(54) Butt, J. N.; Armstrong, F. A.; Breton, J.; George, S. J.; Thomson, A. J.; Hatchikian, E. C. Investigation of Metal Ion Uptake Reactivities of [3Fe-4S] Clusters in Proteins: Voltammetry of Co-Adsorbed Ferredoxin-Aminocyclitol Films at Graphite Electrodes and Spectroscopic Identification of Transformed Clusters. *J. Am. Chem. Soc.* **1991**, *113* (17), 6663–6670.

(55) Zhou, J.; Raebiger, J. W.; Crawford, C. A.; Holm, R. H. Metal Ion Incorporation Reactions of the Cluster $[Fe_3S_4(LS_3)]^{3-}$, Containing the Cuboidal $[Fe_3S_4]^0$ Core. *J. Am. Chem. Soc.* **1997**, *119* (27), 6242–6250.

(56) Zhou, J.; Holm, R. H. Synthesis and Metal Ion Incorporation Reactions of the Cuboidal Fe_3S_4 Cluster. *J. Am. Chem. Soc.* **1995**, *117* (45), 11353–11354.

(57) Zhou, J.; Hu, Z.; Münck, E.; Holm, R. H. The Cuboidal Fe_3S_4 Cluster: Synthesis, Stability, and Geometric and Electronic Structures in a Non-Protein Environment. *J. Am. Chem. Soc.* **1996**, *118* (8), 1966–1980.

(58) Ciurli, S.; Ross, P. K.; Scott, M. J.; Yu, S. B.; Holm, R. H. Synthetic Nickel-Containing Heterometal Cubane-Type Clusters with $NiFe_3Q_4$ Cores (Q = Sulfur, Selenium). *J. Am. Chem. Soc.* **1992**, *114* (13), 5415–5423.

(59) Zhou, J.; Scott, M. J.; Hu, Z.; Peng, G.; Munck, E.; Holm, R. H. Synthesis and Comparative Reactivity and Electronic Structural Features of $[MFe_3S_4]^{z+}$ Cubane-Type Clusters (M = Iron, Cobalt, Nickel). *J. Am. Chem. Soc.* **1992**, *114* (27), 10843–10854.

(60) Brown, A. C.; Suess, D. L. M. An Open-Cuboidal $[Fe_3S_4]$ Cluster Characterized in Both Biologically Relevant Redox States. *J. Am. Chem. Soc.* **2023**, *145* (4), 2075–2080.

(61) Brown, A. C.; Suess, D. L. M. Controlling Substrate Binding to Fe_4S_4 Clusters through Remote Steric Effects. *Inorg. Chem.* **2019**, *58*, 5273–5280.

(62) Brown, A. C.; Thompson, N. B.; Suess, D. L. M. Evidence for Low-Valent Electronic Configurations in Iron-Sulfur Clusters. *J. Am. Chem. Soc.* **2022**, *144* (20), 9066–9073.

(63) Bostelaar, T. M.; Brown, A. C.; Sridharan, A.; Suess, D. L. A General Method for Metallocluster Site-Differentiation. *Nat. Synth.* **2023**, 1–9.

(64) Deng, L.; Bill, E.; Wieghardt, K.; Holm, R. H. Cubane-Type Co_4S_4 Clusters: Synthesis, Redox Series, and Magnetic Ground States. *J. Am. Chem. Soc.* **2009**, *131* (31), 11213–11221.

(65) Gillen, J. H.; Moore, C. A.; Vuong, M.; Shajahan, J.; Anstey, M. R.; Alston, J. R.; Bejger, C. M. Synthesis and Disassembly of an Organometallic Polymer Comprising Redox-Active Co_4S_4 Clusters and Janus Biscarbene Linkers. *Chem. Commun.* **2022**, *58* (31), 4885–4888.

(66) Ray, M.; Golombek, A. P.; Hendrich, M. P.; Young, Victor G.; Borovik, A. S. Synthesis and Structure of a Trigonal Monopyramidal Fe(II) Complex and Its Paramagnetic Carbon Monoxide Derivative. *J. Am. Chem. Soc.* **1996**, *118* (25), 6084–6085.

(67) Nguyen, D. H.; Hsu, H.-F.; Millar, M.; Koch, S. A.; Achim, C.; Bominaar, E. L.; Münck, E. Nickel(II) Thiolate Complex with Carbon Monoxide and Its Fe(II) Analog: Synthetic Models for CO Adducts of Nickel−Iron-Containing Enzymes. *J. Am. Chem. Soc.* **1996**, *118* (37), 8963–8964.

(68) Davies, S. C.; Durrant, M. C.; Hughes, D. L.; Richards, R. L.; Sanders, J. R. Iron, Cobalt and Vanadium Complexes of the $N(CH_2CH_2S)_3^{3-}$ Ligand with Chloride, Azide, Cyanide and Carbonyl Co-Ligands. *J. Chem. Soc. Dalton Trans.* **2000**, No. 24, 4694–4701.

(69) Lee, Y.; Peters, J. C. Silylation of Iron-Bound Carbon Monoxide Affords a Terminal Fe Carbyne. *J. Am. Chem. Soc.* **2011**, *133* (12), 4438–4446.

(70) Rittle, J.; Peters, J. C. Fe–N_2/CO Complexes That Model a Possible Role for the Interstitial C Atom of FeMo-Cofactor (FeMoco). *Proc. Natl. Acad. Sci.* **2013**, *110* (40), 15898–15903.

(71) Arnett, C. H.; Chalkley, M. J.; Agapie, T. A Thermodynamic Model for Redox-Dependent Binding of Carbon Monoxide at Site-Differentiated, High Spin Iron Clusters. *J. Am. Chem. Soc.* **2018**, *140* (16), 5569–5578.

(72) Detrich, J. L.; Konečný, R.; Vetter, W. M.; Doren, D.; Rheingold, A. L.; Theopold, K. H. Structural Distortion of the TpCo-L Fragment (Tp = Tris(Pyrazolyl)Borate). Analysis by X-Ray Diffraction and Density Functional Theory. *J. Am. Chem. Soc.* **1996**, *118* (7), 1703–

(73) Hu, X.; Castro-Rodriguez, I.; Meyer, K. Dioxygen Activation by a Low-Valent Cobalt Complex Employing a Flexible Tripodal *N*-Heterocyclic Carbene Ligand. *J. Am. Chem. Soc.* **2004**, *126* (41), 13464–13473.

(74) Chomitz, W. A.; Arnold, J. Substitution and Reaction Chemistry of Cobalt Complexes Supported by $[N_2P_2]$ Ligands. *Inorg. Chem.* **2009**, *48* (7), 3274–3286.

(75) MacNeil, C. S.; Mendelsohn, L. N.; Zhong, H.; Pabst, T. P.; Chirik, P. J. Synthesis and Reactivity of Organometallic Intermediates Relevant to Cobalt-Catalyzed Hydroformylation. *Angew. Chem. Int. Ed.* **2020**, *59* (23), 8912–8916.

(76) Pasynskii, A. A.; Eremenko, I. L.; Katugin, A. S.; Gasanov, G. Sh.; Turchanova, E. A.; Ellert, O. G.; Struchkov, Yu. T.; Shklover, V. E.; Berberova, N. T.; Sogomonova, A. G.; Okhlobystin, O. Yu. The Effect of Electron Deficit on the Geometry of Sulphide Bridged Methylcyclopentadienylmetal Tetrahedra. Synthesis, Physicochemical Characteristics, and Molecular Structures of $Cp'_3Cr_3(\mu_3\text{-}S)_4Co(CO)$, $Cp'_4Cr_4(\mu_3\text{-}O)(\mu_3\text{-}S)^{3+}$ $ZnCl_3\cdot C_4H_8O^-$, and $Cp'_4V_4S_4$ ($Cp' = \pi\text{-}CH_3C_5H_4$). *J. Organomet. Chem.* **1988**, *344* (2), 195–213.

(77) Curtis, M. D.; Riaz, U.; Curnow, O. J.; Kampf, J. W.; Rheingold, A. L.; Haggerty, B. S. Molecular Structures of the Bimetallic Sulfido Clusters $Cp'_2Mo_2Co_2S_4(CO)_2$, $Cp'_2Mo_2Co_2S_3(\mu_3\text{-}PPh)(CO)_2$, $Cp'_3Mo_3CoS_4(CO)$, and $Cp'_3Mo_3FeS_4(SH)$. *Organometallics* **1995**, *14* (11), 5337–5343.

(78) Herbst, K.; Dahlenburg, L.; Brorson, M. Synthesis of the New, Cubane-like W_3S_4Co Cluster Core. Completion of the Homologous Series $[(\eta^5\text{-}Cp')_3M_3S_4Co(CO)]$ (M = Cr, Mo, W). *Inorg. Chem.* **2004**, *43* (11), 3327–3328.

(79) Feliz, M.; Llusar, R.; Uriel, S.; Vicent, C.; Coronado, E.; Gómez-García, C. J. Cubane-Type Mo_3CoS_4 Molecular Clusters with Three Different Metal Electron Populations: Structure, Reactivity and Their Use in the Synthesis of Hybrid Charge-Transfer Salts. *Chem. – Eur. J.* **2004**, *10* (17), 4308–4314.

(80) Alberola, A.; Llusar, R.; Vicent, C.; Andrés, J.; Polo, V.; Gómez-García, C. J. Synthesis and Molecular and Electronic Structures of a Series of Mo_3CoSe_4 Cluster Complexes with Three Different Metal Electron Populations. *Inorg. Chem.* **2008**, *47* (9), 3661–3668.

(81) Kisko, J. L.; Hascall, T.; Parkin, G. The Synthesis, Structure, and Reactivity of Phenyl Tris(3-Tert-Butylpyrazolyl)Borato Iron Methyl, $[^{Ph}Tp^{Bu^t}]$FeMe: Isolation of a Four-Coordinate Monovalent Iron Carbonyl Complex, $[^{Ph}Tp^{Bu^t}]$FeCO. *J. Am. Chem. Soc.* **1998**, *120* (40), 10561–10562.

(82) Deng, L.; Holm, R. H. Stabilization of Fully Reduced Iron− Sulfur Clusters by Carbene Ligation: The $[Fe_nS_n]^0$ Oxidation Levels (n = 4, 8). *J. Am. Chem. Soc.* **2008**, *130* (30), 9878–9886.

(83) Ye, S.; Bill, E.; Neese, F. Electronic Structures of the $[Fe(N_2)(SiP^iPr_3)]^{+1/0/-1}$ Electron Transfer Series: A Counterintuitive Correlation between Isomer Shifts and Oxidation States. *Inorg. Chem.* **2016**, *55* (7), 3468–3474.

(84) Beinert, H.; Holm, R. H.; Munck, E. Iron-Sulfur Clusters: Nature's Modular, Multipurpose Structures. *Science* **1997**, *277* (5326), 653–659.

(85) Carney, M. J.; Papaefthymiou, G. C.; Spartalian, K.; Frankel, R. B.; Holm, R. H. Ground Spin State Variability in $[Fe_4S_4(SR)_4]^{3-}$. Synthetic Analogues of the Reduced Clusters in Ferredoxins and Other Iron—Sulfur Proteins: Cases of Extreme Sensitivity of Electronic State and Structure to Extrinsic Factors. *J. Am. Chem. Soc.* **1988**, *110* (18), 6084–6095.

(86) Carney, M. J.; Papaefthymiou, G. C.; Frankel, R. B.; Holm, R. H. Alternative Spin States in Synthetic Analogues of Biological $[4Fe\text{-}4S]^+$ Clusters: Further Cases of Variable Ground

States and the Structure of $(Et_4N)_3[Fe_4S_4(S\text{-}o\text{-}C_4H_4S^tBu)_4]$, Containing a Reduced Cluster with a Compressed Tetragonal Distortion. *Inorg. Chem.* **1989**, *28* (8), 1497–1503.

(87) Pangborn, A. B.; Giardello, M. A.; Grubbs, R. H.; Rosen, R. K.; Timmers, F. J. Safe and Convenient Procedure for Solvent Purification. *Organometallics* **1996**, *15* (5), 1518–1520.

(88) Hintermann, L. Expedient Syntheses of the *N*-Heterocyclic Carbene Precursor Imidazolium Salts IPrHCl, IMesHCl and IXyHCl. *Beilstein J. Org. Chem.* **2007**, *3*, 22.

(89) Bantreil, X.; Nolan, S. P. Synthesis of *N*-Heterocyclic Carbene Ligands and Derived Ruthenium Olefin Metathesis Catalysts. *Nat. Protoc.* **2011**, *6* (1), 69–77.

(90) Herdtweck, E.; Peters, F.; Scherer, W.; Wagner, M. Sterically Demanding Ferrocene-Based Tris (1-Pyrazolyl) Borate Ligands. *Polyhedron* **1998**, *17* (7), 1149–1157.

(91) Connelly, N. G.; Geiger, W. E. Chemical Redox Agents for Organometallic Chemistry. *Chem. Rev.* **1996**, *96* (2), 877–910.

(92) Peters, J. C.; Johnson, A. R.; Odom, A. L.; Wanandi, P. W.; Davis, W. M.; Cummins, C. C. Assembly of Molybdenum/Titanium μ-Oxo Complexes via Radical Alkoxide C−O Cleavage. *J. Am. Chem. Soc.* **1996**, *118* (42), 10175–10188.

(93) Gabbaï, F. P.; Chirik, P. J.; Fogg, D. E.; Meyer, K.; Mindiola, D. J.; Schafer, L. L.; You, S.-L. An Editorial About Elemental Analysis. *Organometallics* **2016**, *35* (19), 3255–3256.

(94) Sridharan, A.; Brown, A. C.; Suess, D. L. M. A Terminal Imido Complex of an Iron–Sulfur Cluster. *Angew. Chem. Int. Ed.* **2021**, *60* (23), 12802–12806.

(95) McSkimming, A.; Suess, D. L. M. Dinitrogen Binding and Activation at a Molybdenum–Iron–Sulfur Cluster. *Nat. Chem. 2021 137* **2021**, *13* (7), 666–670.

(96) Kuveke, R. E. H.; Barwise, L.; van Ingen, Y.; Vashisth, K.; Roberts, N.; Chitnis, S. S.; Dutton, J. L.; Martin, C. D.; Melen, R. L. An International Study Evaluating Elemental Analysis. *ACS Cent. Sci.* **2022**, *8* (7), 855–863.

(97) Smallcombe, S. H.; Patt, S. L.; Keifer, P. A. WET Solvent Suppression and Its Applications to LC NMR and High-Resolution NMR Spectroscopy. *J. Magn. Reson. A* **1995**, *117* (2), 295–303.

(98) Stoll, S.; Schweiger, A. EasySpin, a Comprehensive Software Package for Spectral Simulation and Analysis in EPR. *J. Magn. Reson.* **2006**, *178* (1), 42–55.

(99) Prisecaru, I. WMOSS4 Mössbauer Spectral Analysis Software. www.wmoss.org.

(100) Hubschle, C. B.; Sheldrick, G. M.; Dittrich, B. ShelXle: A Qt Graphical User Interface for SHELXL. *Journal of Applied Crystallography*, 2011, *44*, 1281–1284.

(101) Bain, G. A.; Berry, J. F. Diamagnetic Corrections and Pascal's Constants. *J. Chem. Educ.* **2008**, *85* (4), 532.

(102) Spek, A. L. PLATON SQUEEZE: A Tool for the Calculation of the Disordered Solvent Contribution to the Calculated Structure Factors. *Acta Crystallogr. Sect. C Struct. Chem.* **2015**, *71* (1), 9–18.